



Mehran Kiani-Oshtorjani

**REAL-TIME EFFICIENT COMPUTATIONAL APPROACHES
FOR HYDRAULIC COMPONENTS AND PARTICULATE
ENERGY SYSTEMS**



Mehran Kiani-Oshtorjani

REAL-TIME EFFICIENT COMPUTATIONAL APPROACHES FOR HYDRAULIC COMPONENTS AND PARTICULATE ENERGY SYSTEMS

Dissertation for the degree of Doctor of Science (Technology) to be presented with due permission for public examination and criticism at Lappeenranta-Lahti University of Technology LUT, Lappeenranta, Finland on the 11th of December, 2020, at 14:00 pm.

Acta Universitatis
Lappeenrantaensis 944

Supervisors Associate Professor Payman Jalali
LUT School of Energy Systems
Lappeenranta-Lahti University of Technology LUT
Finland

Professor Aki Mikkola
LUT School of Energy Systems
Lappeenranta-Lahti University of Technology LUT
Finland

Reviewers Distinguished Professor Goodarz Ahmadi
Department of Mechanical and Aeronautical Engineering
Clarkson University
USA

Professor Kari Koskinen
Automation Technology and Mechanical Engineering
Tampere University
Finland

Opponents Distinguished Professor Goodarz Ahmadi
Department of Mechanical and Aeronautical Engineering
Clarkson University
USA

Professor Kari Koskinen
Automation Technology and Mechanical Engineering
Tampere University
Finland

ISBN 978-952-335-608-5
ISBN 978-952-335-609-2 (PDF)
ISSN-L 1456-4491
ISSN 1456-4491

Lappeenranta-Lahti University of Technology LUT
LUT University Press 2020

Abstract

Mehran Kiani-Oshtorjani

Real-Time Efficient Computational Approaches for Hydraulic Components and Particulate Energy Systems

Lappeenranta, 2020

83 pages

Acta Universitatis Lappeenrantaensis 944

Diss. Lappeenranta-Lahti University of Technology LUT

ISBN 978-952-335-608-5, ISBN 978-952-335-609-2 (PDF), ISSN-L 1456-4491, ISSN 1456-4491

The so-called fourth industrial revolution requires high-speed data transmission and application of real-time computation to the phenomena. These two technologies highlight the potential of the digital-twin concept for industrial applications: cyber-physical systems form the core of ‘Industry 4.0’, in which physical systems are integrated with doubles created in cyberspace. The most important feature of cyber-physical systems is precisely the data-transmission and calculation speeds involved. Thanks to 5G technology, data transmission is substantially expedited without unacceptable losses in reliability. A challenge remains, however: developing a reliable and cost-effective way to increase the speed of calculations sufficiently for real-time simulation. Two main strategies are employed to this end. The first approach is to adjust the algorithms to perform fewer mathematical operations while designing them to be appropriate for parallel computing in line with MPI or OpenMP standards. The other approach entails using hardware such as GPUs, FPGA micro-controllers, and other systems with high-speed clocks. The latter solution is not suitable for some sensitive applications, wherein such factors as cost, weight, and other issues of economy render fast algorithms the only viable option. Industrial devices can be roughly grouped into machinery and energy systems. Usually in a machinery system, a multibody mechanism operates as a subsystem with a fluid power module and a control circuit. As the literature shows, the greatest challenge such a system presents for real-time simulation is related to fluid power systems. Indeed, if the singularity problem of fluid power systems can be resolved, one could simulate the whole package in real time. Therefore, the author set out to shed some light on the origin of this problem, from a mathematical point of view and then with regard to its physical interpretation. Recognising that the stiffness problem associated with hydraulic circuits follows primarily from three elements – the orifice model, the presence of a small volume in the circuit, and bulk modulus models – the author developed several recommendations. The author suggests using a two-regime orifice model, documented in the literature, wherever the pressure drop approaches zero. Introducing a perturbed model to eliminate the stiffness problem arising from the smallness of the volume, the author implemented corresponding algorithms with a simple hydraulic circuit and found this model able to increase the integration time step by one order. In addition, the model is successfully applied to a four-bar mechanism and determined that it can make the computation 2.5 times faster. After investigating several methods to alleviate the stiffness problem created by the small volume, it

is concluded that the perturbed model is best suited to a wide range of conditions, irrespective of the complexity of the hydraulic circuit. At the core of the stiffness challenge posed by fluid power systems is the difference in responses between time scales; however, because the small time scales can be ignored in hydraulic systems, the perturbed model poses no problem. Energy systems, on the other hand, involve various phenomena, occurring on different spatial scales. Therefore, coupling simulations performed at two scales improves accuracy and increases the simulation speed. Some algorithms are introduced for either of these scales, suitable for parallel computing, and implemented for a GPU via CUDA C and PGI CUDA Fortran compilers. By employing the lattice Boltzmann methods (LBM) developed, the author investigated the fluid flow through a porous medium created with spherical particles. In addition, the thermal behaviour of saturated porous media was studied under several heat-source conditions. The lattice Boltzmann model was validated by comparing its results with those of another LBM model and also Fluent software. The project also investigated the effects of external load on the thermal response of a packed bed– generated with spherical particles– by using thermal discrete element method (TDEM). It became evident that increasing the external load reduced the probability of vertically oriented contacts, thereby diminishing the effective thermal conductivity. Also, from among the particle shapes examined, TTeT offered the highest thermal effective thermal conductivity, followed by a packed bed generated with cubic particles. The author ascertained that, while the contact area alone is not a sufficient parameter to express the effective thermal conductivity behaviour of granular packed beds, contact angle isotropy emerged as a parameter that can explain the trend of effective thermal conductivity. For the shapes investigated, an exponential relationship was identified between effective thermal conductivity and contact angle isotropy. To investigate the effects of the fluid on the thermal conduction, several particle clusters are chosen at random and resolved the temperature field both for fluid and for solid. The author concluded that the fluid presence is more influential if the solid-to-fluid thermal conductivity ratio is below 10. Above this threshold, the vacuum and different fluids do not have a significant effect on the effective thermal conductivity of packed bed and one can simply assume vacuum in TDEM simulations.

Keywords: real-time simulation, multi-scale simulation, parallel computing, fluid power systems, granular materials, heat transfer, multiphase flows, algorithm design, lattice Boltzmann method, thermal discrete-element method, discrete-element method, graphics processing unit

Acknowledgements

The research was carried out at the School of Energy Systems in LUT University, Finland, within 2016 and 2020.

I would like to express my sincerest thanks to my supervisors, Associate Professor Payman Jalali and Professor Aki Mikkola, for providing me with the opportunity for the research and for their guidance over these years. Your encouragement and trust have been a source of inspiration and motivation for me, keeping me moving forward. I wish to express my sincerest gratitude also to my preliminary examiners, Professor Goodarz Ahmadi and Professor Kari Koskinen, for their efforts in reviewing this work and offering valuable and constructive comments and suggestions.

I express my most profound gratitude to Professor Charley Wu at the University of Surrey for giving me the opportunity to visit his laboratory and collaborate with the people working there. Deserving special thanks is Dr Nicolin Govender, for his support at the University of Surrey and for giving me the opportunity to become one of the developers of Blaze-DEM GPU-based code. We have had many Skype talks and chats, and we will continue this pleasant and fruitful collaboration.

I am grateful to Professor Heikki Handroos for his guidance, my discussions with him, and all our collaboration, and I extend special thanks to Professor Tero Tynjälä and to my friends and colleagues in both the Mechanical Engineering Department and the Energy Technology Department.

Finally, my deepest and eternal thanks to my mother and father, who showed me the path of love and beauty. I am forever grateful also to my brothers, Mahdi and Mehrdad, for their encouragement and support.

Mehran Kiani-Oshtorjani
December 2020
Lappeenranta, Finland

To my lovely mother and father

Contents

Abstract

Acknowledgements

Contents

List of publications	11
1 Introduction	13
1.1 The Internet of things	13
1.2 The digital twin	14
1.2.1 Digital-twin applications	16
1.2.2 Digital twins for reconfigurable manufacturing systems	16
1.2.3 Digital twins in gauging remaining service life	17
1.2.4 Digital twins' challenges	17
1.3 Real-time machinery simulation	18
1.4 Real-time energy systems' simulation	20
1.5 Real-time simulation tools and standards	21
1.5.1 Standardised interfaces: the Functional Mock-up Interface	22
1.5.2 Parallel computing	22
2 Real-time simulation of machinery systems	23
2.1 The stiffness problem in fluid power systems	25
2.1.1 The lumped-fluid theory	25
2.1.2 Mathematical description of the stiffness problem	26
2.1.3 Physical interpretation of the stiffness problem	27
2.2 Fluid power stiffness due to orifice models	28
2.3 Fluid power stiffness due to small volumes	30
2.3.1 The pseudo-dynamic method	31
2.3.2 Singular perturbation theory	32
2.3.3 The method of multiple scales	33
2.4 Bulk modulus models	36
2.5 Results and discussion	38
3 Real-time simulation of energy systems	45
3.1 Porous media	46
3.2 The lattice Boltzmann method	47
3.2.1 The BBGKY hierarchy of equations	48
3.2.2 The Boltzmann transport equation	49
3.2.3 A lattice Boltzmann model for granular materials	50
3.2.4 A thermal lattice Boltzmann model for granular materials	53
3.2.5 A conjugate lattice Boltzmann model for granular materials	54

3.3	The discrete-element method	55
3.4	The thermal discrete-element method	59
3.5	Results and discussion	61
4	Summary and conclusions	67
	References	71
	Publications	

List of publications

Publication I

M. Kiani-Oshtorjani, A. Mikkola, P. Jalali, ‘Numerical treatment of singularity in hydraulic circuits using singular perturbation theory’, *IEEE/ASME Transactions on Mechatronics*, vol. 24, pp. 144–153, 2018.

Publication II

J. Rahikainen, M. Kiani-Oshtorjani, J. Sopanen, P. Jalali, A. Mikkola, ‘Computationally efficient approach for simulation of multibody and hydraulic dynamics’, *Mechanism and Machine Theory*, vol. 130, pp. 435–446, 2018.

Publication III

M. Kiani-Oshtorjani, P. Jalali, ‘Thermal and hydraulic properties of sphere packings using a novel lattice Boltzmann model’, *International Journal of Heat and Mass Transfer*, vol. 130, pp. 98–108, 2019.

Publication IV

M. Kiani-Oshtorjani, P. Jalali, ‘Thermal discrete element method for transient heat conduction in granular packing under compressive forces’, *International Journal of Heat and Mass Transfer*, vol. 145, pp. 118753, 2019.

Other Publications

M. Kiani-Oshtorjani, S. Ustinov, H. Handroos, P. Jalali, A. Mikkola, ‘Real-time simulation of fluid power systems containing small oil volumes, using the method of multiple scales’, *IEEE Access*, vol. 8, pp. 196940–196950, 2020.

N. Govender, P.W. Cleary, M. Kiani-Oshtorjani, D.N. Wilke, C.Y. Wu, H. Kureck, ‘The effect of particle shape on the packed bed effective thermal conductivity based on DEM with polyhedral particles on the GPU’, *Chemical Engineering Science*, vol. 219, pp. 115584, 2020.

M. Mohammadi, M. Kiani-Oshtorjani, A. Mikkola, ‘The effects of oil entrained air on the dynamic performance of a hydraulically driven multibody system’, *International Review on Modelling and Simulations*, vol. 13, pp. 141–147, 2020.

Q. Lu, J. Tiainen, M. Kiani-Oshtorjani, J. Ruan, ‘Radial flow force at the annular orifice of a two-dimensional hydraulic servo valve’, *IEEE Access*, vol. 8, pp. 207938–207946, 2020.

M. Kiani-Oshtorjani, A. Mikkola, P. Jalali, ‘Novel Thermodynamics-based model to estimate bulk modulus in hydraulic systems: A verification of the LMS model’, *Submitted*.

M. Kiani-Oshtorjani, A. Mikkola, P. Jalali, ‘Conjugate heat transfer in isolated granular clusters with interstitial fluid using a novel lattice Boltzmann method on the GPU’, *Submitted*.

The author's contribution

Publication I

Mehran Kiani-Oshtorjani introduced the perturbed model and implemented it in Simulink for a hydraulic circuit as presented in the paper. He wrote the article and investigated the results.

Publication II

Jointly, Mehran Kiani-Oshtorjani and Jarkko Rahikainen implemented the perturbed model with a four-bar mechanism and wrote the paper. The simulations were handled via MATLAB code.

Publication III

Mehran Kiani-Oshtorjani introduced a novel lattice Boltzmann model for simulation of fluid flow through a porous zone. He derived the mathematical formulae and implemented the model in the Fortran programming language. In addition, he introduced a new thermal lattice Boltzmann model to resolve the energy equation for phenomena in porous media by considering local heat sources. Mehran Kiani-Oshtorjani investigated the results and wrote the paper.

Publication IV

Mehran Kiani-Oshtorjani introduced a novel thermal discrete element model to resolve the energy equation for granular materials. He derived the mathematical description of the model and implemented it in C/C++ programming. Also, he both analysed the results and wrote the paper.

1 Introduction

Product complexity and demands for higher quality are increasing every day. Alongside that, pressure to bring products to market more rapidly is still growing and has become a key parameter for many corporations hoping to compete in today's marketplace. In addition, the performance of industrial devices is often important to consider, as energy prices are high and environmental issues are critical for humanity. Attention to these parameters is leading to what has been termed the fourth industrial revolution, or Industry 4.0 [1]. The first industrial revolution brought mechanisation, hydraulic and steam-powered machines, and use of such energy resources as coal and water [2], and the second one took place when the potential of electricity and of mass production were harnessed for advanced manufacturing techniques (e.g., on production lines) [3], in developments associated with changes described as ushering in the 'new economy' [4]. The third revolution in industry began gaining momentum in 1950 with the invention of computers and the Internet. It can be characterised as the implementation of information technology with electronic and other control systems that enable automated production [5]. It is expected that, with the Internet and computers having transformed the world economy, this change will continue, propelled with the concept of the Internet of things (IoT), and thereby complete a fourth industrial revolution [6]. Hence, the Industry 4.0 era is linked with machinery and energy devices equipped with sensors, cameras, and other interfaces that obtain data about machines' state of operation, their performance, product quality, and any errors that may arise – all in real time. Consequently, real-time analysis of said data should aid in enhancing performance, making efficiency improvements, and preventing system errors [7, 1].

One of the key facets of the IoT is the speed at which the calculations should be performed, for a real-time platform. With simulation in real time, the computation time must be no greater than the physical time the relevant phenomenon (process) takes to occur in nature (industry). At the same time, real-time computation serves as an important source for Big Data operations. The data produced should be processed on a real-time platform when one uses such techniques as Internet of Things technology and what is known as the digital-twin approach.

At this juncture, it is important to distinguish correctly between the IoT and the digital-twin mechanism. The target with the former is to establish connections among more than two physical objects and control them via the Internet, while a digital twin (DT) is a replica of a physical device, process, system, product, etc. in computation software, with this replica exchanging data with the physical entity. Both technologies entail connections involving subsystems; however, one of the subsystems in the digital-twin approach is a replica of the physical one while in the IoT each of the subsystems can be distinguished as a separate entity.

1.1 The Internet of things

The Internet of things, also called the industrial Internet or the Internet of everything, is defined as a global network among diverse industrial devices and machines, sending and

receiving data to/from each other over the network. Every physical object connecting to the IoT is regarded as an ‘edge node’ of the IoT system [8]. Five technologies for development of IoT products have been highlighted as particularly important [9]:

- radio frequency identification (RFID)
- wireless sensor networks (WSNs)
- middleware
- cloud computing
- IoT application software

In this list, ‘cloud computing’ refers to a central server that stores and processes the masses of data produced by the IoT edge nodes. The numerous links enabling the interaction between edge nodes generate an enormous quantity of data, which cannot be stored and processed at these nodes themselves, for reason of their limited capabilities [8]. These data are usually created by means of ‘smart’ embedded devices such as cameras, sensors, and other measurement tools that act as an interface between physical spaces and cyber-spaces.

Sometimes, the computations require a real-time platform because of the IoT’s nature as a multidisciplinary ecosystem demanding real-time data-processing and feedback. Chen et al. recently introduced the ‘Real-Time Internet of Things’ (RT-IoT) concept to highlight the strict safety and timing requirements involved, as any deviations from the normal operation of such systems could damage the system/environment or even threaten the human safety [10]. Still, this concept does not address high-speed **calculations**, in that cloud computing is not applicable in circumstances wherein real-time processing, low latency, and high quality of service (QoS) are important [11]. At the same time, for cost and efficiency reasons, smaller enterprises desire a solution to utilize the most of their local computing resources [12, 13]. Responding to such challenges necessitates a flexible technology. Hence, edge computing is emerging as a distributed computing technology that improves on cloud computing.

The European Telecommunications Standards Institute (ETSI) has presented the network concept of multi-access edge computing (MEC), intended to empower cloud computing with real-time operation. According to ETSI [14], MEC can be utilised to connect with and control remote devices, with real-time processing of data and feedback. It aggregates and distributes the IoT services in a mobile base-station environment which is highly distributed and allows fast response to the users of applications in real time.

1.2 The digital twin

The replica of a physical device can be considered an edge-of-IoT system connected to the physical one and exchanging data with it. Under this definition, there are three levels of integrity for the cyber-physical system coupling – namely, ‘digital-model’, ‘digital-shadow’, and ‘digital-twin’, sometimes wrongly regarded as synonyms [15, 16]. The

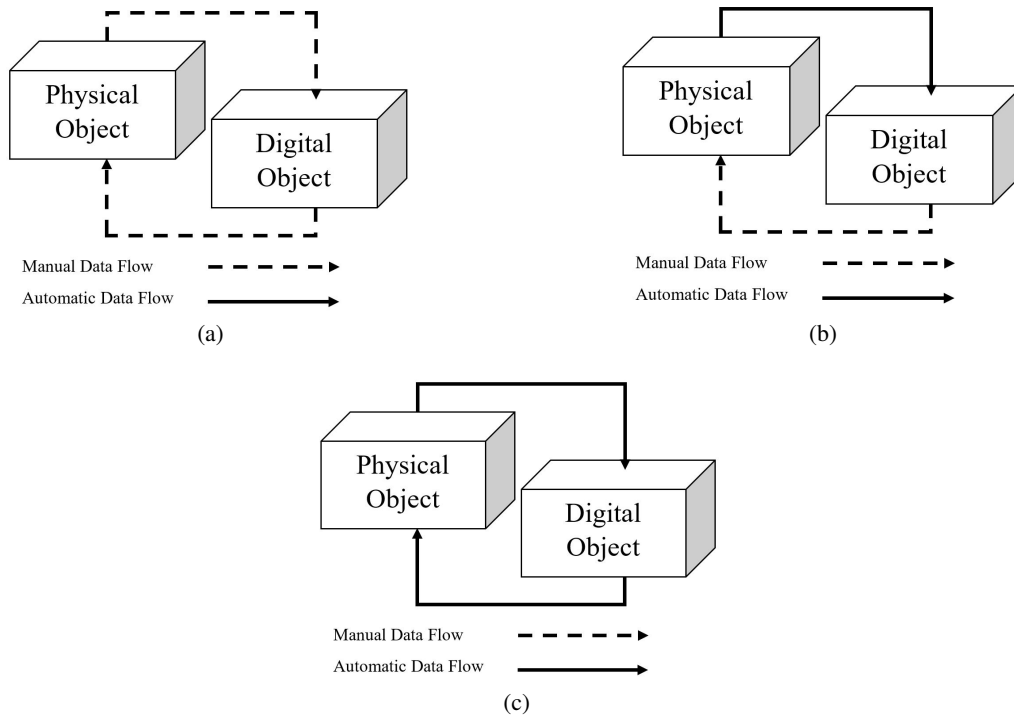


Figure 1.1: Data flow with a digital model (a), a digital shadow (b), and a digital twin (c).

differentiation is based on the type of data exchange between the physical and the ‘cyber’ parts of the cyber-physical system. The system is called a digital model if the digital representation of the physical entity is not connected to the existing device and the data flow is manual during modelling, as depicted in Figure 3.12a. In a digital model, system data flow neither from physical object to digital one nor *vice versa*. If data flow from the physical object to the digital one and not in the opposite direction, as illustrated in Figure 3.12b, the system is called a digital shadow. In systems of this sort, any change to the physical device affects the simulations performed in the digital system, while the simulation results do not have any influence over the physical device.

Finally, in a digital-twin set-up, as shown in Figure 3.12e, the digital and physical subsystems are fully integrated, so the real-time exchange of data keeps them updated and synchronised, and the simulations are performed in a time span comparable with true physical time. The subsystem updating takes place via instantaneous data flow from the physical entity to its digital twin and *vice versa*. For various purposes, including product design, energy-efficiency enhancements to industrial devices, a reconfigurable manufacturing system (RMS) approach, and assessment of the remaining useful life (RUL) of industrial equipment [17], digital-twin technology is vital. It affords monitoring and maintenance services, and it aids in management, optimisation, and safety work for production lines and products [18].

1.2.1 Digital-twin applications

Although the digital twin (DT) has a wide range of applications, the discussion here continues with a brief explanation that focuses on the last two of those listed above: RMS development and RUL assessments.

1.2.2 Digital twins for reconfigurable manufacturing systems

In a flexible (or smart) production line, specific sets of changes in the process or materials cause various other products to be produced. Reconfigurable manufacturing systems were originally introduced in a paper by Koren et al. [19] in which the authors suggested that high-frequency change in the competitive global market demands quick and cost-effective responses. Even highly controllable production lines suffer from flexibility constraints, as many industrial robots are mapped with characteristics of complex functions and the manufacturing devices are restricted by inflexible programming [20]. Traditional production lines can only accommodate tiny variations in the product [21]. On the other hand, customisation of products is rapidly leading factories toward flexible production lines on which reconfiguration of hardware–software elements is performed easily. This is challenging: reconfiguration of elements should consider multidimensional optimisation variables such as business and marketing concerns, the timing/schedules for delivery of products, the sequence of processes, environmental impact, etc. To achieve manufacturing that is smart enough to cope with such a landscape, a digital twin of the process should be available for investigation of whether or not the planned changes to the production line truly are going to yield the desired product. Also, they can inform checking for mistakes in the practical reconfiguration and making sure all the requirements are met [22]. This technology provides a powerful simulation tool for examining any variations in the configuration of a manufacturing system [23].

Zhang et al. [20] have proposed a digital-twin virtual entity (DTVE) model for a reconfigurable DT-based manufacturing system (RDTMS). Their model covers five dimensions: a geometric model (GM), physical model (PM), capability model (CM), behaviour model (BM), and rule model (RM). The first, $GM = f(\text{Shape, Size, Location, Rotation, etc.})$, represents the need to perform 3D virtual visualisation of the process for monitoring and management purposes [24]. The physical one, $PM = f(\text{Speed, Mass, Friction, Abrasion, etc.})$, is necessary for assessing the functionality of various configurations by predicting the results, evaluating performance, and planning the optimisation of various alternatives [25, 26]. With the CM, in turn, the goal is to identify the complementary devices that should be connected as functional interfaces. Therefore, it is essential to know the capabilities of each entity in the physical layer in this model [27]: what it can do and what can be done [20], $CM = f(\text{Cando, Isdoing, Canbedone, Isbeingdone, etc.})$.

Each of a production line's devices has a function to perform in completing the production of a product. Some of these elements – e.g., robots and machining tools under computer control – apply patterns of logical behaviour and should be dealt with as independent units to reduce the inflexible programming [20]. Consequently, the behaviour logic of all entities in the physical manufacturing system should be determined through the BM [28], $BM = f(\text{Take, Motor}_n, \text{Wait, Fault})$. In the final stage, some rules derived by

experts or mined from Big Data would be expected, to ensure the safety of all the entities' operations (the interfaces' rules should be compatible, the larger system must comply with certain standards, etc.).

1.2.3 Digital twins in gauging remaining service life

The digital-twin concept was proposed for public use in a NASA document on technology roadmaps, Technology Area 11 [29]. This document describes a DT collecting sensor data from a vehicle's on-board Integrated Vehicle Health Management (IVHM) system, the historical data available from maintenance services, etc. obtained via text-mining and other data-mining. Combining all of this information, the digital twin would instantaneously forecast the mission success probability, the health of the vehicle/system, and its remaining useful life. The DT's on-board systems would be capable of performance degradation or mitigating damages in the system by suggesting changes in operation profile that increase both likelihood of operation accomplishment and the lifespan [30, 29]. Therefore, digital-twin technology has been considered a framework for predictive maintenance strategy [31].

1.2.4 Digital twins' challenges

Several challenges stand in the way of a highly capable digital-twin service. such as lack of extensive enough IT infrastructure, accuracy issues with the data generated, matters of the data's trustworthiness, and security issues related to the algorithms and technologies used in the DT, as mentioned by [15].

The IT infrastructure should be capable of executing very computationally expensive algorithms for either carrying out simulations or obtaining a reliable result from the corresponding Big Data. The way to handle expensive computations is to use multiple graphics processing units (GPUs) to provide the essential computation resources. The alternative to GPUs is on-demand use of cloud computing, taking advantage of online resources provided by Google, Amazon, Nvidia, etc. These resources are accompanied by such trade-offs as the cost of GPUs being higher than that of on-demand cloud resources whereas GPUs allow higher-speed operation.

On the other hand, the speed and accuracy of simulations are inversely proportional; i.e., the higher the accuracy, the lower the speed. Therefore, the only way to maintain their accuracy while increasing the computation speed without simplifying the algorithms is to develop new algorithms, ones that do not demand as many computation operations and are better suited to parallel computing.

Another challenge in the shift toward DTs is to convince companies, other organisations, and users as to the gains with this technology. These parties might have concerns related to the reliability of the simulations, machine-learning algorithms, and system performance. One important means of increasing trust is to assure the managers that the data are secure and privacy is preserved. As they might deal with sensitive data of their customers, protection of digital-twin data is a matter of great importance.

1.3 Real-time machinery simulation

A machinery device constitutes a complex multi-physics system that has many components, including mechanical parts, hydraulic power systems, and control and electrical elements. The mechanical mechanism actuated with a hydraulic power system constitutes the main part of simulations, as these are governed by highly sophisticated equations with respect to the control system. The equations governing mechanical operations differ substantially from those dictating the behaviour of hydraulic systems, so different approaches are appropriate for solving them. In other words, multibody dynamics (MBD) is the main approach to simulating the behaviour of a mechanical mechanism, whereas the lumped fluid theory (LFT) is used for the hydraulic simulations. Clearly, the mechanics and the hydraulic power system should be considered as two separate subsystems.

The kinematics and dynamics of a mechanical mechanism are affected by the hydraulic forces exerted at various joint positions, and, in turn, it influences the hydraulic power system by imposing the reaction force on the piston in accordance with Newton's third law of motion. Thus, a two-way coupling can be said to exist between MBD and the LFT, with data to be exchanged accordingly at each time step.

The relationship between MBD and the LFT can be addressed via two commonplace strategies – a strong coupling strategy and a strategy of weak coupling [32]. With the former, also known as the unified approach [33], the MBD and LFT approaches are brought together in a single set of equations even though each is governed by its own distinct equation set. This approach is referred to also as monolithic simulation, since a single-part integrator can be used in which the integration technique and the time steps are identical between the two subsystems. Thus, the data transfer is made easier and less time-consuming. However, in most cases using the same time step leads to wasting computation resources for one of the subsystems, the one requiring larger time steps (usually, it is the MBD work that requires larger time steps while the LFT operations act with finer granularity, so employing the same integration time step expends CPU/GPU resources without significant change in the MBD output). Consequently, another approach, the strategy of weak coupling, has been introduced as an alternative especially for large systems in which the computation time difference is significant.

In that strategy, also known as the co-simulation or co-integration approach [34], the subsystems are separately integrated in a sequential and parallel manner via one or several environments (in co-integration and co-simulation, respectively) exchanging data at some points in the integration process [35]. Many commercial programs that use block diagram representations, Simulink among them, prioritise this strategy [32]. The advantage of the approach lies in the use of different integration time steps for various subsystems [36]. The main objective behind multi-rate integration is to reduce the integration time for those variables that change more slowly than do other variables, 'faster' ones that require a smaller integration time step [37]. In this approach, the subsystem requiring the larger integration time step 'leads' the simulation: it waits for a finer-granularity subsystem's calculations. Therefore, the subsystems are separately integrated and data exchange takes place at certain points in time when the subsystems have accomplished their tasks. The simulation platform has a significant influence over the data-exchange time. If simulation

of both subsystems is performed in a single environment (in co-integration), there is less data-transfer delay than exists when the solving work for each subsystems is handled in separate software (i.e., in a co-simulation approach). In both co-integration and co-simulation, finishing the calculations sooner frees resources for other tasks.

Weak-coupling-style simulations enjoy some advantages over those following a strong-coupling strategy, among which the modularity of the model can be highlighted as the most important. Each module is straightforwardly modelled by experts experienced in the corresponding fields. This produces specialised modelling. In addition, using special simulation tools allows one to modify the model with minimal effort without impinging much on other subsystems [35, 38]. Furthermore, the use of specific integrators with suitable time steps aids in preventing computation resources from going to waste, as they are targeted well for a specific purpose and with the relevant discipline in mind [39]. Nonetheless, for robust and trustworthy simulation, the issues of data-exchange delay, the stability of the solution, and speeds of interaction between modules must be addressed [33]. Common standards for interfacing between various modules have facilitated data exchange. Among these are such programming standards as that for the Functional Mock-up Interface (FMI) [40], elaborated upon further along in this chapter.

From a real-time simulation point of view, the first and fastest option is to create a unified set of equations (co-integration) in which the hydraulic system operates with the same time step as the multibody mechanism. It is worth mentioning that in a combined hydraulic and multibody system the hydraulic simulation takes smaller integration time steps than the multibody system integrator. Consequently, the hydraulics-governing equations constitute the more challenging part of the co-integration. From the modelling angle, a mechanical system actuated by hydraulics behaves differently at small vs. large time scale. In hydraulic circuit modelling wherein the large bulk modulus is divided into small volumes, small time scales appear. These increase the computation costs of simulations. As reported by Pfeiffer and Borchsenius [41], the high computation costs are rooted mainly in the mathematical representation of the hydraulic systems used in the simulations, which applies non-linear, first-order differential equations.

To achieve real-time co-integration (or co-simulation) of coupled systems, many algorithms have been proposed for speeding up the hydraulic simulations. Among these, iterative approaches such as a pseudo-dynamic method [42, 43, 44], the use of machine-learning techniques [45, 46, 47], and a perturbed model [48, 49] can be mentioned.

The main assumption under the LFT is that of a uniform pressure distribution within hydraulic volumes. Therefore, LFT hydraulic equation stiffness manifests itself principally with small hydraulic volumes, especially when the hydraulic effective bulk modulus is large. In qualitative terms, if the hydraulic volume is large, the hydraulic integration time step can be comparable with that involved in multibody dynamics and co-integration can lead to real-time simulation.

In circumstances in which small volumes appear in the circuit, one can avoid a small value for the volume, setting a bigger volume value instead. The assumption of this ‘artificial volume’, which forms the basis of the pseudo-dynamic method, leads to faster simulation and yields an estimated pressure that should be iteratively corrected. The estimated pressure is used for calculation of the in-flow and out-flow rates, through which

a correction gets made to the pressure, producing a closer approximation, and so on. This iterative loop ultimately yields a pressure approximate to the correct one for the small volume. Although this approach is fast on account of starting with a large volume, the iteration process can end up highly costly, to such an extent that the entire simulation falls outside the real-time domain.

Alongside such models presented to alleviate the stiffness of hydraulic systems, there have been several efforts to model the hydraulic components by means of machine-learning tools – e.g., a neural network [45, 46, 47]. However, these tools seem to be time-consuming, in that the number of neuron layers increases on the basis of the response resolution and the system’s complexity. Furthermore, the models are valid only within a limited operation range, which depends on the algorithms’ training data. In addition, as a black-box model, a neural model cannot guarantee physically appropriate behavior in all possible conditions.

With the origin of stiffness in the hydraulic equation being evident, its mathematical representation suggests that it follows a singular perturbation model [50]. The perturbed model simplifies the non-linear derivative equation to an algebraic equation [48] assembled into other non-stiff hydraulic equations. The resulting large time step for hydraulic integration, comparable with that for a multibody system, allows coupling in co-integration for real-time use.

1.4 Real-time energy systems’ simulation

Optimisation of the design and performance of energy systems such as boilers, mixers, dryers, industrial cyclones, and heat exchangers is crucial since they account for a large proportion of the facility’s energy consumption and their functioning significantly influences the quality of the products. In contrast against hydraulic and multibody systems, which may be stiff in some circumstances, calculations for fluid mechanics and heat transfer do not suffer from such a condition, because their numerical techniques do not employ an integrator.

The computation domain is continuous for fluids and discrete for particulate matter. The continuous medium of a fluid is usually valid for Knudsen numbers less than 0.01 (i.e., $Kn < 0.01$). The formula is $Kn = \frac{\lambda}{L}$, where λ is the mean free path length and L is characteristic physical length. Computational fluid dynamics (CFD) is the primary tool for solving for the velocity, pressure, and temperature fields in a continuous domain, with the finite-difference method (FDM), finite-volume method (FVM), and finite-element method (FEM) being some of the traditional approaches. Among the non-traditional, meshless approaches are smoothed-particle hydrodynamics (SPH) and the lattice Boltzmann method (LBM).

Using lattice Boltzmann (LB) equations is the fastest of the above-mentioned approaches [51, 52, 53]. For instance, solving them is 12–15 times faster than using Navier–Stokes (NS) equations with comparable mesh size and accuracy for large-eddy simulation (LES) of cavity-closed nose landing gear, as reported by NASA [27]. In this ‘apples-to-apples’ comparison, the same CPU types were used for the two approaches and the LBM was not optimised. The researchers mentioned that LB for 1.6 billion nodes is almost twice as fast

as NS solvers that work with 298 million cells. One can conclude that data localisation contributes critically to LB's computation efficiency in comparison to other, NS solvers. Therefore, there is a tendency to prefer the LBM for real-time applications such as those presented by [54], [55], [56], and [57]. In addition to possessing inherent speed, the LBM is highly suitable for parallel computing by means of either OpenMP/MPI standards or programming tailored for GPUs [58, 59].

Within the last decade, researchers have started to develop new LB models in line with their observations of complex phenomena in nature and sophisticated technologies in industry. Accordingly, various LB models have been proposed, for turbulent flow [60, 61, 62], multi-phase flow [63, 64, 65], reactive flow [66, 67, 68], heat transfer [69, 70] and phase change [71, 72], acoustics [73], combustion [74, 75, 76], fluid–solid interaction [77], etc., each of them working under quite specific conditions. Well-developed LBM models encourage the use of an LB solver to determine fluid flows in real time.

Although LBM models have the power to simulate a wide range of industrial applications, the individual energy devices operating and/or interacting with particulate matter should be independently modelled. For instance, dryers are used on many production lines processing such particulate matter as milk powders, whey products, coffee and tea, pulp and paper materials, pharmaceutical products, cocoa, ceramics, and carbon black. While the motion and related dynamics of particles of these sorts are most often tracked via a discrete-element method (DEM), the thermal response of granular materials may be simulated separately through specific thermal DEM, or TDEM, techniques.

In simulation of a sophisticated energy device, both the LBM and a DEM should be applied, to bring out all the details required for design purposes. Therefore, coupling these two sorts of solvers has been viewed as critical for two decades already. Their coupling is more efficient if both solvers are at the level of code; however, coupling pieces of commercial software is possible too: some provide the necessary interface and enable joint operation with certain other software. For instance, Ansys products can be linked with Rocky DEM easily. Meanwhile, the only approach for software that does not offer this capability is to write data to text files. In this scenario, the fastest method is to write the data to a FIFO special file in Windows or pipes in Linux, since these make use of memory available in RAM without having to resort to the hard disk.

Coupling two pieces of code proves far more efficient than software interfaces, because essential programming libraries such as MPI routines enable exploiting the multiple program, multiple data (MPMD) concept.

To protect intellectual property rights during coupling yet allow for exchange of models between the various sectors involved in a given project, the FMI initiative referred to earlier in this chapter was introduced. The core ideas behind it and similar standards are explained in the next section.

1.5 Real-time simulation tools and standards

Although algorithms such as the perturbed model presented in Section 1.3 can ameliorate some issues that plague coupling and can speed up simulations, the integration method, the use of parallel computing techniques either on the CPU side (e.g., MPI and OpenMP)

or on GPUs, the data-transfer platform and standards, processor clock speed, and the correct choice of operating system (OS) etc. all have significant influence on simulation costs. The most important factors affecting a real-time platform are introduced below. In addition, S-functions in MATLAB, user-defined functions in MSC's ADAMS and Fluent, the Silver module API for Silver, the External Model Interface in SimulationX, and user routines in Simpack are some examples of the tools provided for coupling purposes, each of them limited to certain applications.

1.5.1 Standardised interfaces: the Functional Mock-up Interface

One of the more recently developed tools facilitating model exchange and multi-physics co-simulation is the concept of the FMI. The corresponding standard provides users with the ability to combine their models within a Functional Mock-up Unit (FMU) package. An FMU, in turn, refers to the interaction between a text-based database (XML files) and C code [78]. This modelling is under development by the Modelica Association [79]. An alternative to the FMI standard is the High Level Architecture (HLA) [80], used for complex systems for which several simulations should be combined.

1.5.2 Parallel computing

The first prerequisite to real-time simulation is maximally efficient utilisation of the computing resources. These computation resources might consist of a few dedicated computers in a network, each with its own memory and no access to other computers' memory. Resources of this sort are referred to as distributed memory [81]. For exchanging the data between individual computers in the network, there has to be a standard. The MPI standard, covering up to 250 procedures, explicitly facilitates data exchange between a cluster's nodes for purposes of high-performance computing. This standard has been implemented for many programming languages, including Fortran and C/C++.

If, on the other hand, the memory is shared across several processors, the arrangement is a 'shared memory multiprocessor' set-up. Each processor can independently access the main memory. In a shared-memory multiprocessor, each processor has its own control system, allowing it to operate at any time. The CPUs typically contain several cores as independent processing units, each of them able, on its own, to handle several independent threads, which are instructions to be executed [82]. For instance, each core of an Intel Xeon Phi can execute four threads instantaneously [82]. The OpenMP standard provides subroutines to manage the threads executed by the program running on the shared-memory system.

The emergence of GPUs in the world of scientific computing has led many researchers to implement their programs on this platform [83]. The idea behind GPUs' use here is to have thousands of processing units, simpler and less powerful than what the CPU provides, each able to instantaneously act on one subroutine, with distinct data [82]. This approach offers a very powerful tool for performing the heavy calculation work needed in many areas of research.

2 Real-time simulation of machinery systems

Machinery devices are categorised as complex systems comprising many components – a multibody mechanism, fluid power system, control circuit, etc. – all interacting with each other simultaneously. Efforts at real-time simulation for this sort of complex system face several challenges:

- The first challenge, the main one, is created by differences in the simulation time required for various system entities, or ‘packages’. This challenge arises primarily from the stiffness aspect of fluid power systems in comparison to multibody mechanisms.
- The linkage in handling of the packages poses the second challenge. In circumstances involving separate packages developed by different research or industrial centres, both good exchange of data and the data’s confidentiality should be ensured.
- Delays can arise from using multiple pieces of software in the simulation process. For instance, if the solver for the hydraulic circuit is not the same as that for the multibody mechanism, there might be some delays in data exchange, especially if interface software is used to provide a connection between the two.



Figure 2.1: The main packages in an excavator are multibody mechanisms and the fluid power system.

Of the challenges listed, the first one, that created by simulation-time differences between packages, has the strongest effects on simulation time. Although there are many physical systems in a machinery system such as an excavator, as Figure 2.1 illustrates, the mechanical mechanism and fluid power systems are the most important ones from a real-time

simulation standpoint. Therefore, the comparison of time steps is between the solvers for these two. As reported in the literature [84, 49], the fluid power system most often requires smaller integral time steps in comparison to multibody solvers. The difference could be one or two orders, depending on the hydraulic system's complexity. Because the hydraulic and the multibody system are coupled, the solver for the latter should wait until the hydraulic solver accomplishes its calculations. In many cases, the fluid power system cannot be addressed on a real-time horizon, so simulation of the larger entity will be beyond the reach of real-time simulation. Therefore, it is critical to make the hydraulic solver faster. Before that, however, one must understand the origin of the problem. The difference in integral time steps between the two solvers could be due to the following factors:

- The orifice flow model can make the hydraulic model stiff. The orifice model can cause stiffness to rise as the pressure drop approaches zero. To avoid this problem, a two-regime orifice model should be used.
- It is typical for a small volume to be present in the fluid power system. This may create a reason for a small integral time step. In fluid power systems, the hydraulic components are usually modelled as hydraulic volumes in which the pressure is uniformly distributed and governed by the LFT. The stiffness challenge in hydraulic simulations appears when the hydraulic volume is small in comparison to neighbouring volumes.
- A large and inaccurate bulk modulus can render the whole system stiff. If the value of the bulk modulus is high and not predicted accurately, the small term $\frac{V}{B_e}$ appearing in hydraulic equations can create a singular problem.

The next section offers mathematical proof that the above-mentioned causes of stiffness in a fluid power system truly lie behind the problem.

For a sense of the situations in which these problems can accumulate, consider the excavator in Figure 2.1 to be at rest. In this case, the flow passing through the orifices is negligible and the pressure drop across them approaches zero; hence, the first problem can appear when machinery is at rest.

The hydraulic circuit of this excavator consists of several hydraulic cylinders and pistons as marked in Figure 2.2. The main role of these cylinder-and-piston arrangements is to exert hydraulic force on the mechanical mechanism and thereby bring the bucket into the desired position. In circumstances in which the piston reaches the end of the cylinder, the cylinder volume approaches zero – at this point, the volume of the component is very small. This is one of the conditions wherein the second challenge arises: the boom, arm, or bucket cylinders being small and reaching a 'dead volume'. The directional control valves are further hydraulic components in which a small volume can appear. In addition, some fingerprints of small volumes may appear in modelling of hydraulic pipes.

The third challenge related to bulk modulus models cannot be readily seen in real-time simulation conditions. However, its effects on system performance are obvious: with a higher bulk modulus value, less energy consumption will be required for transferring a given amount of energy.



Figure 2.2: The hydraulic cylinder and piston set-up of an excavator fluid power system.

2.1 The stiffness problem in fluid power systems

One must remember that the stiffness problem is not a meaningful concept with regard to real-world fluid power systems. After all, the physical system ‘finds a way’. Rather, it is a problem in the **modelling** of hydraulic circuits. Hence, carefully investigating the modelling of a fluid power system and its influencing parameters should shed light on the origin of this problem and, thereby, its solution. The LFT is a well-known approach utilised to model the hydraulic system described as this chapter progresses. Owing to the mathematical nature of the stiffness problem, its origin should be mathematically revealed also. To this end, the second subsection below presents a mathematical characterisation of the problem. This is followed by interpretation of the stiffness problem in physical terms.

2.1.1 The lumped-fluid theory

The theory of lumped fluids is often used in modelling of hydraulic systems. In the LFT, the hydraulic circuit is divided into volumes, throughout each of which the pressure is assumed to be evenly distributed. Differential equations are formed for the volumes, via which one can solve directly or indirectly for the pressure of the system at any given time. Volumes are assumed to be separated by means of a throttling mechanism through which the fluid can flow. In the model, the directional, pressure, and flow-control valves are replaced by throttles that control the rates of flow between individual volumes. The same is true of the long pipelines used in real systems.

The pressure in a volume within the hydraulic circuit, as depicted in Figure 2.3, can be calculated via a differential equation thus [85]:

$$\frac{dp}{dt} = \frac{\beta_e}{V} (Q_{in} - Q_{out} - \frac{dV}{dt}) \quad (2.1)$$

Here, p is the pressure, β_e is the effective bulk modulus, V is the volume, Q_{in} and Q_{out}

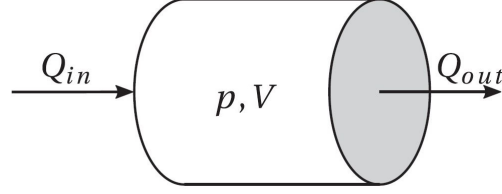


Figure 2.3: A schematic diagram of a hydraulic volume.

are the rates of incoming and out-bound volumetric flow, and dV/dt is the rate of changes in volume V over time. The effective bulk modulus represents the bulk modulus of the fluid by taking into account the effects of the container's flexibility and dissolved air [86]. The volumetric turbulent flow rate, Q_t , in a throttle can be expressed [87, 88, 89] as

$$Q_t = C_d A_t \sqrt{\frac{2\Delta p}{\rho}} \quad (2.2)$$

where C_d is the discharge coefficient, Δp is the pressure difference between the sides of the throttle valve, A_t is the cross-sectional area of the valve, and ρ is the density of the fluid. In the work described here, the volumetric flow rate was obtained via semi-empirical methods in which one can arrive at the parameters for the valve via measurement [90].

2.1.2 Mathematical description of the stiffness problem

For mathematically shedding some light on the origin of the stiffness issue with fluid power systems, consider a simple circuit such as the one in Figure 2.4. Using the LFT, one can write the equations governing the volumes V_{i-1} , V_i , and V_{i+1} as

$$\begin{cases} \dot{p}_{i-1} = \frac{\beta_e}{V_{i-1}} (Q_{i-\frac{3}{2}} - Q_{i-\frac{1}{2}}) \\ \dot{p}_i = \frac{\beta_e}{V_i} (Q_{i-\frac{1}{2}} - Q_{i+\frac{1}{2}}) \\ \dot{p}_{i+1} = \frac{\beta_e}{V_{i+1}} (Q_{i+\frac{1}{2}} - Q_{i+\frac{3}{2}}) \end{cases} \quad (2.3)$$

where the volumetric flow rate of orifice $i + \frac{1}{2}$ can be expressed as $Q_{i+\frac{1}{2}} = \Lambda_{i+\frac{1}{2}} \Delta p_{i+\frac{1}{2}}$, in which $\Delta p_{i+\frac{1}{2}} = p_{i+1} - p_i$ and $\Lambda_{i+\frac{1}{2}} = \frac{C_d A_{i+\frac{1}{2}}}{2\rho \Delta p_{i+\frac{1}{2}}}$. Consequently, by considering the Λ s estimated from the previous time step, Equation 2.3 can be rewritten in matrix form:

$$\begin{bmatrix} \dot{p}_{i-1} \\ \dot{p}_i \\ \dot{p}_{i+1} \end{bmatrix} = B_e \begin{bmatrix} \frac{\Lambda_{i-\frac{3}{2}} + \Lambda_{i-\frac{1}{2}}}{V_{i-1}} & -\frac{\Lambda_{i-\frac{1}{2}}}{V_{i-1}} & 0 \\ -\frac{\Lambda_{i-\frac{1}{2}}}{V_i} & \frac{\Lambda_{i-\frac{1}{2}} + \Lambda_{i+\frac{1}{2}}}{V_i} & -\frac{\Lambda_{i+\frac{1}{2}}}{V_i} \\ 0 & -\frac{\Lambda_{i+\frac{1}{2}}}{V_{i+1}} & \frac{\Lambda_{i+\frac{1}{2}} + \Lambda_{i+\frac{3}{2}}}{V_{i+1}} \end{bmatrix} \begin{bmatrix} p_{i-1} \\ p_i \\ p_{i+1} \end{bmatrix} + \begin{bmatrix} -\frac{\Lambda_{i-\frac{3}{2}}}{V_{i-1}} p_P \\ 0 \\ -\frac{\Lambda_{i+\frac{3}{2}}}{V_{i+1}} p_T \end{bmatrix} \quad (2.4)$$

The solution to the homogeneous part of Equation 2.4 can be expressed as

$$\mathbf{p} = c_1 \exp(\lambda_1 t) \mathbf{x}_1 + c_2 \exp(\lambda_2 t) \mathbf{x}_2 + c_3 \exp(\lambda_3 t) \mathbf{x}_3 \quad (2.5)$$

where $\mathbf{p} = [p_{i-1} \ p_i \ p_{i+1}]$ and, respectively, λ and \mathbf{x} are eigenvalues and eigenvectors. To obtain the eigenvalues, one should solve for the following determinant:

$$\begin{vmatrix} \frac{\Lambda_{i-\frac{3}{2}} + \Lambda_{i-\frac{1}{2}}}{V_{i-1}} - \lambda & -\frac{\Lambda_{i-\frac{1}{2}}}{V_{i-1}} & 0 \\ -\frac{\Lambda_{i-\frac{1}{2}}}{V_i} & \frac{\Lambda_{i-\frac{1}{2}} + \Lambda_{i+\frac{1}{2}}}{V_i} - \lambda & -\frac{\Lambda_{i+\frac{1}{2}}}{V_i} \\ 0 & -\frac{\Lambda_{i+\frac{1}{2}}}{V_{i+1}} & \frac{\Lambda_{i+\frac{1}{2}} + \Lambda_{i+\frac{3}{2}}}{V_{i+1}} - \lambda \end{vmatrix} = 0 \quad (2.6)$$

Doing so yields this equation:

$$\begin{aligned} & \left(\frac{\Lambda_{i-\frac{3}{2}} + \Lambda_{i-\frac{1}{2}}}{V_{i-1}} - \lambda \right) \left(\frac{\Lambda_{i-\frac{1}{2}} + \Lambda_{i+\frac{1}{2}}}{V_i} - \lambda \right) \left(\frac{\Lambda_{i+\frac{1}{2}} + \Lambda_{i+\frac{3}{2}}}{V_{i+1}} - \lambda \right) - \\ & \frac{\Lambda_{i-\frac{1}{2}}}{V_{i-1}} \frac{\Lambda_{i-\frac{1}{2}}}{V_i} \left(\frac{\Lambda_{i+\frac{1}{2}} + \Lambda_{i+\frac{3}{2}}}{V_{i+1}} - \lambda \right) = 0 \end{aligned} \quad (2.7)$$

Therefore, generally speaking, one can state that two factors affect the eigenvalues. The first variable is the pressure drop encapsulated in Λ , implying the importance of orifice modelling, and the second is the hydraulic volumes. These two parameters' values can be set such that the eigenvalues differ significantly in their order. If these conditions are met, the system is referred to as a stiff system. This problem would be a singular problem because the order difference in eigenvalues is equivalent to some rapid and some slow responses; e.g., if $\lambda_1 \gg \lambda_2, \lambda_3$, then the term $c_1 \exp(\lambda_1 t) \mathbf{x}_1$ in Equation 2.5 is produced rapidly, relative to the other terms.

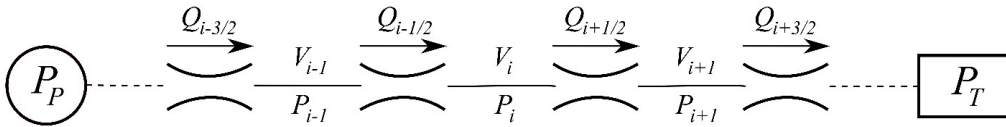


Figure 2.4: A simple hydraulic circuit [91].

2.1.3 Physical interpretation of the stiffness problem

Solving Equation 2.7 produces three eigenvalues, corresponding to the solution of the homogeneous part of Equation 2.4. The order difference of eigenvalues is a critical parameter indicating how stiff and close to singular the system is. The pipe-orifice circuit depicted in Figure 2.4 is the simplest possible hydraulic circuit containing three volumes. By considering $\Lambda_{i-\frac{3}{2}} = \Lambda_{i-\frac{1}{2}} = \Lambda_{i+\frac{1}{2}} = \Lambda_{i+\frac{3}{2}} = 10^{-7} m^3/s\sqrt{Pa}$, $V_{i-1} = V_{i+1}$ within the range 0–1 L, and V_i values of 0 to 0.1 litres, eigenvalues can be calculated by using Equation 2.7. For each pair (V_i, V_{i+1}) , there would, hence, be a maximum for the eigenvalue

ratios. Therefore, mapping the maximum eigenvalue ratios on the V_i - V_{i+1} plane can yield insight about the volumes for which the eigenvalues are of different orders. Such a map is depicted in Figure 2.5a, which shows the order difference of eigenvalues in different conditions. As this figure illustrates, the maximum eigenvalue ratio reaches 400 if V_i is less than 0.005 litres and V_{i+1} is sufficiently in excess of 0.4 litres. It is concluded that if V_i is small in relation to neighbouring volumes, the fluid power system is going to be stiff. It is worth mentioning that if V_{i+1} is small and on the same order as V_i , stiffness might not occur in the manner this figure suggests.

Another parameter appearing in Equation 2.7 that affects the eigenvalues and, consequently, their maximum ratio is Λ . This parameter depends on the manufacturing specification for the orifice, fluid density, and the pressure drop across the orifice. If the drop in pressure approaches zero in the relationship mentioned, $\Lambda = \frac{C_d A}{2\rho\sqrt{\Delta p}}$, then Λ will be large and cause the maximum eigenvalue ratios to reach higher values, as depicted in Figure 2.5b. This plot is obtained by assuming the same size for all hydraulic volumes, one litre. In addition, $\Lambda_{i-\frac{3}{2}} = \Lambda_{i+\frac{1}{2}} = \Lambda_{i+\frac{3}{2}} = 10^{-7} m^3/s\sqrt{Pa}$ are kept constant and only $\Lambda_{i-\frac{1}{2}}$ is changed. As the figure suggests, there is a linear relation between $\Lambda_{i-\frac{1}{2}}$ and $\frac{\lambda_{max}}{\lambda_{min}}$. Therefore, the analysis implies that the orifice model being employed is not suitable for conditions wherein the pressure drop nears zero.

It should be mentioned that in this analysis the bulk modulus is assumed to be constant and equal for all volumes. In actuality, it can be a function of the pressure in each volume, so the effects of this parameter should be separately investigated.

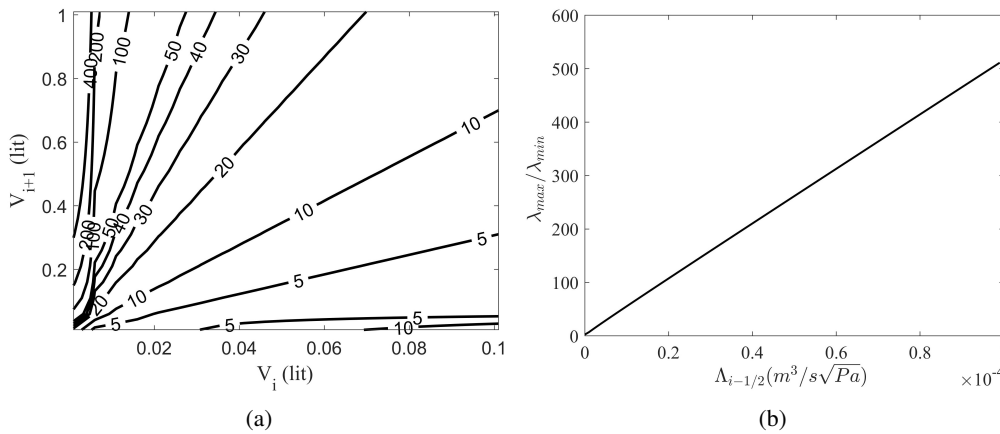


Figure 2.5: The contour of the maximum ratio of eigenvalues $\frac{\lambda_{max}}{\lambda_{min}}$ on the V_i - V_{i+1} plane (a) and the maximum ratio of eigenvalues $\frac{\lambda_{max}}{\lambda_{min}}$ versus $\Lambda_{i-\frac{1}{2}}$ (b).

2.2 Fluid power stiffness due to orifice models

As explained in the previous part of the chapter, the orifice model can create the stiffness problem if the pressure drop nears zero (i.e., if there is a low flow rate in the laminar

regime). It is worth mentioning that the effect can change while a machinery system is in operation, depending on external load conditions. At base, the orifice model should be such that it can predict the resting condition when there is no pressure drop across the orifice. For situations of the pressure drop approaching zero, the traditional turbulent-flow orifice equation becomes inefficient for determining the first derivative of the flow because it approaches infinity. This causes numerical problems to arise during the simulation. In efforts to resolve the difficulty, Ellman and Piché [92, 93] introduced several orifice models featuring laminar and turbulent orifice equations, in the latter half of the 1990s. The most accurate and computationally efficient solution thus far did not come about until 2008, with what Åman et al. suggested [94]: using a polynomial relationship between flow rate and pressure drop in the small areas experiencing a pressure drop. Theirs is a so-called two-regime flow model in which the third-order polynomial is used for describing the laminar and transition area of flow while the traditional square-root relationship for flow rate is used for the turbulence regime. Using the boundary condition for the region where the laminar and the turbulent model meet, the authors obtained the constants for their model. This method provides a continuous finite partial derivative of flow with respect to the pressure drop in all conditions. Borutzky et al. [87] proposed an empirically obtained polynomial function for the orifice volumetric flow rate. With their approach, which exhibits a smooth transition between the laminar- and the turbulent-flow regime, one can avoid singularities when the pressure difference approaches zero.

The volumetric flow rate through an orifice is estimated via Equation 2.2, which can be rewritten to describe two-directional flows as

$$Q_t = C_d A_t \sqrt{\frac{2\Delta p}{\rho}} \text{sign}(\Delta p) \quad (2.8)$$

This flow rate is suitable for the turbulent regime though displaying some drawbacks for laminar flow where the pressure drop approaches zero, as pointed out by Åman et al. [95]. They found that the derivative of this flow rate with respect to the pressure drop approaches infinity as the drop nears zero. Therefore, they suggested a new flow rate relation in which the flow rate is deemed to be zero if the pressure drop reaches zero. This relation, called the two-regime flow rate, is expressed as

$$Q = \begin{cases} C_d A_t \sqrt{\frac{2\Delta p}{\rho}} \text{sign}(\Delta p) & \Delta p \geq \Delta p_0 \\ a_0 + a_1 \Delta p + a_2 \Delta p^2 \text{sign}(\Delta p) + a_3 \Delta p^3 & \Delta p < \Delta p_0 \end{cases} \quad (2.9)$$

where the following coefficients are used:

$$[a_1 \quad a_2 \quad a_3 \quad a_4] = \left[\sqrt{\frac{2C_d A_t \Delta p_0}{\rho}} \quad \sqrt{\frac{C_d A_t}{2\rho \Delta p_0}} \quad -\sqrt{\frac{2C_d A_t \Delta p_0}{\rho}} \quad -\sqrt{\frac{C_d A_t}{2\rho \Delta p_0}} \right] \quad (2.10)$$

In the above, $\Delta p_0 = \frac{Re_{tr}^2 \nu^2 \pi \rho}{8C_{d\infty} \sqrt{C_d A_t}}$ is determined by means of the transition Reynolds number Re_{tr} for where the flow regime is changed from laminar to turbulent [95].

2.3 Fluid power stiffness due to small volumes

The numerical stiffness can be explained by the fact that hydraulic circuits include volumes with different orders of magnitude. This brings difficulties in numerical integration with ordinary differential equations, for which classical integrators are not able to generate a stable dynamic response at large integration time steps and hence slow down the simulation by implementing significantly smaller time steps [96]. Again, numerical stiffness of the system can often be linked to small volumes in the hydraulic circuit. For systems with small volumes, the solution should be derived by means of numerical solvers designed specifically to avoid the problem of instability in dynamic models of a fluid power circuit. One can point to implementation of specific integrators to handle singularities, use of iterative methods, machine-learning algorithms, and perturbed models as the approaches that best alleviate stiffness in hydraulic systems.

The accuracy and stability issues with various two-stage semi-implicit Runge–Kutta methods were investigated by Piché and Ellman [96]. They recognised that ordinary differential equations applicable for different volume sizes are challenging to solve, and they proposed an L-stable integrator as the most suitable. Also, Esque et al. [97], who studied the real-time simulation of a hydraulic crane by using an L-stable Rosenbrock integration scheme, discovered that the maximum integration time step should be assessed via stability and computation-time criteria. These two factors led them to choose a time step of 0.1 ms for their application.

Iterative methods have been investigated in many works. Bowns and Wang [98] reported on difficulties in simulation of hydraulic pipe systems with small volumes. In particular, they noticed that if one or several pipes have a small volume, very small simulation time steps are required. To overcome this problem, they proposed iterative models. However, these iterative methods are computationally expensive and similar to applying small time steps in the integration. Another iterative method was introduced and studied in an endeavour to reduce the numerical problems via algorithmically searching for the steady-state value for the small-volume pressure [42, 43, 44]. The main idea was to replace the small volume in traditional continuity equations with an artificial volume that is large enough to afford a stable response of pressure. After this, the pressure is integrated in a separate loop until the convergence criterion is met. This solver provided a numerically stable solution and rather fast response.

Alongside models presented to overcome stiffness of hydraulic systems, there have been several attempts to model the hydraulic components through machine-learning tools, such as a neural network [45, 46, 47], as noted above. These tools still seem time-consuming for the reason cited in the previous chapter: the number of neuron layers rises with the response resolution and the complexity of the system. The models' other issues are relevant too – they have a limited range of valid operation, dictated in part by the training data used, and such a black-box model cannot guarantee that the behavior is always going to meet the relevant physical demands.

I have taken the third path mentioned above, proposing a perturbed model to decrease the difficulties associated with the stiffness problem that affects fluid power system simulations [48]. Available in the appended material, this model was applied in co-simulation

with a four-bar mechanism and the results validated the functionality of the model: it reduced the computation time by approximately one order of magnitude, as reported in earlier work [49]. An article presenting the model more fully is appended to the dissertation.

The pseudo-dynamic method, categorised as an iterative method, is presented next, after which the perturbed model is explained. The discussion is tied together with description of the method of multiple scales as a way to deal with the existence of a small volume in the fluid power systems.

2.3.1 The pseudo-dynamic method

The pseudo-dynamic solver is based on the steady-state pressure response in a small volumes at every time step. The solver does not take into account the dynamic behaviour of flow and, in fact, completely ignores it. One must remember that the algorithm is applied only to the small volumes, while the larger ones are addressed with conventional methods and integrators.

The main assumption in this method is that the high frequencies (time constants) arising from the small volume are negligible relative to the frequencies of the fluid power circuit [99]. Therefore, as the volumes' high frequencies have no influence over the design of hydraulic circuits, it is possible to ignore them and instead use the steady-state pressure in small volumes [44].

In the algorithm thus constructed, the main idea is to assume and define a larger volume to stand in for the small one. This volume should not be so large as to create convergence difficulty. Neither should it be so small that it requires a small integration time step. It is worth mentioning that this volume does not have any effect on the final solution, because of the steady-state nature of the final solution.

Therefore, we would have two layers of integration in this algorithm, the outer loop and inner loop. The inner loop applies an iterative procedure to find the steady-state pressure by using the large volume assumed by the user. The outer loop is executed conventionally, and the inner (pseudo-)loop embedded in it functions to find the static value for the pressures in small volumes, as pre-defined by the user. The static value of the pressure is obtained within a single main-loop integration step by means of the embedded integration loop, which obtains the steady-state value for pressure upon integration of the pressure formation from an artificial larger fluid volume. Thus, the mathematical model of a fluid power circuit can be described in terms of the implementation of two integration loops.

Let us consider volume V_i in Figure 2.4 as our small volume. One would calculate the flow passing through this volume by using the following relation:

$$Q_{pseudo} = C_d A_i \sqrt{\frac{2 |p_i - p_{i-1}|}{\rho}} \text{sign}(p_i - p_{i-1}) \quad (2.11)$$

Consequently, the pressure p_i in the small volume V_i can be calculated by integrating this

equation:

$$\dot{p}_i = \frac{\beta_e}{V_{pseudo}}(Q_{pseudo} - Q_{i+\frac{1}{2}}) \quad (2.12)$$

In this formula, V_{pseudo} is the assumed volume substituted for the small volume. It is worthy of note that the V_{pseudo} value chosen affects the inner integration time step and should be set carefully. After calculating p_i , the flow rate can be calculated again, using Equation 2.11, and then the pressure, by means of Equation 2.12. Iteration continues until the convergence threshold is reached, where the criterion for convergence is a pressure derivative below the small value selected, $\dot{p}_i < set\ value$. This criterion implies that the pressure derivative changes little and, therefore, that the pressure has reached a steady state.

After the steady-state pressure is calculated, the inner loop is complete for the relevant time step, and the outer loop should move forward one time step upon knowing the pressure value for the small volume. This iterative procedure should be performed at each time step.

There are two integration time steps in this algorithm, one for the outer loop and the other for the inner loop. The outer-loop integration time steps depends on the system's other hydraulic components and should be determined by the designer. In contrast, V_{pseudo} determines the integration time for the inner loop. A very small V_{pseudo} makes that loop's integration time step very small, so a very small V_{pseudo} should be avoided for reasons of simulation-time constraints and computation efficiency. On the other hand, a very large volume makes the inner loop's iterative procedure inefficient since more iteration will be required, which calls for higher computation capacity.

Therefore, the main drawback of this method is connected with its iterative nature, and it ends up especially time-consuming for a circuit containing numerous small volumes.

2.3.2 Singular perturbation theory

Because the stiffness problem encountered with fluid power systems is a modelling and mathematical problem – again, no such problem exists in actual circuits – one should apply mathematical tools to solve it. The small volume appearing in the hydraulic equation is divided by a large bulk modulus value, which makes for an infinitely small parameter ε multiplied by the highest derivative of pressure as

$$\varepsilon \dot{p}_i = (Q_{i-\frac{1}{2}} - Q_{i+\frac{1}{2}}) \quad (2.13)$$

The small value cropping up for this parameter in the governing differential equations is important. If the small-valued parameter is set to zero and the differential equation is solved accordingly, the result could differ from the true solution to the equation containing the adjusted parameter. While these two solutions are the same in some systems, usually called regular systems, the solutions may differ, in which case the system is termed a singular system.

With singular systems, one obtains two distinct solutions if calculating the mathematical

limits by approximating the small parameter to zero both before and after solving the equations.

In these systems, the infinitesimal parameter is multiplied by the highest derivative term, which usually results in rapid variation on small time scales [100]. This region is known as the boundary layer, and its stability constitutes a criterion for using singular perturbation theory, as explained in detail in related work [48].

Considering the general order of ε , determined by the small volume divided by the effective bulk modulus $\varepsilon = V/B_e$, one can express the set of hydraulic differential equations for the simple circuit presented in Figure 2.4 thus:

$$\varepsilon \dot{p}_{i-1} = (Q_{i-\frac{3}{2}} - Q_{i-\frac{1}{2}}) \quad (2.14)$$

$$\varepsilon \dot{p}_i = (Q_{i-\frac{1}{2}} - Q_{i+\frac{1}{2}}) \quad (2.15)$$

$$\varepsilon \dot{p}_{i+1} = (Q_{i+\frac{1}{2}} - Q_{i+\frac{3}{2}}) \quad (2.16)$$

Equations 2.14–2.16 represent a set of singular equations, as setting ε equal to zero produces a solution different from that in the case in which ε is not considered to be zero. Related work [48] presents a perturbed model based on singular perturbation theory and results wherein the numerical integration algorithm is sped up and rendered stable for small integrating time steps. In keeping with that work, presented in detail in the appendix, p_i (the pressure of the small volume) can be represented as

$$p_i = \frac{p_{i+1} + \alpha p_{i-1}}{1 + \alpha} \quad (2.17)$$

where $\alpha = \left(\frac{A_i}{A_{i-1}}\right)^2$.

2.3.3 The method of multiple scales

The singular perturbation method yields only the steady-state solution for systems that display dynamic behaviour on different scales – i.e., it represents the response on the largest scale. Each scale can be treated as an independent variable reproducing a set of equations rather than just one. For instance, t and εt can be two independent variables, each representing a distinct scale of time. Although the perturbed hydraulic model returns the steady-state response, the error due to the smaller scale may accumulate over time and thus create a substantial deviation from the actual response, especially in circumstances in which the systems' dynamic behaviour cannot safely be ignored. To shed light on the parameters producing the error and to compensate for it in the perturbed model, one can employ the method of multiple scales (MMS) [91]. This approach introduces the new independent time variables as

$$T_n = \varepsilon^n t \quad n = 0, 1, 2, \dots \quad (2.18)$$

Accordingly, the derivatives in the equation can be rewritten in line with the chain rule:

$$\frac{d}{dt} = \frac{dT_0}{dt} \frac{\partial}{\partial T_0} + \frac{dT_1}{dt} \frac{\partial}{\partial T_1} + \dots \quad (2.19)$$

In addition, one may assume that the solution of Equation 1 can be expressed as

$$p_i(t, \varepsilon) = p_0(T_0, T_1, \dots) + \varepsilon p_1(T_0, T_1, \dots) + O(\varepsilon^2) \quad (2.20)$$

It is worth noting that the number of time scales is a function of the accuracy required. If someone wants to expand the solution to the second order, $O(\varepsilon^2)$, the time scales T_0 and T_1 are needed. When one substitutes from equations 2.20 and 2.19, the result when plugged into Equation 1 yields the following:

$$\left(\frac{\partial}{\partial T_0} + \varepsilon \frac{\partial}{\partial T_1} + \varepsilon^2 \frac{\partial}{\partial T_2} \right) (p_0 + \varepsilon p_1 + \varepsilon^2 p_2) = \frac{\beta_e}{V_i} (Q_{i-\frac{1}{2}} - Q_{i+\frac{1}{2}}) \quad (2.21)$$

On the other hand, flow rates $Q_{i-\frac{1}{2}}$ and $Q_{i+\frac{1}{2}}$ are both a function of the pressure in the small volume. If these flow rates are calculated from the perturbed pressure, they are going to include some error. Consequently, one must obtain them by using the exact value of p_i . By means of Equation 2.2, one can obtain $Q_{i+\frac{1}{2}}$ as

$$Q_{i+\frac{1}{2}} = C_c A \sqrt{p_i - p_{i+1}} = C_c A \sqrt{p_0 - p_{i+1} + \varepsilon p_1 + \varepsilon^2 p_2} \quad (2.22)$$

Therefore, by obtaining $p_0 - p_{i+1}$ from the square-root function and implementing the Taylor series for $\sqrt{1+x} \cong 1 + \frac{x}{2} - \frac{x^2}{8}$ in which $x < 1$, we have

$$Q_{i+\frac{1}{2}} = C_c A \sqrt{p_0 - p_{i+1}} \left(1 + \frac{p_1 \varepsilon + p_2 \varepsilon^2}{2(p_0 - p_{i+1})} - \frac{p_1^2 \varepsilon^2}{8(p_0 - p_{i+1})^2} \right) = \bar{Q}_{i+\frac{1}{2}} \left(1 + \frac{p_1 \varepsilon + p_2 \varepsilon^2}{2(p_0 - p_{i+1})} - \frac{p_1^2 \varepsilon^2}{8(p_0 - p_{i+1})^2} \right) \quad (2.23)$$

Here, $\bar{Q}_{i+\frac{1}{2}} = C_c A \sqrt{p_0 - p_{i+1}}$ is the flow rate calculated on the basis of the perturbed pressure, referred to as the perturbed flow rate from here on in the dissertation. The same logic is valid for $Q_{i-\frac{1}{2}}$, resulting in the following relationship:

$$Q_{i-\frac{1}{2}} = \bar{Q}_{i-\frac{1}{2}} \left(1 - \frac{p_1 \varepsilon + p_2 \varepsilon^2}{2(p_{i-1} - p_0)} - \frac{p_1^2 \varepsilon^2}{8(p_{i-1} - p_0)^2} \right) \quad (2.24)$$

Substituting the flow rates from equations 2.23 and 2.24 into Equation 2.21 and separating the equations for order $O(\varepsilon^0)$, $O(\varepsilon^1)$, and $O(\varepsilon^2)$ produces the following set of equations:

$$O(\varepsilon^0) : \frac{\partial p_0}{\partial T_0} = \frac{\beta_e}{V_i} (\bar{Q}_{i-\frac{1}{2}} - \bar{Q}_{i+\frac{1}{2}}) \quad (2.25)$$

$$O(\varepsilon^1) : \frac{\partial p_1}{\partial T_0} + \frac{\beta_e}{V_i} p_1 \left(\frac{\bar{Q}_{i-\frac{1}{2}}}{2(p_{i-1} - p_0)} + \frac{\bar{Q}_{i+\frac{1}{2}}}{2(p_0 - p_{i+1})} \right) = -\frac{\partial p_0}{\partial T_1} \quad (2.26)$$

$$O(\varepsilon^2) : \frac{\partial p_2}{\partial T_0} + \frac{\beta_e}{V_i} p_2 \left(\frac{\bar{Q}_{i-\frac{1}{2}}}{2(p_{i-1} - p_0)} + \frac{\bar{Q}_{i+\frac{1}{2}}}{2(p_0 - p_{i+1})} \right) = \frac{\beta_e}{V_i} \left(\frac{\bar{Q}_{i+\frac{1}{2}} p_1^2}{8(p_0 - p_{i+1})^2} - \frac{\bar{Q}_{i-\frac{1}{2}} p_1^2}{8(p_{i-1} - p_0)^2} \right) - \frac{\partial p_1}{\partial T_1} - \frac{\partial p_0}{\partial T_2} \quad (2.27)$$

Equation 2.25 is equivalent to the perturbed model because of the presence of a small volume V_i . It yields the perturbed pressure as obtained from Equation 2.17, as $p_0 = \frac{p_{i+1} + \alpha p_{i-1}}{1 + \alpha}$. Therefore, $\frac{\partial p_0}{\partial T_1} = 0$. Recalling the $\bar{Q}_{i-\frac{1}{2}}$ and $\bar{Q}_{i+\frac{1}{2}}$ relations also, one can solve Equation 2.26 thus:

$$p_1 = \Lambda(T_1) \exp \left(- \int_0^{T_0} \frac{\beta_e}{V_i} \left[\frac{\bar{Q}_{i-\frac{1}{2}}}{2(p_{i-1} - p_0)} + \frac{\bar{Q}_{i+\frac{1}{2}}}{2(p_0 - p_{i+1})} \right] dT_0 \right) \quad (2.28)$$

Considering $\frac{dp_1}{p_1} = \frac{d(\varepsilon p_1)}{\varepsilon p_1}$, and assuming a constant pressure drop through the small volume $\sqrt{p_{i-1} - p_{i+1}}$, one can solve Equation 2.28 as

$$\begin{aligned} \frac{\partial p_2}{\partial T_0} + \frac{\beta_e}{V_i} p_2 \left(\frac{\bar{Q}_{i-\frac{1}{2}}}{2(p_{i-1} - p_0)} + \frac{\bar{Q}_{i+\frac{1}{2}}}{2(p_0 - p_{i+1})} \right) &= \frac{\beta_e}{V_i} \left(\frac{\bar{Q}_{i-\frac{1}{2}}}{8(p_{i-1} - p_0)} + \frac{\bar{Q}_{i+\frac{1}{2}}}{8(p_0 - p_{i+1})} \right) \Lambda^2 \exp \left(- 2 \int_0^{T_0} \frac{\beta_e}{V_i} \left[\frac{\bar{Q}_{i-\frac{1}{2}}}{2(p_{i-1} - p_0)} + \frac{\bar{Q}_{i+\frac{1}{2}}}{2(p_0 - p_{i+1})} \right] dT_0 \right) - \\ &\frac{\partial \Lambda}{\partial T_1} \exp \left(- \int_0^{T_0} \frac{\beta_e}{V_i} \left[\frac{\bar{Q}_{i-\frac{1}{2}}}{2(p_{i-1} - p_0)} + \frac{\bar{Q}_{i+\frac{1}{2}}}{2(p_0 - p_{i+1})} \right] dT_0 \right) \end{aligned} \quad (2.29)$$

The terms on the right-hand side in Equation 2.29 are secular, meaning that they can grow to infinity with time. To avoid such infinities, those terms must be set to zero, so we obtain

$$\begin{aligned} \frac{\partial \Lambda}{\partial T_1} - \Lambda^2 \frac{\beta_e}{V_i} \left(\frac{\bar{Q}_{i-\frac{1}{2}}}{8(p_{i-1} - p_0)} + \frac{\bar{Q}_{i+\frac{1}{2}}}{8(p_0 - p_{i+1})} \right) \exp \left(- \int_0^{T_0} \frac{\beta_e}{V_i} \left[\frac{\bar{Q}_{i-\frac{1}{2}}}{2(p_{i-1} - p_0)} + \frac{\bar{Q}_{i+\frac{1}{2}}}{2(p_0 - p_{i+1})} \right] dT_0 \right) &= 0 \end{aligned} \quad (2.30)$$

This gives us

$$\Lambda = -\frac{1}{fT_1} \quad (2.31)$$

in which $f = \frac{\beta_e}{V_i} \left(\frac{\bar{Q}_{i-\frac{1}{2}}}{8(p_{i-1}-p_0)} + \frac{\bar{Q}_{i+\frac{1}{2}}}{8(p_0-p_{i+1})} \right) \exp \left(- \int_0^{T_0} \frac{\beta_e}{V_i} \left[\frac{\bar{Q}_{i-\frac{1}{2}}}{2(p_{i-1}-p_0)} + \frac{\bar{Q}_{i+\frac{1}{2}}}{2(p_0-p_{i+1})} \right] dT_0 \right)$.
Substituting Equation 2.31 into Equation 2.28 yields

$$p_1 = -\frac{1}{T_1} \frac{8V_i}{\beta_e} \left(\frac{\bar{Q}_{i-\frac{1}{2}}}{(p_{i-1}-p_0)} + \frac{\bar{Q}_{i+\frac{1}{2}}}{(p_0-p_{i+1})} \right)^{-1} \quad (2.32)$$

By considering $T_1 = \varepsilon t$ and combining p_0 and εp_1 in line with Equation 2.20, one can express small-volume pressure p_i as

$$p_i = \frac{p_{i+1} + \alpha p_{i-1}}{1 + \alpha} - \frac{1}{t + \delta t} \frac{8V_i}{\beta_e} \left(\frac{\bar{Q}_{i-\frac{1}{2}}}{(p_{i-1}-p_0)} + \frac{\bar{Q}_{i+\frac{1}{2}}}{(p_0-p_{i+1})} \right)^{-1} \quad (2.33)$$

This equation reveals that the deviation of the perturbed model from the exact solution hinges mainly on the pressure drop through the small volume $p_{i-1} - p_{i+1}$, bulk modulus β_e , and volume V_i . If the pressure drop across the small volume is near zero, $p_{i-1} - p_{i+1} \rightarrow 0$ (there is no pressure change from p_{i-1} to p_{i+1}), then $\varepsilon p_1 \rightarrow 0$, and the perturbed model produces the same result as an exact solver.

The same logic is valid for bulk modulus and volume size. Obviously, the perturbed model is more accurate the closer the small volume's size comes to zero, as $\varepsilon p_1 \rightarrow 0$ if $V_i \rightarrow 0$.

2.4 Bulk modulus models

In fluid power systems, the compressibility of the oil is a significant factor in performance and efficiency. Entrained air in the oil enters the system through low-pressure regions in conditions of either cavitation or relative vacuum [101]. In other effects, air can become entrained in the oil through nitrogen gas leaking from accumulators. The literature reports on numerous studies centred on how to account for the effects of gas. These studies are based on either two-phase flow simulations [102, 103] or single-phase flow models [104, 105, 106, 107]. The two-phase flow simulations utilise CFD methods to examine the interfaces between fluids and thereby investigate the bubble dynamics. Doing so is computationally resource-heavy. In contrast, single-phase models consider a continuous medium with an embedded gas-volume fraction [108]. Although the CFD methods reveal more details of the dynamics of hydraulic oil, the single-phase approach is often considered well suited to calculating such properties of fluids as density and the bulk modulus, as this assumption is consistent with the lumped-fluid theory applied in the modelling of hydraulic circuits.

As Zhou et al. [109] have outlined, continuous fluid approaches can be categorised on the basis of the dynamic features of gas release and adsorption, which are not instantaneous processes. According to their study, even applying Henry's law to predict the amount of air dissolved in the oil as a function of pressure involves a static explanation of a transient process, since it relies on an equilibrium-state hypothesis. The authors cited the key limitation of Henry's law as most prominent with regard to rapid processes such as those

in hydraulic systems. However, they assumed a constant value for the law's coefficient and, hence, a linear relationship between the dissolved air and pressure. In contrast, other researchers [110] have introduced a modified form in which the constant from Henry's law takes the form of a variable. In response, Zhou et al. [103] have suggested solving the simplified version of the transport equations for free air and vapour, involving the bubble-dynamics relations. This led them to propose a relationship for the bulk modulus that extends from its primary definition. In this, the air- and vapor-volume fractions should be estimated by solving the corresponding transport equations.

Models that use neither the gas-transport equations nor Henry's law to account for the process of dissolving are usually referred to as compression-only models [104, 105, 106]. In contrast, other models consider the process of air bubbles' compression simultaneously with that of dissolving in response to high pressure levels. Merritt [111] derived a relationship for the bulk modulus that assumes a uniform distribution of air bubbles in oil and ignores the solubility of air in the oil. In this model, the ideal gas assumption is accepted and the secant bulk modulus relation, $\beta = \rho \frac{\Delta p}{\Delta \rho}$, is used. Cho et al. [112] developed a model using the same assumptions as Merritt except that they used the standard tangent bulk modulus definition, $\beta = \rho \frac{\partial p}{\partial \rho}$. Tian and Van de Ven [101], in turn, recently modified Cho et al.'s model by accounting for the air solubility as the mass is transferred across the oil-gas interface, and their approach updates the gas-volume fraction at each time step accordingly. Yu et al. [113] have proposed a model that considers both compression and dissolution processes, using the tangent formula for β . To tackle the matter of air solubility, they introduced a parameter dubbed the coefficient of bubble volume variation. As they explained, setting its value to zero can simplify the formula to represent a case with negligible air solubility. Gholizadeh et al. [114] found the result to be the same as in Cho et al.'s work [112], and Kajaste et al. [115] have attempted to verify this output of compression-only models experimentally. It is worth mentioning that the model developed for the bulk modulus by LMS Imagine SA has been applied in AMESim commercial software and assumes the time-dependence of both the gas content and the saturation pressure (i.e., critical pressure).

The research team developed a thermodynamics-based bulk modulus relationship that brings fuller understanding of the process of air's dissolution into hydraulic oil. This new relationship expression shows that the amount of air entrained in hydraulic oil remains constant up to a critical pressure, beyond which air starts to dissolve (in a manner following Henry's law). The new bulk modulus relation is obtained as

$$\beta = \frac{k\gamma\delta_d V P^{\frac{1}{k}+1}}{C_n(\delta_d + \frac{\gamma P^{\frac{1}{k}}\theta}{\rho_l} + \frac{k\gamma\theta P^{\frac{1}{k}+1}}{C_n\rho_l}\delta_d)} \quad (2.34)$$

where k and γ represent the process, C_n and δ_d indicate the variations in the air density, and ρ_l is the oil density. In Equation 2.34, γ and θ implicitly define the air-volume fraction in the hydraulic-system formulae.

The compressibility of the oil can change the time scale of the system. In other words, non-compressible oil yields a very small time scale for the hydraulic components and consequently renders the system singular (singularity usually occurs in a system with very

small time scales). In contrast, compressible oil can increase the time it takes the system to respond (i.e., the time scale) and seems conducive to larger integration time steps – at least at first glance. In reality, all hydraulic oil contains entrained air to some extent, so taking the oil’s compressibility into consideration in the simulation of hydraulic circuits may necessitate a larger integration time step. That said, it is conducted some simulations that demonstrate bulk modulus not to have any effect on simulation speed.

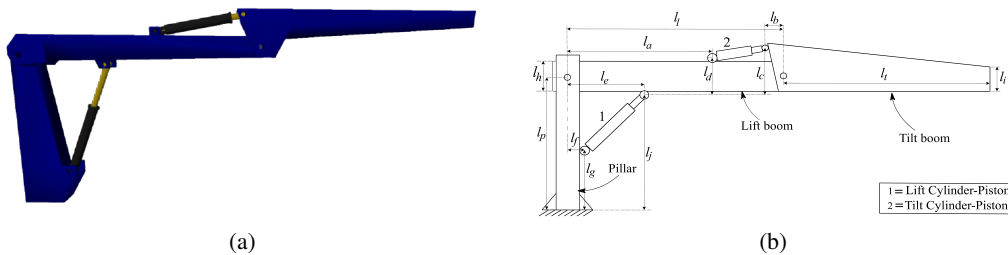


Figure 2.6: A jib crane in Mevea software (a) and a schematic diagram of it (b) [116], used to study the effects of the bulk modulus on computation efficiency.

To investigate the effects of the bulk modulus model on simulation speed, the four-bar mechanism is considered as depicted in Figure 2.6a, created in software by Mevea. In addition, the fluid power system was modelled via C/C++ code written as an FMU for easy input to the multibody solver. This FMU combines an XML model description with C code to solve the hydraulic circuit problem. It enabled easy modification of the bulk modulus relationship expressed in the code to adjust the amount of entrained air. It is observed that change in the bulk modulus does not affect computational time. After performing this test with several air-volume fractions, it is concluded that the bulk modulus values used are all safe since this factor is not the source of singularity in fluid power systems.

Finally, it should be noted that, obviously, a simpler bulk modulus would be a little faster, on account of the number of operations that should go into calculating the bulk modulus itself.

2.5 Results and discussion

Examination of the three factors affecting the degree of stiffness of a fluid power system (the orifice model, the presence of one or more small volumes in the circuit, and the bulk modulus model) clarified that using a two-regime orifice model rules out the stiffness problem arising from the orifice model and demonstrated that the bulk modulus models presented in the literature can be used safely, since the bulk modulus does not have any effect on the hydraulic system’s stiffness. Therefore, the only challenging scenario remaining is the circumstances wherein the hydraulic circuit contains a small volume. The first publication forming part of the dissertation presents a derivation of the perturbed model for a simple circuit, also presented in the article. It should be highlighted that, for

a relatively large volume, a correction factor ought to be applied to the rate of flow from the small volume, as elaborated upon in the article.

To investigate the effects of the perturbed model on the computation time demanded by a coupled multibody and hydraulic system, that model was applied to the fluid power system of the four-bar mechanism depicted in Figure 2.7a. The actuator of this mechanism is a simple hydraulic cylinder and piston (depicted in Fig. 2.7b). In an illustrative figure from the relevant article (presented here as Fig. 2.8), the volume flow rate is plotted against time for the small volume in question. As this figure attests, the lumped-fluid theory can correctly predict the system's behaviour by using an integral time step of 2 ms. This is the largest step with which the simulation remains stable. The perturbed model, meanwhile, produces acceptable results to a value 2.5 times larger. With this 5 ms step, it is demonstrated that the perturbed model can increase the simulation speed for the mechanism in question by a factor of 2.5. Publication II presents further results and discussion pertaining to the study carried out [49].

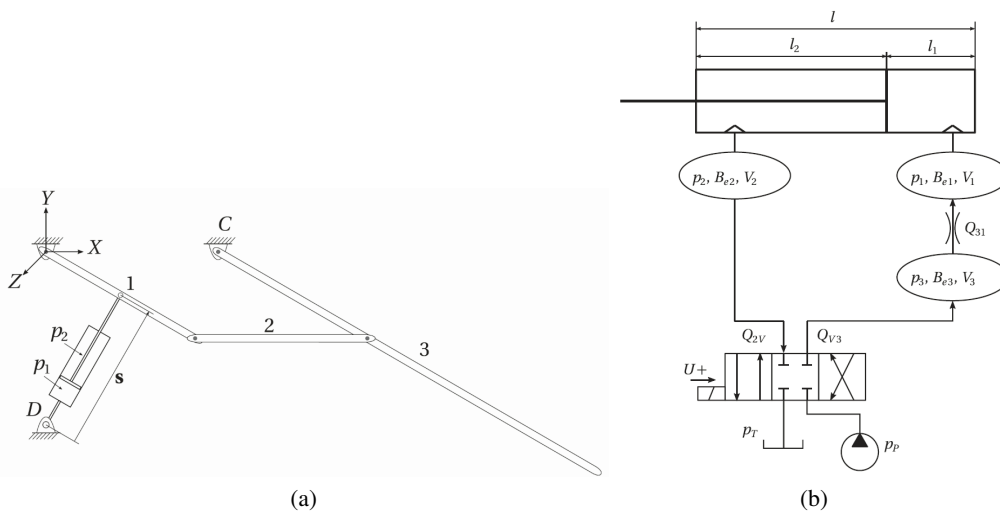


Figure 2.7: a) The four-bar mechanism and b) the cylinder-and-piston hydraulic circuit used as an actuator for the mechanism [49].

The perturbed model is applicable for any small hydraulic volume surrounded by bigger neighbouring volumes. To investigate the functionality of the perturbed model further, it is applied to a fluid power system operating with digital valves, as depicted in Figure 2.9 and 2.10a. This hydraulic circuit is composed of an ideal pump and tank, digital valves, and a hydraulic multi-chamber cylinder and piston. The pump and the tank operate with 150 and 20 bar of pressure, respectively. Each chamber is connected to two digital flow-control units (DFCUs), and each of them can be either *on* or *off*. This setting determines the maximum and the minimum flow passing through. There are, in total, eight *on/off* valves in the system, with each *on/off* DFCU pair being modelled as a block in Simulink, where one input signal is used to determine which of the eight should

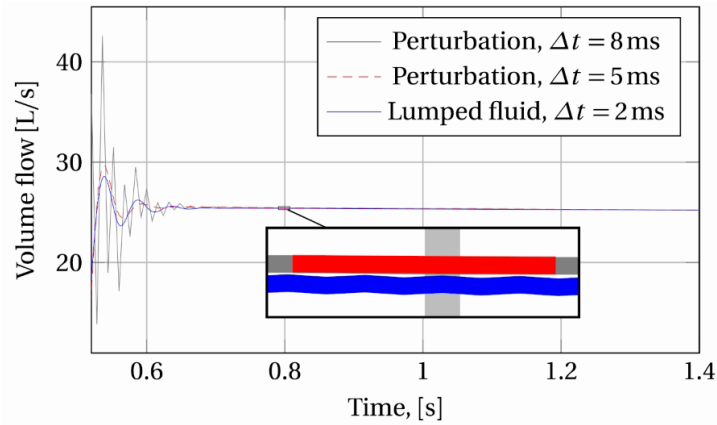


Figure 2.8: The volume flow rate Q_{31} under the LFT and the perturbed model [49].

be activated (Fig. 2.10b illustrates this). The cylinder is constructed of four chambers connected to DFCUs. Each chamber's flow and pressure are controlled by two DFCUs, one of which is connected to a high-pressure source while the other leads to the low-pressure line. The pipeline before a digital valves is modelled as a hydraulic volume with a one-litre capacity, and the volume of the pipe after the digital valves and before the cylinder is considered a small volume, at 0.05 litres. This is 100 times smaller than its neighbouring volume.

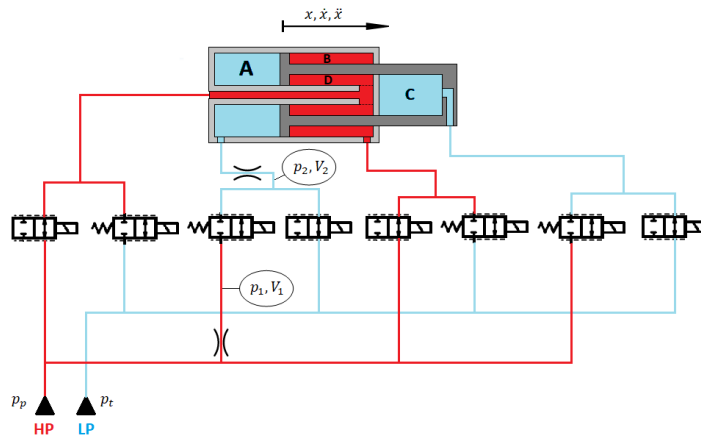
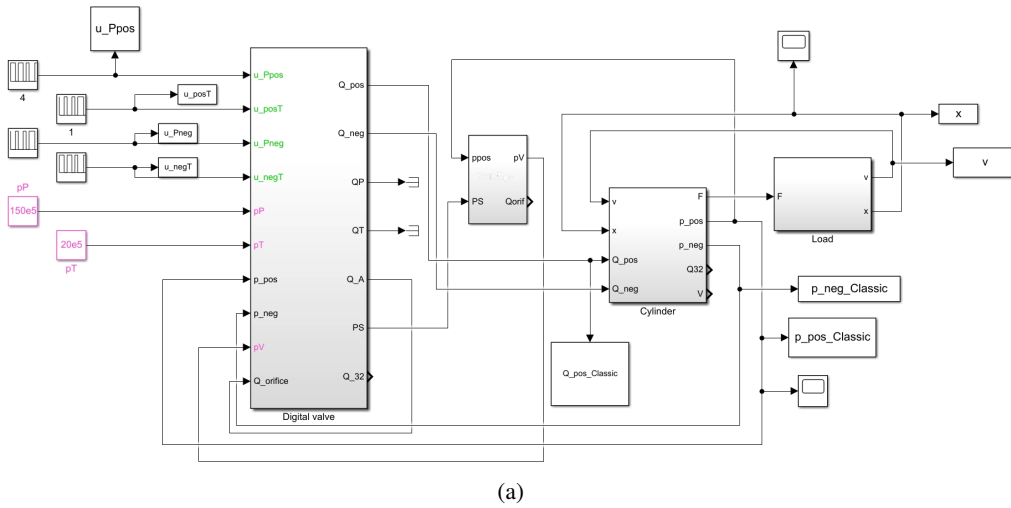


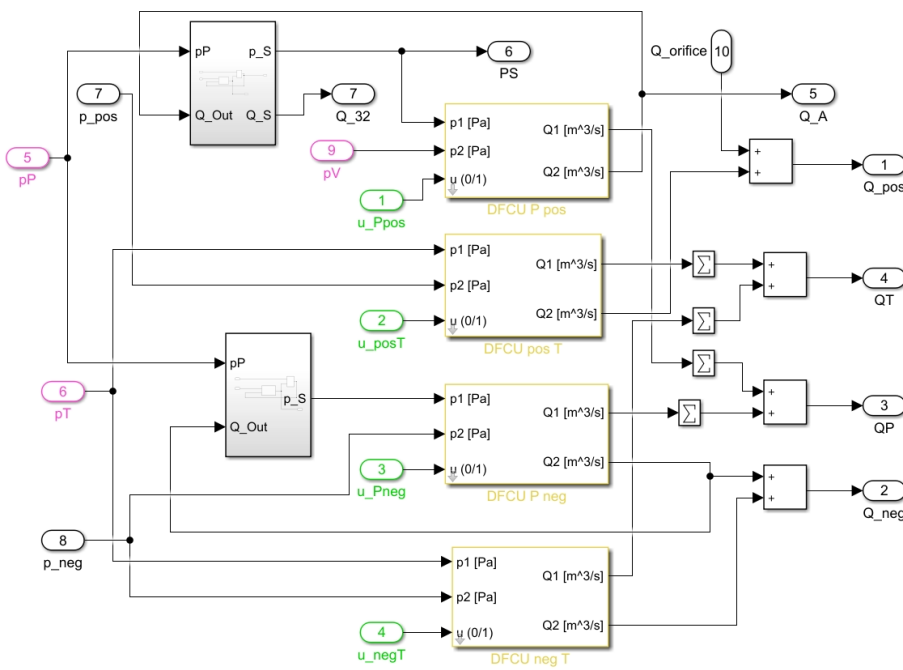
Figure 2.9: Four-chamber cylinder and piston circuit operating with a digital valve.

In Figure 2.11a, piston position is plotted as a function of time for a 1 s period. The position obtained when the small volume is handled by the LFT is represented by a solid black line and blue dashed line for time steps of 10^{-5} s and 10^{-4} s, respectively, and that with the perturbed model is indicated by a solid red line. As this figure demonstrates, 10^{-5} s is the largest time step that yields a stable simulation. The blue dashed line, plotted

for applying the LFT approach with a step of 10^{-4} s for the small volume, is far from the correct response. As the figure illustrates, in 1 s of simulation, the difference in predicted positions reaches 0.25 cm between the 10^{-5} s and 10^{-4} s steps, whereas the perturbed model can closely track the correct response even with a large time step, 10^{-4} s.



(a)



(b)

Figure 2.10: a) The four-chamber cylinder and piston operating with a digital valve containing b) four pairs of DFCUs.

For showing the cumulative error associated with the large time step in the lumped-fluid theory approach, the piston position is sketched for a longer time also (5 s), in Figure 2.11b. This figure was prepared for the same cases as Figure 2.11a, showing deviation of response under the LFT model with a large time step, 10^{-4} s. The accumulation of error makes the deviation higher, reaching more than 1 cm after 5 s relative to the LFT model with a time step of 10^{-4} s. In contrast, the perturbed model matches the correct response very well when a step one order higher is used, 10^{-4} s.

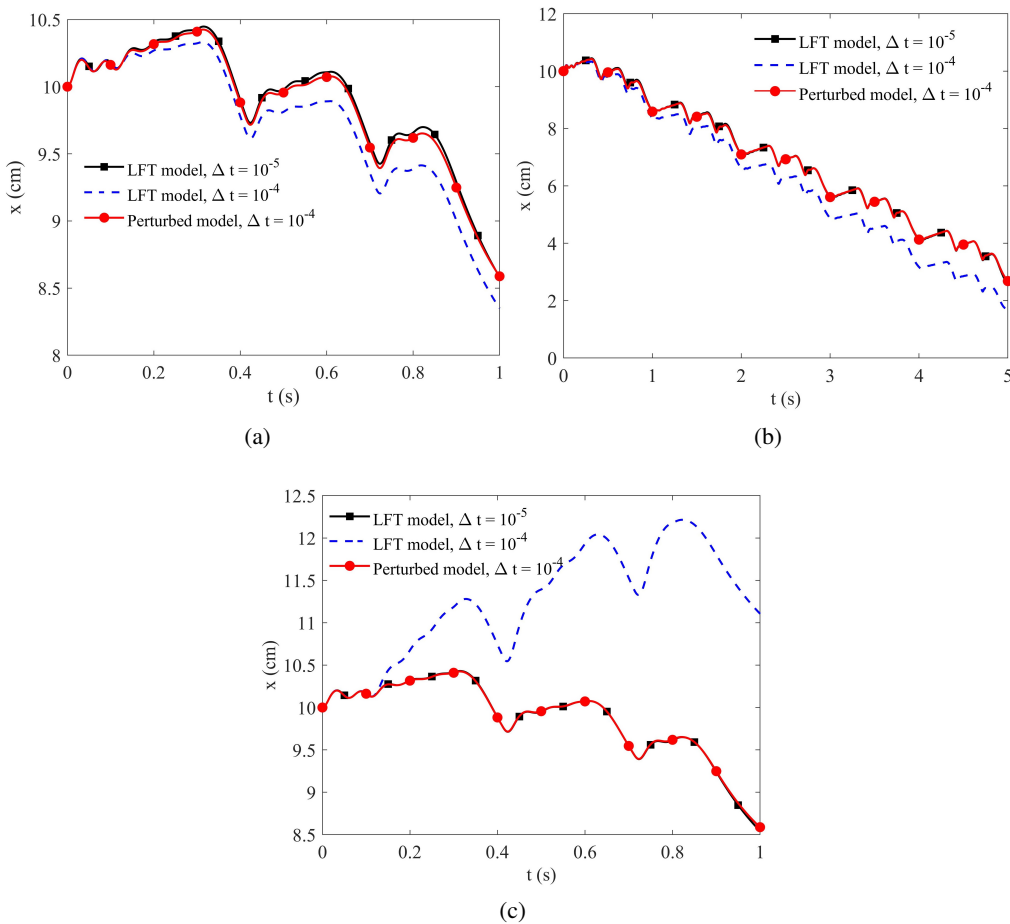


Figure 2.11: Comparison of piston position between the LFT and the perturbed model for a) 1 s and b) 5 s for a 0.05 L small volume and c) a 0.01 L one.

When the small volume is decreased from 0.05 litres to 0.01 litres, the simulation becomes unstable if the LFT model is used with a time step of 10^{-4} s, as the dashed blue line plotted in Figure 2.11c makes clear. Comparing figures 2.11a and 2.11c reveals that the perturbed model is closer to the correct response if the volume is smaller. Figure 2.11c shows that the perturbed model's response follows the correct response line when an integral time

step and is used and the order is one level higher.

The investigation highlighted two main points. The first one is that the presence of a small volume in a fluid power system leads to the stiffness problem, irrespective of the complexity of the circuit. Secondly, the perturbed model is a reliable solution even when the hydraulic circuit is complex.

3 Real-time simulation of energy systems

According to the definition presented by [117], an energy system comprises any device designed to produce energy for end-user consumption. Therefore, boilers, cyclones, dryers, etc. are categorised as energy-system components. The performance of these devices directly affects the performance and efficiency of the relevant production line and should be designed in an efficient way and operated so as to offer the highest possible performance. For achieving the best design, usually commercial software is utilised (Ansys Fluent, COMSOL products, OpenFOAM, etc.). However, the best performance is arrived at during operation by setting of suitable inputs. As explained in Chapter 1, maximal performance for each energy device is achievable by means of a digital twin of that device simulating the process on the basis of data received from the physical device. Since DT simulation of an energy device requires real-time simulation of the process, which is computationally expensive and beyond the capability of any of the above-mentioned commercial software, it is essential to develop fast algorithms that are applicable for real-time simulation of energy-system processes.

At the same time, commercial software is of limited utility even for initial design purposes. The issue is that the results' validity is constrained by the validity of the governing equations implemented in this software, which are restricted to certain pre-determined conditions. Yet the small-scale details of these devices have especially significant effects on functionality at larger scales. For example, the gas drag force exerted on the particles in boilers is usually modelled in terms of semi-empirical or empirical relations, such as what the Ergun equation tells us about the resulting drag force. Therefore, obtaining truly the best performance demands a multi-scale investigation in which operations on the smallest scale are responsible for providing correct and reliable information to be fed to larger-scale entities for large-scale simulation. The small-scale simulation, as its name suggests, is itself confined to a small domain where periodic boundary conditions usually are present; however, its main function is to reveal all the important details to be used in large-scale simulations.

Consequently, the concept of multi-scale simulation is employed. Usually, this involves two level of simulations being available: small-scale ones to supply the data for large-scale simulations and large-scale ones to product results that can inform design. In multi-scale simulation, exchange of data between the two scales of simulations occurs only when needed. For instance, the heat transfer in a dryer can be understood through simulating a small portion of powders entering the device, and the resulting data can be passed to the large-scale simulations for correct estimation of the field variables.

The algorithms and simulations that were presented in Chapter 2 are at system level, meaning that they are applicable for the largest scale of the system. In contrast, in **energy systems**, small-scale simulations too are needed. Such details as accurate estimates of the effective thermal conductivity of granular materials, permeability of porous media, and drag forces exerted in the porous region are essential input to the large-scale simulation if reliable results are desired.

In this chapter, the DEM, TDEM, and LBM techniques are elaborated on. These constitute the main tools for both small- and large-scale simulations. In addition, the LBM

and TDEM use inherently fast algorithms that can be employed for real-time simulation in connection with digital-twin applications. Although these simulation algorithms can be applied to all devices used in the energy sector, here the example of porous media illustrates their use.

3.1 Porous media

The two strategies commonly used to model fluid flow through porous media are direct simulation and representative elementary volume (REV). In direct simulation, the complexities of the solid domain are not simplified and a no-slip boundary condition is applied to the surface. The fluid flow through the pore spaces is modelled, which provides the information about the velocity, pressure, and temperature fields. In addition, one can obtain the flow details and such porous-medium characterisations as permeability, tortuosity, and channelling properties through this approach. The method is suitable for use in small-scale simulations to calculate the properties of a porous zone correctly. Although this technique reveals the local details of flow, the random distribution of microscopic pores (due to the complexity of the geometry) makes the simulation computationally expensive. In this context, the porous zone's full geometry, inclusive of all tortuous pore spaces, is required. X-ray photo scanning can reveal these details [118], but an alternative way to build a packed bed with a porous zone is to use DEM code, preferably accounting for multiple particle shapes. A packed bed generated with various particle shapes and sizes may resemble a real-world packed bed. For instance, Figure 3.1 presents a packed bed generated with 1,000 cubic particles. This packed bed's solid volume fraction is approximately 0.6, so it qualifies as a densely packed bed. For a dilute packed bed (i.e., one whose solid volume fraction is fairly small), a random number generator can be used for generation. For densely packed beds, however, the particles should be allowed to settle under gravity in a DEM solver.

In the alternative approach, applying REV scale [119], the effects of pores are omitted, so there would be a control volume (approximately 10 times larger than the particle diameter) whose solid volume fraction gets calculated in line with the amount of solid embedded in that volume. Consequently, the domain should be discretised to several relatively large control volumes, to each of which a suitable solid volume fraction gets assigned. This method is applicable in particular for those large-scale simulations wherein a fast algorithm such as the LBM's is employed.

On this scale, the effects of porosity are represented by using randomly distributed particles and considering the fluid-particle drag relations in conjunction with the Navier-Stokes equations. From a modelling point of view, every REV should be assigned an average solid volume fraction via appropriate averaging over the pore network within that REV. On the other hand, the drag force is added to the Navier-Stokes calculations as a source term that is a function of the solid volume fraction. It is worth mentioning at this point that many LB models have been proposed for adding suitable source terms to the Navier-Stokes equations [120, 121, 122]. The literature offers numerous local semi-empirical relations posited for the drag force [123, 124].

Nithiarasu et al. [125] were the first to derive the momentum and energy equations for

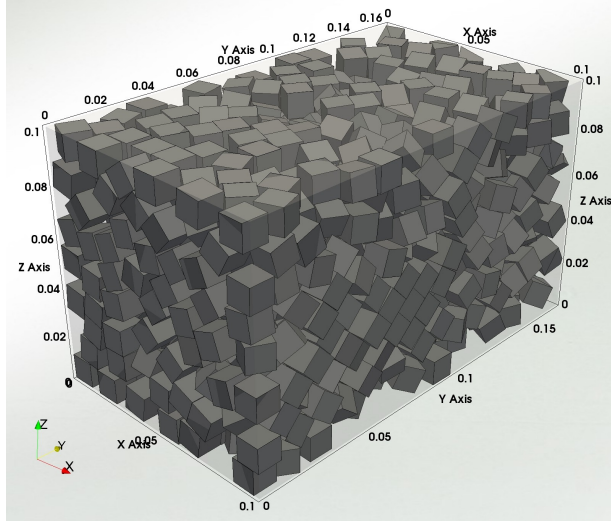


Figure 3.1: A porous medium containing 1,000 cubic particles built with a DEM solver as particles that have settled through gravity.

porous media on REV scales [126, 127], thus:

$$\partial_{\beta} \bar{u}_{\beta} = 0 \quad (3.1)$$

$$\partial_t \bar{u}_{\alpha} + \bar{u}_{\beta} \partial_{\beta} \left(\frac{\bar{u}_{\alpha}}{\varepsilon} \right) = - \frac{\varepsilon}{\rho_0} \partial_{\alpha} (\bar{p} / \varepsilon) + \nu \partial_{\beta} \partial_{\beta} \bar{u}_{\alpha} + F_{\alpha} \quad (3.2)$$

$$\partial_t (\sigma T) + \partial_{\beta} (T \bar{u}_{\beta}) = \partial_{\beta} (k_m \partial_{\beta} T) + Q \quad (3.3)$$

Here, \bar{u} and \bar{p} stand for averaged velocity and pressure; F_{α} and Q are the source terms added to the momentum and energy equations, respectively; ρ_0 is density; and ν is the fluid's kinematic viscosity. The ε value denotes the fluid volume fraction, the β subscript denotes summation, and α indicates the direction.

Note that the energy equation above, Equation 3.3, is a combination of the solid and fluid energy equations. Therefore, in this equation, $\sigma = \varepsilon + (1 - \varepsilon)(\rho C_p)_s / (\rho C_p)_f$, with ε varying with the space, and effective heat diffusivity $k_m = \eta / (\rho C_p)_f$ is defined as effective thermal conductivity divided by fluid heat capacitance.

3.2 The lattice Boltzmann method

By the early 1990s, scientists' interest had shifted from lattice-gas automata [128] toward the lattice Boltzmann method, which is based on kinetic theory [129, 130].

In kinetic theory, the fluid field is assumed to be a large collection of molecules whose interactions are based on Newton's laws of motion. Whereas the DEM approach entails attempting to track the motion of all the individual particles, in kinetic theory it is the col-

lective behaviour of the molecules that receives the most attention. Since it is impossible to solve even a very small system containing 6.0221422×10^{23} molecules (Avogadro's number, denoting one mole of matter) with the computation resources currently available, the statistical representation of the system can serve as an alternative way of obtaining the information that describes the system. The full statistical description of a fluid at thermal equilibrium is assumed to be captured by a function known as the distribution function: $f(x_\alpha, \eta_\alpha, t)$, where x_α , η_α , and t are position, velocity, and time, respectively. This assumption is similar to Callen's second postulate for statistical thermodynamics, which states that 'there exists a function of the extensive variables of any composite system, defined for all equilibrium states and having the following property: the values assumed by the extensive parameters in the absence of an internal constraint are those which maximize the entropy over the manifold of constrained equilibrium states' [131, 132]. Accordingly, knowing the distribution function with regard to time forms the underpinning to statistical description of the system; e.g., the moments of the distribution function will yield the macroscopic quantities.

The transport equation encapsulating the distribution function is the main challenge of kinetic theory: on account of the collision term, its formulation and solution are not straightforward. On the basis of Liouville's theorem, the transport equation can be written as

$$\frac{Df}{Dt} \equiv \partial_t f + \eta_\alpha \partial_\alpha f = \Omega(f) \quad (3.4)$$

where η is the microscopic velocity vector, α denotes the direction, and Ω is the collision operator to be determined. One should bear in mind that this equation is derived in a phase-space volume, so there are six independent variables, three of them spacial coordinates r_α and the other three momentum variables p_α .

3.2.1 The BBGKY hierarchy of equations

Let us consider a set of N particles having an N -particle distribution function F_N . The evolution of F_N can be completely determined by means of Liouville's theorem:

$$\partial_t F_N + \frac{p_{\alpha i}}{m_0} \partial_{r_{\alpha i}} F_N + F_{\alpha i} \partial_{p_{\alpha i}} F_N = 0 \quad (3.5)$$

In this equation, m_0 is the particle mass and $F_{\alpha i}$ is the force exerted on the i th particle. Now, if we define a new set of particles in which M particles are removed from the N -particle set, the integral over F_N will be a function of the variables for those M particles that have been taken away. Therefore, the M -particle-reduced distribution function can be defined as

$$F_M(r_{\alpha 1}, \dots, r_{\alpha M}, p_{\alpha 1}, \dots, p_{\alpha M}, t) = \int F_N(r_{\alpha 1}, \dots, r_{\alpha N}, p_{\alpha 1}, \dots, p_{\alpha N}, t) dr_{\alpha M+1} \dots dr_{\alpha N} dp_{\alpha M+1} dp_{\alpha N} \quad (3.6)$$

To derive the famous Bogoliubov–Born–Green–Kirkwood–Yvon (BBGKY) equation, one can simply substitute Equation 3.6 into Equation 3.5, which produces

$$\begin{aligned} & \partial_t F_M + \dot{r}_{\alpha i} \partial r_{\alpha i} F_M - \partial r_{\alpha i} V_{ij} \partial p_{\alpha i} F_M = \\ & (N - M) \int dr_{\alpha M+1} dp_{\alpha M+1} \partial r_{\alpha i} V_{iM+1} \left(\partial p_{\alpha i} F_{M+1} - \partial p_{\alpha M+1} F_{M+1} \right) \end{aligned} \quad (3.7)$$

Hence, some interesting cases emerge when we remove only one or two particles. This yields

$$\partial_t F_1 + \dot{r}_{\alpha 1} \partial r_{\alpha 1} F_1 = (N - 1) \int dr_{\alpha 2} dp_{\alpha 2} \partial r_{\alpha 1} V_{12} \left(\partial p_{\alpha 1} F_2 - \partial p_{\alpha 2} F_2 \right) \quad (3.8)$$

and

$$\begin{aligned} & \partial_t F_2 + \dot{r}_{\alpha 1} \partial r_{\alpha 1} F_2 + \dot{r}_{\alpha 2} \partial r_{\alpha 2} F_2 = \\ & (N - 2) \int dr_{\alpha 3} dp_{\alpha 3} \left[\partial r_{\alpha 1} V_{13} \left(\partial p_{\alpha 1} F_3 - \partial p_{\alpha 3} F_3 \right) + \partial r_{\alpha 2} V_{23} \left(\partial p_{\alpha 2} F_3 - \partial p_{\alpha 3} F_3 \right) \right] \end{aligned} \quad (3.9)$$

3.2.2 The Boltzmann transport equation

The derivation for the single-particle distribution function F_1 is not closed, so we need a closure equation. The well-known Boltzmann transport equation is a closure integro-differential equation operating on the distribution function f [133]. This equation can be derived via any of several approaches, either physical or mathematical [134]. Although the BBGKY hierarchy was introduced long after the Boltzmann equation was proposed, it is actually the first-order truncation of that equation, in mathematical terms [135]. The Boltzmann transport equation is expressed as follows [136, 137, 135]:

$$\frac{Df}{Dt} = \frac{1}{m} \int (f' f'_p - f f_p) \|\eta_{\alpha 1} - \eta'_\alpha\| d\eta'_{\alpha 1} dA \quad (3.10)$$

The prime mark is used to denote the pre-collision variables and functions. Therefore, $f' = f(x_\alpha, \eta'_\alpha, t)$, $f'_p = f(x_\alpha, \eta'_{\alpha p}, t)$, $f = f(x_\alpha, \eta_\alpha, t)$, and $f_p = f(x_\alpha, \eta_{\alpha p}, t)$. In addition, η'_α and $\eta'_{\alpha p}$ are the microscopic velocities before collision, while η_α and $\eta_{\alpha p}$ represent the velocities after it occurs. The integral variable dA is over the collision surface of the particles that is perpendicular to the direction of their relative velocity.

The right-hand side of Equation 3.10 is a non-linear collision operator that we refer to as $\Omega(f)$:

$$\Omega(f) = \frac{1}{m} \int (f' f'_p - f f_p) \|\eta_{\alpha 1} - \eta'_\alpha\| d\eta'_{\alpha 1} dA \quad (3.11)$$

As the collision operator is a non-linear term, theoretically solving the Boltzmann equation for non-equilibrium conditions is difficult. However, one can solve it in the equilibrium condition and thereby obtain the equilibrium distribution function f_{eq} . In a condition of equilibrium, the distribution function is independent of time. In addition, in the absence of any external forces, it is independent of position also. In consequence, the collision operator becomes zero, $\Omega(f) = 0$. Hence, by means of Equation 3.11, it can be shown

that

$$\int \Omega(f) \ln(f) d\eta_\alpha = \frac{1}{m} \int (f' f'_p - f f_p) \|\eta_{\alpha 1} - \eta'_\alpha\| \ln\left(\frac{f f_p}{f' f'_p}\right) d\eta'_{\alpha 1} d\eta_\alpha dA = 0 \quad (3.12)$$

Consequently, this equation is satisfied if and only if

$$f' f'_p = f f_p \quad (3.13)$$

This conclusion is referred to as the H-theorem, and the solution to this equation takes the form of an exponential function, $f_{eq} = \exp(g)$. By using the hydrodynamic moments of the distribution function, defined as

$$\rho(x_\alpha, t) = \int f(x_\alpha, \eta_\alpha, t) d\eta_\alpha \quad (3.14)$$

and as

$$\rho(x_\alpha, t) u(x_\alpha, t) = \int \eta_\alpha f(x_\alpha, \eta_\alpha, t) d\eta_\alpha \quad (3.15)$$

and

$$\rho(x_\alpha, t) e(x_\alpha, t) = \int \eta_\alpha \eta_\alpha f(x_\alpha, \eta_\alpha, t) d\eta_\alpha \quad (3.16)$$

we can obtain the equilibrium distribution function

$$f_{eq} = \rho \left[\frac{m}{2\pi k_b T} \right]^{\frac{D}{2}} e^{-mv_{r\alpha}^2/2k_b T} \quad (3.17)$$

where k_b is the Boltzmann constant, D is the dimension, T is temperature, $v_{r\alpha} = \eta_\alpha - u_\alpha$, and u_α is macroscopic velocity.

Calculating the exponential function is computationally expensive. Therefore, the equilibrium distribution function is approximated by Taylor-series expansion up to the second order of velocity (the Mach number) by assuming the Mach number to be much smaller than 1 ($Ma \ll 1$), per the literature [138, 139]:

$$f_{eq} = \rho \omega(\eta_\alpha) \left[1 + \frac{\eta_\alpha u_\alpha}{cc} + \frac{\eta_\alpha^2 u_\alpha^2}{2cc^2} - \frac{u_\alpha^2}{2cc} \right] \quad (3.18)$$

In this formulation, $cc = \frac{k_b T}{m}$ and $\omega(\eta_\alpha) = (2\pi cc)^{-\frac{D}{2}} \exp\left(\frac{-\eta_\alpha^2}{2cc}\right)$.

3.2.3 A lattice Boltzmann model for granular materials

Guo and Zhao [119] began utilising the lattice Boltzmann method to simulate an REV-scale porous medium with incompressible fluid flow passing through it. The effects of porosity appearing as a drag force (under the Ergun equation) have been added as a pre-estimated source term arising from the particle–fluid interaction. In this model, the static

pressure exists in a relationship with the medium's density and porosity that is consistent with the $p = c_s^2 \rho / \varepsilon$ relation. Constant density (incompressible flow) would imply, therefore, that the pressure will be merely a function of the porosity known in advance. Importantly, however, this model assumes that density does **not** have a strictly constant value ($\rho \approx \rho_0$) and it can vary slightly ($\rho = \sum f_i$). Therefore, it should be highlighted that variations in density in incompressible flows change the momentum balance in the model. This, in turn, leads to errors in calculation of the pressure drop. In a contrasting approach, He and Luo [140] proposed an LB model (called the HL model) to separate pressure from density. This renders the model suitable for dealing with incompressible flows. It is utilised [141] to investigate solid–liquid flows by means of a collision operator modified to represent the effects of the solid volume fraction as well. Still, it cannot directly operate from the semi-empirical relations as a source term.

To overcome the difficulties associated with Guo–Zhao-type models for granular materials, the author has introduced an LB approach to deal with an incompressible fluid flow interacting with a solid phase. In this model, pressure can change while density is strictly constant, with no variation whatsoever. In addition, the porosity effects appearing as a drag force (under the Ergun equation or any other relations the literature describes for fluid–solid interaction) can be included as a source term. The details of this model are presented in Publication III [142]. In this model, the following modified Boltzmann equation is proposed:

$$f_i(x + e_i \delta t, t + \delta t) - f_i(x, t) = \frac{f_i(x, t) - f_i^{eq}(x, t)}{\tau} + T_i \delta t = \Omega_i \quad (3.19)$$

Here, e_i denotes the discretised fluid particle velocity, and f and f_i^{eq} are the distribution function and equilibrium distribution function, respectively. The relaxation time is τ , and δx and δt are the lattice length unit and time step, respectively. Several relations for $T_i \delta t$ are proposed for taking into account external forces that appear in the NS equation. This term is used also as a correction term for the pressure gradient (see Publication III for more details).

The following relationship is proposed for T_i :

$$T_i = \frac{w_i n}{c_s^2} e_{id} F_d + \frac{w_i n}{c_s^2} (1 - \varepsilon) e_{id} \partial_d p \quad (3.20)$$

The dummy index (d) is used for performing the summation over three dimensions, and c_s is the speed of sound. This equation satisfies the following conditions, without which Navier–Stokes equations cannot be derived from the LB equation by means of a Chapman–Enskog expansion:

$$\sum T_i = 0, \quad \sum T_i e_{i\alpha} = n F_\alpha + n(1 - \varepsilon) \nabla p, \quad \sum T_i e_{i\alpha} e_{i\beta} = 0 \quad (3.21)$$

In Equation 3.20, $n = 1 - \frac{1}{2\tau}$, ε is the fluid volume fraction, and p refers to the hydrostatic pressure. The w_i value is the vector for weighting numbers as presented below for a

three-dimensional grid with nineteen distinct velocities $D3Q19$:

$$\omega_i = [12 \ 2 \ 2 \ 2 \ 2 \ 2 \ 2 \ 1 \ 1 \ 1 \ 1 \ 1 \ 1 \ 1 \ 1 \ 1 \ 1 \ 1 \ 1] / 36 \quad (3.22)$$

At this point, it should be stressed that the model works for all LBM schemes $DdQq$, irrespective of the d and q values. Since $D3Q19$ is the best-known one for three-dimension simulations, the discrete velocity vectors for this scheme are presented below:

$$\begin{aligned} e_{ix} &= [0 \ 1 \ -1 \ 0 \ 0 \ 0 \ 0 \ 1 \ 1 \ 1 \ 1 \ -1 \ -1 \ -1 \ -1 \ 0 \ 0 \ 0 \ 0] \\ e_{iy} &= [0 \ 0 \ 0 \ 1 \ -1 \ 0 \ 0 \ 1 \ -1 \ 0 \ 0 \ 1 \ -1 \ 0 \ 0 \ 1 \ 1 \ -1 \ -1] \\ e_{iz} &= [0 \ 0 \ 0 \ 0 \ 0 \ 1 \ -1 \ 0 \ 0 \ 1 \ -1 \ 0 \ 0 \ 1 \ -1 \ 1 \ -1 \ 1 \ -1] \end{aligned} \quad (3.23)$$

In Bhatnagar–Gross–Krook (BGK) LBM models, the collisions of particles occur such that they are brought to instantaneous relaxation (i.e., they enter instantaneous equilibrium). Consequently, the streaming and collision steps are followed by an equilibrium step in which the macroscopic quantities can be calculated. The equilibrium distribution function used in Equation 3.19 is introduced as

$$f_i^{eq}(x) = w_i p + w_i c_s^2 \rho_0 \varepsilon \left[3 \frac{e_{i\alpha} \cdot u_\alpha}{c^2} + \frac{9}{2} \frac{(e_{i\alpha} \cdot u_\alpha)^2}{c^4} - \frac{3}{2} \frac{u_\alpha^2}{c^2} \right] \quad (3.24)$$

in which ρ_0 denotes the constant fluid density, c expands to $\frac{\delta x}{\delta t}$, and u_α is fluid velocity. This relation satisfies the following constraints, which are essential for the above-mentioned derivation of Navier–Stokes equations from the LB model via Chapman–Enskog theory (again, the third paper provides details):

$$p = \sum f_i^{eq} \quad (3.25)$$

$$c_s^2 \rho_0 \varepsilon u_\alpha = \frac{1}{2} c_s^2 F_\alpha \delta t + \sum e_{i\alpha} f_i^{eq} \quad (3.26)$$

$$c_s^2 \rho_0 \varepsilon u_\alpha u_\beta + c_s^2 p \delta_{\alpha\beta} = \sum e_{i\alpha} e_{i\beta} f_i^{eq} \quad (3.27)$$

The velocity and pressure variables get calculated at each time step in line with the constraints indicated above. This procedure should use distribution function f whenever a state of equilibrium is reached. The final Navier–Stokes equation form produced by derivation from the LB space by means of Chapman–Enskog expansions is

$$\begin{aligned} \frac{\partial(\rho_0 \varepsilon u_\alpha)}{\partial t} + \frac{\partial(\rho_0 \varepsilon u_\alpha u_\beta)}{\partial x_\beta} &= -\varepsilon \frac{\partial p}{\partial x_\alpha} + \mu \frac{\partial}{\partial x_\beta} \{ \partial x_\beta (\varepsilon u_\alpha) + \partial x_\alpha (\varepsilon u_\beta) + \partial x_\gamma (\varepsilon u_\gamma) \delta_{\alpha\beta} \} + F_\alpha \\ &\quad - \nabla \cdot \partial x_\gamma (u_\alpha u_\beta u_\gamma) \end{aligned} \quad (3.28)$$

In this expression, the dynamic viscosity is $\mu = c_s^2 \rho_0 (\tau - \frac{1}{2} \delta)$.

3.2.4 A thermal lattice Boltzmann model for granular materials

The coupling between the momentum equation and heat-transfer equation is one-directional when the fluid is incompressible: the heat-transfer equation does not exert any influence over the momentum equation, while momentum does affect heat transfer. Therefore, by knowing the velocity field, one can implicitly solve for the temperature field. Guo and Zhao [143] presented a thermal LB model for fluid-saturated porous media. For a medium of this nature, the assumption of local thermal equilibrium (LTE) between the solid and the saturated fluid is valid, so the solid and fluid in the given node (control volume) have the same temperature. Accordingly, combining the equations governing the solid and the fluid portion yields the following governing equation:

$$\sigma \partial_t T + \nabla_\alpha (T u_\alpha) = \nabla_\alpha k_m \nabla_\alpha T \quad (3.29)$$

where σ is a function of solid volume fraction ε_s .

Liu and He [144] introduced a multiple-relaxation-time (MRT) model, arguing that these are numerically more stable than BGK single-relaxation-time (SRT) models. However, BGK models' algorithmic simplicity and computation-cost-efficiency prompted Wang et al. [145] to propose a BGK model that improves the numerical stability at low viscosity and thermal diffusivity levels. In this model, referred to as the WMG model, the external force appearing in both the momentum and the energy equation connects the two. To solve the convection–diffusion equation in the D3Q5 scheme, Zheng and colleagues [146] proposed an LB model that covers this equation to second-order accuracy without requiring any additional terms. This model – a special case of the WMG model that does not consider the heat-source term or porosity – is not a local model as referred to by Chai and Zhao [147], so it needs to use neighbourhood information when applied to the collision process. Therefore, the authors recommended using a local scheme to calculate the gradients.

Chen et al. [148] identified a shortcoming of Guo–Zhao sorts of models associated with non-reliability for domains wherein there is spatial variation of heat capacitance σ . To rectify this, they introduced σ_0 , which is a constant reference value for σ to control for thermal diffusivity. Thus, σ is permitted to display spatial variation in the domain without creating concerns about constant thermal diffusivity. A serious problem remains with this thermal model and others of the Guo–Zhao type, though: their accuracy level. These models provide first-order accuracy and require further terms before they can cover the thermal governing equation to second-order accuracy. For instance, Chen et al.'s model covers the equation $\partial_t(\sigma T) + \nabla_\alpha (T u_\alpha) = \nabla_\alpha (k_m \nabla_\alpha T) + \delta \left(\tau_T - \frac{1}{2} \right) \partial_t \nabla_\alpha (T u_\alpha) + O(\delta^2)$, which has the additional term $\delta \left(\tau_T - \frac{1}{2} \right) \partial_t \nabla_\alpha (T u_\alpha)$, alternatively providing first-order accuracy as $\partial_t(\sigma T) + \nabla_\alpha (T u_\alpha) = \nabla_\alpha (k_m \nabla_\alpha T) + O(\delta)$ (see Publication III for details of the model).

The doctoral project introduced a thermal LB model to solve the energy equation to second-order accuracy without necessitating any additional terms. In this model, a heat-source term is added that can apply a local heat source to any node in the domain. This model is detailed in the third paper (Publication III).

The LB equation proposed for the thermal LB model is

$$h_i(x + e_i \delta t, t + \delta t) = \chi h_i(x, t) + (1 - \chi) h_i(x + e_i \delta t, t) + \frac{h_i(x, t) - h_i^{eq}(x, t)}{\tau_T} + Q_i \delta t \quad (3.30)$$

where h_i^{eq} and h_i are the equilibrium and non-equilibrium distribution function, respectively; Q_i is the heat-source term; and τ_T is the thermal relaxation factor. Note that the χ parameter determines the accuracy of model. If $\chi = 1$, the model will display first-order accuracy, while relaxing this parameter has been shown to yield energy-equation solutions that demonstrate second-order accuracy. The author obtained the idea for such a parameter from the work of Zheng et al. [146], who used this trick for the Cahn–Hilliard equation for interface tracking in multi-phase flows in connection with a D3Q5 scheme. The equilibrium distribution function (h_i^{eq}) that appears in Equation 3.30 is introduced here as

$$h_i^{eq}(x) = \begin{cases} T(\sigma - \sigma_0) + w_i T(\sigma_0 + \frac{e_{i\alpha} u_\alpha}{c_s^2 \chi}) & i = 0 \\ w_i T(\sigma_0 + \frac{e_{i\alpha} u_\alpha}{c_s^2 \chi}) & i \neq 0 \end{cases} \quad (3.31)$$

where $\chi = 1/(0.5 + \tau_T)$ results in the energy equation being solved with second-order accuracy. In the equilibrium step, the local temperature is calculated by means of the following relationship:

$$T = \frac{\sum h_i^{(0)}}{\sigma} \quad (3.32)$$

The heat-source term in the energy equation is needed in many circumstances. For instance, in additive manufacturing, the laser beam on the metal powders requires a heat-source term. Accordingly, a source term is added to our model with the following representation:

$$Q_i = \bar{Q} \frac{w_i \sum e_{i\alpha} e_{i\alpha} - c_s^2}{\sum e_{i\alpha} e_{i\alpha} - q c_s^2} \quad (3.33)$$

where \bar{Q} is the value for the heat source in SI units and q is the number of discrete velocities for the $DdQq$ scheme.

3.2.5 A conjugate lattice Boltzmann model for granular materials

The two LB models presented in the subsections above are based on REV scale, which involves relatively large-scale modelling. These models are inherently fast because LB algorithms do not demand a larger number of operations. In addition, the new LB models can be easily implemented on GPUs for parallel computing or in line with the MPI or OpenMP standard. Therefore, using fast algorithms in combination with parallel computing makes LB a viable candidate for large-scale real-time simulations. However, it should be stressed that the high-level nature of REV scales obscures the details found on smaller scales. Recall, for instance, that an REV volume in porous media is usually 10

times larger than a particle, so only an averaged volume fraction is assigned to each control volume, without regard for particle shape or size, pore shapes, channelling properties, etc. To offset the drawbacks of large-scale simulations and allow for small-scale simulation, the author presented a conjugate LB model for heat transfer. It is worth mentioning that the model for fluid flow described in Subsection 3.2.3 can be used for either large- or small-scale simulation work. For large scales, ε should be set equal to the amount of the solid volume fraction assigned to the relevant control volume, while for small-scale simulations it should be 1 if the node is fluid or 0 if it is solid.

Packed beds such as the one in Figure 3.2a are commonplace in industrial applications. Although this packed bed is a small one, containing only 30,000 particles, LB simulation of heat transfer through its solid and fluid portions would still be out of reach for a real-time platform. Another option is available, however – the thermal discrete-element method, which is far faster than the LBM and can be used for large-scale simulation in many research and industrial investigations. In this method, elaborated on in the next subsection, the fluid's effects on heat transfer should be addressed as thermal resistance assigned to each individual particle. This is vital: valid and reliable results hinge on correctly estimating these effects on heat transfer. If we use a conjugate LB model to solve the energy equation for a cluster of particles such as what Figure 3.2b depicts, we can calculate the effective thermal conductivity (ETC) of the cluster and, through this, a middle particle's thermal resistance. This simulation set-up should be implemented for a small-scale domain with only a few particles, because 1) the energy equation has to be solved for both fluid and solid and 2) each particle should have several nodes, which require tremendous computation resources. The resulting estimate of thermal resistance gets fed to the TDEM algorithm, to account for the effects of the fluid. The method is applicable for all modes of heat transfer through fluid: conduction, convection, and radiation.

Although the candidate developed a conjugate heat-transfer model to study the effects of interstitial fluid on a granular cluster's heat conduction, an article reporting on this has not been published yet, so this work is not represented in the publications. This model solves the energy equation for both solid and fluid zones in a cluster of particles as depicted in Figure 3.2b. As the figure illustrates, only a few particles make up this cluster, which is part of the bigger system illustrated in Figure 3.2a.

Importantly, a TDEM solver following this approach is inherently fast, especially if written to exploit GPU architecture. Therefore, in such simulation work, the TDEM is responsible for large-scale simulations while the LBM is used for small-scale ones, providing the data needed as input to the TDEM (e.g., the fluid's effects on thermal resistances).

Also essential for the TDEM solver is information on the particles' contact interactions. This should be provided by the DEM, which is dealt with in the section below, followed by elaboration on the TDEM itself.

3.3 The discrete-element method

The DEM is a well-known Lagrangian technique for tracking solid particles over time by considering the particle–particle and particle–wall interactions. The dynamics of particles are controlled by Newton's second law of motion, dictating that an individual particle's

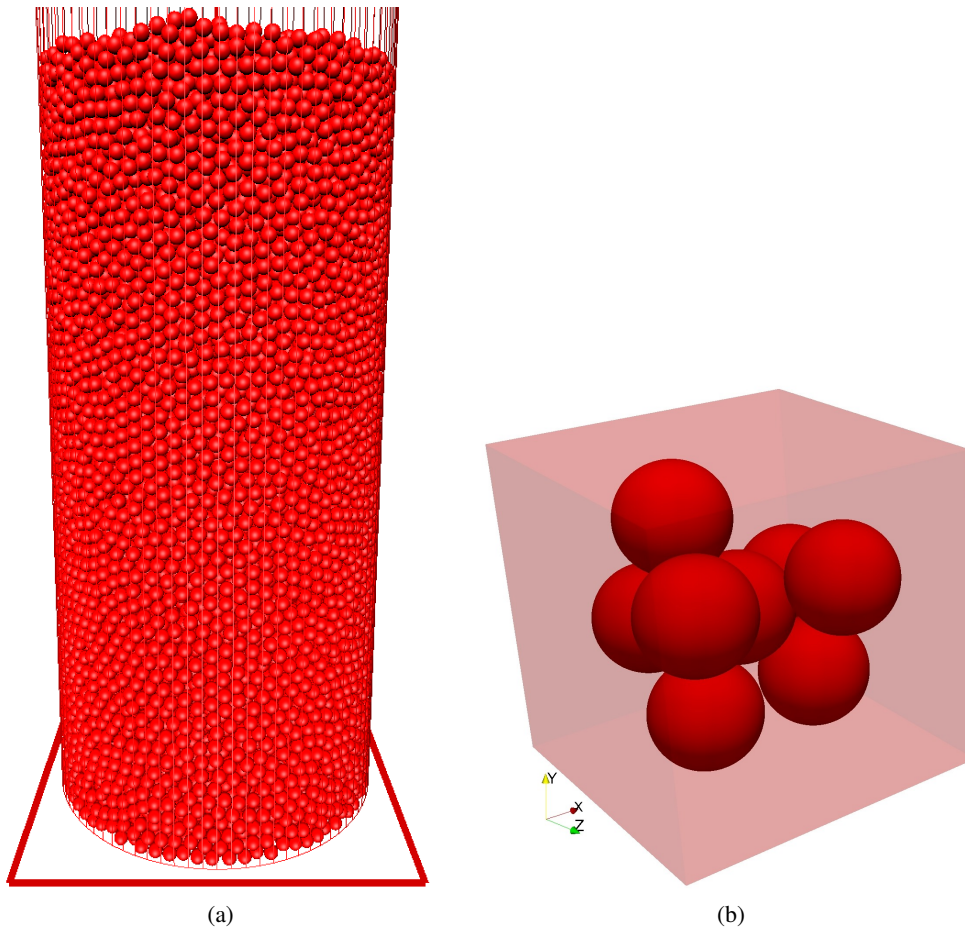


Figure 3.2: a) A typical packed bed containing 30,000 particles, from which b) one is selected at random, a particle in contact with several neighbouring ones.

acceleration can be obtained by taking the net force exerted on the particle and dividing by its mass. Therefore, the velocity and position of the particles are calculated by integrating acceleration and velocity, respectively. Several commercial software applications are available for DEM simulations (EDEM, Rocky DEM, LIGGGHTS, ThreeParticle, etc.); however, the author has used in-house code written in Fortran and CUDA C.

The simplest and most computation-light particle shape is the sphere, because the computer need store only the particle centre and radius. In addition, the well-known Hertzian contact model is usually employed to calculate the particles' overlaps, which are within analytical reach. The details and a mathematical description of the DEM for spherical particles are presented in Publication III. However, this does not represent a sophisticated approach: spherical shape is far from reality in many applications, so simulation results suffer accordingly. Defining particles as polyhedra is a powerful alternative whereby researchers can model an arbitrary particle shape.

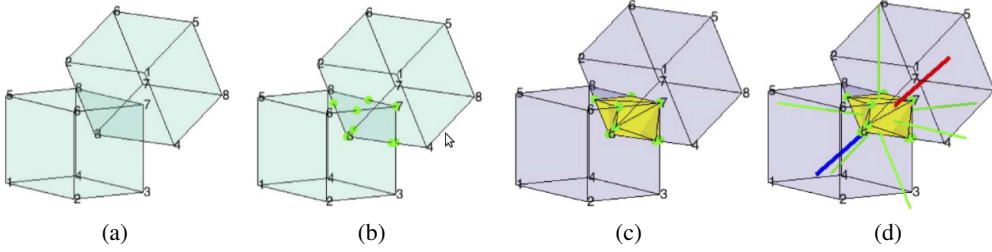


Figure 3.3: Detecting contact between two polyhedral particles (a) by searching for the contact vertices (b), from which the convex hull is recognised (c) and the contact volume is computed by means of the contact normal vectors (d) [149].

The most computationally expensive part of DEM code is that for contact detection, which accounts for 90% of the computation time if the particles are polyhedral. Therefore, large-scale real-time simulation is achievable only if the algorithms are implemented on GPUs to take advantage of parallel computing. In contrast to a spherical-particles solver, which needs only neighbour search (particles' deformation is obtained via an analytical Hertzian contact model), the polyhedral solver requires this search plus an algorithm for detailed description of contacts.

Our Blaze-DEM GPU code features a volume-based contact model that determines the contact volume and the contact normal vectors precisely, as Figure 3.3 (a–d) illustrates [149]. The contact volume is the volume between the polyhedra in contact, as depicted in Figure 3.3d.

In the first step, the broad phase contact is determined by a bounding-sphere approach known as potential contact [149]. This is followed by resolution of detailed contact. The detailed contact detection provides information on the contact vertices, faces, and volume, as panes a–d in Figure 3.3 show. Because the first step is to search for the vertices formed by the intersection of faces and edges of the contact volume, as shown in Figure 3.3b, the contact volume faces can be constructed on the basis of the pre-determined vertices and the knowledge that the contact volume is ‘stuck’ between the polyhedral particles as Figure 3.3c illustrates. The volume of the contact informs calculation of the forces acting on the particles, and, since it changes contact by contact, that volume's estimation for each of them is crucial. The contact volume can be calculated in a GPU set-up on the basis of a divergence theorem expressing the conversion of the volume integral to a surface one as

$$\iiint_V (\nabla \cdot \mathbf{G}) dV = \oint_{S(V)} \mathbf{G} \cdot d\mathbf{S} \quad (3.34)$$

Here, V is the contact volume, S is the boundary surface, and \mathbf{G} is a field vector. If \mathbf{G} is chosen to satisfy $\nabla \cdot \mathbf{G} = 1$, then the integral on the left-hand side will be equal to the contact volume.

The contact force exerted on the particle passes through the centre of mass (COM) of the contact volume and is associated with a direction and magnitude. The direction of this

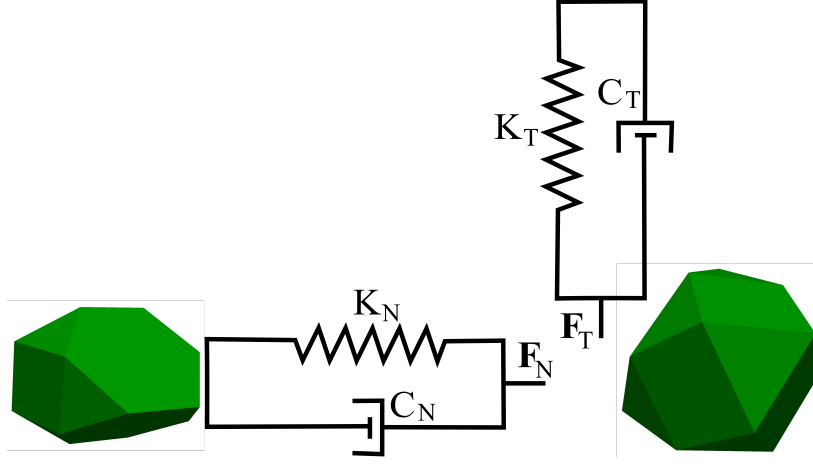


Figure 3.4: The contact forces broken into normal and tangential components, modelled with a spring and a dashpot.

force is computed for each individual contacting particle via integration of the surface normal vector over all the contact boundary surfaces. For instance, the unit vector representing the direction of the contact force for either of the particles p depicted in Figure 3.3d can be calculated as

$$\mathbf{n}_p^F = \frac{\int_S \mathbf{n}_p^S dS}{|\int_S \mathbf{n}_p^S dS|} \quad (3.35)$$

where \mathbf{n}_p^S is the surface normal vector of particle p pointing outward.

As noted in the literature [150], the most popular contact models are linear-spring-dashpot (LSD) and a non-linear Hertzian model. The magnitude of the normal and tangential contact force can be calculated via the Kelvin–Voigt LSD model as

$$\mathbf{F}_N = K_N \Delta V \mathbf{n}_p^F - C_N (\mathbf{V}_R \cdot \mathbf{n}_p^F) \mathbf{n}_p^F \quad (3.36)$$

where K_N and C_N are the linear spring stiffness ($\frac{N}{m^3}$) and damping coefficient ($\frac{Ns}{m}$), respectively, and \mathbf{V}_R represents the relative velocity of the particles. Finally, \mathbf{n}_p^F is the unit vector along which the force is exerted. In Equation 3.36, the spring and the damping coefficient are calculated by means of the following relations:

$$K_N = \frac{m_{\text{eff}}}{\Delta t_{\text{cont}}^2} \ln(e)^2 + \pi^2 \quad (3.37)$$

$$C_N = \frac{2 \ln(e) \sqrt{K_N m_{\text{eff}}}}{\sqrt{\ln(e)^2 + \pi^2}} \quad (3.38)$$

The effective mass of particles is defined per this equation as $m_{\text{eff}} = (\frac{1}{m_1} + \frac{1}{m_2})^{-1}$, Δt_{cont}^2 is the contact time determined by the material properties, e is the coefficient of restitution, and ΔV is the contact volume resolved by the algorithm presented schematically in Figure

3.3 (a–d).

The tangential component of the contact force is resolved by means of a stick-slip friction model in which Coulomb's law is used to couple the tangential and the normal component of contact force. Through this process, the initial tangential force is calculated as a summation of the tangential component of spring and viscous forces:

$$\mathbf{F}_T = -K_T(\mathbf{V}_T dt + \mathbf{L}) - C_T \mathbf{V}_T \quad (3.39)$$

Here, K_T which is typically defined to be at least $\frac{1}{2}K_N$ is tangential spring stiffness, and \mathbf{V}_T is the tangential component of relative velocity. The \mathbf{L} and C_T parameters reflect, respectively, the tangential displacement of the spring from its equilibrium position and the tangential damping coefficient, both calculated in line with the following relations:

$$\mathbf{L} = \int_{t_{Cont.start}}^{t_{Cont.end}} \mathbf{V}_T dt \quad (3.40)$$

$$C_T = \frac{2 \ln(\epsilon) \sqrt{K_T m_{eff}}}{\sqrt{\ln(\epsilon)^2 + \pi^2}} \quad (3.41)$$

It should be highlighted that the \mathbf{L} term that appears in Equation 3.39 as part of the tangential component of the contact force is computed, via Equation 3.40, for sliding friction only. For static friction, the value will be zero.

3.4 The thermal discrete-element method

As mentioned in Subsection 3.2.5, when a large-scale simulation is involved, the LBM is extremely computationally expensive because a huge number of nodes should be allocated for each particle. The same drawback exists in the FEM and other traditional CFD methods. Hence, for rapid and reliable solving of the energy equation for a large-scale system, the TDEM is a viable alternative.

The author has introduced a TDEM model suited to resolving the energy-equation problem for granular materials. Its details are available in Publication IV [151]. The model's foundation rests on a two-particle pipe model representing the heat flux between two particles as transported through a pipe connecting their centres (depicted in Fig. 3.5). Accordingly, two contacting particles, P and L , that experience temperatures $T_P^0 > T_L^0$ will form a pipe through which the energy flux is from particle P toward particle L across the particles' contact areas (i and m , for particles P and L , respectively). Our TDEM model takes into account the contacting particles' cumulative effects on the temperature of contact i . The temperature at the i th contact of particle P is obtained, T_P^i , that is due to the heat flux from particle L . This temperature can be expressed as

$$T_P^i = -Re_P \bar{Q}_{PL} + T_P^0 \quad (3.42)$$

and the temperature at the m th contact of particle L , T_L^m , arising from the flux from

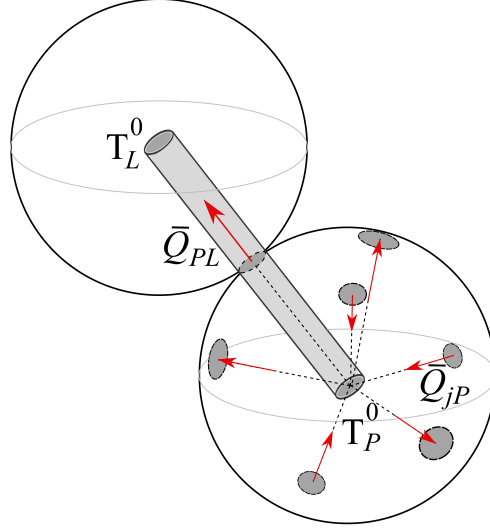


Figure 3.5: A pipe model applied between two spherical particles in mutual contact.

particle P is calculated as

$$T_L^m = Re_L \bar{Q}_{PL} + T_L^0 \quad (3.43)$$

where $Re_P = \frac{-\lambda}{2\kappa_P R_P \Delta\phi_i}$, $Re_L = \frac{-\lambda}{2\kappa_L R_L \Delta\phi_m}$, and λ is a constant with the value -0.6846. This allows one to consider a pipe with a heat flow of \bar{Q}_{PL} and a flow-resistance of Re_P . Obviously, we have $T_P^i = T_L^m$ and $\Delta\phi_i = \Delta\phi_m$. By subtracting Equation 3.43 from Equation 3.42, we arrive at the following equation for heat flux:

$$k_{PL} \begin{bmatrix} 1 & -1 \\ -1 & 1 \end{bmatrix} \begin{bmatrix} T_P^0 \\ T_L^0 \end{bmatrix} = \begin{bmatrix} Q^{PL} \\ -Q^{PL} \end{bmatrix} \quad (3.44)$$

where $k_{PL} = 1/(Re_P + Re_L)$.

Balancing the steady and transient terms in the heat-conservation equation yields the transient-energy equation. This allows us to express the energy equation governing the transient heat conduction in any individual particle p as

$$C_P \dot{T}_P^0(t) + \sum_{J=1}^N Q_{PJ} = 0 \quad (3.45)$$

where J denotes the neighbouring particles in contact with particle P . In addition, from Equation 3.44 we have $Q_{PJ} = k_{PJ}(T_J^0 - T_P^0)$, and $C_P = \frac{4}{3}\pi\rho R^3 c_P$. This equation can be solved via a time-marching method.

For two particles in mutual contact, the contact's thermal conductivity is derived as

$$k_{PL} = 2.066\kappa_P \left(\frac{3F_n(1-\sigma^2)R_P}{4E} \right)^{\frac{1}{3}} \quad (3.46)$$

where F_n is the magnitude of the normal contact force. This equation is quite similar to that for contact thermal conductivity presented by Batchelor and O'Brien (i.e., in the BOB model) [152], Carslaw and Jaeger [153], and Yovanovich [154]. For instance, the only difference between the BOB formula and the new one lies in the coefficient of 2.066, as opposed to the BOB relation's 2. The reason for this difference can be linked to how each individual contact considered in our model is affected by others. Again, further details are presented in Publication IV. Defining the thermal conductance as $H_c = \frac{1}{k_{PL}}$, we have $Q_{PL} = H_c \Delta T$, in which ΔT refers to the apparent temperature difference between particles. In the BOB model, $H_c = 2\kappa_P \sqrt{A_c}$ for spherical particles [155, 156], where A is the contact area calculated by means of a theoretical Hertzian contact model. We have offered the following attempt to generalise the thermal conductance formula to any particle shape [149]:

$$H_c = \alpha \kappa_P \sqrt{A_c} \quad (3.47)$$

The α parameter should be calibrated on the basis of the shape.

3.5 Results and discussion

There are two main factors to be considered in the context of developing and utilising real-time simulation of energy devices. The first is the benefits of a multi-scale method for preventing unnecessary expenditure of computation resources wherever possible, and the other is those of rapid algorithms for each scale. In this chapter, the author has introduced several LBM models that are inherently fast either for small-scale or for large-scale simulations. The work included developing the LBM model described above for simulation of fluid flow through porous zones that one can apply for either scale by setting an appropriate value for ε . Alongside this, the thermal LBM model is suitable for saturated porous media with an embedded thermal-source term. Figure 3.6a depicts a porous medium built with spherical particles that are randomly distributed in a $3.5 \times 3.5 \times 21$ cm³ domain for a solid volume fraction of 0.2. In this set-up, a heat source is placed within $0.23X/L$ and $0.27X/L$, where L is the length of the bed in the X direction. The inlet and outlet temperatures are kept at 300 K, and the surrounding boundaries are considered insulated. Also, the inlet velocity is specified as $u = 0.3 \frac{m}{s}$ with no slip boundary condition at the surrounding walls. The temperature distribution and the packed bed are illustrated in Figure 3.6b, with different lines corresponding with different times. The details of the relevant study are presented in Publication III.

In this LB model, the solid volume fraction is computed within control volumes at least 10 times larger than the particle diameter. Therefore, both LB models, that for fluid flow and that for the thermal solution, can be regarded as algorithms for large scales. However, if averaging is not performed, the former can be used for small-scale simulations too, by setting ε to either 1 for fluid or 0 for solid. Finally, a model such as the conjugate thermal LB model the author developed to solve the energy equation in both the fluid domain and the solid zone (again, with details yet to be published) should enable computing the thermal resistance corresponding to the fluid and feeding it to our TDEM solver.

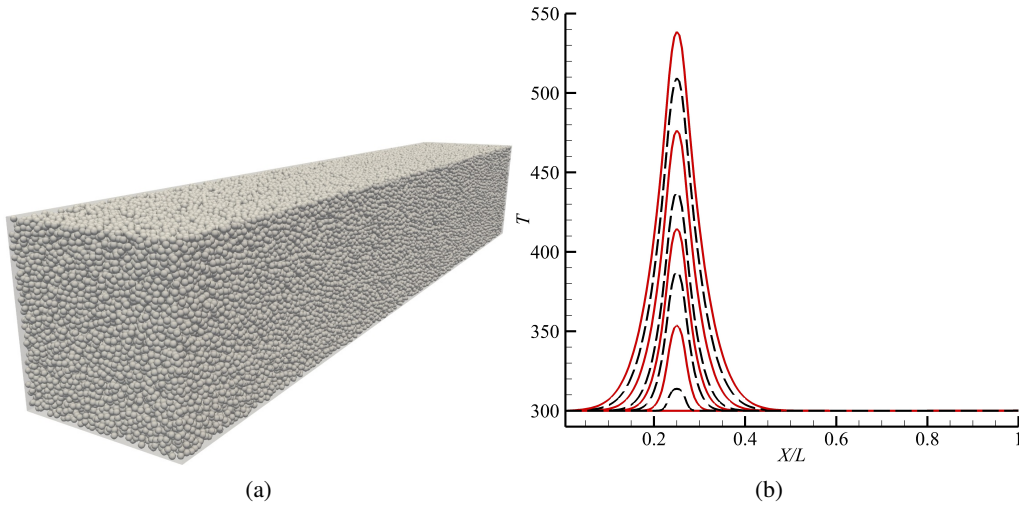


Figure 3.6: a) A diagram of the porous medium with spherical particles and b) the temperature distribution with length for various times: 0, 98, 196, 294, 392, 490, 589, 687, 785, 883, and 981 μs .

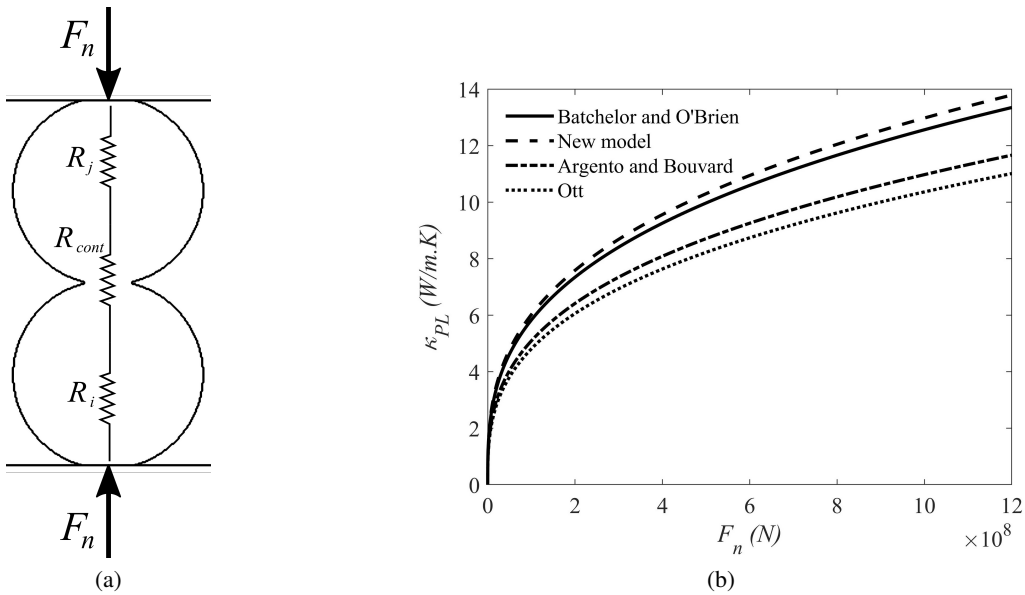


Figure 3.7: a) Two particles in mutual contact that illustrate the thermal resistances through which the heat flux should pass in the pipe model. b) A comparison of thermal contact modelling between our new model and those available in the literature.

Our TDEM model can be verified by comparing the contact thermal conductivity between two particles with what prior models yield. Let us consider two spherical particles in mutual contact that exert force F_n on each other as shown in Figure 3.7a. The contact thermal conductivity obtained in line with Equation 3.46 is compared with other models' output in Figure 3.7b. This comparison demonstrates that our model is fairly close to the others, especially the BOB model. Where our model and the BOB one differ is that ours considers the effects of a given contact on the temperature at other contacts – obviously, one particle can be in contact with several others at the same time. Furthermore, the effects of compressive forces on the conduction of heat through a packed bed constructed with spherical particles are investigated (with the set-up and results presented in Publication IV), though without examining the effects of the surrounding fluid on the ETC. The pipe model entails the heat flux flowing through a pipe that displays some thermal resistance, and if the fluid's effects are ignored, the total resistance is the same as the contact resistance, $R_{total} = R_{cont}$. In reality, however, the effects of the fluid may have a significant role in the heat transfer between two particles. To account for these effects, the total resistance should be represented as $R_{total} = R_{cont} + R_i + R_j$, where R_i and R_j are the thermal resistances that the fluid creates for particles i and j , respectively.

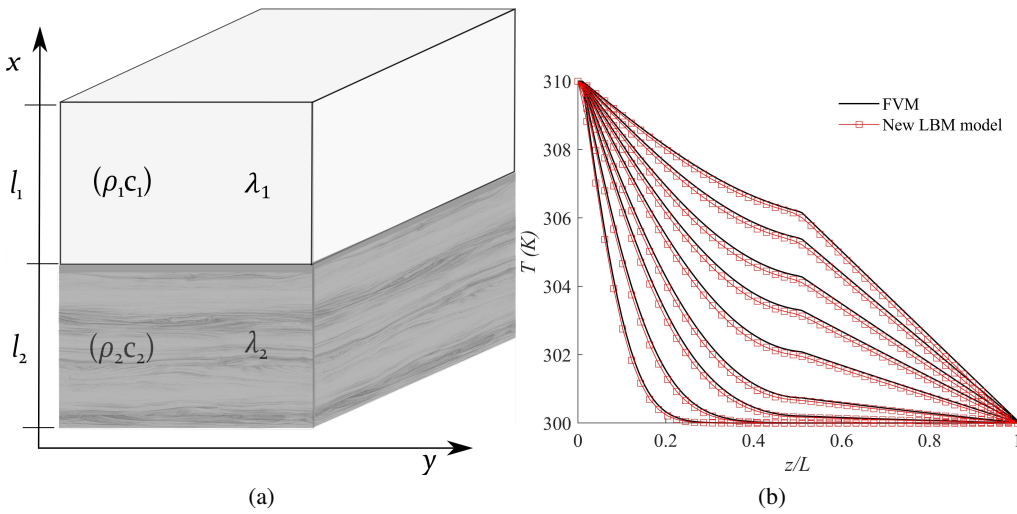


Figure 3.8: a) A schematic diagram of a two-layer composite and b) the temperature distribution along its height.

While the TDEM is an algorithm for large scales, the estimation of R_i and R_j necessitates simulation on smaller scales. It is in consideration of this that the author developed a conjugate thermal LB model to solve the energy equation for both fluid and solid. For a two-phase composite material such as that presented in Figure 3.8a, one can validate this conjugate model by comparing its results with those produced by the FVM, as presented for various times in Figure 3.7b. Any particle in a packed bed is in contact with several other particles, which together constitute a cluster of particles (Fig. 3.9 illustrates this). One can solve the energy equation for these clusters via a small-scale simulation and

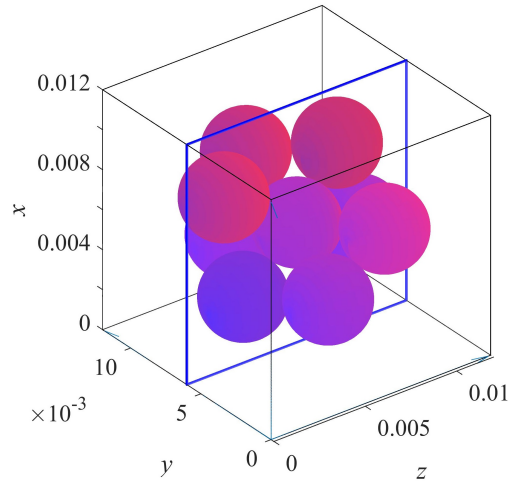


Figure 3.9: A cluster of spherical particles in a cubic domain filled with fluid, modelled to investigate a fluid's effects on heat conduction.

thereby estimate the thermal resistance value that should be assigned to the central particle in TDEM-based simulations.

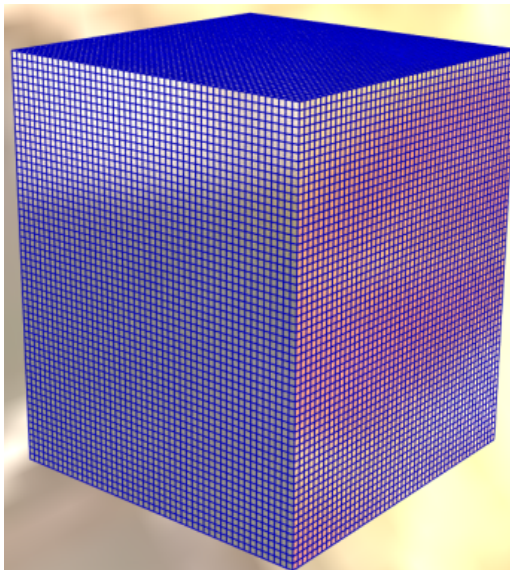


Figure 3.10: Cubic particles form a solid material the effective thermal conductivity of which is the same as its thermal conductivity.

Our TDEM model was developed for spherical particles initially. However, we proceeded to extend it for use with any shape by means of the α parameter in Equation 3.47, a value representing the particle shape. We conducted a very simple test by constructing a solid

material with cubic particles as depicted in Figure 3.10. The effective thermal conductivity of this solid packed bed should be identical to the material's thermal conductivity, so adjusting the α value allowed us to obtain an ETC equal to the material's thermal conductivity, with $\alpha = 0.86$.

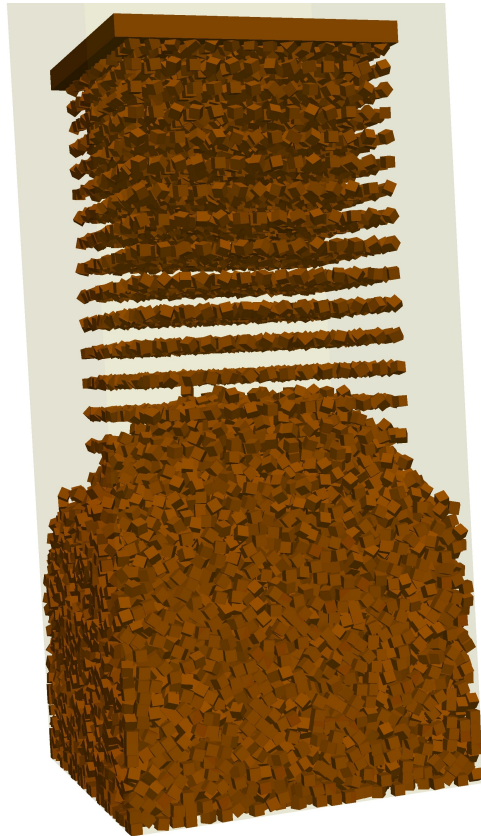


Figure 3.11: The generation of a packed bed for investigation of the effects of particle shape on granular materials' thermal behaviour.

To investigate the effects of particle shape on ETC, several packed beds are created similar to what Figure 3.11 depicts, with randomly generated particles allowed to settle under gravity. A prior publication [149] presents this work, in which we examined the particle shapes presented in Figure 3.12. For that research, the effects of the fluid were ignored and we assumed the Biot number to be small enough that the assumption of a constant temperature for each particle holds. In addition, the volume was set to be the same across all particle shapes, 0.25 cm^3 , to avoid any influence of particle volume on the results. We concluded that for all particle shapes except the hexagonal prism (HexP), the ETC increases if the contact area grows, as plotted in Figure 3.13a. Therefore, contact area is not the best parameter for characterisation of particle shape. We discovered that if we weight the contact angle for the contact area, the ETC shows an exponential relationship

with this weighting (which we refer to as contact angle isotropy) as illustrated in Figure 3.13b.

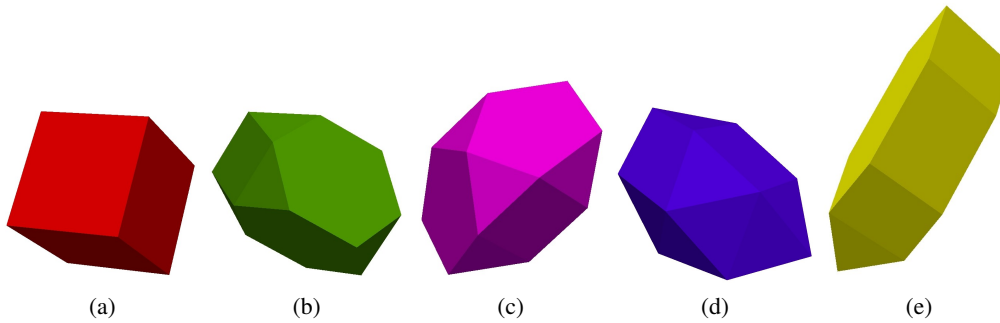


Figure 3.12: The various particle shapes investigated: a) cubic, b) truncated tetrahedron, c) bilunabirotunda, d) sphenomegacorona, and e) flattened augmented hexagonal prism.

It should be highlighted here that GPU use in simulation of particle dynamics, the TDEM approach, and other algorithms put parallel computing to the fullest advantage to speed up the calculations, which is essential for digital-twin applications (as detailed in Chapter 1). In this context, dividing the algorithms between large and small scales prevents computation resources from going to waste and simultaneously makes available the essential data required for accurate and reliable simulation.

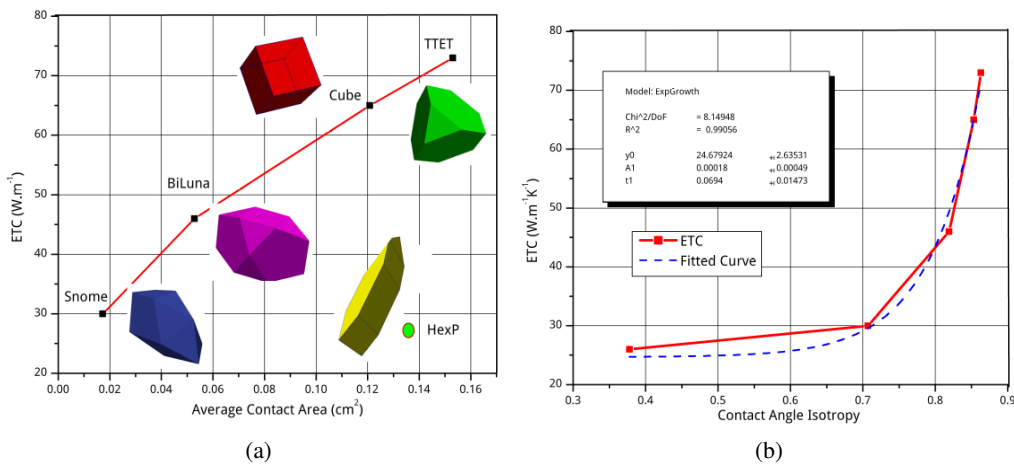


Figure 3.13: Effective thermal conductivity plotted against average contact area (a) and the contact angle isotropy for various particle shapes (b) [149].

4 Summary and conclusions

Reaching the potential of Industry 4.0, which represents the fourth industrial revolution, relies on high-speed data transmission, thereby rendering the digital-twin concept especially pertinent for industrial applications. Indeed, cyber-physical systems constitute the core of Industry 4.0, in which the physical systems are integrated with their doubles created in cyberspace. For this to become reality, the most important feature of cyber-physical systems is the speed of calculation and data transmission they require. The development of 5G technology has brought substantial increases to data-transmission speeds while still maintaining acceptable reliability, so the remaining challenge is to increase the speed of the calculations via a reliable and cost-effective approach that permits real-time simulation. This chapter offers a summary of the challenge and of the research project's response to it.

Two main strategies are applied toward enabling real-time simulation. The first approach is to advance the algorithms so as to employ fewer mathematical operations. In addition, the algorithms should be designed to be appropriate for parallel computing (afforded by the MPI and OpenMP standards). The second approach is to use hardware with high-speed clocks, such as GPUs, and FPGA micro-controllers. There are several applications for which the only possible way forward is the first one, on account of cost, weight, economy, and other considerations.

Industrial devices can be roughly categorised as either machinery or energy systems. Usually in a machinery system, a multibody mechanism operates as a subsystem with a fluid power module and a control circuit. As is evident from the literature, the most challenging part of this package with regard to real-time simulation is the fluid power system. In fact, if the singularity problem of fluid power systems is solved, the entire package can be simulated in a real-time manner. With that aim, the researcher, firstly, sought to shed some light on the origin of the problem, from a mathematical point of view and then on the basis of its physical interpretation. On this basis, the author determined that the stiffness problem associated with hydraulic circuits arises from three parameters in general: the orifice model used, the presence of a small volume in the circuit, and bulk modulus models.

Each of these issues can be addressed. A two-regime orifice model (as presented in the literature) should be used in all conditions involving a pressure drop approaching zero. Secondly, the author introduced a perturbed model to overcome the stiffness issue created by the presence of a small volume. The algorithm in question is implemented for a simple hydraulic circuit and ascertained that this model can increase the integration time step by one order. In addition, we have successfully applied this model to a four-bar mechanism and determined that it can increase the computation speed by a factor of $2.5\times$. Investigation of diverse approaches to alleviating the stiffness problem arising from a small volume led us to conclude that a perturbed model works best under various conditions, whatever the complexity level of the hydraulic circuit. While the stiffness challenge imposed by fluid power systems is created by differences in responses across time scales, the negligibility of the small time scales in hydraulic systems means that one can safely use a perturbed model.

Energy systems, in turn, involve a variety of phenomena, which occur on different spatial scales. Hence, they are referred to as complex systems. In fluid power systems, the stiffness problem arises from a difference in time scales (small vs. large), whereas in energy systems it is the difference not in time scales but of spatial scale that affects the results' accuracy and reliability. One can omit small-scale simulation, but the results then do not end up as accurate as one might expect. If, on the other hand, one chooses to simulate a large system via small-scale approaches, inefficiency arises and real-time operation demands tremendous computation resources. Using the two scales together can aid in reaching the best possible performance, for speed and accuracy both. Therefore, we have contributed algorithms suitable for either scale, amenable to parallel computing, and implemented some of them on GPUs. These algorithms are listed below:

- An LB model was developed for simulation of fluid flow through porous media. This model can be used for either scale, depending on the settings. The ε parameter in the formulation determines the scale of the simulation. If the domain is large and the number of particles enormous, one might average the particles within a given control volume to compute an average solid volume fraction ($1 - \varepsilon$) and assign the value accordingly. The control volumes should be defined such that there are at least 10–15 particles along each edge of the volume. With this sort of set-up, the algorithm is suitable for large-scale simulations. For small-scale ones, it can be rendered well-functioning by considering a node to be either a solid node or a fluid node, with ε getting assigned only a value of either 0 or 1, for, respectively, solid or fluid.
- A thermal LB model was introduced to address the heat transfer in saturated porous media. The accuracy of this model is second-order, $O(\delta^2)$, covering the energy equation without any additional terms. This model includes a heat-source term that functions extremely well for applications such as additive manufacture and the like, in which there is a local heat source, and the melting process is modelled accordingly. This model is appropriate for larger-scale simulation applications.
- We have introduced a conjugate thermal LB model to solve the energy equation for both solid and fluid parts of porous media. This model is particularly appropriate for small-scale simulations because each particle in the system needs several LB nodes, which would be computationally expensive to process at the level of a large-scale application. The value of such algorithms lies in informing scientific studies and providing data input for large-scale simulation.
- Finally, we have developed a new TDEM model to investigate the heat flux in granular materials. This model, used in combination with a DEM solver, is applicable for large-scale particulate systems. The model was derived for spherical particles and then generalised for application to any particle shape.

The author has implemented the algorithms in the Fortran and C/C++ programming languages and optimised them to some extent to run on GPUs (CUDA C and PGI CUDA Fortran compilers were used in this endeavour).

Employing the methods developed, the author investigated the fluid flow through a porous medium created with spherical particles. In addition, the thermal behaviour of saturated porous media was studied under several heat-source conditions. Our LB models are validated by comparing their results to those from another LB model and also the Fluent software.

The author has also investigated the effects of external load on the thermal response of a packed bed generated with spherical particles. It is noticed that increasing the external load reduced the probability of vertically oriented contacts, thereby decreasing the effective thermal conductivity. Also, the work led us to conclude that, of the particle shapes studied, TTeT provides the highest effective thermal conductivity, followed by a packed bed generated with cubic particles. We became aware that the contact area is not in itself a sufficient parameter to express the effective thermal conductivity behaviour of granular packed beds; however, we found an interesting parameter, contact angle isotropy, that can explain the effective thermal conductivity trend. For the shapes considered, we observed an exponential relationship between ETC and contact angle isotropy.

To investigate the effects of the fluid portion of the system on thermal conduction, a quantity of particle clusters are chosen at random and resolved the temperature field for both fluid and solid. It is concluded that the fluid's presence is more influential if the solid-to-fluid thermal conductivity ratio is less than 10. Above that threshold, the vacuum and different fluids do not have a significant effect on the packed bed's effective thermal conductivity and one can simply assume vacuum in TDEM simulations.

References

- [1] H. Lasi, P. Fettke, H.-G. Kemper, T. Feld, and M. Hoffmann, "Industry 4.0," *Business & Information Systems Engineering*, vol. 6, no. 4, pp. 239–242, 2014.
- [2] G. Li, Y. Hou, and A. Wu, "Fourth industrial revolution: Technological drivers, impacts and coping methods," *Chinese Geographical Science*, vol. 27, no. 4, pp. 626–637, 2017.
- [3] B. E. Penprase, "The fourth industrial revolution and higher education," pp. 207–229, Palgrave Macmillan Singapore, 2018.
- [4] A. Atkeson and P. J. Kehoe, "Modeling the transition to a new economy: Lessons from two technological revolutions," *American Economic Review*, vol. 97, no. 1, pp. 64–88, 2007.
- [5] M. Xu, J. M. David, and S. H. Kim, "The fourth industrial revolution: Opportunities and challenges," *International Journal of Financial Research*, vol. 9, no. 2, pp. 90–95, 2018.
- [6] R. Morrar, H. Arman, and S. Mousa, "The fourth industrial revolution (industry 4.0): A social innovation perspective," *Technology Innovation Management Review*, vol. 7, no. 11, pp. 12–20, 2017.
- [7] N. Karanjkar, A. Joglekar, S. Mohanty, V. Prabhu, D. Raghunath, and R. Sundaresan, "Digital twin for energy optimization in an smt-pcb assembly line," in *2018 IEEE International Conference on Internet of Things and Intelligence System (IO-TAIS)*, pp. 85–89, IEEE, 2018.
- [8] S. Ahmad, S. Malik, I. Ullah, D.-H. Park, K. Kim, and D. Kim, "Towards the design of a formal verification and evaluation tool of real-time tasks scheduling of iot applications," *Sustainability*, vol. 11, no. 1, p. ID 204, 2019.
- [9] I. Lee and K. Lee, "The internet of things (iot): Applications, investments, and challenges for enterprises," *Business Horizons*, vol. 58, no. 4, pp. 431–440, 2015.
- [10] C.-Y. Chen, M. Hasan, and S. Mohan, "Securing real-time internet-of-things," *Sensors*, vol. 18, no. 12, p. 4356, 2018.
- [11] P. Corcoran and S. K. Datta, "Mobile-edge computing and the internet of things for consumers: Extending cloud computing and services to the edge of the network," *IEEE Consumer Electronics Magazine*, vol. 5, no. 4, pp. 73–74, 2016.
- [12] X. Zhang, S. Tang, X. Liu, R. Malekian, and Z. Li, "A novel multi-agent-based collaborative virtual manufacturing environment integrated with edge computing technique," *Energies*, vol. 12, no. 14, p. 2815, 2019.

- [13] B. Chen, J. Wan, A. Celesti, D. Li, H. Abbas, and Q. Zhang, "Edge computing in iot-based manufacturing," *IEEE Communications Magazine*, vol. 56, no. 9, pp. 103–109, 2018.
- [14] Y. C. Hu, M. Patel, D. Sabella, N. Sprecher, and V. Young, "Mobile edge computing – a key technology towards 5g," *ETSI white paper 11*, vol. 11, no. 11, p. 16 pages, 2015.
- [15] A. Fuller, Z. Fan, and C. Day, "Digital twin: Enabling technology, challenges and open research," *arXiv preprint arXiv:1911.01276*, 2019.
- [16] W. Kritzinger, M. Karner, G. Traar, J. Henjes, and W. Sihn, "Digital twin in manufacturing: A categorical literature review and classification," *IFAC-PapersOnLine*, vol. 51, no. 11, pp. 1016–1022, 2018.
- [17] P. Aivaliotis, K. Georgoulas, and G. Chryssolouris, "The use of digital twin for predictive maintenance in manufacturing," *International Journal of Computer Integrated Manufacturing*, vol. 32, no. 11, pp. 1067–1080, 2019.
- [18] C. Cimino, E. Negri, and L. Fumagalli, "Review of digital twin applications in manufacturing," *Computers in Industry*, vol. 113, p. 103130, 2019.
- [19] Y. Koren, U. Heisel, F. Jovane, T. Moriwaki, G. Pritschow, G. Ulsoy, and H. Van Brussel, "Reconfigurable manufacturing systems," *CIRP Annals*, vol. 48, no. 2, pp. 527–540, 1999.
- [20] C. Zhang, W. Xu, J. Liu, Z. Liu, Z. Zhou, and D. T. Pham, "Digital twin-enabled reconfigurable modeling for smart manufacturing systems," *International Journal of Computer Integrated Manufacturing*, pp. 1–25, 2019.
- [21] J. Leng, Q. Liu, S. Ye, J. Jing, Y. Wang, C. Zhang, D. Zhang, and X. Chen, "Digital twin-driven rapid reconfiguration of the automated manufacturing system via an open architecture model," *Robotics and Computer-Integrated Manufacturing*, vol. 63, p. 101895, 2020.
- [22] Q. Liu, H. Zhang, J. Leng, and X. Chen, "Digital twin-driven rapid individualised designing of [an] automated flow-shop manufacturing system," *International Journal of Production Research*, vol. 57, no. 12, pp. 3903–3919, 2019.
- [23] F. Tao, J. Cheng, Q. Qi, M. Zhang, H. Zhang, and F. Sui, "Digital twin-driven product design, manufacturing and service with big data," *The International Journal of Advanced Manufacturing Technology*, vol. 94, no. 9–12, pp. 3563–3576, 2018.
- [24] J. Bao, D. Guo, J. Li, and J. Zhang, "The modelling and operations for the digital twin in the context of manufacturing," *Enterprise Information Systems*, vol. 13, no. 4, pp. 534–556, 2019.

- [25] Q. Qi, F. Tao, T. Hu, N. Anwer, A. Liu, Y. Wei, L. Wang, and A. Nee, “Enabling technologies and tools for [a] digital twin,” *Journal of Manufacturing Systems*, 2019.
- [26] F. Tao, F. Sui, A. Liu, Q. Qi, M. Zhang, B. Song, Z. Guo, S. C.-Y. Lu, and A. Nee, “Digital twin-driven product design framework,” *International Journal of Production Research*, vol. 57, no. 12, pp. 3935–3953, 2019.
- [27] B. R. Barricelli, E. Casiraghi, and D. Fogli, “A survey on [the] digital twin: Definitions, characteristics, applications, and design implications,” *IEEE Access*, vol. 7, pp. 167653–167671, 2019.
- [28] J. Cheng, H. Zhang, F. Tao, and C.-F. Juang, “Dt-ii: Digital twin enhanced industrial internet reference framework towards smart manufacturing,” *Robotics and Computer-Integrated Manufacturing*, vol. 62, p. 101881, 2020.
- [29] M. Shafto, M. Conroy, R. Doyle, E. Glaessgen, C. Kemp, J. LeMoigne, and L. Wang, “Modeling, simulation, information technology & processing roadmap,” *National Aeronautics and Space Administration*, 2012.
- [30] S. Boschert and R. Rosen, “Digital twin – the simulation aspect,” in *Mechatronic futures* (P. Hehenberger and D. Bradley, eds.), pp. 59–74, Springer, 2016.
- [31] K. Sivalingam, M. Sepulveda, M. Spring, and P. Davies, “A review and methodology development for remaining useful life prediction of offshore fixed and floating wind turbine power converter with digital twin technology perspective,” in *2018 2nd International Conference on Green Energy and Applications (ICGEA)*, pp. 197–204, IEEE, 2018.
- [32] J.-C. Samin, O. Brüls, J.-F. Collard, L. Sass, and P. Fisette, “Multiphysics modeling and optimization of mechatronic multibody systems,” *Multibody System Dynamics*, vol. 18, no. 3, pp. 345–373, 2007.
- [33] A. Peiret, F. González, J. Kövecses, and M. Teichmann, “Multibody system dynamics interface modelling for stable multirate co-simulation of multiphysics systems,” *Mechanism and Machine Theory*, vol. 127, pp. 52–72, 2018.
- [34] M. A. Naya, J. Cuadrado, D. Dopico, and U. Lugris, “An efficient unified method for the combined simulation of multibody and hydraulic dynamics: Comparison with simplified and co-integration approaches,” *Archive of Mechanical Engineering*, vol. 58, no. 2, pp. 223–243, 2011.
- [35] F. González, M. Á. Naya, A. Luaces, and M. González, “On the effect of multi-rate co-simulation techniques in the efficiency and accuracy of multibody system dynamics,” *Multibody System Dynamics*, vol. 25, no. 4, pp. 461–483, 2011.

- [36] M. Arnold, “Numerically stable modular time integration of multiphysical systems,” in *Proceedings of the First MIT Conference on Computational Fluid and Solid Mechanics*, vol. 2, pp. 1062–1064, Elsevier, 2001.
- [37] C. W. Gear and D. Wells, “Multirate linear multistep methods,” *BIT Numerical Mathematics*, vol. 24, no. 4, pp. 484–502, 1984.
- [38] R. Kübler and W. Schiehlen, “Two methods of simulator coupling,” *Mathematical and Computer Modelling of Dynamical Systems*, vol. 6, no. 2, pp. 93–113, 2000.
- [39] N. Doquier, *Multiphysics modelling of multibody systems: Application to railway pneumatic suspensions*. PhD thesis, PhD thesis, Catholic University of Louven, Belgium, 2010.
- [40] T. Blochwitz, M. Otter, J. Akesson, M. Arnold, C. Clauss, H. Elmqvist, M. Friedrich, A. Junghanns, J. Mauss, D. Neumerkel, *et al.*, “Functional mockup interface 2.0: The standard for tool independent exchange of simulation models,” in *Proceedings of the 9th International Modelica Conference*, pp. 173–184, Linköping University Electronic Press, 2012.
- [41] F. Pfeiffer and F. Borchsenius, “New hydraulic system modelling,” *Modal Analysis*, vol. 10, no. 10, pp. 1493–1515, 2004.
- [42] R. Åman and H. Handroos, “Pseudo-dynamic solution of pressures in small volumes in fluid power circuit simulation,” in *Proceedings, 5th FPNI-PhD Symposium, Krakow 2008: An initiative of Fluid Power Net International*, pp. 406–416, 2008.
- [43] R. Åman and H. Handroos, “Comparison of numerical effectiveness of three methods for modelling 2-way flow control valves,” in *Proceedings of the Seventh International Conference on Fluid Power Transmission and Control*, pp. 711–715, Beijing World Publishing Corporation, 2009.
- [44] R. Åman and H. Handroos, “Optimization of parameters of [a] pseudo-dynamic solver for real-time simulation of fluid power circuits,” in *Workshop proceedings, 7th International Fluid Power Conference Aachen*, vol. 1, pp. 495–507, 2010.
- [45] G. Bidini and F. Mariani, “Simulation of hydraulic power plant transients using neural networks,” *Proceedings of the Institution of Mechanical Engineers, Part A: Journal of Power and Energy*, vol. 211, no. 5, pp. 393–398, 1997.
- [46] M. Krishna and J. Bares, “Hydraulic system modeling through memory-based learning,” in *Proceedings: 1998 IEEE/RSJ International Conference on Intelligent Robots and Systems*, vol. 3, pp. 1733–1738, 1998.
- [47] M. Krishna and J. Bares, “Constructing fast hydraulic robot models for optimal motion planning,” January 1999.

- [48] M. K. Oshtorjani, A. Mikkola, and P. Jalali, "Numerical treatment of singularity in hydraulic circuits using singular perturbation theory," *IEEE/ASME Transactions on Mechatronics*, vol. 24, no. 1, pp. 144–153, 2018.
- [49] J. Rahikainen, M. Kiani, J. Sapanen, P. Jalali, and A. Mikkola, "Computationally efficient approach for simulation of multibody and hydraulic dynamics," *Mechanism and Machine Theory*, vol. 130, pp. 435–446, 2018.
- [50] A. N. Tikhonov, "Systems of differential equations containing small parameters in the derivatives," *Matematicheskii Sbornik*, vol. 73, no. 3, pp. 575–586, 1952.
- [51] M. F. Barad, J. G. Kocheemoolayil, and C. C. Kiris, "Lattice boltzmann and navier-stokes cartesian cfd approaches for airframe noise predictions," in *23rd AIAA Computational Fluid Dynamics Conference*, pp. AIAA–2017–4404, 2017.
- [52] N. Delbosc, J. L. Summers, A. Khan, N. Kapur, and C. J. Noakes, "Optimized implementation of the lattice boltzmann method on a graphics processing unit towards real-time fluid simulation," *Computers & Mathematics with Applications*, vol. 67, no. 2, pp. 462–475, 2014.
- [53] M. Gaedtke, S. Wachter, S. Kunkel, S. Sonnack, M. Rädle, H. Nirschl, and M. J. Krause, "Numerical study on the application of vacuum insulation panels and a latent heat storage for refrigerated vehicles with a large eddy lattice boltzmann method," *Heat and Mass Transfer*, vol. 56, pp. 1189–1201, 2019.
- [54] M. A. I. Khan, N. Delbosc, C. J. Noakes, and J. Summers, "Real-time flow simulation of indoor environments using [a] lattice boltzmann method," *Building Simulation*, vol. 8, no. 4, pp. 405–414, 2015.
- [55] M.-F. King, A. Khan, N. Delbosc, H. L. Gough, C. Halios, J. F. Barlow, and C. J. Noakes, "Modelling urban airflow and natural ventilation using a gpu-based lattice-boltzmann method," *Building and Environment*, vol. 125, pp. 273–284, 2017.
- [56] J. Wen and H. Ma, "Real-time smoke simulation based on vorticity preserving lattice boltzmann method," *The Visual Computer*, vol. 35, no. 9, pp. 1279–1292, 2019.
- [57] M. A. Woodgate, G. N. Barakos, R. Steijl, and G. J. Pringle, "Parallel performance for a real time lattice boltzmann code," *Computers & Fluids*, vol. 173, pp. 237–258, 2018.
- [58] C. Janßen and M. Krafczyk, "Free surface flow simulations on gpgpus using the lbm," *Computers & Mathematics with Applications*, vol. 61, no. 12, pp. 3549–3563, 2011.
- [59] E. Wu, Y. Liu, and X. Liu, "An improved study of real-time fluid simulation on gpu," *Computer Animation and Virtual Worlds*, vol. 15, no. 3–4, pp. 139–146, 2004.

- [60] C. K. Aidun and J. R. Clausen, "Lattice-boltzmann method for complex flows," *Annual Review of Fluid Mechanics*, vol. 42, pp. 439–472, 2010.
- [61] S. Chikatamarla, C. Frouzakis, I. Karlin, A. Tomboulides, and K. Boulouchos, "Lattice boltzmann method for direct numerical simulation of turbulent flows," *Journal of Fluid Mechanics*, vol. 656, pp. 298–308, 2010.
- [62] J. G. Eggels, "Direct and large-eddy simulation of turbulent fluid flow using the lattice-boltzmann scheme," *International Journal of Heat and Fluid Flow*, vol. 17, no. 3, pp. 307–323, 1996.
- [63] S. Chen and G. D. Doolen, "Lattice boltzmann method for fluid flows," *Annual Review of Fluid Mechanics*, vol. 30, no. 1, pp. 329–364, 1998.
- [64] X. He, S. Chen, and R. Zhang, "A lattice boltzmann scheme for incompressible multiphase flow and its application in simulation of rayleigh–taylor instability," *Journal of Computational Physics*, vol. 152, no. 2, pp. 642–663, 1999.
- [65] T. Inamuro, T. Ogata, S. Tajima, and N. Konishi, "A lattice boltzmann method for incompressible two-phase flows with large density differences," *Journal of Computational Physics*, vol. 198, no. 2, pp. 628–644, 2004.
- [66] Q. Kang, P. C. Lichtner, and D. Zhang, "Lattice boltzmann pore-scale model for multicomponent reactive transport in porous media," *Journal of Geophysical Research: Solid Earth*, vol. 111, no. B5, 2006.
- [67] Q. Kang, P. C. Lichtner, and D. Zhang, "An improved lattice boltzmann model for multicomponent reactive transport in porous media at the pore scale," *Water Resources Research*, vol. 43, no. 12, 2007.
- [68] L. Chen, Q. Kang, B. Carey, and W.-Q. Tao, "Pore-scale study of diffusion–reaction processes involving dissolution and precipitation using the lattice boltzmann method," *International Journal of Heat and Mass Transfer*, vol. 75, pp. 483–496, 2014.
- [69] Z. Guo and T. S. Zhao, "A lattice boltzmann model for convection heat transfer in porous media," *Numerical Heat Transfer, Part B: Fundamentals*, vol. 47, no. 2, pp. 157–177, 2005.
- [70] J. Wang, M. Wang, and Z. Li, "A lattice boltzmann algorithm for fluid-solid conjugate heat transfer," *International Journal of Thermal Sciences*, vol. 46, no. 3, pp. 228–234, 2007.
- [71] W.-S. Jiaung, J.-R. Ho, and C.-P. Kuo, "Lattice boltzmann method for the heat conduction problem with phase change," *Numerical Heat Transfer: Part B: Fundamentals*, vol. 39, no. 2, pp. 167–187, 2001.

- [72] Q. Li, K. H. Luo, Q. J. Kang, Y. L. He, Q. Chen, and Q. Liu, "Lattice boltzmann methods for multiphase flow and phase-change heat transfer," *Progress in Energy and Combustion Science*, vol. 52, pp. 62–105, 2016.
- [73] P. Lallemand and L.-S. Luo, "Theory of the lattice boltzmann method: Acoustic and thermal properties in two and three dimensions," *Physical Review E*, vol. 68, no. 3, p. 036706, 2003.
- [74] K. Yamamoto, X. He, and G. D. Doolen, "Simulation of [a] combustion field with lattice boltzmann method," *Journal of Statistical Physics*, vol. 107, no. 1–2, pp. 367–383, 2002.
- [75] K. Yamamoto, N. Takada, and M. Misawa, "Combustion simulation with lattice boltzmann method in a three-dimensional porous structure," *Proceedings of the Combustion Institute*, vol. 30, no. 1, pp. 1509–1515, 2005.
- [76] S. Chen, Z. Liu, C. Zhang, Z. He, Z. Tian, B. Shi, and C. Zheng, "A novel coupled lattice boltzmann model for low mach number combustion simulation," *Applied Mathematics and Computation*, vol. 193, no. 1, pp. 266–284, 2007.
- [77] A. De Rosis, G. Falcucci, S. Ubertini, F. Ubertini, and S. Succi, "Lattice boltzmann analysis of fluid–structure interaction with moving boundaries," *Communications in Computational Physics*, vol. 13, no. 3, pp. 823–834, 2013.
- [78] T. Blochwitz, "Functional mock-up interface – FMI for model exchange and co-simulation," <https://www.fmi-standard.org/downloads> (accessed January 2016), 2014.
- [79] Modelica Association, "The Modelica Language Specification version 3.4," 2017.
- [80] IEEE Standards Association et al., "IEEE Standard for modeling and simulation (M&S) High level architecture (HLA)," 2012.
- [81] V. Eijkhout, *Parallel programming in MPI and OpenMP*. Lulu.com, 2017.
- [82] R. Trobec, B. Slivnik, P. Bulić, and B. Robič, *Introduction to parallel computing: From algorithms to programming on state-of-the-art platforms*. Springer, 2018.
- [83] M. Papadrakakis, G. Stavroulakis, and A. Karatarakis, "A new era in scientific computing: Domain decomposition methods in hybrid cpu–gpu architectures," *Computer Methods in Applied Mechanics and Engineering*, vol. 200, no. 13–16, pp. 1490–1508, 2011.
- [84] J. Rahikainen, A. Mikkola, J. Sopanen, and J. Gerstmayr, "Combined semi-recursive formulation and lumped fluid method for monolithic simulation of multi-body and hydraulic dynamics," *Multibody System Dynamics*, vol. 44, no. 3, pp. 293–311, 2018.

- [85] J. Yao, Z. Jiao, D. Ma, and L. Yan, "High-accuracy tracking control of hydraulic rotary actuators with modeling uncertainties," *IEEE/ASME Transactions on Mechatronics*, vol. 19, no. 2, pp. 633–641, 2014.
- [86] J. Watton, *Fluid power systems: Modeling, simulation, analog and microcomputer control*. Prentice-Hall, 1989.
- [87] W. Borutzky, B. Barnard, and J. Thoma, "An orifice flow model for laminar and turbulent conditions," *Simulation Modelling Practice and Theory*, vol. 10, no. 3, pp. 141–152, 2002.
- [88] N. D. Manring and R. C. Fales, *Hydraulic control systems*. John Wiley & Sons, 2019.
- [89] Q. Lu, J. Tiainen, M. Kiani-Oshtorjani, and J. Ruan, "Radial flow force at the annular orifice of a two-dimensional hydraulic servo valve," *IEEE Access*, vol. 8, pp. 207938–207946, 2020.
- [90] H. Handroos and M. Vilenius, "Flexible semi-empirical models for hydraulic flow control valves," *Journal of Mechanical Design*, vol. 113, no. 3, pp. 232–238, 1991.
- [91] M. Kiani-Oshtorjani, S. Ustinov, H. Handroos, P. Jalali, and A. Mikkola, "Real-time simulation of fluid power systems containing small oil volumes, using the method of multiple scales," *IEEE Access*, vol. 8, pp. 196940–196950, 2020.
- [92] A. Ellman and R. Piché, "A modified orifice flow formula for numerical simulation of fluid power systems," *Fluid Power Systems and Technology, ASME*, vol. 3, pp. 59–63, November 1996.
- [93] A. Ellman and R. Piché, "A two regime orifice flow formula for numerical simulation," *Journal of Dynamic Systems, Measurements, and Control*, vol. 121, no. 4, pp. 721–724, 1999.
- [94] R. Åman, H. Handroos, and T. Eskola, "Computationally efficient two-regime flow orifice model for real-time simulation," *Simulation Modelling Practice and Theory*, vol. 16, no. 8, pp. 945–961, 2008.
- [95] R. Åman, H. Handroos, and T. Eskola, "Computationally efficient two-regime flow orifice model for real-time simulation," *Simulation Modelling Practice and Theory*, vol. 16, no. 8, pp. 945–961, 2008.
- [96] R. Piché and A. Ellman, "Numerical integration of fluid power circuit models using two-stage semi-implicit Runge–Kutta methods," *Proceedings of the Institution of Mechanical Engineers, Part C: Journal of Mechanical Engineering Science*, vol. 208, no. 3, pp. 167–175, 1994.
- [97] S. Esqué, A. Raneda, and A. Ellman, "Techniques for studying a mobile hydraulic crane in virtual reality," *International Journal of Fluid Power*, vol. 4, no. 2, pp. 25–35, 2003.

- [98] D. Bowns and L. Wang, "The digital computation of pressures in hydraulic pipes with small volume using an iterative technique," *Proceedings of the Institution of Mechanical Engineers, Part C: Mechanical Engineering Science*, vol. 204, no. 1, pp. 29–36, 1990.
- [99] R. Åman, *Methods and models for accelerating dynamic simulation of fluid power circuits*. DSc thesis, Lappeenranta University of Technology, 2011.
- [100] L.-Y. Chen, N. Goldenfeld, and Y. Oono, "Renormalization group and singular perturbations: Multiple scales, boundary layers, and reductive perturbation theory," *Physical Review E*, vol. 54, no. 1, pp. 376–394, 1996.
- [101] H. Tian and J. D. Van de Ven, "Modeling and experimental studies on the absorption of entrained gas and the influence on fluid compressibility," *Journal of Fluids Engineering*, vol. 139, no. 10, p. 101301, 2017.
- [102] S. Li, N. Z. Aung, S. Zhang, J. Cao, and X. Xue, "Experimental and numerical investigation of [the] cavitation phenomenon in [the] flapper–nozzle pilot stage of an electrohydraulic servo-valve," *Computers & Fluids*, vol. 88, pp. 590–598, 2013.
- [103] J.-y. Qian, B.-z. Liu, Z.-j. Jin, J.-k. Wang, H. Zhang, and A.-l. Lu, "Numerical analysis of flow and cavitation characteristics in a pilot-control globe valve with different valve core displacements," *Journal of Zhejiang University Science A*, vol. 17, no. 1, pp. 54–64, 2016.
- [104] H. Gholizadeh, D. Bitner, R. Burton, and G. Schoenau, "Modeling and experimental validation of the effective bulk modulus of a mixture of hydraulic oil and air," *Journal of Dynamic Systems, Measurement, and Control*, vol. 136, no. 5, p. 51013, 2014.
- [105] S. Kim and H. Murrenhoff, "Measurement of effective bulk modulus for hydraulic oil at low pressure," *Journal of Fluids Engineering*, vol. 134, no. 2, p. 21201, 2012.
- [106] L. I. SA, "HYD advanced fluid properties," *Technical Bulletins*, no. 117, 2008.
- [107] J. Zhou, C. Wei, and J. Hu, "A novel approach for predicting thermal effects of gas cavitation in hydraulic circuits," *Energy*, vol. 83, pp. 576–582, 2015.
- [108] J. Zhou, J. Hu, and C. Jing, "Lumped parameter modelling of cavitating orifice flow in hydraulic systems," *Strojñiski Vestnik / Journal of Mechanical Engineering*, vol. 62, no. 6, pp. 373–380, 2016.
- [109] J. Zhou, A. Vacca, and B. Manhartgruber, "A novel approach for the prediction of dynamic features of air release and absorption in hydraulic oils," *Journal of Fluids Engineering*, vol. 135, no. 9, p. 91305, 2013.
- [110] P. Righettini, R. Strada, S. Valilou, and E. KhademOlama, "Nonlinear model of a servo-hydraulic shaking table with [a] dynamic model of effective bulk modulus," *Mechanical Systems and Signal Processing*, vol. 110, pp. 248–259, 2018.

- [111] H. E. Merritt, *Hydraulic control systems*. John Wiley & Sons, 1967.
- [112] B.-H. Cho, H.-W. Lee, and J.-S. Oh, “Estimation technique of air content in automatic transmission fluid by measuring effective bulk modulus,” tech. rep., 2000.
- [113] Y. Jinghong, C. Zhaoneng, and L. Yuanzhang, “The variation of oil effective bulk modulus with pressure in hydraulic systems,” *Journal of Dynamic Systems, Measurement, and Control*, vol. 116, no. 1, pp. 146–150, 1994.
- [114] H. Gholizadeh, R. Burton, and G. Schoenau, “Fluid bulk modulus: Comparison of low pressure models,” *International Journal of Fluid Power*, vol. 13, no. 1, pp. 7–16, 2012.
- [115] J. Kajaste, H. Kauranne, A. Ellman, and M. Pietola, “Experimental validation of different models for effective bulk modulus of hydraulic fluid,” in *The Ninth Scandinavian Conference on Fluid Power, SICFP '05, June 1–3, 2005, Linköping, Sweden*, pp. 14–15, 2005.
- [116] M. Mohammadi, M. Kiani, and A. Mikkola, “The effects of oil entrained air on the dynamic performance of a hydraulically driven multibody system,” vol. 13, pp. 141–147, 2020.
- [117] H.-M. Groscurth, T. Bruckner, and R. Kümmel, “Modeling of energy-services supply systems,” *Energy*, vol. 20, no. 9, pp. 941–958, 1995.
- [118] M. Liu, Y. Shi, J. Yan, and Y. Yan, “Lattice Boltzmann simulation of flow and heat transfer in random porous media constructed by simulated annealing algorithm,” *Applied Thermal Engineering*, vol. 115, pp. 1348–1356, 2017.
- [119] Z. Guo and T. Zhao, “Lattice Boltzmann model for incompressible flows through porous media,” *Physical Review E*, vol. 66, pp. 1–9, 2002.
- [120] J. Buick and C. Greated, “Gravity in a lattice Boltzmann model,” *Physical Review E*, vol. 61, no. 5, pp. 5307–5320, 2000.
- [121] S. Farnoush and M. T. Manzari, “An investigation on the body force modeling in a lattice Boltzmann BGK simulation of generalized Newtonian fluids,” *Physica A*, vol. 415, pp. 315–332, 2014.
- [122] Z. Guo, C. Zheng, and B. Shi, “Discrete lattice effects on the forcing term in the lattice Boltzmann method,” *Physical Review E*, vol. 65, pp. 1–6, 2002.
- [123] S. Ergun, “Fluid flow through packed columns,” *Chemical Engineering Progress*, vol. 48, pp. 89–94, 1952.
- [124] D. Nihad, B. Özer, and M. Özdemir, “Experimental flow in various porous media and reconciliation of Forchheimer and Ergun relations,” *Experimental Thermal and Fluid Science*, vol. 57, pp. 425–433, 2014.

- [125] P. Nithiarasu, K. Seetharamu, and T. Sundararajan, "Natural convective heat transfer in a fluid saturated variable porosity medium," *International Journal of Heat and Mass Transfer*, vol. 40, no. 16, pp. 3955–3967, 1997.
- [126] P. Nithiarasu, K. Seetharamu, and T. Sundararajan, "Effect of porosity on natural convective heat transfer in a fluid saturated porous medium," *International Journal of Heat and Fluid Flow*, vol. 19, pp. 56–58, 1998.
- [127] W. Zhong, M. Zhang, B. Jin, and Z. Yuan, "Flow behaviors of a large spout-fluid bed at high pressure and temperature by 3D simulation with kinetic theory of granular flow," *Powder Technology*, vol. 175, no. 2, pp. 90–103, 2007.
- [128] U. Frisch, B. Hasslacher, and Y. Pomeau, "Lattice-gas automata for the navier-stokes equation," *Physical Review Letters*, vol. 56, no. 14, pp. 1505–1508, 1986.
- [129] P. Lallemand and L.-S. Luo, "Theory of the lattice boltzmann method: Dispersion, dissipation, isotropy, galilean invariance, and stability," *Physical Review E*, vol. 61, no. 6, pp. 6546–6562, 2000.
- [130] Y.-H. Qian, D. d'Humières, and P. Lallemand, "Lattice bgk models for [the] navier-stokes equation," *EPL (Europhysics Letters)*, vol. 17, no. 6, pp. 479–484, 1992.
- [131] H. Callen, *Thermodynamics and an introduction to thermostatistics*. John Wiley & Sons, New York, 1985.
- [132] R. H. Swendsen, "Thermodynamics, statistical mechanics and entropy," *Entropy*, vol. 19, no. 11, p. 603, 2017.
- [133] L. Boltzmann, "Weitere studien über das wärmeleichgewicht unter gasmolekülen," in *Kinetische Theorie II* (S. G. Brush, ed.), pp. 115–225, Springer, 1970.
- [134] K. Mattila, "Implementation techniques for the lattice boltzmann method," *Jyväskylä Studies in Computing*, no. 117, 2010.
- [135] L.-S. Luo, *Lattice-gas automata and lattice Boltzmann equations for two-dimensional hydrodynamics*. PhD thesis, School of Physics of the Georgia Institute of Technology, US, 1993.
- [136] R. E. Alcouffe, R. S. Baker, F. W. Brinkley, D. R. Marr, R. D. O'Dell, and W. F. Walters, "Dantsys: A diffusion accelerated neutral particle transport code system," tech. rep., Los Alamos National Lab., 1995.
- [137] J. G. Kirkwood, "The statistical mechanical theory of transport processes ii: Transport in gases," *The Journal of Chemical Physics*, vol. 15, no. 1, pp. 72–76, 1947.
- [138] X. He and L.-S. Luo, "Theory of the lattice boltzmann method: From the boltzmann equation to the lattice boltzmann equation," *Physical Review E*, vol. 56, no. 6, pp. 6811–6817, 1997.

- [139] L.-S. Luo, "Theory of the lattice boltzmann method: Lattice boltzmann models for nonideal gases," *Physical Review E*, vol. 62, no. 4, pp. 4982–4996, 2000.
- [140] X. He and L.-S. Luo, "Lattice Boltzmann model for the incompressible Navier–Stokes equation," *Journal of Statistical Physics*, vol. 88, no. 3, pp. 927–944, 1997.
- [141] J. Third, Y. Chen, and C. Müller, "Comparison between finite volume and lattice-Boltzmann method simulations of gas-fluidised beds: Bed expansion and particle–fluid interaction force," *Computational Particle Mechanics*, vol. 3, no. 3, pp. 373–381, 2016.
- [142] M. K. Oshtorjani and P. Jalali, "Thermal and hydraulic properties of sphere packings using a novel lattice boltzmann model," *International Journal of Heat and Mass Transfer*, vol. 130, pp. 98–108, 2019.
- [143] Z. Guo and T. Zhao, "A lattice Boltzmann model for convection heat transfer in porous media," *Numerical Heat Transfer, Part B: Fundamentals*, vol. 47, pp. 157–177, 2005.
- [144] Q. Liu and Y.-I. He, "Double multiple-relaxation-time lattice Boltzmann model for solid–liquid phase change with natural convection in porous media," *Physica A*, vol. 438, pp. 94–106, 2015.
- [145] L. Wang, J. Mi, and Z. Guo, "A modified lattice Bhatnagar–Gross–Krook model for convection heat transfer in porous media," *International Journal of Heat and Mass Transfer*, vol. 94, pp. 269–291, 2016.
- [146] H. Zheng, C. Shu, and Y.-T. Chew, "A lattice Boltzmann model for multiphase flows with large density ratio," *Journal of Computational Physics*, vol. 218, no. 1, pp. 353–371, 2006.
- [147] Z. Chai and T. Zhao, "Lattice Boltzmann model for the convection–diffusion equation," *Physical Review E*, vol. 87, no. 6, p. 63309, 2013.
- [148] S. Chen, B. Yang, and C. Zheng, "A lattice Boltzmann model for heat transfer in porous media," *International Journal of Heat and Mass Transfer*, vol. 111, pp. 1019–1022, 2017.
- [149] N. Govender, P. W. Cleary, M. Kiani-Oshtorjani, D. N. Wilke, C.-Y. Wu, and H. Kureck, "The effect of particle shape on the packed bed effective thermal conductivity based on dem with polyhedral particles on the gpu," *Chemical Engineering Science*, vol. 219, p. 115584, 2020.
- [150] C. Coetzee, "Calibration of the discrete element method," *Powder Technology*, vol. 310, pp. 104–142, 2017.
- [151] M. Kiani-Oshtorjani and P. Jalali, "Thermal discrete element method for transient heat conduction in granular packing under compressive forces," *International Journal of Heat and Mass Transfer*, vol. 145, p. 118753, 2019.

-
- [152] G. K. Batchelor and R. O'Brien, "Thermal or electrical conduction through a granular material," *Proceedings of the Royal Society of London. A. Mathematical and Physical Sciences*, vol. 355, no. 1682, pp. 313–333, 1977.
- [153] H. S. Carslaw and J. C. Jaeger, *Conduction of heat in solids*. Clarendon Press, 1992.
- [154] M. M. Yovanovich, "Thermal contact resistance across elastically deformed spheres," *Journal of Spacecraft and Rockets*, vol. 4, no. 1, pp. 119–122, 1967.
- [155] B. Chaudhuri, F. J. Muzzio, and M. S. Tomassone, "Modeling of heat transfer in granular flow in rotating vessels," *Chemical Engineering Science*, vol. 61, no. 19, pp. 6348–6360, 2006.
- [156] B. Chaudhuri, F. J. Muzzio, and M. S. Tomassone, "Experimentally validated numerical modeling of heat transfer in granular flow in rotating vessels," *Heat Transfer: Mathematical Modelling, Numerical Methods and Information Technology*, pp. 271–306, 2011.

Publication I

M. Kiani-Oshtorjani, A. Mikkola, and P. Jalali,

**Numerical treatment of singularity in hydraulic circuits using
singular perturbation theory**

Reprinted with permission from
IEEE/ASME Transactions on Mechatronics

Vol. 24, pp. 144–153, 2018

© 2018, IEEE

Numerical Treatment of Singularity in Hydraulic Circuits Using Singular Perturbation Theory

Mehran Kiani Oshtorjani , Aki Mikkola, and Payman Jalali

Abstract—Hydraulic cylinders and motors are commonly used in actuator systems of mobile machines and industrial applications. Hydraulic actuators have the ability to offer large amounts of energy density. To analyze the dynamic behavior of a hydraulic actuator system, the hydraulic circuit is generally divided into volumes in which pressure is assumed to be equally distributed. The pressure within these volumes can be predicted by employing first-order differential equations. To achieve an accurate numerical presentation of a hydraulic circuit, pressures within very small volumes must often be calculated. The small volumes involved in the hydraulic circuits make the models numerically stiff, and consequently, a very small integration time-step is required. In this paper, the singular perturbation theory, which can be applied to problems in which a small value appears with singularity effects, is implemented as a computationally efficient method for modeling hydraulic circuits. The implementation is performed in two stages, i.e., the derivation of the perturbed equations and the modification of their effects. It is shown that the usage of a perturbation theory based approach alleviates problems associated with small volumes in hydraulic system modeling and substantially enhances computational efficiency, thus facilitating real-time simulation.

Index Terms—Boundary-layer stability analysis, hydraulic system, perturbation theory, Runge–Kutta integration, time and frequency responses.

1. INTRODUCTION

PRODUCTS and machinery in the mechanical and electromechanical industry, such as mobile machines, are complex devices and their development requires knowledge of different areas of technology, including applied mechanics, and the operation of actuation and control systems. The various subsystems involved in a mechanical device interact closely. The actuators are mounted on the mechanism and produce forces

acting on the mechanism, which are converted into the constrained motion of the original system of bodies.

In product development, hydraulic actuators and associated hydraulic circuits are often designed with the help of computer simulation. To this end, the lumped fluid theory can be used to form differential equations for volumes where the pressure is assumed to be equally distributed. In practice, the usage of the lumped fluid theory leads to a situation in which small volumes exist in the locations of the pressure calculations. This model has been used frequently in literature [1]–[3] as well as the commercial packages, such as AMESim, to model various hydraulic components, as mentioned in [4]. However, several challenging issues in computational time and stability remain for the simulation of a hydraulic circuit itself and its controller. For instance, in [1], Kaddissi *et al.* reported that a large value of the bulk modulus can easily overwhelm the effects of controller parameters if there is a poor controller design.

Bowns and Wangs [5] reported that there is a difficulty in the simulation of hydraulic pipe systems with small volumes. They noticed that if the volume of one or several pipes is small, the required simulation time-steps become very small. To overcome this problem, they proposed iterative models; however, these iterative methods are computationally costly and similar to applying small time-steps in the integration.

Piche and Ellman [6] also noticed that different volumes are difficult to solve forward in time because the corresponding ordinary differential equations of the model are numerically stiff. They investigated the accuracy and numerical stability of different two-stage semi-implicit Runge–Kutta methods. They used the time-step of 2 ms in all simulations and proposed that the *L*-stable approach is the best-suited approach for the application under investigation. Borutzky *et al.* [7] proposed an empirically obtained polynomial function for the orifice volumetric flow-rate, which has a smooth transition between laminar and turbulent flow regimes. With this approach, singularities can be avoided when the pressure difference approaches zero.

From the modeling point of view, a mechanical system actuated by hydraulics behaves differently at small and large time-scales. In hydraulic circuit modeling where the large bulk modulus is divided into small volumes, small time-scales will appear. This small time-scale increases the computational costs of simulations. As reported by Pfeiffer and Borchsenius [8], the high computational costs are mainly due to the mathematical representations of the hydraulic systems used in the simulations, which are nonlinear first-order differential equations.

Manuscript received August 3, 2017; revised March 6, 2018 and May 31, 2018; accepted October 11, 2018. Date of publication October 15, 2018; date of current version February 14, 2019. Recommended by Technical Editor Hyungpil Moon. This work was supported by the SIM-Platform, Lappeenranta University of Technology. (Corresponding author: Mehran Kiani Oshtorjani.)

M. Kiani Oshtorjani and P. Jalali are with the Laboratory of Thermodynamics, School of Energy Systems, and the SIM-Platform, Lappeenranta University of Technology, Lappeenranta 53850, Finland (e-mail: mehran.kiani@lut.fi; Payman.Jalali@lut.fi).

A. Mikkola is with the Department of Mechanical Engineering, School of Energy Systems, and the SIM-Platform, Lappeenranta University of Technology, Lappeenranta 53850, Finland (e-mail: aki.mikkola@lut.fi).

Color versions of one or more of the figures in this paper are available online at <http://ieeexplore.ieee.org>.

Digital Object Identifier 10.1109/TMECH.2018.2876157

Esque *et al.* [9] studied the real-time simulation of a hydraulic crane using the L -stable Rosenbrock integration scheme. They remarked that the maximum time-step of integration is imposed by stability and computational time criteria. Based on these two factors, they selected the time-step as 0.1 ms in their application.

To overcome the stiffness of the hydraulic equations, the time-step can be reduced. To this end, some values as small as 0.001 ms have been reported [10]. The problem gets more difficult if the hydraulic circuit is coupled with a mechanical system. There are two common approaches for dealing with a system of combined mechanical model and hydraulic circuits. The first is called the unified approach [11], [12], wherein the hydraulic equations and equations for the mechanical system are combined as a single system in which the integration scheme and the time-step are identical in both subsystems. In the multirate integration approach [13], [14], different time-steps are used for the mechanical system and hydraulics. The multirate integration method can be computationally less costly as the hydraulic simulation usually needs a smaller time-step [15].

Ylinen *et al.* [16] developed a monolithic algorithm in which the hydraulic system is coupled with the mechanical system. The whole system is solved with a single-step Crank Nicolson scheme (trapezoidal rule). They used a time-step of 1 ms for the coupled system. However, the predictor–corrector used in their work would double the computational cost.

Bauchau and Liu [17] used a multi-integration algorithm to solve a finite element based mechanical system coupled with hydraulic equations. They used a time-step of 0.1 ms for the structural dynamics analysis and a four-step Runge–Kutta integrator with a time-step 48 times smaller than the structural solver in the hydraulic integration.

Naya *et al.* [18] compared the unified and co-integration approaches. They noted that the unified scheme is computationally 20% more costly than the simplified simulation that considers only the mechanical system. However, they suggested the use of the simplified simulation only when the computational efficiency has priority because the response of this approach shows many oscillations around the correct answers. It is important to note that these oscillations make it difficult to use this method for many applications, especially for real-time applications. In their study, the utilized time-step was 10 ms for the unified scheme, 0.2 ms for a co-integration scheme with a forward Euler integrator, and 5 ms for a co-integration scheme with a trapezoidal integrator.

In summary, the behavior of hydraulic circuits resembles some other engineering systems that suffer from numerical stiffness [19]. Accordingly, from the mathematical point of view, the singular perturbation theory and, practically, Tikhonov's theorem may be considered permissible as an approach to address numerical problems in such systems.

The objective of this paper is to investigate the application of the singular perturbation theory to remove the singularities and numerical difficulties associated with the simulation of hydraulic systems. The response of a typical hydraulic system is investigated before and after applying the perturbation theory based calculations to find out how, and to what extent, the use of the theory is able to improve the numerical efficiency

of formulations associated with the hydraulic model. This paper is organized as follows. Section II describes the hydraulic formulation, which is followed by a brief introduction to the singular perturbation theory in Section III. The numerical model of the hydraulic system is explained in Section IV, where the mathematical equations are first described and the perturbation method, then, applied to handle singularity. Results are presented and discussed in Section V. The final section gives a brief summary and presents conclusions.

II. HYDRAULIC FORMULATION

The theory of lumped fluids is often used in the modeling of hydraulic systems. In the lumped fluid theory, the hydraulic circuit is divided into volumes in which the pressure is assumed to be evenly distributed. Differential equations are formed for the volumes with which the pressure of the system at a certain time can be solved directly or indirectly. Different volumes are assumed to be separated by throttling through which the fluid can flow. The directional pressure and flow control valves as well as long pipelines used in real systems are replaced by throttles that control the flow-rate between the different volumes.

The pressure in a volume of the hydraulic circuit can be calculated using differential equation as follows [20]:

$$\frac{dp}{dt} = \frac{B_e}{V} \left(Q_{in} - Q_{out} - \frac{dV}{dt} \right) \quad (1)$$

where p is the pressure, B_e is the effective bulk modulus, V is the volume, Q_{in} and Q_{out} are the incoming and outgoing volumetric flow-rates, respectively, and dV/dt is the time-rate changes of volume V . The effective bulk modulus represents the bulk modulus of the fluid by taking into account the effects of the flexibility of the container and dissolved air [21].

The volumetric turbulent flow-rate Q_t in a throttle can be written [7] as follows:

$$Q_t = C_d A_t \sqrt{\frac{2(P_3 - P_1)}{\rho}} \quad (2)$$

where C_d is the discharge coefficient, P_1 and P_3 are pressures at both sides of the throttle valve, A_t is the cross-sectional area of the valve, and ρ is the density of the fluid. In this study, the volumetric flow-rate is described using semiempirical methods in which the parameters of the valve can be obtained from measurements [22].

A hydraulic cylinder can be modeled based on its dimensions and the input pressures. The model of the cylinder can be formed based on a diagram, as shown in Fig. 1. The hydraulic cylinder volume is related to the cylinder stroke as follows:

$$V_{in} = x A_A \quad (3a)$$

$$V_{out} = (l - x) A_B \quad (3b)$$

where A_A and A_B are the surface area of the front side of the piston and the area of the rod side of the piston, respectively, and l is the maximum stroke length. The volumetric flow-rates

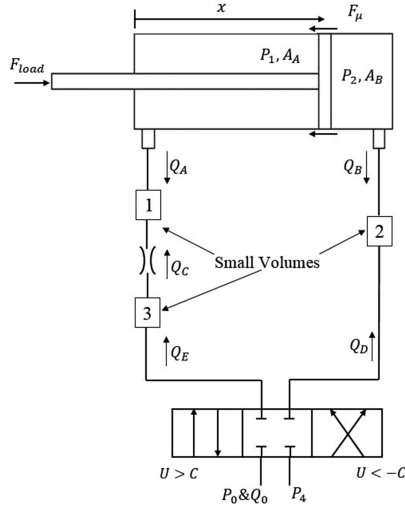


Fig. 1. Hydraulic circuit studied.

produced based on the piston motion can be written as follows:

$$Q_{\text{in}} = \dot{x}A_A \quad (4)$$

$$Q_{\text{out}} = -\dot{x}A_B. \quad (5)$$

The force F_s produced by the cylinder can be written as follows:

$$F_s = P_1A_A - P_2A_B + F_{\text{load}} - F_{\mu} \quad (6)$$

where F_{load} is the load force, F_{μ} is the friction force, and P_1 and P_2 are the pressure values in the cylinder chambers.

III. SINGULAR PERTURBATION THEORY

In this section, the concept of the singular perturbation theory is briefly introduced. Considering the state variables of $[\phi, \psi]$, the singular system can be represented by the following relations:

$$\dot{\phi} = f(\phi, \psi, t, \varepsilon), \quad \phi(t_0) = \zeta(\varepsilon) \quad (7a)$$

$$\dot{\psi} = g(\phi, \psi, t, \varepsilon), \quad \psi(t_0) = \xi(\varepsilon) \quad (7b)$$

where $\phi \in R^m$ and $\psi \in R^n$, and ε is an infinitesimal parameter.

The quasi-steady state model of the above-mentioned system is [23] given by

$$\dot{\phi} = f(\phi, h(t, \phi), t, \varepsilon) \quad (8a)$$

$$\bar{\psi}(t) = h(t, \bar{\phi}). \quad (8b)$$

Note that the dot represents the time derivative, and the overbar indicates the perturbed variables. Based on Tikhonov's theorem [24] in the singular perturbation theory, Wang *et al.* [25] stated the following strategy. Assume the functions f and g to be smooth enough, and the boundary-layer model is exponentially stable. Also, assume that the reduced-order system (8a) is

exponentially stable and has unique solutions on a convex set. Then, a positive constant ε^* can be found in a way that for every $0 < \varepsilon < \varepsilon^*$, the system (7) has a unique solution for $[t, \infty)$, and $\phi(t, \varepsilon) - \bar{\phi}(t) = O(\varepsilon)$. Moreover, for any given $t_b > t_0$, there is $0 < \varepsilon < \varepsilon^*$, which satisfies $\psi(t, \varepsilon) - h(t, \bar{\phi}) = O(\varepsilon)$, and it holds uniformly for $t \in [t_b, \infty)$ [25]–[27].

In other words, it is possible to reduce the system of (7) into (8) while maintaining the accuracy as the corresponding errors on the response of system (8) are in the order of $O(\varepsilon)$. This theory is applied to remove the singularities associated with the hydraulic systems.

IV. NUMERICAL MODEL OF THE HYDRAULIC SYSTEM

In this section, the hydraulic circuit illustrated in Fig. 1 is introduced. First, in Section IV-A, the mathematical model of the system is presented, and then, the perturbation theory is applied to the system in Section IV-B.

A. Mathematical Model of the System

In this section, the hydraulic system with two valves illustrated in Fig. 1 is modeled. The governing equations are first presented, followed by the development of the model in the state space when the control signal is greater than C , i.e., $U > C$.

1) *Physical Model*: Here, the mathematical formulation of the hydraulic circuit is presented. All constant parameters used are given in Table I. The governing equations can be written as follows:

$$\dot{P}_1 = \frac{B_1}{V_1}(Q_A + Q_C) \quad (9)$$

$$\dot{P}_2 = \frac{B_2}{V_2}(Q_B + Q_D) \quad (10)$$

$$\dot{P}_3 = \frac{B_2}{V_2}(Q_E - Q_C) \quad (11)$$

$$\ddot{x} = \frac{1}{m}(P_1A_A - P_2A_B) + \frac{F_{\text{load}}}{m} \quad (12)$$

where B_i represents the bulk modulus, and V_i is the volume for $i = 1, 2, 3$. The relations of volumetric flow-rates are obtained as presented in Table II, in which pressures are embedded. Note that there are several parameters appearing in this table, the values of which are presented in Table I. The ‘‘Step’’ function used in Table II is defined in Appendix A.

Assuming an ideal directional valve (where the flow, friction, and pressure forces have no effect on the valve spool position), U represents the position of the spool whose model is given in Appendix A. Hence, there are three positions for a 4/3 directional valve (4 ways and 3 positions), which are identified with the parameter C .

2) *State-Space Representation*: If the hydraulic system is represented in the state space, the calculations associated with the boundary-layer stability analysis, presented in Section IV-B1, will be simpler and more efficient. The state variables for the problem under investigation are given in Table III.

The first state equation, i.e., (13), can be derived from the derivative of the first state variable X_1 and considering (9)–(12).

TABLE I
SET VALUES FOR DIFFERENT QUANTITIES

A_A/m^2	A_B/m^2	$B_i/Pa(\text{Bulk modulus})$	V_1/m^3	V_2/m^3	V_3/m^3	$P_0/Pa(\text{Pump pres.})$
0.0122718	0.084234	$70000.0\sqrt{P_1}$	0.0061359	0.042117	0.005	10^7
C_C	C_{PV}	$F_{load}/N(\text{External force})$	C_{TV}	m/kg	C	$P_4/Pa(\text{Tank pres.})$
5×10^{-5}	10^{-7}	-5000	8×10^{-8}	50.0	10^{-4}	2×10^9

TABLE II
FLOW-RATE RELATIONS USED IN THE CALCULATIONS

	$U < -C$	$-C < U < C$	$U > C$
Q_A	$-\dot{x}A_A$	$-\dot{x}A_A$	$-\dot{x}A_A$
Q_B	$\dot{x}A_B$	$\dot{x}A_B$	$\dot{x}A_B$
Q_C	$C_C\sqrt{P_1 - P_3}\text{Step}(P_3 - P_1)$	$C_C\sqrt{ P_1 - P_3 }\text{Step}(P_3 - P_1)$	$C_C\sqrt{P_3 - P_1}\text{Step}(P_3 - P_1)$
Q_D	$UC_{PV}\sqrt{P_0 - P_2}\text{Step}(P_2 - P_0)$	0	$UC_{TV}\sqrt{P_2 - P_4}\text{Step}(P_4 - P_2)$
Q_E	$UC_{TV}\sqrt{P_3 - P_4}\text{Step}(P_3 - P_4)$	0	$UC_{PV}\sqrt{P_0 - P_3}\text{Step}(P_0 - P_3)$

TABLE III
STATE VARIABLES

$X_1 = \sqrt{P_3 - P_1}$	$X_3 = \sqrt{P_0 - P_3}$
$X_2 = \sqrt{P_2 - P_4}$	$X_4 = \sqrt{\dot{x}}$

The final form of state equations can be obtained as follows:

$$2X_1\dot{X}_1 = \frac{B_1}{V_1}A_A X_4^2 + \frac{B_3}{V_3}UC_{PV}X_3 - \left(\frac{B_1}{V_1} + \frac{B_3}{V_3}\right)C_C X_1 \quad (13)$$

$$2X_2\dot{X}_2 = \frac{B_2}{V_2}A_B X_4^2 + \frac{B_2}{V_2}UC_{TV}X_2 - \dot{P}_4 \quad (14)$$

$$2X_3\dot{X}_3 = -\frac{B_3}{V_3}A_B X_4^2 + \frac{B_3}{V_3}UC_C X_1 + \dot{P}_0 \quad (15)$$

$$2X_4\dot{X}_4 = -\frac{A_A}{m}X_1^2 - \frac{A_A}{m}X_3^2 - \frac{A_B}{m}X_2^2 + \frac{F_{load}}{m} + \frac{A_A}{m}P_0 - \frac{A_B}{m}P_4. \quad (16)$$

These equations introduce a multi-input multioutput nonlinear system with the nonlinearities in the form of polynomial terms. If the control signal is negative, the state variables are defined as given in Table III. However, the governing equations will be different from (13)–(16).

B. Perturbation Theory Applied to Mathematical Equations

In this section, the perturbation theory is applied to the hydraulic system. As mentioned in Section II, the perturbation theory is applied to the desired equation. Equations (9)–(11) can be rewritten as follows:

$$\varepsilon\dot{P}_1 = (Q_A + Q_C) \quad (17)$$

$$\varepsilon\dot{P}_2 = (Q_B + Q_D) \quad (18)$$

$$\varepsilon\dot{P}_3 = (Q_E - Q_C) \quad (19)$$

where ε is determined by the small volume divided by the effective bulk modulus, which is lowered by the entrained air [17], [28]. It is often observed when a hydraulic system is turned-on after a period of shutdown, which allows air to collect in the system. However, it can be assumed that the effective bulk modulus is a constant or changes slowly under normal working conditions since the entrained air in the system has a relatively stable level [25].

1) *Boundary-Layer Stability Analysis:* The small values for some parameters appearing in the governing differential equations are important. If the small parameters are set to zero, and the differential equations are then solved, the results could differ from the exact solution of the differential equations containing the small parameter. In some systems, these two solutions are the same; such systems are usually called regular systems. However, if the two solutions differ, the system is referred to as a singular system.

In singular systems, two distinct solutions are obtained if the mathematical limits are calculated by approaching the small parameter to zero before and after solving the equations.

In these systems, the infinitesimal parameter is multiplied by the highest derivative term, which usually makes a rapid variation in the small time-scales [28]. This region is known as the boundary layer, the stability of which puts forward a criterion for using the singular perturbation theory.

To this end, the following variables are defined:

$$y_1 \triangleq P_1 - \bar{P}_1 = -\frac{1}{C_C^2}(C_C^2 X_1^2 - A_A^2 X_4^4) \quad (20)$$

$$y_2 \triangleq P_2 - \bar{P}_2 = -\frac{1}{UC_{TV}^2}(U^2 C_{TV}^2 X_2^2 - A_B^2 X_4^4) \quad (21)$$

$$y_3 \triangleq P_3 - \bar{P}_3 = \frac{X_1^2 - \alpha X_3^2}{1 + \alpha} \quad (22)$$

where the overbar represents the perturbed variable. Taking the derivative of (20) gives

$$\varepsilon\dot{y}_1 = \varepsilon\frac{dy_1}{dt} = \frac{dy_1}{d\tau} = \varepsilon\dot{P}_1 - \varepsilon\dot{\bar{P}}_1. \quad (23)$$

Using (17), the following relation can be achieved when $\varepsilon \rightarrow 0$:

$$\frac{dy_1}{d\tau} = \varepsilon \dot{P}_1 = C_C X_1 - A_A X_4^2. \quad (24)$$

On the other hand, we have

$$\begin{aligned} -C_C^2 y_1 &= (C_C^2 X_1^2 - A_A^2 X_4^4) = (C_C X_1 - A_A X_4^2) \\ &\times (C_C X_1 + A_A X_4^2). \end{aligned} \quad (25)$$

If $(C_C X_1 - A_A X_4^2) > 0$ and $(C_C X_1 + A_A X_4^2) > 1$, then $-C_C^2 y_1 > (C_C X_1 - A_A X_4^2)$. Thus, we have

$$0 < \frac{dy_1}{d\tau} < -C_C^2 y_1. \quad (26)$$

Assuming $y_1 = Be^{At}$, we obtain

$$0 < BA < -C_C^2 B. \quad (27)$$

As a result, B must be negative; hence, A will be negative too.

Now, if $(C_C X_1 - A_A X_4^2) < 0$ and $(C_C X_1 + A_A X_4^2) > 1$, then $-C_C^2 y_1 < (C_C X_1 - A_A X_4^2)$, and

$$-C_C^2 y_1 < \frac{dy_1}{d\tau} < 0. \quad (28)$$

Again, assuming $y_1 = Be^{At}$ leads to

$$-C_C^2 B < BA < 0. \quad (29)$$

Here, B must be positive; hence, A will be negative. In this problem, following $(C_C X_1 + A_A X_4^2) > 1$ holds. However, it can be demonstrated mathematically that for the condition of $0 < (C_C X_1 + A_A X_4^2) < 1$, the boundary-layer model of (20) is exponentially stable.

The time derivative of (21) yields

$$\varepsilon \dot{y}_2 = \varepsilon \frac{dy_2}{dt} = \frac{dy_2}{d\tau} = \varepsilon \dot{P}_2 - \varepsilon \bar{P}_2. \quad (30)$$

Using (18), when $\varepsilon \rightarrow 0$, the following relation can be obtained:

$$\frac{dy_2}{d\tau} = \varepsilon \dot{P}_2 = UC_{TV} X_2 + A_B X_4^2. \quad (31)$$

On the other hand, we have

$$\begin{aligned} UC_{TV}^2 y_2 &= (U^2 C_{TV}^2 X_2^2 - A_B^2 X_4^4) = (UC_{TV} X_2 \\ &- A_B X_4^2)(UC_{TV} X_2 + A_B X_4^2). \end{aligned} \quad (32)$$

If $(UC_{TV} X_2 - A_B X_4^2) > 1$, then $U^2 C_{TV}^2 y_2 > (UC_{TV} X_2 + A_B X_4^2)$. Thus, we have

$$0 < \frac{dy_2}{d\tau} < U^2 C_{TV}^2 y_2. \quad (33)$$

Assuming $y_1 = Be^{At}$ yields

$$0 < BA < U^2 C_{TV}^2 B \quad (34)$$

where B must be positive, and consequently, A will be positive too. Thus, for this condition, the boundary layers of (21) are not exponentially stable. For other conditions, it can be shown that the boundary-layer model is stable.

It can be proved that the boundary layers of (22) are exponentially stable by following the same procedure. Thus, the only

concern in this analysis is associated with (21), which is not partially stable. The results of this analysis are used in Section V, where the results of the perturbed equation are discussed.

Based on the boundary-layer stability analysis of the system, it has been obtained that (17) and (19) have no challenges in applying the perturbation theory to the control signal $U > C$. It should be noted that the boundary-layer stability analysis is performed if the control signal is less than C , i.e., $U < -C$. By taking a similar approach as mentioned previously, it can be found that the boundary layers of (17) are not unconditionally stable; thus, the perturbation theory cannot be applied.

In summary, it is shown that the perturbation theory can only be applied to (19). This equation satisfies all necessary conditions mentioned in the singular perturbation theory. In order to confirm this analysis, the theory was also applied to (17) and (18), and it was observed that the algorithm became unstable.

2) Perturbation Theory Applied to P_3 : Here, the perturbation theory is applied to (19). Thus, by putting the corresponding equation off, and considering it as ψ (see Section III), other state variables are considered as ϕ . According to the analysis in Section III, the reduced system with the accuracy of $O(\varepsilon)$ can be used. After applying the perturbation theory to the system, (19) will change. Accordingly, the perturbed equation for $U > C$ will be given by

$$P_3 = \frac{P_1 + \alpha_p P_0}{1 + \alpha_p} \quad (35)$$

where $\alpha_p = (\frac{UC_{pv}}{C_C})^2$, and in the state space, we have

$$X_3 = \frac{X_1}{\sqrt{\alpha_p}}. \quad (36)$$

Equation (35) will be used instead of (19). The response of the perturbed equation is close to the original equation, except for small time-scales.

On the other hand, for $U < -C$, we have

$$P_3 = \frac{P_1 + \alpha_T P_4}{1 + \alpha_T} \quad (37)$$

where $\alpha_p = (\frac{UC_{TV}}{C_C})^2$. Also, when $-C < U < C$, the Tikhonov theorem results in $P_3 = P_1$.

An important note that must be made here is the effect of the perturbed equation on the other circuit variables. In other words, \bar{P}_3 will be involved in other relations, such as (17). In this equation, $\varepsilon \dot{P}_1 = (Q_A + Q_C)$, in which

$$Q_C = C_C \sqrt{P_3 - P_1} \text{Step}(P_3 - P_1) \quad (38)$$

for $U > C$. Thus, there is a small error between $\Delta P = P_3 - P_1$ and $\Delta \bar{P} = \bar{P}_3 - \bar{P}_1$. Therefore, it is necessary to modify \bar{Q}_C (the volumetric flow-rate in the perturbed system). This modification is done by introducing a parameter multiplied by the perturbed volumetric flow-rate, known as the correction factor. Thus, considering \bar{Q}_C to be

$$\bar{Q}_C = \lambda C_C \sqrt{\bar{P}_3 - \bar{P}_1} \text{Step}(\bar{P}_3 - \bar{P}_1) \quad (39)$$

for $U > C$, it can be rewritten as follows:

$$\bar{Q}_C = \lambda C_C \sqrt{\frac{\alpha_p}{1 + \alpha_p}} \sqrt{P_0 - \bar{P}_1} \text{Step}(\Delta \bar{P}), \quad (40)$$

using (35). On the other hand,

$$d\bar{Q}_C = \lambda^2 C_C^2 \frac{\alpha_p}{1 + \alpha_p} \text{Step}^2(\Delta \bar{P}) + \bar{Q}_C \frac{d\text{Step}(\Delta \bar{P})}{\text{Step}(\Delta \bar{P})} \quad (41)$$

where $\Delta \bar{P} = \bar{P}_3 - \bar{P}_1$. Next, we have

$$Q_C = C_C \sqrt{P_3 - P_1} \text{Step}(P_3 - P_1) \quad (42)$$

and

$$dQ_C = \frac{C_C^2}{2Q_C} (dP_3 - dP_1) \text{Step}^2(\Delta P) + Q_C \frac{d\text{Step}(\Delta P)}{\text{Step}(\Delta P)}. \quad (43)$$

Assuming $\bar{Q}_C = Q_C$ and $d\bar{P}_1 = dP_1$, and by equating $d\bar{Q}_C = dQ_C$, we obtain

$$\begin{aligned} & \lambda^2 C_C^2 \frac{\alpha_p}{1 + \alpha_p} \frac{d\bar{P}_1}{2Q_C} \text{Step}^2(\Delta \bar{P}) + \bar{Q}_C \frac{d\text{Step}(\Delta \bar{P})}{\text{Step}(\Delta \bar{P})} \\ &= \frac{C_C^2}{2Q_C} (dP_3 - dP_1) \text{Step}^2(\Delta P) + Q_C \frac{d\text{Step}(\Delta P)}{\text{Step}(\Delta P)}. \end{aligned} \quad (44)$$

Considering $\Delta P = \Delta \bar{P} + \sigma$, it can be shown that

$$\frac{d\text{Step}(\Delta P)}{\text{Step}(\Delta P)} - \frac{d\text{Step}(\Delta \bar{P})}{\text{Step}(\Delta \bar{P})} \cong \begin{cases} 0, & \Delta \bar{P} \neq 0 \\ -\sigma, & \Delta \bar{P} = 0 \end{cases}. \quad (45)$$

As a result, we obtain

$$\lambda^2 \frac{\alpha_p}{1 + \alpha_p} d\bar{P}_1 \cong (dP_3 - dP_1). \quad (46)$$

Thus, to find the value of λ , a relation between dP_3 and dP_1 needs to be identified. Considering (17) and (19), we have

$$\frac{\varepsilon_1 dP_1}{\varepsilon_2 dP_3} = \frac{Q_A + Q_C}{Q_E - Q_C} = \frac{1}{\gamma} \quad (47)$$

when the velocity is equal to zero. Therefore, $dP_3 = \gamma \frac{\varepsilon_1}{\varepsilon_2} dP_1 = \gamma \frac{V_1}{V_3} dP_1$. Finally, $\lambda^2 \frac{\alpha_p}{1 + \alpha_p} d\bar{P}_1 \cong (\gamma \frac{V_1}{V_3} - 1) dP_1$, and

$$\lambda \cong \sqrt{\frac{\alpha_p}{1 + \alpha_p} (\gamma \frac{V_1}{V_3} - 1)}. \quad (48)$$

This is an estimation of the parameters affecting λ . As this relation shows, the correction factor depends on the volumes V_1 and V_3 , in addition to α_p . Therefore, by knowing the values of V_1 , V_3 , and α_p and by estimating the constant value of γ for one scenario, we can use the algorithm for other scenarios.

V. RESULTS AND DISCUSSION

In this section, the results of the introduced hydraulic modeling approach are shown. The results also shed a light on the origin of difficulties associated with efficient computing. In addition, how the perturbation theory can help to overcome these problems and the conditions needed for its use are demonstrated.

Fig. 2(a) shows the response of the hydraulic system under investigation in the time-domain for a volume of $V_3 = 10^{-4} \text{ m}^3$.

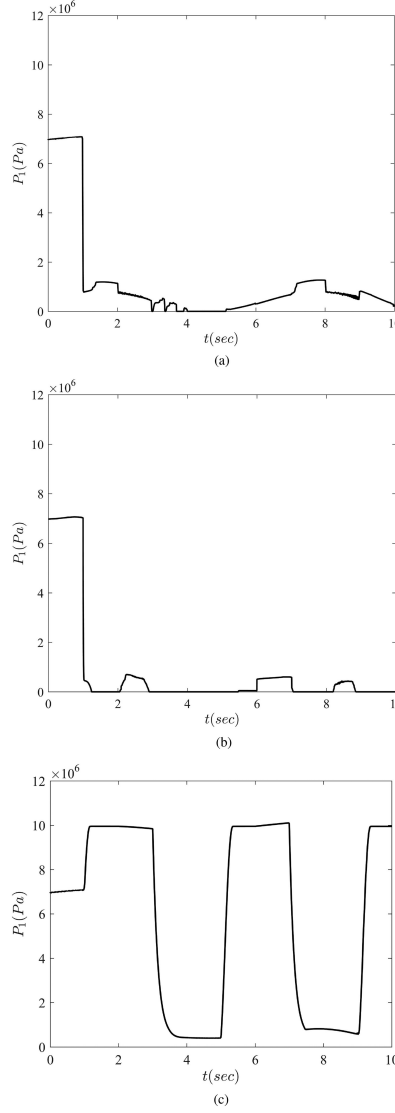


Fig. 2. Response of the original system for different conditions. (a) $V_3 = 10^{-4} \text{ m}^3$, time-step = 10^{-4} s . (b) $V_3 = 5 \times 10^{-3} \text{ m}^3$, time-step = 10^{-3} s . (c) $V_3 = 5 \times 10^{-3} \text{ m}^3$, time-step = 10^{-4} s .

The system is solved using the Runge–Kutta numerical integration algorithm with a fixed time-step of 10^{-4} s . As shown in Fig. 2(a), the time response is not acceptable. The parameters and initial values of the integration used in the simulation are given in Table I. In Fig. 2(b), the volume used in the

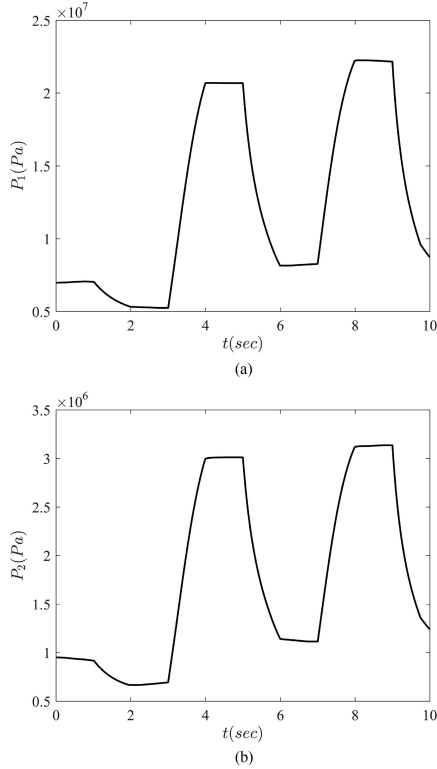


Fig. 3. Response of the perturbed system without volumetric flow-rate modification with a time-step of 10^{-3} s. (a) P_1 versus time, and (b) P_2 versus time.

calculations is increased to $V_3 = 5 \times 10^{-3}$ m³, where the time-step is increased to 10^{-3} s. The results demonstrate that the same problem of stability remains, as shown in Fig. 2(a).

Fig. 2(c) shows how the results can take an anticipated trend when $V_3 = 5 \times 10^{-3}$ m³ and the time-step is 10^{-4} s. Comparing Fig. 2(a) and (c), it can be concluded that the volume decrease of V_3 by 50 times leads to the failure in the integration of the system. On the other hand, comparing Fig. 2(b) and (c), it can be seen that all conditions are the same but the time-step size is greater by one order of magnitude in Fig. 2(b) than in Fig. 2(c). These results in Fig. 2 indicate that the selection of suitable values for the time-step size and the volume can directly affect the stability of the solution. As small volumes occur in many applications, the choice of smaller time-steps may lead to a slower computational process.

As mentioned previously, a stable integration requires the time-step to decrease as the volume reduces. When the volume size approaches zero, the integration will eventually fail. This problem can be resolved by employing the singular perturbation theory.

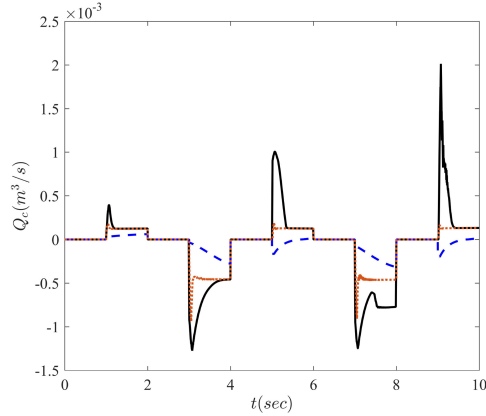


Fig. 4. Volumetric flow-rate Q_C for different systems: Solid black line for the original system with $V_3 = 10^{-4}$ m³ and a time-step of 10^{-4} s; dashed blue line for the perturbed system without modification with a time-step of 10^{-3} s; and pointed brown line for the perturbed system with volumetric flow-rate modification with a time-step of 10^{-3} s and $\gamma = 49$.

Fig. 3 depicts the pressures on both sides of the piston [point 1 in Fig. 3(a) and point 2 in Fig. 3(b)] as a function of time. These values are for a perturbed system, without any additional corrections and calculations. In other words, only (35) and (37) are used instead of (19). Comparing Figs. 3(a) and 2(c) reveals that the results of the perturbed system do not match the results of the original system with a lower time-step. Therefore, applying the perturbation theory alone is not enough to obtain reasonable results.

As mentioned in Section IV, and as depicted in Fig. 3, the errors associated with the volumetric flow-rate Q_C are responsible for this inconsistency. Fig. 4 depicts the volumetric flow-rate Q_C in different systems, namely, the original system, the perturbed system, and the perturbed system with modifications. From the figure, it can be noted that there is a significant difference between the volumetric flow-rate of the original system and that of the perturbed system, which requires modification of the perturbed system, as mentioned in Section IV-B2.

The modification is performed by introducing a correction factor λ , which is multiplied by the volumetric flow-rate. The correction factor is estimated as $\lambda \cong \frac{1+\alpha_p}{\alpha_p} (\gamma \frac{V_1}{V_3} - 1)$ for $U > C$ (see Section IV-B2). For instance, by setting parameters as $V_3 = 2.45 \times 10^{-3}$ m³ and $V_3 = 5 \times 10^{-3}$ m³, by calculating $\alpha_p = (UC_{PV}/C_c)^2 = 2.56 \times 10^{-4}$ using the values given in Table 1, and by assuming $\gamma = 49$, the correction factor is obtained as $\lambda = 300$. From Fig. 4, it can be seen that results based on the modified volumetric flow-rate Q_C agree with the original system. Therefore, the modified volumetric flow-rate relation needs to be used to get acceptable results. It is important in terms of realistic results, however, that the volume V_3 is accounted for. This volume can be treated with the modification done on the volume flow-rate, for which reason the modification done on the volumetric flow-rate is essential.

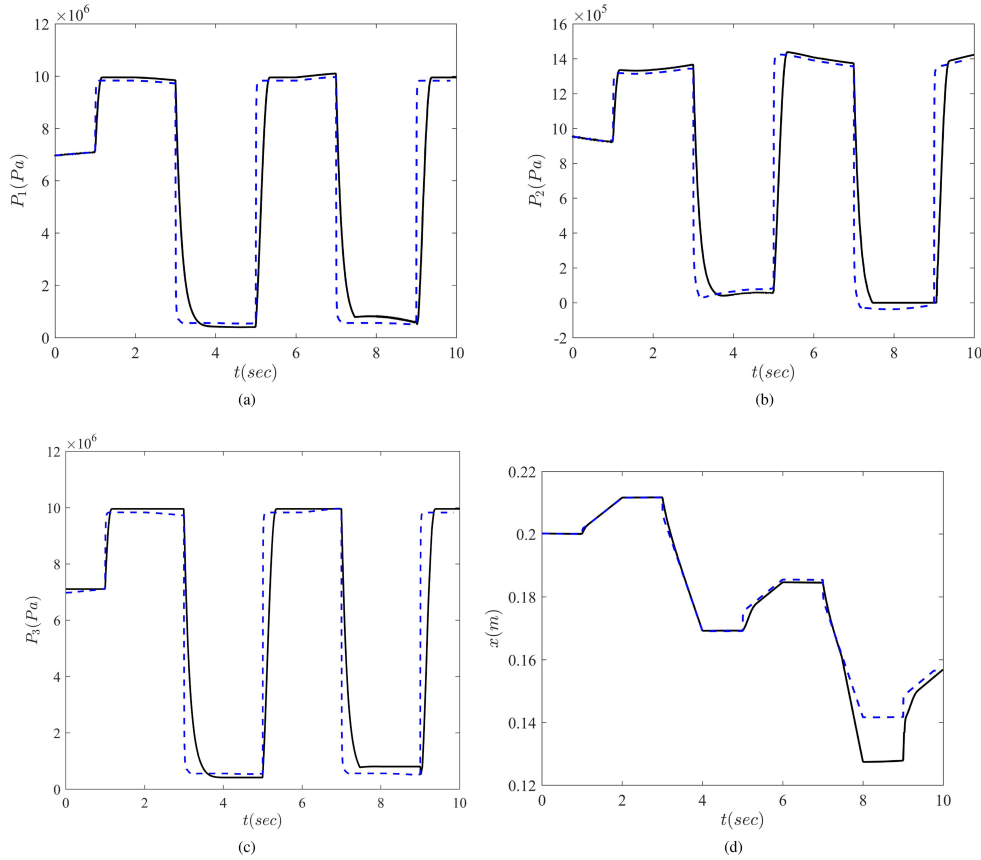


Fig. 5. Response of the original (black solid line) and perturbed systems with volumetric flow-rate modification (blue dash line). Variation of (a) P_1 , (b) P_2 , (c) P_3 , and (d) x with time. The original system corresponds to $V_3 = 5 \times 10^{-3} \text{ m}^3$ and a time-step of 10^{-4} s , and the perturbed system to a time-step of 10^{-3} s and $\gamma = 49$.

Fig. 5 shows the results of the perturbed system with the modified volumetric flow-rate (blue dash line) and the results of the original system (black solid line). Fig. 5(a)–(d) depicts the variations of P_1 , P_2 , P_3 , and x with time, respectively. Within the first second, the valve spool position is placed in the mid-position, where it does not let the oil flow. Both pressures and piston position remain fixed. In the next stage of time, i.e., $1 < t < 2 \text{ s}$, the valve piston is placed at the left position, and pressures P_1 and P_3 approach the pump pressure. As a result, the piston is pushed to the right. In the next stage of time, i.e., $2 < t < 3 \text{ s}$, the valve spool position is brought back to the middle position. However, the pressures on both sides of the piston with the external load are balanced by the same magnitudes as in the previous stage of $1 < t < 2 \text{ s}$; thus, the piston position remains fixed during this stage. In the next stage, i.e., $3 < t < 4 \text{ s}$, the valve spool goes to the right position, and con-

sequently, the pressures P_1 and P_3 are decreased to near the tank pressure. Thus, as shown in Fig. 5(d), the piston goes back to the left.

Fig. 5 shows the comparison of the response of the modified system based on the perturbation theory against that of the original system in which the used time-step is 10 times smaller than the one used in the modified system. As can be seen, the perturbed system agrees well with the original system. As mentioned previously, the accuracy of the modeling based on perturbation mostly depends on the modification done for the volumetric flow-rate. This explains the small difference in piston displacement within $8 < t < 9 \text{ s}$. As a conclusion, the more accurate the volumetric flow-rate modification, the closer is the response to the original system. It should be noted that the original system uses a time-step of 10^{-4} s , while the perturbed system is solved with a time-step of 10^{-3} s . It was observed

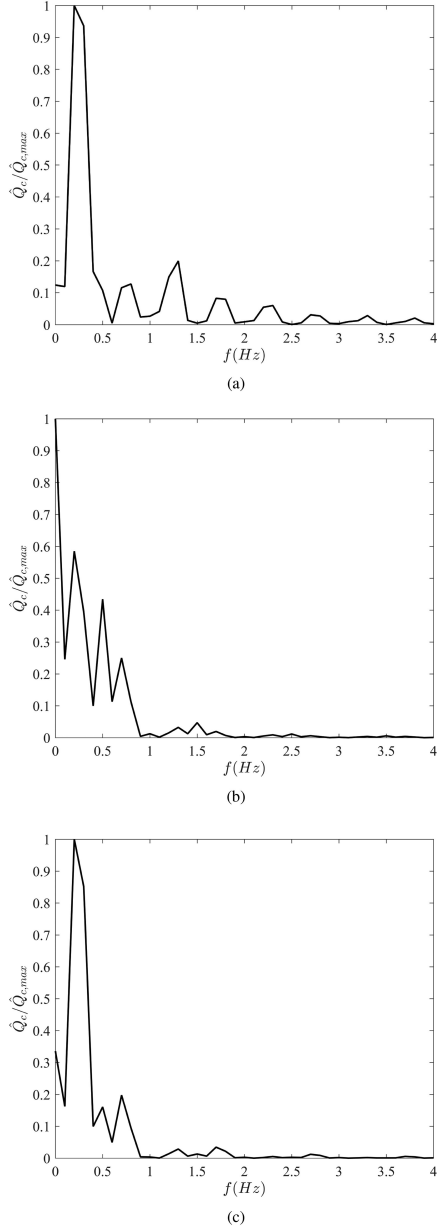


Fig. 6. Normalized Fourier transform of volumetric flow-rate versus frequency. (a) Original system with $V_3 = 5 \times 10^{-3} \text{ m}^3$ and a time-step of 10^{-4} s . (b) Perturbed system without volumetric flow-rate modification with a time-step of 10^{-3} s . (c) Perturbed system with volumetric flow-rate modification with a time-step of 10^{-3} s and $\gamma = 49$.

that this time-step could be increased up to 0.003 s without any stability problem.

The frequency responses of the original and perturbed systems with and without volumetric flow-rate correction are illustrated in Fig. 6(a)–(c). In this figure, the normalized Fourier transform of the volumetric flow-rate in the time-domain is displayed against frequency. In Fig. 6(a) and (c), a peak occurs at a frequency of 0.25 Hz, which is the frequency of the piston. However, Fig. 6(b) does not display any peak at that frequency. Thus, it can be claimed that the volumetric flow-rate modification reproduces the same frequencies in the original and the perturbed systems.

VI. CONCLUSION

In this paper, the singular perturbation theory is implemented as an alternative way to model hydraulic circuits with small volumes. First, this technique was applied to the system to show that all necessary conditions, especially the stability of the boundary-layer model, were satisfied. Then, the perturbed equations were derived and implemented in other relations affected by this theory, such as the volumetric flow-rate in the studied case. It was shown that a small volume V_3 has a significant effect on the results and must be kept in the modeling formulation. The small volume is omitted when applying the perturbation theory based approach; it is, however, involved in the modified relation. The presented perturbation theory can speed-up the computation by allowing the use of larger time-steps while maintaining accuracy in both the time and frequency spaces, which makes it suitable for application in real-time simulations. Future studies will be devoted to the application of this method in other hydraulic systems with different configurations as well as systems consisting of several smaller systems.

APPENDIX A

The “Step” function used in the simulation is given by Step =

$$\begin{cases} 1, & \Delta P > 10^5 \\ 1 - 2 \left(3 + \frac{\Delta P - 10^5}{10^5} \right) \left(\frac{\Delta P - 10^5}{2 \times 10^5} \right)^2, & -10^5 < \Delta P < 10^5 \\ -1, & -10^5 < \Delta P \end{cases} \quad (\text{A1})$$

The spool position can be modeled using the following relation:

$$\dot{U} = \frac{U_{\text{in}} - U}{\tau} \quad (\text{A2})$$

where U_{in} is an input equal to 10, and τ has a value of 0.1. Thus, the solution of (A2) gives U .

REFERENCES

- [1] C. Kaddissi, J.-P. Kenne, and M. Saad, “Identification and real-time control of an electrohydraulic servo system based on nonlinear backstepping,” *IEEE/ASME Trans. Mechatronics*, vol. 12, no. 1, pp. 12–22, Feb. 2007.
- [2] B. Xu, R. Ding, J. Zhang, and Q. Su, “Modeling and dynamic characteristics analysis on a three-stage fast-response and large-flow directional valve,” *Energy Convers. Manage.*, vol. 79, pp. 187–199, 2014.

- [3] F. Wang and Y. Chen, "Dynamic characteristics of pressure compensator in underwater hydraulic system," *IEEE/ASME Trans. Mechatronics*, vol. 19, no. 2, pp. 777–787, Apr. 2014.
- [4] B. Xu, R. Ding, J. Zhang, L. Sha, and M. Cheng, "Multiphysics-coupled modeling: Simulation of the hydraulic-operating mechanism for a SF6 high-voltage circuit breaker," *IEEE/ASME Trans. Mechatronics*, vol. 21, no. 1, pp. 379–393, Feb. 2016.
- [5] D. E. Bowns and L. M. Wang, "The digital computation of pressures in hydraulic pipes with small volume using an iterative technique," *Proc. Institution Mech. Engineers, Part C: J. Mech. Eng. Sci.*, vol. 204, no. 1, pp. 29–36, 1990.
- [6] R. Piché and A. Ellman, "Numerical integration of fluid power circuit models using two-stage semi-implicit Runge–Kutta methods," *Proc. Institution Mech. Engineers, Part C: J. Mech. Eng. Sci.*, vol. 208, no. 3, pp. 167–175, 1994.
- [7] W. Borutzky, B. Barnard, and J. Thoma, "An orifice flow model for laminar and turbulent conditions," *Simul. Model. Pract. Theory*, vol. 10, no. 3–4, pp. 141–152, 2002.
- [8] F. Pfeiffer and F. Borchsenius, "New hydraulic system modelling," *J. Vibration, Control*, vol. 10, no. 10, pp. 1493–1515, 2004.
- [9] S. Esqué, A. Rana, and A. Ellman, "Techniques for studying a mobile hydraulic crane in virtual reality," *Int. J. Fluid Power*, vol. 4, no. 2, pp. 25–35, 2003.
- [10] W. A. Welsh, "Simulation and correlation of a helicopter air–oil strut dynamic response," in *Proc. 43rd Annu. Forum Amer. Helicopter Soc.*, St. Louis, MO, USA, vol. 1, pp. 231–242, 1987.
- [11] F. Pfeiffer, M. Foerg, and H. Ulbrich, "Numerical aspects of non-smooth multibody dynamics," *Comput. Methods Appl. Mechanics Eng.*, vol. 195, no. 50, pp. 6891–6908, 2006.
- [12] O. Brüls and M. Arnold, "The generalized- α scheme as a linear multistep integrator: Toward a general mechatronic simulator," *J. Comput. Nonlinear Dyn.*, vol. 3, no. 4, 2008, Art. no. 041007.
- [13] K. J. Bathe, *Finite Element Procedures*. Englewood Cliffs, NJ, USA: Prentice-Hall, 1996.
- [14] A. Cardona and M. Geradin, "Modeling of a hydraulic actuator in flexible machine dynamics simulation," *Mechanism Mach. Theory*, vol. 25, no. 2, pp. 193–207, 1990.
- [15] A. Ylinen, J. Mäkinen, and R. Kouhia, "Two models for hydraulic cylinders in flexible multibody simulations," in *Computational Methods for Solids and Fluids*, A. Ibrahimbegovic, Ed., AG Switzerland: Springer, 2016, pp. 463–493.
- [16] A. Ylinen, H. Marjamäki, and J. Mäkinen, "A hydraulic cylinder model for multibody simulations," *Comput. Struct.*, vol. 138, pp. 62–72, 2014.
- [17] O. A. Bauchau and H. Liu, "On the modeling of hydraulic components in rotorcraft systems," *J. Amer. Helicopter Soc.*, vol. 51, no. 2, pp. 175–184, 2006.
- [18] M. Naya, J. Cuadrado, D. Dopico, and U. Lugris, "An efficient unified method for the combined simulation of multibody and hydraulic dynamics: Comparison with simplified and co-integration approaches," *Arch. Mech. Eng.*, vol. 58, no. 2, pp. 223–243, 2011.
- [19] T. R. Young and J. P. Boris, "A numerical technique for solving stiff ordinary differential equations associated with the chemical kinetics of reactive-flow problems," *J. Physical Chemistry*, vol. 81, no. 25, pp. 2424–2427, 1977.
- [20] J. Yao, Z. Jiao, D. Ma, and L. Yan, "High-accuracy tracking control of hydraulic rotary actuators with modeling uncertainties," *IEEE/ASME Trans. Mechatronics*, vol. 19, no. 2, pp. 633–641, Apr. 2014.
- [21] J. Watton, *Fluid Power Systems: Modeling, Simulation, Analog and Microcomputer Control*. Hemel Hempstead, U.K.: Prentice-Hall, 1989.
- [22] H. M. Handroos and M. J. Vilenius, "Flexible semi-empirical models for hydraulic flow control valves," *J. Mech. Design*, vol. 113, no. 3, pp. 232–238, 1991.
- [23] L. Noethen and S. Walcher, "Tikhonov's theorem and quasi-steady state," *Discrete Continuous Dynamical Syst.—Ser. B*, vol. 16, no. 3, pp. 945–961, 2011.
- [24] A. N. Tikhonov, "Systems of differential equations containing small parameters in the derivatives," *Matematicheskii Sbornik*, vol. 73, no. 3, pp. 575–586, 1952.
- [25] L. Wang, W. J. Book, and J. D. Huggins, "Application of singular perturbation theory to hydraulic pump controlled systems," *IEEE/ASME Trans. Mechatronics*, vol. 17, no. 2, pp. 251–259, Apr. 2012.
- [26] H. K. Khalil and J. W. Grizzle, *Nonlinear Systems*, vol. 3. Englewood Cliffs, NJ, USA: Prentice-Hall, 1996.
- [27] P. Kokotović, H. K. Khalil, and J. O'Reilly, *Singular Perturbation Methods in Control: Analysis and Design*. Philadelphia, PA, USA: SIAM, 1999.
- [28] L.-Y. Chen, N. Goldenfeld, and Y. Oono, "Renormalization group and singular perturbations: Multiple scales, boundary layers, and reductive perturbation theory," *Physical Rev. E Statist. Phys., Plasmas, Fluids, Related Interdisciplinary Topics*, vol. 54, no. 1, pp. 376–394, 1996.



Mehran Kiani Oshtorjani received the B.S. degree in mechanical engineering from Yazd University, Yazd, Iran, in 2013, and the M.S. degree in aerospace engineering from the Sharif University of Technology, Tehran, Iran, in 2015. Since 2016, he has been a doctoral student at the Lappeenranta University of Technology, Lappeenranta, Finland.

His research interests include hydraulic systems, real-time simulations, mechanical design, computational fluid dynamics, heat transfer, multiphase flows, and granular systems.



Aki Mikkola received the Ph.D. degree in the field of machine design from Lappeenranta University of Technology in 1997.

Since 2002, he has been a Professor with the Department of Mechanical Engineering, Lappeenranta University of Technology, Lappeenranta, Finland. He has been awarded five patents, has contributed to more than 90 peer-reviewed journal papers, and has presented more than 100 conference articles. His research interests include flexible multibody dynamics, rotating structures, and biomechanics.



Payman Jalali received the B.S. degree in mechanical engineering from AmirKabir University, Tehran, Iran, in 1995, the M.S. degree in mechanical engineering from Tehran University, Tehran, Iran, in 1997, and the Ph.D. degree in energy technology from the Lappeenranta University of Technology (LUT), Lappeenranta, Finland, in 2000.

From 2001 to 2003, he was a Postdoctoral Fellow with the Georgia Institute of Technology, Atlanta, GA, USA. From 2004 to 2006, he was a Researcher, and since 2006, he has been an Adjunct Professor with LUT. Since 2011, he has been an Associate Professor of energy technology with LUT. He has also been a Visiting Professor with Duke University, Durham, NC, USA, since 2016. He has been the Principal Investigator (PI) or Co-PI of four major projects from the Academy of Finland. He has authored or co-authored nearly 80 peer-reviewed articles. His research interests include computational and experimental fluid flows, heat transfer, multiphase flows, and complex systems with applications in hydraulic circuits, gas–solid multiphase flows in energy technology, physics of granular and particle systems, and biomedical research.

Publication II

J. Rahikainen, M. Kiani-Oshtorjani, J. Sopanen, P. Jalali, and A.
Mikkola

**Computationally efficient approach for simulation of multibody and
hydraulic dynamics**

Reprinted with permission from
Mechanism and Machine Theory

Vol. 130, pp. 435–446, 2018

© 2018, Elsevier



Contents lists available at ScienceDirect

Mechanism and Machine Theory

journal homepage: www.elsevier.com/locate/mechmachtheory

Research paper

Computationally efficient approach for simulation of multibody and hydraulic dynamics

Jarkko Rahikainen^{a,*}, Mehran Kiani^b, Jussi Sopenan^a, Payman Jalali^b, Aki Mikkola^a^a Department of Mechanical Engineering, Lappeenranta University of Technology, Skinnarilankatu 34, 53850, Finland^b Department of Energy Technology, Lappeenranta University of Technology, Skinnarilankatu 34, 53850, Finland

ARTICLE INFO

Article history:

Received 20 April 2018

Revised 21 August 2018

Accepted 22 August 2018

Available online 15 September 2018

Keywords:

Multibody dynamics

Hydraulic dynamics

Monolithic integration

Real-time simulation

Singular perturbation theory

ABSTRACT

A realistic real-time simulation of a complex system, such as an excavator, requires detailed description of the machinery and its components. To take into account the dynamics of entire systems, the model must encompass descriptions of non-mechanical systems, such as hydraulics. For the multibody systems, use of the semi-recursive methods has often been found to be the most efficient solution when the system size increases. For the hydraulic dynamics, in turn, the recently introduced application of the singular perturbation method is a potential candidate for the real-time applications. The main benefit of the application of the singular perturbation method over the conventionally used lumped fluid method is that it overcomes the challenges that the lumped fluid method encounters when numerical stiffness caused by small hydraulic volumes is present in the circuit. Objective of this paper is to improve a recently proposed monolithic formulation for the combined simulation of multibody and hydraulic dynamics via the introduction of the singular perturbation method. Results indicate that the proposed method improves efficiency and robustness when compared to the formulation proposed earlier.

© 2018 Elsevier Ltd. All rights reserved.

1. Introduction

The use of the multibody-based real-time simulation tools has become more widespread as computation power has grown more affordable. Applications of this real-time simulation are found, for instance, in user training and, recently, in product development [1]. Since real-world mechanical systems are often accompanied by other dynamic systems, such as hydraulics, descriptions of the both dynamic systems are required if an accurate model is to be built.

Several approaches have been proposed to couple the descriptions of the dynamic subsystems, such as co-simulation [2,3] and co-integration [4,5], both of which allow different time steps to be used for each subsystem. These methods are often used to address the significantly different time scale that certain systems, such as multibody and hydraulic dynamics, possess, or, more commonly, to allow the use of the domain-specific tools and solvers developed for each field. This increases modularity in the design process and adds a possibility to hide the internal details of subsystems, for intellectual property protection, but it increases the complexity of the coupling interface.

* Corresponding author.

E-mail addresses: jarkko.rahikainen@lut.fi (J. Rahikainen), mehran.kiani@lut.fi (M. Kiani), jussi.sopenan@lut.fi (J. Sopenan), payman.jalali@lut.fi (P. Jalali), aki.mikkola@lut.fi (A. Mikkola).

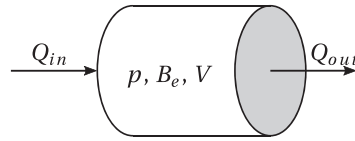


Fig. 1. Idealisation of a volume in the lumped fluid method.

However, if equations for each subsystem are available in the same simulation environment, as seen in [6], use of a monolithic approach, which yields a single set of nonlinear equations to be solved, can provide a straightforward approach for the coupling. This approach has been presented multiple times in the literature, for instance, in [7,8]. In the latter work, the augmented Lagrangian method based on position level constraints and projections [9,10] for constraint stability is coupled with the lumped fluid [11] method and integrated with the implicit single-step trapezoidal rule. As the penalty scheme with iterated Lagrange multipliers and implicit integrator can provide a robust approach for multibody dynamics [10], the work presented in [8] seems interesting from the coupled simulation point of view.

The efficiency of the method proposed in [8] is, however, hindered by the global approach used for the multibody dynamics. To address this, Rahikainen et al. [12] proposed to use the semi-recursive formulation proposed by Cuadrado et al. in [13] for the monolithic simulation of multibody and hydraulic dynamics, based on work presented in [8]. The multibody method uses the same penalty formulation as the augmented Lagrangian method for closed loop constraints and uses the mass-damping-stiffness orthogonal projections [10] to stabilise them, and it has indicated potential for real-time simulation in multiple applications, as demonstrated in studies of automated differentiation tools [14] and dense, sparse, and parallelisation techniques [15].

However, while the multibody method was selected real-time simulation in mind in [12], the lumped fluid method [11] may in certain cases encounter problems, that hinder its computational efficiency. As demonstrated in the literature [16,17], small volumes in a hydraulic circuit can increase numerical stiffness of the system, and thereby require small time steps for a solution to be sought. This can become an issue especially in the context of the monolithic approach wherein the same time step is also used for the multibody solution.

Recently, Kiani et al. [18] proposed application of the singular perturbation theory [19] to address the issue of numerical stiffness introduced by the small volumes. The results of the study indicated potential for the real-time simulation of a hydraulic system, as the behaviour of the examined circuit examined was captured with high accuracy while the computational effort was lower than in the lumped fluid approach. Use of the perturbation method allows to increase the integration time step, which, in turn, decreases the time scale difference between the multibody and hydraulic dynamics.

The objective of this paper is to improve the real-time applicability of the method presented in [12] by employing the approach based on the singular perturbation theory presented in [18]. Accordingly, this is the first study to couple the application of the singular perturbation theory [18] with the multibody dynamics. A case example seen in [12] is modified such that the issue of small volumes with the lumped fluid method is demonstrated, and real-time applicability is evaluated relative to the method presented in [12].

The rest of this paper is structured as follows: Section 2 includes the hydraulic modelling with use of the lumped fluid method and provides a brief introduction to the singular perturbation theory, multibody modelling, and the integration scheme. To better illustrate the application of the singular perturbation theory, Section 3 details the differences in the hydraulic modelling with respect to the lumped fluid method. That section also details the hydraulic circuit and the mechanical model used in the example. Results are presented in Section 4, and Section 5 presents the key conclusions.

2. Methods

In this section the lumped fluid method, which is traditionally used to model the hydraulic circuits, along with the singular perturbation theory, the method applied for the hydraulic circuit here, are briefly introduced. Models of hydraulic components related to the case example, and the implementation details of the singular perturbation theory can be found further on, in Section 3. The semi-recursive multibody method and the monolithic integration also are briefly discussed in this section.

2.1. The lumped fluid method

In the lumped fluid method [11] the hydraulic circuit is divided into volumes V in which pressure is assumed to be equally distributed. This is illustrated in Fig. 1, where volume flows Q_{in} and Q_{out} , both of which may consist of multiple separate flows, flow into volume V , which has internally constant pressure p and effective bulk modulus B_e .

In a general form, the pressure variation for each volume l can be expressed as a first-order differential equation as follows:

$$\dot{p}_l = \frac{B_{el}}{V_l} \left(\sum_{j=1}^{n_f} Q_{lj} - \dot{V}_l \right) \tag{1}$$

where \dot{p}_l is the time derivative of the pressure, B_{el} is the effective bulk modulus, V_l is the volume, \dot{V}_l is the rate of change of volume V_l , n_f is the number of incoming and outgoing volume flows, and, finally, Q_{lj} are the incoming and outgoing volume flows. Effective bulk modulus B_{el} represents the compressibility of the volume, and it takes the fluid compressibility due to dissolved air in the fluid and flexibility of containers into account. The general form for the effective bulk modulus can be written as

$$B_{el} = \left(B_o^{-1} + \sum_{j=1}^{n_c} \frac{V_j}{V_l} B_j^{-1} \right)^{-1} \tag{2}$$

where B_o is the bulk modulus of the oil, n_c is the number of subvolumes V_j that form the volume V_l , and B_j is the bulk modulus of each volume j . Subvolumes V_j are components of the circuit, such as pipes and hoses, in which the container has a consistent bulk modulus B_j , and their volume can be computed from the container geometry. Each volume V_l , in turn, is limited by restrictors, such as valves and pistons, that allow volume flows into and from of the volume. The computation of these volume flows is dependent on the component, and in some cases, such as valves, dependent also on the modelling method selected.

2.2. Singular perturbation theory

Consider the pressure derivative given in Eq. (1). Rearranging the equation such that the ratio between the effective bulk modulus and volume is moved to the left side yields an equation with a small-valued parameter. In the perturbation problems, in general, the effect of a parameter that has a small value, as in the case illustrated above, has a key role. For the regular perturbation problems, the solution can be obtained by equating the small valued parameter to zero, whereas in the singular perturbation problems this parameter cannot be neglected without a significant loss of accuracy in the results. Under certain conditions, the pressure variation equations of the lumped fluid theory fall into the latter category.

A well-known approach for perturbation problems of the latter type is the singular perturbation theory. As mentioned in [18], with this theory the ordinary differential equations, that contain the infinitesimal parameter ϵ , are transferred into a quasi-steady state model, in which the accuracy is maintained in the order of ϵ , based on Tikhonov's theorem [19] in singular perturbation theory and the strategy employed by Wang et al. [20]. To illustrate the method, consider the following system of singular equations:

$$\dot{\phi} = f(\phi, \psi, t, \epsilon) \quad \phi(t_0) = \zeta(\epsilon) \tag{3}$$

$$\dot{\psi} = g(\phi, \psi, t, \epsilon) \quad \psi(t_0) = \xi(\epsilon) \tag{4}$$

where ϵ is the infinitesimal value, t is time, and ϕ and ψ are the state variables. According to [21], the above system can be reduced to

$$\dot{\phi} = f(\phi, h(t, \phi), t, \epsilon) \tag{5}$$

$$\bar{\psi} = h(t, \bar{\phi}) \tag{6}$$

where the overbar denotes the perturbed variables and h is an algebraic equation that is determined during the order reduction. For the reduction to be possible, functions f and g are assumed to be smooth enough and their boundary layers to be exponentially stable. In addition, the reduced-order system of Eq. (6) is assumed to be exponentially stable and to have unique solutions on a convex set.

To elaborate it in a simple manner, the set of singular equations of (4) can be transformed into a set of ordinary equations in which the small parameter ϵ can be simply set to zero without a loss of accuracy. The order of Eq. (4) is reduced and Eq. (6) is an algebraic instead of a first order differential equation. Thus, this method reduces the numerical stiffness and, therefore, enables us to use a larger time step in integration. It is important to note, that $\bar{\phi}$ in Eq. (6) is not unknown but an algebraic equation with an explicit solution, and, therefore, Eqs. (5) and (6) do not constitute a set of differential algebraic equations. The application details in context of the lumped fluid method will be described later with the case example in Section 3.2.

2.3. Multibody modeling

In this paper, the semi-recursive method described by Cuadrado et al. [13] is used to describe the multibody dynamics. In the modelling phase fully Cartesian or natural coordinates are used to define constraint equations and the geometry of each body whereas positions and velocities of the open loops are computed recursively. Hence, the method uses a double set of coordinates.

The first set of coordinates, used to define the dynamic terms, is defined for a body k at the velocity level as

$$\mathbf{Z}_k = \begin{bmatrix} \dot{\mathbf{r}}_k^0 \\ \boldsymbol{\omega}_k \end{bmatrix} \quad (7)$$

where $\dot{\mathbf{r}}_k^0$ is the velocity 3×1 vector of the body k particle located at the current instant in time at the origin of the global coordinate system and $\boldsymbol{\omega}_k$ is the angular velocity vector of the same size, both expressed in the global frame. The use of these coordinates allows the recursive expressions to be written without a velocity transformation matrix, as follows:

$$\mathbf{Z}_k = \mathbf{Z}_{k-1} + \mathbf{b}_k \dot{\mathbf{z}}_k \quad (8)$$

where $\dot{\mathbf{z}}_k$ is the relative velocity of the joint k . The term \mathbf{b}_k is a matrix whose number of columns corresponds to the degrees of freedom of the joint between bodies k and $k-1$, and its form depends on the joint type. Matrix forms of these Cartesian velocities can be expressed, for a system of m bodies, as $\mathbf{Z} = [\mathbf{Z}_1^T \quad \mathbf{Z}_2^T \quad \dots \quad \mathbf{Z}_m^T]^T$.

A velocity transformation matrix \mathbf{R} can be defined between Cartesian velocities \mathbf{Z} and relative velocities $\dot{\mathbf{z}}$ as follows:

$$\mathbf{Z} = \mathbf{R}\dot{\mathbf{z}} = \mathbf{TR}_d\dot{\mathbf{z}} \quad (9)$$

where \mathbf{T} is a path matrix describing the system topology and matrix \mathbf{R}_d is a block-diagonal matrix containing \mathbf{b}_k .

The derivation of the equations of motion with the selected set of coordinates has been presented in literature on numerous occasions [13,22]. The virtual power of an open-loop system can be expressed in terms of \mathbf{Z} , $\bar{\mathbf{M}}_k$ being the mass matrix and $\bar{\mathbf{Q}}_k$ the force vector. The velocity transformations can be introduced to the virtual power equation, which yields independent virtual velocities that can be eliminated from the equation. Accordingly, the following set of differential equations describing the open-loop motion can be obtained:

$$\mathbf{R}_d^T \mathbf{T}^T \bar{\mathbf{M}} \mathbf{TR}_d \dot{\mathbf{z}} = \mathbf{R}_d^T (\mathbf{T}^T (\bar{\mathbf{Q}} - \bar{\mathbf{M}} \mathbf{TR}_d \dot{\mathbf{z}})) \quad (10)$$

Eq. (10) can be simplified by denoting the left-hand-side system matrix as \mathbf{M} and the right-hand-side force vector as \mathbf{Q} . This yields the simple expression of $\mathbf{M}\dot{\mathbf{z}} = \mathbf{Q}$.

The method presented in [13] uses a penalty technique to deal with closed kinematic chains, resulting in an equation of motion similar to the augmented Lagrangian method with position-level constraints [9]:

$$\mathbf{M}\dot{\mathbf{z}} + \Phi_z^T \alpha \Phi + \Phi_z^T \lambda^* = \mathbf{Q} \quad (11)$$

where Φ are the constraint equations, Φ_z is the constraint Jacobian, and α is the penalty factor. While this expression does not take nonholonomic constraints into account, the multibody method can work also with them [23], as they are imposed in the projection phase presented in the next section. Vector λ^* contains the iterated Lagrangian multipliers, which are iterated at each time step n as follows:

$$\lambda_n^{*(i+1)} = \lambda_n^{*(i)} + \alpha \Phi_n^{(i+1)} \quad (12)$$

where i is the iteration number in Newton's method. The final value of λ^* calculated in the time step $n-1$ is reused for $\lambda_n^{*(0)}$.

2.4. Monolithic integration

An integration scheme for the monolithic simulation is presented in [12]. That method, followed here, has its origins in the work presented by Naya et al. [8]. After the multibody and the hydraulic system equations are assembled, the following set of equations can be obtained:

$$\begin{aligned} \mathbf{M}\dot{\mathbf{z}} + \Phi_z^T \alpha \Phi + \Phi_z^T \lambda^* &= \mathbf{Q}(\mathbf{z}, \dot{\mathbf{z}}, \mathbf{p}) \\ \dot{\mathbf{p}} &= \mathbf{h}(\mathbf{p}, \mathbf{z}, \dot{\mathbf{z}}) \end{aligned} \quad (13)$$

where \mathbf{p} is the vector of pressures and \mathbf{h} denote the pressure variation equations.

The implicit single-step trapezoidal rule is applied for Eq. (13). This yields the following dynamic equilibrium at the time step $n+1$:

$$\begin{aligned} \mathbf{M}\mathbf{z}_{n+1} + \frac{\Delta t^2}{4} \Phi_{z,n+1}^T (\alpha \Phi_{n+1} + \lambda_{n+1}^*) - \frac{\Delta t^2}{4} \mathbf{Q}_{n+1} + \frac{\Delta t^2}{4} \mathbf{M}\dot{\mathbf{z}}_n &= \mathbf{0} \\ \frac{\Delta t}{2} \mathbf{p}_{n+1} - \frac{\Delta t^2}{4} \mathbf{h}_{n+1} + \frac{\Delta t^2}{4} \hat{\mathbf{p}}_n &= \mathbf{0} \end{aligned} \quad (14)$$

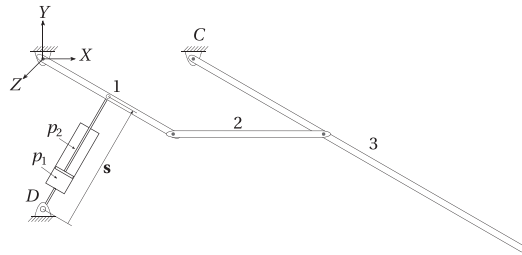


Fig. 2. A four-bar linkage actuated by a hydraulic cylinder [12].

where \mathbf{z}_{n+1} and \mathbf{p}_{n+1} form the vector of unknowns, and Δt is the time step, and

$$\begin{aligned} \hat{\mathbf{z}}_n &= -\left(\frac{4}{\Delta t^2} \mathbf{z}_n + \frac{4}{\Delta t} \dot{\mathbf{z}}_n + \ddot{\mathbf{z}}_n\right) \\ \hat{\mathbf{p}}_n &= -\left(\frac{2}{\Delta t} \mathbf{p}_n + \dot{\mathbf{p}}_n\right) \end{aligned} \tag{15}$$

Eq. (14) can be written in a simpler form as $\mathbf{f}(\mathbf{x}_{n+1}) = \mathbf{0}$, where $\mathbf{x} = [\mathbf{z}^T \ \mathbf{p}^T]^T$. This nonlinear system of equations can be solved by means of the well-known Newton–Raphson iteration. To address magnitude differences in \mathbf{z} and \mathbf{p} during the iteration, integration tolerances are specified individually for these vectors.

While a symbolic formulation of the tangent matrix required for the Newton–Raphson scheme is possible [8], numerical computation yields a more general-purpose approach [14,15] and is less prone to implementation errors. In this study, the forward differentiation is used:

$$\frac{df(x_0)}{dx} \approx \frac{f(x_0 + \delta) - f(x_0)}{\delta} \tag{16}$$

where δ is computed as motivated by the differentiation formula given by Brenan et al. [24], as follows:

$$\delta = 1 \times 10^{-8} \max(1 \times 10^{-2}, |x_0|) \tag{17}$$

where 1×10^{-2} limits the minimum value for the differentiation increment to 1×10^{-10} .

In the Newton’s iteration, a solution for positions \mathbf{z}_{n+1} is sought such that the equation of motion, i.e. Eq. (11), and constraint conditions $\Phi = \mathbf{0}$ are satisfied. Velocities and accelerations, however, are not accounted for during the iteration, and, therefore, $\dot{\Phi} = \mathbf{0}$ and $\ddot{\Phi} = \mathbf{0}$ are not expected to be satisfied. This issue can be addressed via mass–damping–stiffness orthogonal projections [9] to project the velocities and accelerations to the corresponding constraint manifolds. Let $\dot{\mathbf{z}}^*$ and $\ddot{\mathbf{z}}^*$, correspondingly, be the velocities and accelerations obtained from the Newton’s iteration. When the rows and columns of the tangent matrix that correspond to the multibody problem are denoted as $\frac{\partial \mathbf{f}(\mathbf{z})}{\partial \mathbf{z}}$, the final values for $\dot{\mathbf{z}}$ and $\ddot{\mathbf{z}}$ can be solved for via

$$\frac{\partial \mathbf{f}(\mathbf{z})}{\partial \mathbf{z}} \dot{\mathbf{z}} = \mathbf{P} \dot{\mathbf{z}}^* - \frac{\Delta t^2}{4} \Phi_z^T \alpha \Phi_t \tag{18}$$

$$\frac{\partial \mathbf{f}(\mathbf{z})}{\partial \mathbf{z}} \ddot{\mathbf{z}} = \mathbf{P} \ddot{\mathbf{z}}^* - \frac{\Delta t^2}{4} \Phi_z^T \alpha (\Phi_z^T \dot{\mathbf{z}} + \dot{\Phi}_t) \tag{19}$$

where weight matrix \mathbf{P} can be extracted from the tangent matrix as follows:

$$\mathbf{P} = \frac{\partial \mathbf{f}(\mathbf{z})}{\partial \mathbf{z}} - \frac{\Delta t^2}{4} (\Phi_z^T \alpha \Phi_z) \tag{20}$$

3. Case study

A case study seen in [12] is reused with a minor modification in this paper to compare the perturbation and lumped fluid methods. The example, a hydraulically actuated four-bar linkage, is depicted in Fig. 2, and the hydraulic circuit is presented in Fig. 3. Details of the hydraulic circuit and the above mentioned differences are presented next, followed by the implementation of the singular perturbation approach, in Section 3.2, and the mechanical model and the coupling, in Section 3.3.

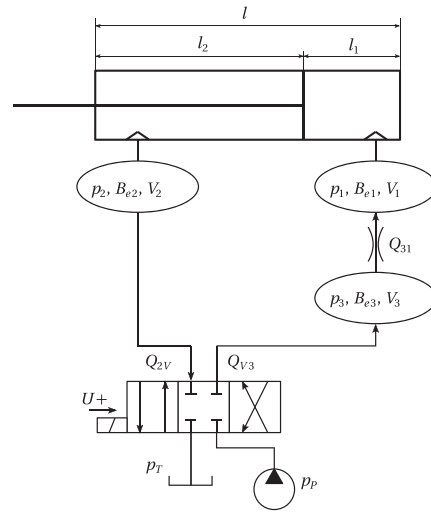


Fig. 3. The case example modified from the work of Rahikainen et al. [12].

Table 1
Parameters for the example circuit modified from Rahikainen et al. [12].

Parameter	Symbol	Value
Length of the piston	l	0.7 m
	l_{1_0}	0.2 m
	l_{2_0}	0.5 m
Initial actuator length	s_0	0.866 m
Fluid density	ρ	850 kg/m ³
Oil bulk modulus	B_o	1500 MPa
Cylinder bulk modulus	B_c	31500 MPa
Hose bulk modulus	B_h	550 MPa
Volume of hose 1	V_{h1}	3.14×10^{-5} m ³
	V_{h2}	7.85×10^{-5} m ³
	V_{h3}	7.85×10^{-7} m ³
Diameter of piston	d_1	80 mm
Diameter of piston rod	d_2	35 mm
Tank pressure	p_T	0.1 MPa
Pump pressure	p_P	7.6 MPa
Cylinder efficiency	η	0.88
Throttle discharge coefficient	C_d	0.8
Semi-empirical coefficient	C_v	$2.138 \times 10^{-8} \text{ m}^3/\text{s}\sqrt{\text{Pa}}$
Correction factor	γ_+	1.16
Correction factor	γ_-	1.05

3.1. Hydraulic circuit

For a better demonstration of the application of the perturbation theory, the case-example depicted in Fig. 3 is considered. In the figure, p_p is the pump pressure, p_T is the tank pressure, U is the control signal and l , l_1 , and l_2 are the total, piston-side and rod-side lengths, respectively. The positive direction of the volume flows Q_{2V} , Q_{V3} , and Q_{31} is also shown in the figure.

Compared to the example presented in [12], the volume V_3 , shown in Fig. 3, is further reduced from the original, to introduce a small volume to the system. This increases the numerical stiffness of the system and, thus, makes finding the numerical solution more challenging. Otherwise the example has been left unaltered. A full list of the parameters regarding the hydraulic circuit can be found in Table 1.

3.1.1. Modelling of the valves

A semi-empirical modelling approach [25], which allows determination of the flow rate coefficients on the basis of empirical data, is used to model the valves in the system. Volume flow Q_{31} over the throttle valve can be expressed as:

$$Q_{31} = \begin{cases} C_t \sqrt{|\Delta p|}, & \Delta p > 0 \\ 0, & \Delta p = 0 \\ -C_t \sqrt{|\Delta p|}, & \Delta p < 0 \end{cases} \quad (21)$$

where C_t is the semi-empirical flow rate coefficient and Δp is the pressure difference over the valve. As the construction of a throttle valve is rather simple, the semi-empirical coefficient is computed analytically here:

$$C_t = C_d A_t \sqrt{\frac{2}{\rho}} \quad (22)$$

where C_d is the flow discharge coefficient, A_t is the area of the throttle valve, and ρ is the oil density.

For the directional valve, the use of the semi-empirical approach yields the following general form for the volume flow:

$$Q = \begin{cases} C_v U \sqrt{|\Delta p|}, & \Delta p > 0 \\ 0, & \Delta p = 0 \\ -C_v U \sqrt{|\Delta p|}, & \Delta p < 0 \end{cases} \quad (23)$$

where the semi-empirical coefficient C_v can be determined from $Q/(U\sqrt{\Delta p})$ when the volume flow is known at one operational point, and U is relative spool or poppet position. Eq. (23) can be used to compute Q_{2V} and Q_{V3} , the positive directions of which are depicted in Fig. 3.

It must be noted that the numerical solution of Eqs. (21) and (23) can become problematic when the pressure difference is small. Hence, for small pressure differences, that is less than 2 bar, the flow is assumed to be laminar, and the corresponding equations are modified such that volume flow rate and pressure difference are related linearly. In practice, firstly, the volume flow is computed at $\Delta p = 2$ bar, with the current spool position in the case of Eq. (23), and, secondly, the actual volume flow is interpolated between zero and the computed value. The sign of the volume flow follows that presented in Eqs. (21) and (23).

Spool position U , not to be mistaken for the control signal U_{ref} , takes valve behaviour into account and can be expressed via a first-order differential equation as:

$$\dot{U} = \frac{U_{ref} - U}{\tau} \quad (24)$$

where τ is the time constant of the valve, which can be obtained from the Bode-plot provided by the manufacturer.

3.1.2. Cylinder model

A hydraulic cylinder and the related quantities have been presented in Figs. 2 and 3. The rate of change in volumes V_1 and V_2 can be written as thus:

$$\begin{aligned} \dot{V}_1 &= \dot{s} A_1 \\ \dot{V}_2 &= \dot{s} A_2 \end{aligned} \quad (25)$$

where \dot{s} is the piston velocity and A_1 and A_2 are the areas on either side of the piston.

Cylinder force F_s can be expressed for the depicted case as follows:

$$F_s = p_1 A_1 - p_2 A_2 - F_\mu \quad (26)$$

where F_μ is the friction force caused by the sealing, computed in this case as $F_\mu = (p_1 A_1 - p_2 A_2)(1 - \eta)\dot{s}$.

3.2. Application of the singular perturbation theory

For the example shown in Fig. 3, the use of the lumped fluid theory yields the following expressions for the pressure variations in volumes V_1 , V_2 , and V_3 :

$$\dot{p}_1 = \frac{B_{e1}}{V_1} (Q_{31} - \dot{V}_1) \quad (27)$$

$$\dot{p}_2 = \frac{B_{e2}}{V_2} (\dot{V}_2 - Q_{2V}) \quad (28)$$

$$\dot{p}_3 = \frac{B_{e3}}{V_3} (Q_{V3} - Q_{31}) \quad (29)$$

where B_{e1} , B_{e2} , and B_{e3} are the effective bulk moduli of the volumes and \dot{s} is the cylinder elongation velocity.

Application of the singular perturbation theory [18], in turn, allows the use of algebraic equations instead of differential equations for the small volumes in the system. However, as discussed in Section 2.2, for the singular perturbation theory to be applied, a certain set of conditions must be fulfilled. As the singular perturbation theory concerns singular systems, two distinct solutions for the system are obtained if the small parameter is set to zero, or it is left unchanged. Also, the boundary layers of the following equations must be exponentially stable:

$$\epsilon \dot{p}_1 = (Q_{31} - \dot{V}_1) \quad (30)$$

$$\epsilon \dot{p}_2 = (\dot{V}_2 - Q_{2V}) \quad (31)$$

$$\epsilon \dot{p}_3 = (Q_{V3} - Q_{31}) \quad (32)$$

where ϵ represents the small volume divided by the bulk modulus.

As Kiani et al. have shown [18], in the case examined Eq. (32) alone satisfies all the conditions required by the singular perturbation theory. Therefore, it is applied only to computation of pressure p_3 only, as follows:

$$p_3 = \begin{cases} \frac{p_1 + \alpha_P p_P}{1 + \alpha_P} & U > 0 \\ \frac{p_1 + \alpha_T p_T}{1 + \alpha_T} & U < 0 \end{cases} \quad (33)$$

where

$$\alpha_P = \left(\frac{UC_V}{C_t} \right)^2 \quad (34)$$

and, in this case, $\alpha_T = \alpha_P$. In Eq. (34), C_V is the semi-empirical coefficient for the directional valve, given in Table 1, and C_t is the semi-empirical coefficient for the throttle valve, computed on the basis of Eq. (21).

While Eq. (33) allows computation of p_3 with an algebraic equation that has an explicit solution, it should be mentioned that the application of the singular perturbation theory to Eq. (29) introduces error to the value computed for volume flow, Q_{31} , since its value depends on p_3 . Therefore, a correction factor is introduced to obtain the correct value of volume flow, and to remove the perturbation effects on the system. The modified flow rate is introduced by simply multiplying the uncorrected value by factor γ :

$$Q_{31} = \begin{cases} \gamma_+ \bar{Q}_{31} & U > 0 \\ \gamma_- \bar{Q}_{31} & U < 0 \end{cases} \quad (35)$$

where, bar symbol denotes the uncorrected variables computed with the perturbation theory, and γ_+ and γ_- are the correction factors, for either side of the spool. Details of the method are presented in [18], but it is still worth noting here that a manual tuning of the correction factors was suggested. The values presented in Table 1 are the final values used in the simulations.

3.3. Combination with a mechanical system

The mechanism, a four-bar linkage actuated by a hydraulic cylinder, as depicted in Fig. 2, consists of rectangular beams with a cross-section of 0.05 m × 0.05 m that have the lengths of $L_1 = L_2 = 1$ m and $L_3 = 2.5$ m, and masses $m_1 = m_2 = 50$ kg and $m_3 = 250$ kg. The bodies are connected via revolute joints and the cut-joint is located at point C. Similarly, the upper end of the cylinder end is attached to the mechanism at the midpoint of body 1, and the lower end, in the global reference coordinate system, at point D at $\mathbf{r}_D = [0 \quad -1 \quad 0]^T$. Gravity is assumed to act in the negative Y direction, and the gravitational constant is $g = 9.81$ m/s².

Total cylinder length $|\mathbf{s}|$ can be expressed as a function of joint coordinates to minimise the problem size. Thereby, the set of integrated variables defining the problem is as follows:

$$\mathbf{x} = [\mathbf{z}^T \quad \mathbf{p}^T]^T \quad (36)$$

where \mathbf{z} contains the relative coordinates of the multibody system and \mathbf{p} contains the pressures. As was demonstrated above, the length of the latter vector is dependent on the method used for hydraulic formulation. In the case of the lumped fluid method, all three pressures are integrated, yielding the three Eqs. (27)–(29). With the singular perturbation theory, in turn, p_3 is computed algebraically via Eq. (33), so the pressure vector has, in this example, a length of two.

The length of the cylinder can be expressed in terms of the relative coordinates as follows:

$$\mathbf{s} = \mathbf{r}_1 - \mathbf{r}_D \quad (37)$$

where \mathbf{r}_1 is the location of the cylinder attachment point in body 1 and \mathbf{r}_D is the location of the cylinder attachment point at ground. The cylinder elongation velocity is required also, and it takes the following form:

$$\dot{s} = \dot{\mathbf{r}}_1 \cdot \frac{\mathbf{s}}{|\mathbf{s}|} \quad (38)$$

Table 2
Initial values.

z_0 [°]	\dot{z}_0 [°/s]	p_0 [Pa]	\dot{p}_0 [Pa/s]
z_1	\dot{z}_1	p_1	\dot{p}_1
z_2	\dot{z}_2	p_2	\dot{p}_2
z_3	\dot{z}_3	p_3	\dot{p}_3

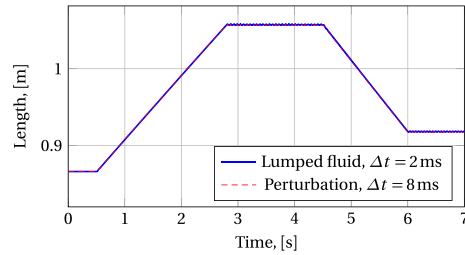


Fig. 4. Cylinder length during the work cycle.

where $\dot{\mathbf{r}}_1$ is the velocity of the attachment point.

Cylinder force F_s can be computed from Eq. (26), and its vector form \mathbf{F}_s , required by the force vector \mathbf{Q}_g , can be obtained as:

$$\mathbf{F}_s = \begin{bmatrix} s_x \\ s_y \\ s_z \end{bmatrix} F_s \quad (39)$$

where s_x , s_y , and s_z are the respective X, Y, and Z components of the cylinder length \mathbf{s} .

Control signal U_{ref} for the directional valve is defined as follows:

$$U_{ref} = \begin{cases} 0 & t < 0.5 \\ 10 & 0.5 \leq t < 2.8 \\ 0 & 2.8 \leq t < 4.5 \\ -10 & 4.5 \leq t < 6 \\ 0 & t \geq 6 \end{cases} \quad (40)$$

Simulations are started from static equilibrium, to avoid instabilities in the simulation process. Table 2 presents the set of initial values used that define a static equilibrium. In the case of the perturbation method, the pressure p_3 and its derivative \dot{p}_3 are excluded from the initial conditions.

4. Results

The proposed method is evaluated with the described example. The seven second work cycle is simulated, and the relative performance is compared to the method proposed in [12]. Since the case example is implemented in Matlab environment, the absolute CPU-times are not shown here. However, the implementation was performed such that comparable times are obtained. The slight differences in the results that were introduced by the use of the singular perturbation method are highlighted.

An overview of the work cycle is given in Fig. 4, wherein the cylinder length during the simulations with both methods is depicted at the largest converged time steps, that is 2 ms for the lumped fluid method and 8 ms for the perturbation method. As can be seen, practically identical results were obtained for the mechanism. Fig. 5, in turn, presents the pressure p_1 in a detail upon valve opening at the same step sizes. It is clear, that the steady-state solution is practically the same between the two hydraulic descriptions, whereas differences occur at the transient phase.

To further illustrate the effects introduced by the use of the singular perturbation method, the volume flow Q_{31} just after the valve opening is depicted in Fig. 6. In addition to the largest converged step sizes, the figure also shows the largest step size with the perturbation method that produced a smooth solution for the studied case, i.e., a solution with $\Delta t = 5$ ms. Slight fluctuation in the lumped fluid solution can be seen at the $28 \times$ magnification. This fluctuation is captured by the integrator, and, as Fig. 7 demonstrates, hence necessitates a larger number of iterations than the proposed method. Similar to the pressures presented in Fig. 5, no significant differences are visible in the steady-state solution.

It must be noted that the accuracy of the correction factors γ_- and γ_+ has a significant effect on the accuracy of them results obtained. Without these factors, error is introduced to the computed volume flow Q_{31} , which propagates to the computed derivative of pressure \dot{p}_1 of Eq. (27). No clear rule to obtain values for the correction factor was observed, so they were tuned manually. These results agree to the work of Kiani et al. [18].

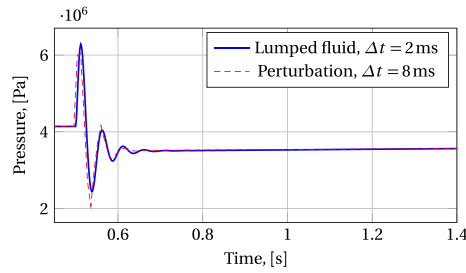


Fig. 5. Pressure p_1 during and after opening of the valve.

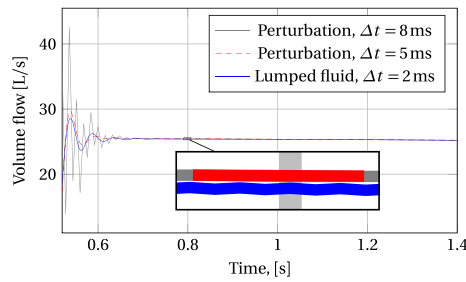


Fig. 6. Volume flow Q_{s1} with the lumped fluid and the perturbation method after opening of the valve.

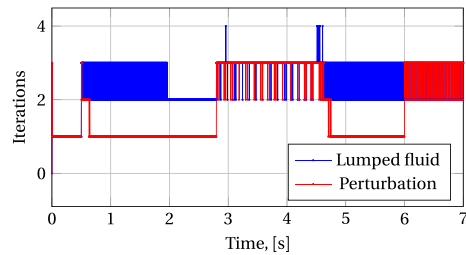


Fig. 7. Number of iterations with the 2 ms time step simulations.

Table 3
Number of iterations and relative CPU-times.

Δt	Iterations - lumped fluid		Iterations - perturbation		CPU-time	
	Avg.	Max.	Avg.	Max.	SP/LL	SP/LL(2 ms)
0.5 ms	1.76	4	1.62	4	0.83	2.34
1 ms	2.26	4	1.76	4	0.71	1.24
2 ms	2.52	4	1.81	3	0.66	0.66
3 ms	fail	fail	1.83	4	-	0.42
5 ms	fail	fail	1.85	3	-	0.27
8 ms	fail	fail	1.90	4	-	0.18

Regarding the efficiency and applicability for real-time applications, Table 3 shows the average and maximum number of iterations required for the convergence, alongside the relative CPU-time between the methods. As can be seen, the lumped fluid method fails to converge under the determined limit of 100 iterations at the experimented time steps larger than 2 ms, whereas convergence properties of the perturbed system do not change meaningfully as the time step increases. Fig. 7, that depicts the number of iterations at 2 ms time step simulations, illustrates the reason for the smaller average number

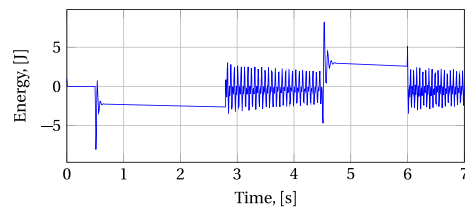


Fig. 8. Energy balance with the perturbation method, at $\Delta t = 8$ ms.

of iterations. As can be seen, the proposed method yields a smaller number of iterations when the valve is fully opened, whereas otherwise the number of iterations is approximately the same or lesser than with the lumped fluid method.

The last two columns in Table 3 give the observed relative CPU-times, computed by dividing the elapsed time with the singular perturbation approach (SP) by that with the lumped fluid method (LL). In the table, the SP/LL column therefore shows the CPU-time relationship at the current step size, and SP/LL(2 ms) is the relative efficiency of the proposed method relative to the fastest simulation with the lumped fluid method. In the former, at 0.5 ms time step the efficiency gain can be explained by the 17% smaller problem size, whereas at the larger step sizes the lower number of iterations take effect. The latter column, in turn, demonstrates the main potential of the singular perturbation method, as the computational time is significantly less than for the fastest converged solution with the lumped fluid method. These results suggest, that use of the singular perturbation method improves the real-time applicability of the method proposed in [12] as it allows larger time steps in cases wherein small volumes exist and it decreases the problem size.

The convergence rate is affected by the penalty factor from Eq. (11) and the integration tolerances. The latter, which are absolute tolerances, are set to 1×10^{-7} for the position-level variables and 1×10^2 for the pressures. Both criteria need to be fulfilled for iteration to stop. Due to the numerical stiffness introduced by the hydraulics, penalty factor, which typically takes values from 1×10^7 to 1×10^9 , had to be increased to 1×10^{11} with both the proposed and the lumped fluid method for good convergence properties to be obtained. This results agrees to [12], and suggests that, while use of the perturbation method allows use of a larger step size and decreases the numerical stiffness, a large penalty factor is still required for good convergence properties to be obtained.

Finally, to check the energy conservation properties of the proposed method, the energy balance of the system at the largest converged time step, 8 ms, is presented in Fig. 8. As can be seen, the energy balance is most of the time less than ± 5 J and even at maximum about 8.1 J. Considered that the actuator work of about 1400 J, these figures are at an acceptable level of accuracy.

5. Conclusions

In this paper, a method for monolithic simulation of multibody and hydraulic dynamics using a penalty-based semi-recursive method and a perturbation method is proposed. The proposed method is compared to monolithic simulation in which the lumped fluid method is coupled with the semi-recursive method. To provide a general approach, a numerically obtained tangent matrix is used in the integration scheme, contrary to the original proposition of the multibody method.

Results indicate that use of the perturbation method in the monolithic simulation of multibody and hydraulic dynamics seems to hold potential, since, when compared to the lumped fluid method, it allows larger step sizes to be taken when small volumes are involved. In addition, again relative to the lumped fluid method, it decreases the computational load by removing the high frequency components of the solution that are introduced by the small volumes. Irrespective of the small scale differences introduced in the solution, the two methods yield practically the same solution. However, more research is needed to find the optimal value for the correction factor required by the perturbation method.

Declarations of interest

None.

Acknowledgments

The authors acknowledge support received for this project from SIM Platform at Lappeenranta University of Technology.

References

- [1] J. Nokka, J.-H. Montonen, E. Bin Baharudin, P. Immonen, A. Rouvinen, L. Laurila, T. Lindh, A. Mikkola, J. Sopenan, J. Pyrhönen, Multi-body simulation based development environment for hybrid working machines, *Int. Rev. Mode. Simult.* 8 (4) (2015) 466–476.
- [2] F. González, M. González, A. Mikkola, Efficient coupling of multibody software with numerical computing environments and block diagram simulators, *Multibody Syst. Dyn.* 24 (3) (2010) 237–253.

- [3] A. Peiret, F. González, J. Kövecses, M. Teichmann, Multibody system dynamics interface modelling for stable multirate co-simulation of multiphysics systems, *Mech. Mach. Theory* 127 (2018) 52–72.
- [4] C.W. Gear, D.R. Wells, Multirate linear multistep methods, *BIT Numer. Math.* 24 (4) (1984) 484–502.
- [5] A. Cardona, M. Geradin, Modeling of a hydraulic actuator in flexible machine dynamics simulation, *Mech. Mach. Theory* 25 (2) (1990) 193–207.
- [6] M.E. Baharudin, A. Rouvinen, P. Korkealaakso, A. Mikkola, Real-time multibody application for tree harvester truck simulator, *Proc. Institut Mech. Eng. Part K* 228 (2) (2014) 182–198.
- [7] G. Sun, J. Liu, Dynamic responses of hydraulic crane during luffing motion, *Mech. Mach. Theory* 41 (11) (2006) 1273–1288.
- [8] M.A. Naya, J. Cuadrado, D. Dopico, U. Ligris, An efficient unified method for the combined simulation of multibody and hydraulic dynamics: Comparison with simplified and Co-integration approaches, *Arch. Mech. Eng.* 58 (2) (2011) 223–243.
- [9] E. Bayo, R. Ledesma, Augmented Lagrangian and mass-orthogonal projection methods for constrained multibody dynamics, *Nonlinear Dyn.* 9 (1–2) (1996) 113–130.
- [10] J. Cuadrado, J. Cardenal, P. Morer, E. Bayo, Intelligent Simulation of Multibody Dynamics: Space-State and Descriptor Methods in Sequential and Parallel Computing Environments, *Multibody Syst. Dyn.* 4 (1) (2000) 55–73.
- [11] J. Watton, *Fluid Power Systems: Modeling, Simulation, Analog and Microcomputer Control*, Prentice-Hall, Inc., 1989.
- [12] J. Rahikainen, A. Mikkola, J. Sopanen, J. Gerstmayr, Combined semi-recursive formulation and lumped fluid method for monolithic simulation of multibody and hydraulic dynamics, *Multibody Syst. Dyn.* (2018).
- [13] J. Cuadrado, D. Dopico, M. Gonzalez, M.A. Naya, A combined penalty and recursive real-time formulation for multibody dynamics, *J. Mech. Des. Trans. ASME* 126 (4) (2004) 602–608.
- [14] A. Callejo, S.H.K. Narayanan, J.G. de Jalón J., B. Norris, Performance of automatic differentiation tools in the dynamic simulation of multibody systems, *Adv. Eng. Softw.* 73 (2014) 35–44.
- [15] A.F. Hidalgo, J. García De Jalón, Real-Time Dynamic Simulations of Large Road Vehicles Using Dense, Sparse, and Parallelization Techniques, *J. Comput. Nonlinear Dyn.* 10 (3) (2015).
- [16] D.E. Bowns, L.M. Wang, The Digital Computation of Pressures in Hydraulic Pipes with Small Volume using an Iterative Technique, *Proc. Institut. Mech. Eng. Part C* 204 (1) (1990) 29–36.
- [17] R. Piché, A. Ellman, Numerical Integration of Fluid Power Circuit Models Using Two-Stage Semi-Implicit Runge-Kutta Methods, *Proc. Institut. Mech. Eng. Part C* 208 (3) (1994) 167–175.
- [18] M. Kiani, A. Mikkola, P. Jalali, Numerical treatment of singularity in hydraulic circuits using singular perturbation theory, *IEEE/ASME Trans. Mechatron.* (2018). Submitted for publication
- [19] A.N. Tikhonov, Systems of differential equations containing small parameters in the derivatives, *Matematicheskii sbornik* 73 (3) (1952) 575–586.
- [20] L. Wang, W.J. Book, J.D. Huggins, Application of singular perturbation theory to hydraulic pump controlled systems, *IEEE/ASME Trans. Mechatron.* 17 (2) (2012) 251–259.
- [21] L. Noethen, S. Walcher, Tikhonovs theorem and quasi-steady state, *Discrete Continuous Dyn. Syst.* 16 (3) (2011) 945–961.
- [22] J. Cuadrado, D. Dopico, M.A. Naya, M. Gonzalez, Real-time multibody dynamics and applications, in: M. Arnold, W. Schiehlen (Eds.), *Simulation Techniques for Applied Dynamics*, Springer Vienna, 2009, pp. 247–311.
- [23] D. Dopico, F. González, J. Cuadrado, J. Kövecses, Determination of holonomic and nonholonomic constraint reactions in an index-3 augmented lagrangian formulation with velocity and acceleration projections, *J. Comput. Nonlinear Dyn.* 9 (4) (2014) 041006.
- [24] K.E. Brenan, S.L. Campbell, L.R. Petzold, *The Numerical Solution of Initial Value Problems in Differential-Algebraic Equations*, Elsevier, 1989.
- [25] H.M. Handroos, M.J. Vilenius, Flexible semi-empirical models for hydraulic flow control valves, *J. Mech. Trans. Autom. Des.* 113 (3) (1991) 232–238.

Publication III

M. Kiani-Oshtorjani, and P. Jalali,

Thermal and Hydraulic Properties of Sphere Packings using a Novel Lattice Boltzmann Model

Reprinted with permission from

International Journal of Heat and Mass Transfer

Vol. 130, pp. 98–108, 2019

© 2019, Elsevier



Contents lists available at ScienceDirect

International Journal of Heat and Mass Transfer

journal homepage: www.elsevier.com/locate/ijhmt

Thermal and hydraulic properties of sphere packings using a novel lattice Boltzmann model



Mehran Kiani Oshtorjani*, Payman Jalali

Laboratory of Thermodynamics, School of Energy Systems, Lappeenranta University of Technology, Lappeenranta, Finland
SIM-Platform, Lappeenranta University of Technology, Lappeenranta, Finland

ARTICLE INFO

Article history:

Received 9 January 2018
Received in revised form 1 October 2018
Accepted 13 October 2018
Available online 24 October 2018

Keywords:

Energy equation
Heat source term
Porosity
Pressure drop

ABSTRACT

A novel LB model is introduced to deal with the thermal and hydraulic properties in porous media. The pressure and density are separated in the proposed incompressible LB model and solid volume fraction is embedded in the formulations. Moreover, a modified thermal LB model is proposed that is shown to be more accurate than the Gue's type of models. This model treats the energy equation with the second order of accuracy without any additional terms. The model is employed in a packing of monodisperse spherical particles within a rectangular channel. The results of new model have been improved as compared to the analytical solution.

© 2018 Elsevier Ltd. All rights reserved.

1. Introduction

Interaction between solid and fluid widely affects the flow pattern in enormous industrial applications such as in porous media and fluidized beds. The solid volume fraction (SVF) ε_s is defined as the ratio of volume occupied by solid to the container volume. It appears in the governing equations of flow and notably influences on the flow characteristics such as pressure drop, velocity components and temperature distribution.

There are two common strategies for modeling porous media. In the first approach, the solid zone is modeled as no-slip zone with all geometric complexities at surface and the fluid flows within the tortuous pore space. This approach provides local details of flow, however, randomly distributed microscopic pores existed in the porous media make the utilization of this approach computationally expensive. In this context, the exclusive geometry of a sample including all voids is needed which can be provided by X-ray photo scanning [1].

Due to complexity of porous media in the microscopic (pore) scales, the alternative approach in the so-called representative elementary volume (REV) scale is usually considered for the classical studies [2]. In this scale, the effects of porosity is constructed by using randomly distributed particles and by adding the fluid-particle drag relations to the Navier-Stokes equations. From modeling point of view, an average SVF should be assigned to any

REV by proper averaging over the pore network within the REV. On the other hand, the drag force is added to the Navier-Stokes equations as a source term that is a function of SVF. There have been proposed many local semiempirical relations in the literature for the drag force [3,4].

The particle packings can be generated via Lagrangian methods, however, the flow and temperature fields are solved using either computational fluid dynamics (CFD), or any other methods such as lattice Boltzmann method (LBM), or smooth particle hydrodynamics (SPH). Among them, LBM has shown a powerful capacity to simulate porous media with either direct and REV scale approaches. It is worth mentioning that there are many LB models proposed for adding source terms in Navier-Stokes equations [5–7].

Guo and Zhao [2] have firstly employed LBM for simulation of incompressible flows through porous media based on the REV scale approach. They added the pre-estimated drag force (Ergun relation) raised from particle-fluid interaction as a source term. In their model, the static pressure is connected to the density and porosity of medium using the relation $p = c_s^2 \rho / \varepsilon$. Therefore, a constant density (incompressible flow) implies that pressure is only a function of pre-known porosity. However, they have assumed that density does not have strictly a constant value $\rho \approx \rho_0$ and it can vary slightly $\rho = \sum f_i$. The variation of density in incompressible flows affects the momentum balance which leads to errors in calculation of pressure drop.

He and Lue [8] suggested an LB model (HL model) in which pressure is separated from density and hence it works for incom-

* Corresponding author.

E-mail addresses: mehran.kiani@lut.fi (M. Kiani Oshtorjani), payman.jalali@lut.fi (P. Jalali).

Nomenclature

\bar{p}	averaged pressure	T	temperature
\bar{u}	averaged velocity	u_x	fluid velocity
η	effective thermal conductivity	δt	lattice time step
η_s	solid thermal conductivity	δx	lattice length unit
μ	fluid dynamic viscosity	τ	relaxation time
ν	fluid kinematic viscosity	τ_T	thermal relaxation factor
ρ_0, ρ_f	fluid density	c_s	sound speed
ρ_s	solid density	d_p	particle diameter
σ	heat capacitance	e_i	discretized fluid particle velocity
ε	fluid volume fraction	F_x	momentum source term
ε_s	solid volume fraction (SVF)	f_i	distribution function
C_p	fluid specific heat	f_i^{eq}	equilibrium distribution function
C_{ps}	solid specific heat	h_i	thermal distribution functions
k_m	ratio of effective thermal conductivity per fluid heat capacitance	h_i^{eq}	thermal equilibrium distribution functions
L	length of porous medium	K	hydraulic permeability of spherical particle packing
p	pressure	Q	energy source term

pressible flows. This model is employed [9] to study the solid-liquid flows by adding a source term into collision operator representing the effects of SVF. However, it cannot directly add the semiempirical relations as a source term.

On the other hand, the heat transfer equation is usually linked to the momentum equation by one way coupling in incompressible flows. On the continuation of proposed model for flow simulation in porous media, Gou and Zhao [10] developed a thermal LB model which is applicable for the fluid saturated porous media. In other words, this model is based on the assumption of local thermal equilibrium (LTE) between solid and saturated fluid which makes a combined thermal governing equation as $\sigma \partial_t T + \nabla_x(Tu_x) = \nabla_x k_m \nabla_x T$, where, σ is a function of SVF ε_s .

Some earlier lattice Boltzmann studies without local thermal equilibrium assumption can be found in [11–13]. Yang et al. [11] investigated the randomness effects of porous media structures composed of either cubes or spheres with different sizes on the flow and heat transfer features. They have used D3Q19 LBM scheme to solve the flow field and D3Q6 scheme to study the thermal behavior of porous media. Wang et al. [12] have used three distribution functions, the one for flow and the two others for the thermal simulations of fluid and solid phases. They have used D2Q9 scheme to validate their model. Gao et al. [13] have extended Guo and Zhao [2] model to simulate porous media under local non-equilibrium thermal conditions. In their work, a three-distribution function LB model has been used to solve the fluid and temperature fields using D2Q9 scheme. In addition, a number of studies have been done in [14–16] considering local thermal non-equilibrium (LTNE) condition with either compressible or incompressible flows.

Unlike Gue's model, a single relation time (SRT) model, Liu and He [17] proposed a multiple relation time (MRT) model. They have argued that MRT models numerically make the algorithm more stable than the Bhatnagar-Gross-Krook (BGK) models. Considering simplicity and cost efficiency of the BGK model, Wang et al. [18] proposed a BGK model (WMG model) enhancing numerical stability at low viscosity and thermal diffusivity. In their model, the external force appears in both momentum and energy equations which links them.

Zheng et al. [19] proposed a model for covering convection diffusion equation in D3Q5 space. This model covers CDE with the second order of accuracy and without any additional terms. However, Chia and Zhao [20] mentioned that this model is not a local model and needs to use their neighborhood information in the col-

lision process. They suggested to use a local scheme for calculation of gradients. Without considering the heat source term and porosity, this model is a special case of WMG model [18].

Chen et al. [21] have mentioned that one of the shortcomings in Guo's like models is associated with their non-reliability for the domains in which heat capacitance σ varies spatially. To overcome this difficulty, they have recently proposed a model (CYZ model) in which σ_0 , which is a constant reference value of σ , is introduced to control heat diffusivity. Using this trick, σ can vary spatially in the investigating domain. One of the most serious problems of this model and other Guo's like thermal models is that they cannot cover the thermal governing equation with the second order of accuracy and without any additional terms. For instance, Chen et al. model covers the equation of $\partial_t(\sigma T) + \nabla \cdot (Tu_x) = \nabla \cdot (k_m \nabla T) + \delta(\tau_T - \frac{1}{2})\partial_t \nabla_x(Tu_x) + O(\delta^2)$ which has the additional term of $\delta(\tau_T - \frac{1}{2})\partial_t \nabla_x(Tu_x)$, or is covered with the first order of accuracy as $\partial_t(\sigma T) + \nabla \cdot (Tu_x) = \nabla \cdot (k_m \nabla T) + O(\delta)$ (see Section 4 for more details).

In this paper, an LB approach is presented for incompressible fluid flow interacting with a solid phase. In this model, density has no effects on the pressure and Ergun equation is added to the momentum equation as a source term. Furthermore, a modified version of CYZ model for thermal LB is proposed which covers the energy equation with the second order of accuracy without any additional terms. Moreover, in the thermal model a heat source term is added.

2. Solid-liquid flow problems

Nithiarasu et al. [22] have derived for the first time the revised formulation of momentum and energy balance valid for porous media in the REV scales as [23,24]:

$$\partial_p \bar{u}_\beta = 0 \quad (1)$$

$$\partial_t \bar{u}_x + \bar{u}_\beta \partial_\beta \left(\frac{\bar{u}_x}{\varepsilon} \right) = - \frac{\varepsilon}{\rho_0} \partial_x (\bar{p}/\varepsilon) + \nu \partial_\beta \partial_\beta \bar{u}_x + F_x \quad (2)$$

$$\partial_t (\sigma T) + \partial_\beta (T \bar{u}_\beta) = \partial_\beta (k_m \partial_\beta T) + Q \quad (3)$$

where u and \bar{p} are averaged velocity and pressure, ρ_0 and ν are fluid density and kinematic viscosity, F_x and Q are source terms for momentum and energy equations, respectively. ε is fluid volume fraction, β is subscript for summation, and α denotes the direction.

It should be mentioned that the above-mentioned energy equation is obtained by combining the energy equations corresponding to solid and fluid. Using this combination, we have $\sigma = \varepsilon + (1 - \varepsilon)(\rho C_p)_s / (\rho C_p)_f$ which is a spatial function of ε . In addition, effective heat diffusivity $k_m = \eta / (\rho C_p)_f$ is the ratio of effective thermal conductivity per fluid heat capacitance.

3. LB formulation for Navier-Stokes equations

In order to transfer the mass and momentum equations to lattice Boltzmann space, the modified standard Boltzmann equation is employed:

$$f_i(x + e_i \delta t, t + \delta t) - f_i(x, t) = \frac{f_i(x, t) - f_i^{eq}(x, t)}{\tau} + T_i \delta t = \Omega_i \quad (4)$$

where e_i is the discretized fluid particle velocity, τ is the relaxation time, f_i is the distribution function, f_i^{eq} is the equilibrium distribution function, δx is the lattice length unit, and δt is the time step. Several relations for $T_i \delta t$ have been proposed for external forces appearing in NS equation. It also works as a correction for the pressure gradient (see Section 3.1 for more details). During the derivation of Navier-Stokes equations from the LB equation using Chapman-Enskog expansion, the following constraints are used:

$$\sum T_i = 0, \quad \sum T_i e_{ix} = n F_x + n(1 - \varepsilon) \nabla p, \quad \sum T_i e_{ix} e_{iy} = 0, \quad (5)$$

which according to them, the following relation have been used:

$$T_i = \frac{W_i n}{c_s^2} e_{id} F_d + \frac{W_i n}{c_s^2} (1 - \varepsilon) e_{id} \partial_d p \quad (6)$$

where the dummy index d is used for getting summation over three dimensions, and c_s is the sound speed. In Eq. (6), $n = 1 - \frac{1}{2\tau}$, p is hydrostatic pressure, ε is the fluid VF, and ω_i are the weighing numbers, which are presented below for three-dimensional grid with nineteen distinct velocities D3Q19:

$$\omega_i = [12 \ 2 \ 2 \ 2 \ 2 \ 2 \ 2 \ 1 \ 1 \ 1 \ 1 \ 1 \ 1 \ 1 \ 1 \ 1 \ 1 \ 1 \ 1 \ 1] / 36 \quad (7)$$

The discrete velocity vectors corresponded to the D3Q19 models have the following directions:

$$\begin{aligned} e_{ix} &= [0 \ 1 \ -1 \ 0 \ 0 \ 0 \ 0 \ 1 \ 1 \ 1 \ 1 \ -1 \ -1 \ -1 \ -1 \ 0 \ 0 \ 0 \ 0] \\ e_{iy} &= [0 \ 0 \ 0 \ 1 \ -1 \ 0 \ 0 \ 1 \ -1 \ 0 \ 0 \ 1 \ -1 \ 0 \ 0 \ 1 \ 1 \ -1 \ -1] \\ e_{iz} &= [0 \ 0 \ 0 \ 0 \ 0 \ 1 \ -1 \ 0 \ 0 \ 1 \ -1 \ 0 \ 0 \ 1 \ -1 \ 1 \ -1 \ 1 \ -1] \end{aligned} \quad (8)$$

It is assumed in BGK LBM models that the collisions of the particles will happen in a way that makes them to go toward an instantaneous relaxation (instantaneous equilibrium). Therefore, after the streaming and collision step, the equilibrium distribution function f_i^{eq} will be used to calculate the macroscopic quantities. The equilibrium distribution function is proposed as:

$$f_i^{eq}(x) = w_i p + w_i c_s^2 \rho_0 \varepsilon \left[3 \frac{e_{ix} \cdot u_x}{c^2} + \frac{9}{2} \frac{(e_{ix} \cdot u_x)^2}{c^4} - \frac{3}{2} \frac{u_x^2}{c^2} \right], \quad (9)$$

in which, ρ_0 is the constant fluid density, u_x is fluid velocity, and $c = \frac{\delta x}{\delta t}$. This relation is proposed to satisfy the following constraints at each time step:

$$p = \sum f_i^{eq} \quad (10)$$

$$c_s^2 \rho_0 \varepsilon u_x = \frac{1}{2} c_s^2 F_x \delta t + \sum e_{ix} f_i^{eq} \quad (11)$$

$$c_s^2 \rho_0 \varepsilon u_x u_y + c_s^2 p \delta_{xy} = \sum e_{ix} e_{iy} f_i^{eq} \quad (12)$$

Using the previous constraints, the velocity and pressure fields are obtained at each time step. Using Chapman-Enskog expansion (see Section 3.1), the model finally covers the Navier-Stokes equation as:

$$\begin{aligned} \frac{\partial(\rho_0 \varepsilon u_x)}{\partial t} + \frac{\partial(\rho_0 \varepsilon u_x u_y)}{\partial x_y} \\ = -\varepsilon \frac{\partial p}{\partial x_x} + \mu \frac{\partial}{\partial x_y} \{ \partial x_y (\varepsilon u_x) + \partial x_x (\varepsilon u_y) + \partial x_y (\varepsilon u_x) \delta_{xy} \} \\ + F_x - \nabla \cdot \partial x_y (u_x u_y u_z) \end{aligned} \quad (13)$$

where the dynamic viscosity is $\mu = c_s^2 \rho_0 (\tau - \frac{1}{2} \delta)$.

3.1. Chapman-Enskog expansion

Starting from the LB formulation, the Navier-Stokes equations are derived in this section using Chapman-Enskog expansion. Considering the following equation:

$$f_i(x + e_i \delta t, t + \delta t) - f_i(x, t) = \frac{f_i(x, t) - f_i^{eq}(x, t)}{\tau} + T_i \delta t = \Omega_i \quad (14)$$

and applying Taylor series expansion, Eq. (15) is obtained:

$$\delta D_i f_i + \frac{\delta}{2} D_i^2 f_i + O(\delta^3) = \Omega_i \quad (15)$$

where $D_i = \partial_t + e_{iy} \frac{\partial}{\partial x_y}$, and δ is either δ_t or δ_x depended on which term it is multiplied.

In the next step, the distribution function as well as derivative operators are decomposed in the scales of $O(\lambda^0)$, $O(\lambda^1)$, and $O(\lambda^2)$ as:

$$\begin{aligned} f_i &= f_i^{(0)} + \lambda f_i^{(1)} + \lambda^2 f_i^{(2)} \\ \partial_t &= \lambda \partial_{t1} + \lambda^2 \partial_{t2} \\ \partial_x &= \lambda \partial_{x1} \\ \Omega_i &= \Omega_i^{(0)} + \lambda \Omega_i^{(1)} + \lambda^2 \Omega_i^{(2)} \\ T_{ii} &= \lambda T_i \end{aligned} \quad (16)$$

and accordingly $D_i = \lambda D_i$.

Substituting operators and variables defined in Eq. (16), into Eq. (15), and separating different scales of lambda λ , the following equations are obtained:

$$O(\lambda^0): \quad f_i^{(0)} = f_i^{(eq)} \quad (17)$$

$$O(\lambda^1): \quad D_i f_i^{(0)} = -\frac{1}{\tau \delta t} f_i^{(1)} + T_{ii} \quad (18)$$

$$O(\lambda^2): \quad \partial_{2t} f_i^{(0)} + (1 - \frac{1}{2\tau}) D_{1t} f_i^{(1)} = -\frac{1}{\tau} \partial_{1t} f_i^{(2)} + \frac{\delta t}{2} D_{1t} T_{1i} \quad (19)$$

Getting summation over Eqs. (18) and (19) for the discrete directions, i.e., $i = 1 : 19$, we have:

$$\partial_{1t} \sum f_i^{(0)} + \partial_{1x} \sum e_{ix} f_i^{(0)} = -\frac{1}{\tau} \partial_{1t} \sum f_i^{(1)} + \sum T_{1i} \quad (20)$$

$$\begin{aligned} \partial_{2t} \sum f_i^{(0)} + (1 - \frac{1}{2\tau})(\partial_{1t} \sum f_i^{(1)} + \partial_{1x} \sum e_{ix} f_i^{(1)}) \\ = -\frac{1}{\tau} \partial_{1t} \sum f_i^{(2)} + \frac{\delta t}{2} (\partial_{1t} \sum T_{1i} + \partial_{1x} \sum e_{ix} T_{1i}) \end{aligned} \quad (21)$$

By the following definitions, the above equation will be more simplified. The definitions are:

$$\begin{aligned} \sum f_i^{(0)} = p, \quad \sum f_i^{(1)} = 0, \quad \sum f_i^{(2)} = 0 \\ \sum e_{ix} f_i^{(0)} = c_s^2 \rho_0 \varepsilon u_x, \quad \sum e_{ix} f_i^{(1)} = m F_{1x} \delta t + m(1 - \varepsilon) \partial_x p \delta t, \\ \sum e_{ix} f_i^{(2)} = 0 \\ \sum e_{ix} e_{ij} f_i^{(0)} = c_s^2 \rho_0 \varepsilon u_x u_j + c_s^2 p \delta_{ij}, \quad \sum e_{ix} e_{ij} f_i^{(1)} = \sum e_{ix} e_{ij} f_i^{(2)} = 0 \\ \sum T_{1i} = 0, \quad \sum e_{ix} T_{1i} = n F_{1x} + n(1 - \varepsilon) \partial_x p, \quad \sum e_{ix} e_{ij} T_{1i} = 0 \end{aligned} \quad (22)$$

Therefore, Eq. (20) is simplified to $\partial_{1t} \sum f_i^{(0)} + \partial_{1x} \sum e_{ix} f_i^{(0)} = 0$ and Eq. (21) to $\partial_{2t} \sum f_i^{(0)} = (\frac{1}{2} n - (1 - \frac{1}{2\tau}) m) (\partial_{1x} F_{1x} + (1 - \varepsilon) \partial_x p)$. Thus, assuming $n = 2(1 - \frac{1}{2\tau}) m$ and adding two simplified equations with their coefficients of λ and λ^2 yields the following equation:

$$(\lambda \partial_{1t} + \lambda^2 \partial_{2t}) \sum f_i^{(0)} + \lambda \partial_{1x} \sum e_{ix} f_i^{(0)} = 0 \quad (23)$$

Consequently, using the definitions of (16) and (22), Eq. (23) is simplified to:

$$\frac{1}{c_s^2} \partial_t(p) + \partial_x(\rho_0 \varepsilon u_x) = 0 \Rightarrow \partial_x(\rho_0 \varepsilon u_x) \approx 0 \quad (24)$$

On the other hand, by multiplying Eqs. (18) and (19) by e_{ix} and getting summation over the discrete directions, the following equations are derived:

$$\partial_{1t} \sum e_{ix} f_i^{(0)} + \partial_{1\beta} \sum e_{ix} e_{i\beta} f_i^{(0)} = -\frac{1}{\tau} \partial_{1t} \sum e_{ix} f_i^{(1)} + \sum e_{ix} T_{1i} \quad (25)$$

$$\begin{aligned} \partial_{2t} \sum e_{ix} f_i^{(0)} + (1 - \frac{1}{2\tau})(\partial_{1t} \sum e_{ix} f_i^{(1)} + \partial_{1\beta} \sum e_{ix} e_{i\beta} f_i^{(1)}) \\ = -\frac{1}{\tau} \partial_{1t} \sum e_{ix} f_i^{(2)} + \frac{\delta t}{2} (\partial_{1t} \sum e_{ix} T_{1i} + \partial_{1\beta} \sum e_{ix} e_{i\beta} T_{1i}) \end{aligned} \quad (26)$$

By taking $n = 2(1 - \frac{1}{2\tau}) m$ as it is already assumed, $(1 - \frac{1}{2\tau}) \sum e_{ix} f_i^{(1)} = \frac{m}{2} \sum e_{ix} T_{1i}$. Then, using this relation and the definitions presented in Eq. (22), Eq. (26) is simplified as:

$$\partial_{2t} \sum e_{ix} f_i^{(0)} + (1 - \frac{1}{2\tau}) \partial_{1\beta} \sum e_{ix} e_{i\beta} f_i^{(1)} = \frac{\delta t}{2} \partial_{1\beta} \sum e_{ix} e_{i\beta} T_{1i} \quad (27)$$

Considering Eq. (18) and multiplying it by $e_{ix} e_{i\beta}$ the following relation is obtained:

$$\begin{aligned} -\frac{1}{\tau} \partial_{1\beta} \sum e_{ix} e_{i\beta} f_i^{(1)} + \delta t \partial_{1\beta} \sum e_{ix} e_{i\beta} T_{1i} \\ = \delta t \partial_{1\beta} (\partial_{1t} \sum e_{ix} e_{i\beta} f_i^{(0)} + \partial_{1\gamma} \sum e_{ix} e_{i\beta} e_{i\gamma} f_i^{(0)}) \end{aligned} \quad (28)$$

Using definitions of Eq. (22), in which $\sum e_{ix} e_{i\beta} T_{1i} = 0$, and combining Eqs. (27) and (28) yield:

$$\partial_{2t} \sum e_{ix} f_i^{(0)} = \tau (1 - \frac{1}{2\tau}) \delta t \partial_{1\beta} (\partial_{1t} \sum e_{ix} e_{i\beta} f_i^{(0)} + \partial_{1\gamma} \sum e_{ix} e_{i\beta} e_{i\gamma} f_i^{(0)}) \quad (29)$$

Multiplying Eq. (25) by λ and Eq. (29) by λ^2 and adding them results to below equation:

$$\begin{aligned} (\lambda \partial_{1t} + \lambda^2 \partial_{2t}) \sum e_{ix} f_i^{(0)} + \lambda \partial_{1\beta} \sum e_{ix} e_{i\beta} f_i^{(0)} \\ = \lambda^2 \tau (1 - \frac{1}{2\tau}) \delta t \partial_{1\beta} (\partial_{1t} \sum e_{ix} e_{i\beta} f_i^{(0)} + \partial_{1\gamma} \sum e_{ix} e_{i\beta} e_{i\gamma} f_i^{(0)}) \\ + \lambda (-\frac{m}{\tau} + n) (F_{1x} + (1 - \varepsilon) \partial_x p) \end{aligned} \quad (30)$$

By finding the values of $m = c_s^2 \delta t / 2$ and $n = c_s^2 (1 - 1/2\tau)$ which satisfy both relations of $n = 2(1 - \frac{1}{2\tau}) m$ and $-\frac{m}{\tau} + n = c_s^2$, and by referring to the definitions of Eq. (16), Eq. (30) is then simplified to:

$$\begin{aligned} \partial_t \sum e_{ix} f_i^{(0)} + \partial_\beta \sum e_{ix} e_{i\beta} f_i^{(0)} \\ = (\tau - \frac{1}{2}) \delta t \partial_{1\beta} (\partial_{1t} \sum e_{ix} e_{i\beta} f_i^{(0)} + \partial_{1\gamma} \sum e_{ix} e_{i\beta} e_{i\gamma} f_i^{(0)}) \\ + c_s^2 F_x + c_s^2 (1 - \varepsilon) \partial_x p \end{aligned} \quad (31)$$

Considering the definitions presented in Eq. (22) and the equality of $\partial_{1t} \sum e_{ix} e_{i\beta} f_i^{(0)} = -\partial_{1\gamma} u_x u_\beta u_\gamma$, we have:

$$\begin{aligned} \partial_t (c_s^2 \rho_0 \varepsilon u_x) + \partial_\beta (c_s^2 \rho_0 \varepsilon u_x u_\beta) \\ = -\varepsilon c_s^2 \partial_x p + v \partial_\beta (\partial_\beta (c_s^2 \rho_0 \varepsilon u_x) + \partial_x (c_s^2 \rho_0 \varepsilon u_\beta) + \partial_\gamma (c_s^2 \rho_0 \varepsilon u_\gamma) \delta_{x\beta}) \\ + c_s^2 F_x - \partial_\beta (\partial_\gamma u_x u_\beta u_\gamma) \end{aligned} \quad (32)$$

where $v = c_s^2 (\tau - \frac{1}{2}) \delta t$. By dividing the above equation by c_s^2 and neglecting the last right hand side term, which is very small, the momentum equations are derived as:

$$\begin{aligned} \partial_t (\rho_0 \varepsilon u_x) + \partial_\beta (\rho_0 \varepsilon u_x u_\beta) \\ = -\varepsilon \partial_x p + v \partial_\beta (\partial_\beta (\rho_0 \varepsilon u_x) + \partial_x (\rho_0 \varepsilon u_\beta) + \partial_\gamma (\rho_0 \varepsilon u_\gamma) \delta_{x\beta}) + F_x \end{aligned} \quad (33)$$

It should be highlighted here that u_x and p are fluid velocity and pressure which are related to averaged velocity and pressure as $\bar{u}_x = \varepsilon u_x$, and $\bar{p} = \varepsilon p$. Using these definitions and considering continuity equation, Eq. (33) will be alternatively reform as:

$$\begin{aligned} \partial_t \bar{u}_x + \bar{u}_\beta \partial_\beta (\frac{\bar{u}_x}{\varepsilon}) = -\frac{\varepsilon}{\rho_0} \partial_x (\bar{p} / \varepsilon) + v \partial_\beta (\partial_\beta (\rho_0 \bar{u}_x) + \partial_x (\rho_0 \bar{u}_\beta) \\ + \partial_\gamma (\rho_0 \bar{u}_\gamma) \delta_{x\beta}) + F_x \end{aligned} \quad (34)$$

4. LB formulation for energy equation

For covering the energy equation of (3), the following LB equation is proposed:

$$\begin{aligned} h_i(x + e_i \delta t, t + \delta t) = \gamma h_i(x, t) + (1 - \gamma) h_i(x + e_i \delta t, t) \\ + \frac{h_i(x, t) - h_i^{eq}(x, t)}{\tau_T} + Q_i \delta t \end{aligned} \quad (35)$$

in which, h_i^{eq} and h_i denote equilibrium and non-equilibrium distribution functions, respectively, τ_T is thermal relaxation factor, and Q_i is the heat source term. The equilibrium distribution function h_i^{eq} will be calculated using the following relation at each timer step:

$$h_i^{eq}(x) = \begin{cases} T(\sigma - \sigma_0) + w_i T(\sigma_0 + \frac{\varepsilon u_x}{c_s^2 \lambda}) & i = 0 \\ w_i T(\sigma_0 + \frac{\varepsilon u_x}{c_s^2 \lambda}) & i \neq 0 \end{cases} \quad (36)$$

Moreover, for having the thermal source term in the D3Q19 framework, the following equation (Eq. (37)) is proposed. This relation is obtained by considering a time independent thermal source term and assuming $\sum Q_i = Q$ which guarantees the full achievement of the energy equation Eq. (3) by using Chapman-Enskog expansion as presented in Section 4.1.

$$Q_i = Q \frac{10w_i - c_s^2}{10 - 19c_s^2}$$

4.1. Chapman-Enskog expansion

Considering the following equation:

$$h_i(x + e_i \delta t, t + \delta t) = \chi h_i(x, t) + (1 - \chi) h_i(x + e_i \delta t, t) + \frac{h_i(x, t) - h_i^{eq}(x, t)}{\tau_T} + Q_i \delta t \tag{37}$$

and applying Taylor series expansion in it, we have:

$$\delta D_t h_i + \frac{\delta^2}{2} D_t^2 h_i = (1 - \chi) \left(\delta (e_i \cdot \nabla_1) h_i + \frac{\delta^2}{2} (e_i \cdot \nabla_1)^2 h_i \right) + \frac{h_i(x, t) - h_i^{eq}(x, t)}{\tau_T} + Q_i \delta t \tag{38}$$

Therefore, the following relations are obtained using the definitions in (16):

$$O(\lambda^0) : h_i^{(0)} = h_i^{(eq)} \tag{40}$$

$$O(\lambda^1) : (\partial_{1t} + \chi e_i \cdot \nabla_1) h_i^{(0)} = -\frac{1}{\tau \delta} h_i^{(1)} + Q_{1i} \tag{41}$$

$$O(\lambda^2) : \partial_{2t} h_i^{(0)} + (1 - \frac{1}{2\tau}) D_{1i} h_i^{(1)} + (\chi - 1) \left(\delta (e_i \cdot \nabla_1) h_i^{(1)} + \frac{\delta^2}{2} (e_i \cdot \nabla_1)^2 h_i^{(1)} \right) = -\frac{1}{\tau \delta} h_i^{(2)} \tag{42}$$

Substituting $h_i^{(1)}$ from Eq. (41) into Eq. (42) and considering a time independent thermal source term, the following relation is achieved:

$$O(\lambda^2) : \partial_{2t} h_i^{(0)} + \delta \left((-\tau_T + \frac{1}{2}) \partial_{1t}^2 + (\frac{\chi}{2} - \tau_T \chi^2) (e_i \cdot \nabla_1)^2 \right) + (-2\chi \tau_T + 1) \partial_{1t} e_i \cdot \nabla_1 h_i^{(0)} = -\frac{1}{\tau \delta} h_i^{(2)} \tag{43}$$

Getting summation over the summation of Eqs. (40) and (43) as $\sum (\lambda O(\lambda) + \lambda^2 O(\lambda^2))$ and using the definitions in (16), the final form of equation is obtained as:

$$\partial_t \sum h_i^{(0)} + \chi \nabla \cdot \sum e_{ix} h_i^{(0)} + \delta \left((-\tau_T + \frac{1}{2}) \partial_t (\sum h_i^{(0)}) + (\frac{\chi}{2} - \tau_T \chi^2) \nabla \cdot \nabla (\sum e_i e_i h_i^{(0)}) \right) + (-2\chi \tau_T + 1) \partial_t \nabla \cdot (\sum e_i h_i^{(0)}) + O(\delta^2) = \sum Q_i \tag{44}$$

By making the following definitions:

$$\sum h_i^{(0)} = \sigma T, \quad \sum h_i^{(0)} e_{ix} = \frac{T u_x}{\chi}, \quad \sum h_i^{(0)} e_{ix} e_{i\beta} = c_s^2 \sigma_0 T \delta_{x\beta} \tag{45}$$

we obtain:

$$\partial_t (\sigma T) + \nabla_x (T u_x) + \delta \left((-\tau_T + \frac{1}{2}) \partial_t (\partial_t (\sigma T)) + (\frac{\chi}{2} - \tau_T \chi^2) \nabla \cdot \nabla (c_s^2 \sigma_0 T \delta_{x\beta}) + \frac{(-2\chi \tau_T + 1)}{\chi} \partial_t \nabla_x (T u_x) \right) + O(\delta^2) = Q \tag{46}$$

which can be rewritten as:

$$\partial_t (\sigma T) + \nabla_x (T u_x) + \delta \left((-\tau_T + \frac{1}{2}) \partial_t (\partial_t (\sigma T) + \nabla_x (T u_x)) + (\frac{\chi}{2} - \tau_T \chi^2) \nabla \cdot \nabla (c_s^2 \sigma_0 T \delta_{x\beta}) + \left(\frac{-2\chi \tau_T + 1}{\chi} + (\tau_T - \frac{1}{2}) \right) \partial_t \nabla_x (T u_x) \right) + O(\delta^2) = Q \tag{47}$$

According to Eq. (47), the following relations are valid:

$$\partial_t (\sigma T) + \nabla_x (T u_x) + O(\delta) = Q \tag{48}$$

$$\partial_t (\sigma T) + \nabla_x (T u_x) = \delta \left(\tau_T \chi^2 - \frac{\chi}{2} \right) c_s^2 \nabla \cdot (\sigma_0 \nabla T) + \delta \left(\frac{2\chi \tau_T - 1}{\chi} - (\tau_T - \frac{1}{2}) \right) \partial_t \nabla_x (T u_x) + O(\delta^2) = Q \tag{49}$$

It should be mentioned here that by setting $\beta = 1$ the CYZ model is obtained in which there is an additional term of $\delta \left(\frac{2\chi \tau_T - 1}{\chi} - (\tau_T - \frac{1}{2}) \right) \partial_t \nabla_x (T u_x)$ which makes the equation to be covered with the first order of accuracy $O(\delta)$. However, by equating $\frac{2\chi \tau_T - 1}{\chi} - \tau_T + \frac{1}{2} = 0$, χ is obtained as: $\chi = 1 / (0.5 + \tau_T)$ which covers the equation with the second order of accuracy $O(\delta^2)$ and without any additional term as:

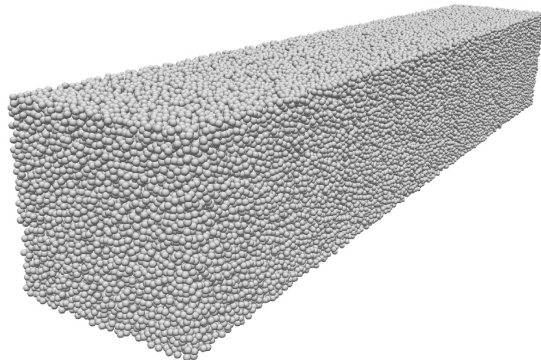


Fig. 1. Illustration of porous media with $\epsilon_p = 0.2$.

$$\partial_t(\sigma T) + \nabla \cdot (\overline{Tu_x}) = \nabla \cdot (k_m \nabla T) + Q \quad (50)$$

where $k_m = \delta c_p^2 (\tau_f \beta^2 - \frac{\rho}{2}) \sigma_0$.

Finally, based on the definitions presented in Eq. (45), the equilibrium distribution function is proposed as:

$$h_i^{eq}(x) = \begin{cases} T(\sigma - \sigma_0) + w_i T(\sigma_0 + \frac{e_{ix} u_x}{c_p^2 \lambda}) & i = 0 \\ w_i T(\sigma_0 + \frac{e_{ix} u_x}{c_p^2 \lambda}) & i \neq 0 \end{cases} \quad (51)$$

5. Porous media

There are generally three different flow regimes occurring in the porous media, namely the Darcy, Forchheimer, and turbulent regimes. Darcy regime refers to the regime of creeping flow, and the pressure gradient is proportional to dynamic viscosity and flow velocity. The coefficient of proportionality is the inverse of hydraulic permeability. The pressure drop across a porous medium made of spherical particles is calculated as:

$$\frac{\Delta P}{Lu} = \frac{\mu}{K} \quad (52)$$

where L is the length of porous medium, u is velocity, μ is dynamic viscosity, $K = \frac{\varepsilon^3 d_p^2}{36 \kappa (1 - \varepsilon)^2}$ denotes the hydraulic permeability of spherical particle packing, ε is the porosity of the packing, and d_p is particle diameter.

On the other hand, the flow is still laminar in Forchheimer flow regime, however, not creeping. It is considered as the transient

regime from the Darcy to turbulent regime in which the pressure drop is proposed by the formula given in Eq. (53).

$$\frac{\Delta P}{Lu} = \frac{\mu}{K} + \frac{\rho F}{\sqrt{K}} |u| \quad (53)$$

in which, $F = 1.75 / \sqrt{150 \varepsilon^3}$ represents the form drag.

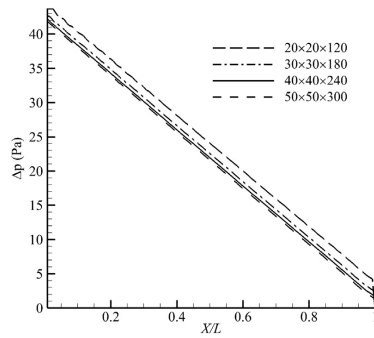


Fig. 3. Grid study for 20 × 20 × 120 (long dashed line), 30 × 30 × 180 (dot dashed line), 40 × 40 × 240 (solid line), 50 × 50 × 300 (dashed line).

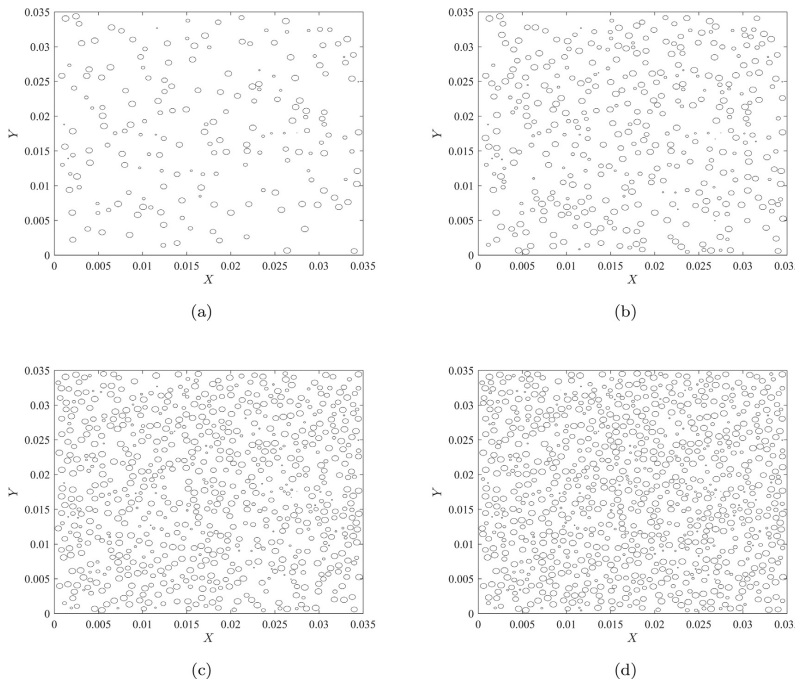


Fig. 2. Slice planes at the middle of domain for different solid VFs (a) $\varepsilon = 0.05$, (b) $\varepsilon = 0.1$ (c) $\varepsilon = 0.2$ (d) $\varepsilon = 0.25$.

5.1. Results and discussion

The domain of study is shown in Fig. 1 which its dimensions are $35 \times 35 \times 210 \text{ mm}^3$. The velocity boundary condition is applied for

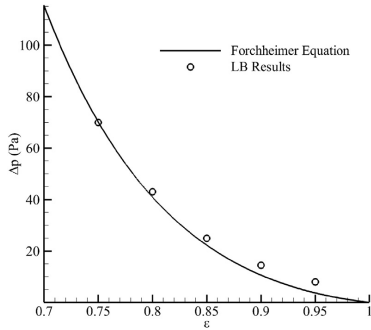


Fig. 4. Comparison of pressure drop obtained with LB (circular symbols) and Forchheimer equation, Eq. (53) (solid line) for the velocity of $u = 0.3 \text{ m/s}$.

the right boundary (inlet), where the left side is set to pressure outlet boundary condition. Other boundaries are considered as walls with no-slip boundary condition. The flowing fluid is air with density and kinematic viscosity of $\rho_f = 1.225 \text{ kg/m}^3$ and $\nu_f = 1.84 \times 10^{-5} \text{ m}^2/\text{s}$. The porous material is chosen as copper with density, specific heat, and thermal conductivity of $\rho_s = 8978$, $C_{ps} = 381 \text{ J}/(\text{kg} \cdot \text{K})$, and $\eta_s = 387.6 \text{ W}/(\text{m} \cdot \text{K})$, respectively.

The effects of porosity is usually modeled by considering particles randomly distributed in a container. The drag force acting on particles has a local semiempirical equation which includes the VF of solid and fluid. For any number of generated particles (with a certain SVF), the size of averaging control volume for SVF is taken as 10–15 LB nodes.

For the sake of validation of LBM results, they are compared to those obtained from theoretical approach as well as the results of commercial package. In this concern, ANSYS-FLUENT v.17.0 is used which works based on finite volume method (FVM). The settings of the model are made to handle laminar flow coupled with energy equation. The domain is defined as a porous medium through cell zone conditions. Then the porous zone permeability is introduced in the model. A heat source term in energy equation is also introduced. Note that the geometry and all other settings, including the air properties, the porous media properties, the value of heat

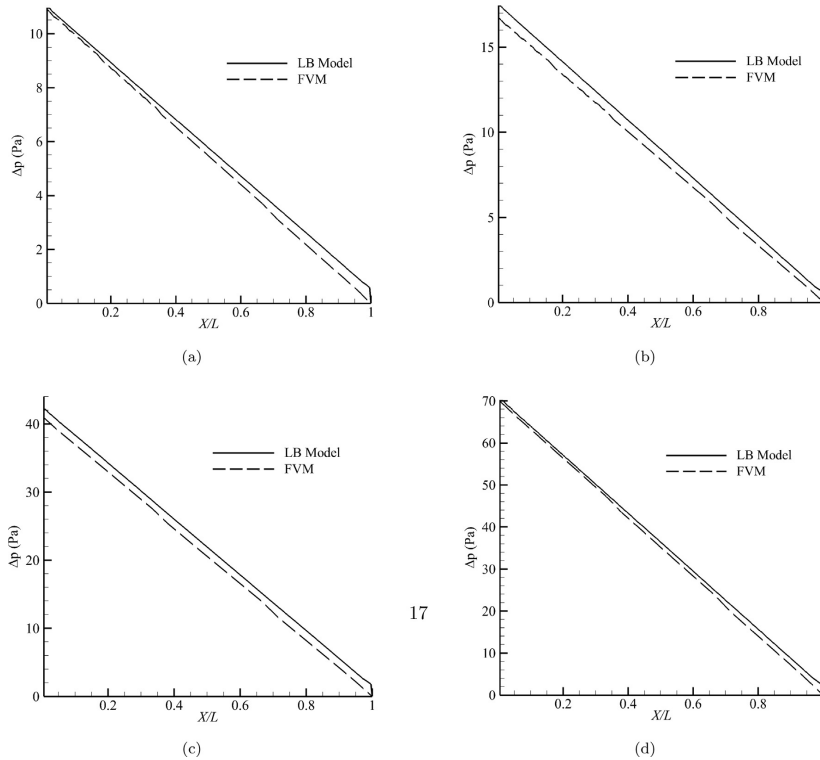


Fig. 5. Comparison of pressure drop obtained with LB model (solid line) and FVM (dashed line), (a) $\epsilon_s = 0.2$, $u = 0.1 \text{ m/s}$ (b) $\epsilon_s = 0.25$, $u = 0.1 \text{ m/s}$ (c) $\epsilon_s = 0.2$, $u = 0.3 \text{ m/s}$ (d) $\epsilon_s = 0.25$, $u = 0.3 \text{ m/s}$.

source term, the initial and boundary conditions are set the same as in the LBM.

The particles embedded in the domain are depicted in Fig. 1 which is sketched for SVF of $\epsilon_s = 0.2$. In addition, the slices across solid zone at the middle of domain are illustrated in Fig. 2a–d for different SVFs.

5.2. Pressure drop

In order to verify the suitability of the grid used in this study, we have examined different grid resolutions. The physical conditions are considered to be same for all grids. The length of porous medium is set to $L = 0.21$ m, inlet velocity as $u = 0.3$ m/s, and its porosity was varied between 0 and 0.25 in different cases. In order to have a reasonable comparison, the pressures drop through the porous media of different grids are plotted in Fig. 3 versus dimensionless length at the same time step. According to this figure, the grid corresponding to $40 \times 40 \times 210$ is appropriate for taking pressure drop values.

As the first validation case, the calculated pressure drops are compared to Forchheimer equation in Fig. 4. The validation study is performed for the SVF values of 0.05, 0.1, 0.15, 0.2 and 0.25. The inlet velocity is set to $u = 0.3$ m/s and gravity is activated. Fig. 4 shows that the LB has predicted the pressure drop values closely to the Forchheimer equation. The smallest difference between

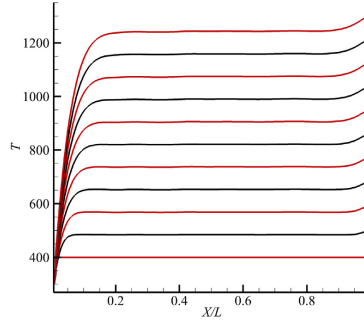


Fig. 7. The cross-sectional mean temperature variation from the LB solution along the porous medium for the case in which source term is applied over the entire domain for different times as 0, 98, 196, 294, 392, 490, 589, 687, 785, 883, 981 μ s. The lowest line with $T = 400$ K corresponds to $t = 0$ and the successive lines upward represent the other times.

the LB solution and the Forchheimer equation for pressure drop corresponds to the highest value of SVF, that is $\epsilon_s = 0.25$. This is due to the implementation of Ergun equation in the LB code which

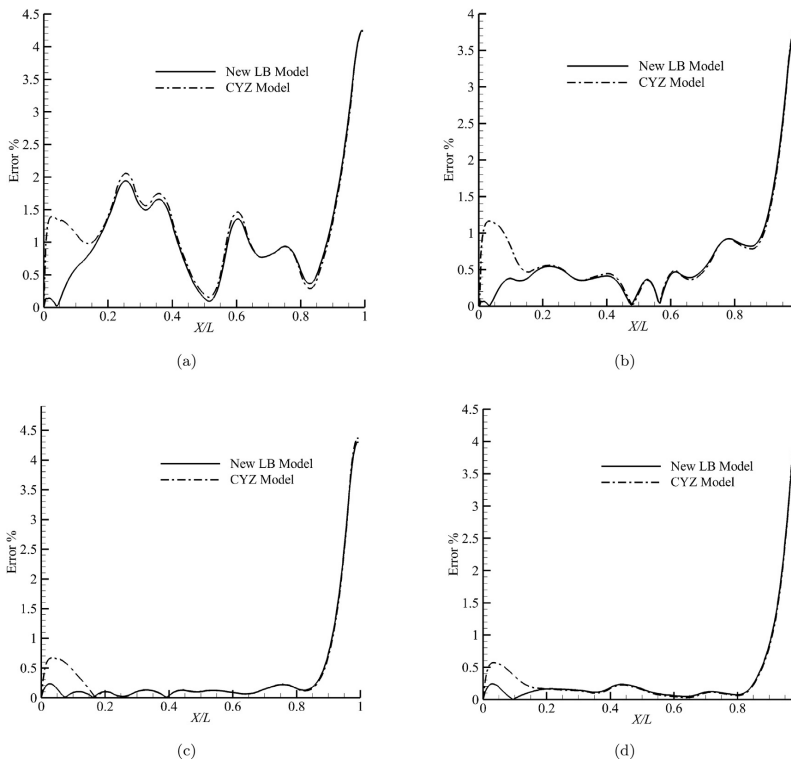


Fig. 6. The temperature error defined as a difference between CYZ (dot-dashed line) or modified model (solid line) and theoretical solution for different VFs (a) $\epsilon_s = 0.05$ (b) $\epsilon_s = 0.1$ (c) $\epsilon_s = 0.2$ (d) $\epsilon_s = 0.25$.

predicts pressure drop more accurately in higher packing fractions. LB results slightly shift above the Forchheimer prediction over the porosity of 0.8 such that the LB prediction becomes about 10 Pa, which is twice as the prediction of Eq. (53) at the porosity of 0.05. It should be noted that the predictions of FVM and LB for total pressure drop nearly coincide. Thus the data related to the FVM results are not shown in Fig. 4. Instead, the differences of the FVM and LB can be observed in the profiles of pressure, which is discussed in Fig. 5 as follows.

The pressure drop profiles from the LB and FVM are compared in two different SVFs and velocities in Fig. 5a–d, which display good agreement with each other. As anticipated, higher velocity and SVF lead to higher pressure drop through porous medium. It can be noted that the LB profile is slightly shifted upward, while the total pressure drop remains the same for the two approaches. The amount of the shift hardly reaches to 2 Pa. At the SVF of 0.2, increasing the velocity from 0.1 to 0.3 m/s boosts the shift from 0.5 to 2 Pa though the total pressure drop rises about 4 times. At

the SVF of 0.25, similar ratio of pressure drop can be observed between the two velocities, while the shift remains below 2 Pa.

5.3. Temperature distribution

Considering a one way coupling between momentum and energy equations, temperature field is solved. The materials are chosen as air and copper for the fluid and solid phases, respectively. The initial temperature of porous media is set to 400 K, whereas the inlet fluid temperature is 300 K. The walls are insulated and there is not any temperature gradient at the outlet. The inlet velocity and SVF are set as $u = 0.3$ m/s and $\epsilon_p = 0.2$, respectively. The heat source term is activated and its value is 5×10^6 w/m³, which is applied in two possible ways as follows.

In the first way of applying heat source, the corresponding term is applied over the entire domain. For the sake of comparison of CYZ and modified models, the same problem is analytically solved as presented in Appendix A. Therefore, both models are compared to analytical solution with the relative error defined as:

$$\text{Error} = 100 \frac{|T_{LB} - T_{Theory}|}{T_{Theory}} \quad (54)$$

The temperature distribution errors of CYZ and modified LB models are compared for different SVF values in Fig. 6a–d. As these figures indicate, the modified model has smaller error than the CYZ model especially at the front side of porous domain where the temperature rapidly increases. In the rest of porous domain, the temperature remains approximately uniform as Fig. 7 reveals and thus the errors coincide in that region. Note that higher SVF yields smaller relative errors.

In the second way of applying heat source, the related term is only applied in the cells located within the thin layer from $X = 0.23L$ to $X = 0.27L$. The temperature distribution obtained by the modified model is depicted in Fig. 8 in various times. Moreover, the temperature distribution within porous medium is compared to the results of the CYZ model as well as the finite volume method (FVM) in Fig. 9a. In addition, the differences between the results of either CYZ model or FVM and the modified LB model are defined as the errors depicted in Fig. 9b.

According to Fig. 9a, FVM could not capture the temperature gradient existed in the entrance region of porous medium. Its relative error with respect to the modified LB model is about 29 per-

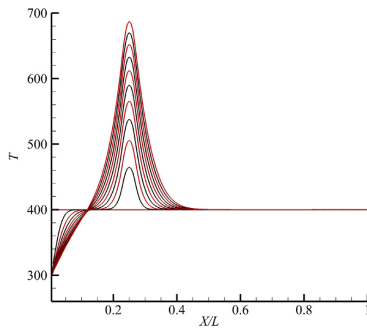


Fig. 8. The cross-sectional mean temperature variation from the LB solution along the porous medium for the case in which source term is applied in the cells located within the thin layer from $X = 0.23L$ to $X = 0.27L$. Different lines correspond to the times 0.98, 196, 392, 490, 589, 687, 785, 883, 981 μ s. The lowest line with $T = 400$ K corresponds to $t = 0$ and the successive lines upward represent the other times.

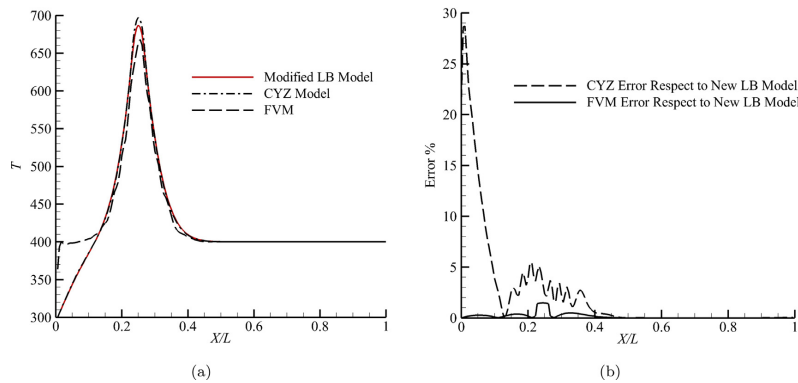


Fig. 9. Solution and relative errors corresponded with case 2 for different methods (a) Comparison of CYZ model (dot-dashed line), new LB model (solid line), and FVM (dashed line) (b) Relative error between CYZ and new LB models (solid line), and between FVM and new LB model (dashed line).

cent in this region. As Fig. 9b indicates, the maximum difference between the CYZ and the modified LB models is about 2 percent at the location of the heat source. In contrast, the FVM relative error at the same position is about 5 percent. In the rest of the porous domain, the temperature is predicted to be constant equal to the initial temperature by all three methods.

6. Conclusion

The pressure drop calculated by a proposed LB model is validated by analytical formulas and FVM method. In addition, the thermal LB model is introduced to cover the energy equation with the second order of accuracy and without any additional terms. The higher accuracy of the proposed model with respect to other Gue's like models is verified by comparing the relative errors of the new model and the CYZ model. Meanwhile, the proposed heat source term is tested and validated in two different ways. The results presented in this paper confirms that the modified LB model introduced here is capable of capturing the hydrodynamics and thermal features of porous media made of monodisperse spheres. In principle, this method can be extended to any other particle packings made of particles of different shape, size and packing properties, which will constitute future extension of this study.

Acknowledgment

The authors would like to acknowledge the financial support for this work by the SIM-Platform at LUT, and also Academy of Finland under Grant No. 311138.

Appendix A. Analytical solution of energy equation

Here, the energy equation Eq. (3) is analytically solved. The heat conductivity of particles is high in our studied porous media that is consistent with that of copper. Therefore, the cross-sectional variation of temperature can be considered negligible. Moreover, the mean fluid velocity component within any cross-section perpendicular to the flow direction is negligible due to the side boundary conditions and the fact that the solid phase particles are uniformly distributed. Therefore, noting that the temperature is not varying within any cross-section, the temperature gradient is considered to be negligible in all directions perpendicular to the flow direction. Consequently, the energy equation can be rewritten as:

$$\bar{\sigma} \partial_t T + \bar{u}_x \partial_x T = k_m \partial_x^2 T + Q_d \tag{A1}$$

where \bar{u} and $\bar{\sigma}$ are averaged velocity and sigma over cross-section area of porous media. The initial and boundary conditions of the problem are as below:

$$\begin{aligned} T(x, 0) &= T_0 \\ T(0, t) &= T_i \\ \partial_x T(\infty, t) &= 0 \end{aligned} \tag{A2}$$

Using dimensionless parameters of $\xi = \bar{u}x/k_m, \zeta = \bar{u}^2 t / (\bar{\sigma} k_m)$, and $\theta = \frac{T-T_0}{T_i-T_0}$, Eq. (A1) reforms as:

$$\partial_t \theta + \partial_\xi \theta = \partial_\xi^2 \theta + Q_d \tag{A3}$$

where $Q_d = \frac{Q_d}{\bar{u}^2 (T_i - T_0)}$. This equation is simplified by introducing the solution of Eq. (A3) as $\theta(\xi, \zeta) = e^{(\zeta-2\xi)/4} K(\xi, \zeta)$ [25]. Consequently, the simplified version of energy equation is presented below:

$$\partial_\zeta K = \partial_\xi^2 K + Q_d e^{(\zeta-2\xi)/4} \tag{A4}$$

with initial and boundary conditions of:

$$\begin{aligned} K(\xi, 0) &= 0 \\ K(0, \zeta) &= 1 \\ \partial_\xi K(\infty, \zeta) + K(\infty, \zeta)/2 &= 0 \end{aligned} \tag{A5}$$

The above equation is solved by applying Laplace transform technique. Getting Laplace transform over ζ and considering initial condition of problem, κ which is the Laplace transition of K is obtained as:

$$\kappa = C_1 e^{\xi\sqrt{s}} + C_2 e^{-\xi\sqrt{s}} + Q_d \frac{e^{-\xi/2}}{(s-1/4)^2} \tag{A6}$$

where C_1 and C_2 are constant to be determined by applying boundary conditions. Considering boundary conditions, κ is rewritten as:

$$\kappa = \frac{e^{-\xi\sqrt{s}}}{s-1/4} - Q_d \frac{e^{-\xi\sqrt{s}}}{(s-1/4)^2} + Q_d \frac{e^{-\xi/2}}{(s-1/4)^2} \tag{A7}$$

Finally, K is obtained by getting inverse Laplace transform of κ as (see Ref. [26] for advanced inverse Laplace transforms):

$$\begin{aligned} K(\xi, \zeta) &= \frac{1}{2} \left(e^{(\zeta-2\xi)/4} \operatorname{erfc}\left(\frac{\xi}{2\sqrt{\zeta}} - \frac{\sqrt{\zeta}}{2}\right) + e^{(\zeta+2\xi)/4} \operatorname{erfc}\left(\frac{\xi}{2\sqrt{\zeta}} + \frac{\sqrt{\zeta}}{2}\right) \right) \\ &\quad - \frac{Q_d}{2} e^{\xi/4} \left((\zeta - \xi) e^{-\xi/2} \operatorname{erfc}\left(\frac{\xi}{2\sqrt{\zeta}} - \frac{\sqrt{\zeta}}{2}\right) \right. \\ &\quad \left. + (\zeta + \xi) e^{\xi/2} \operatorname{erfc}\left(\frac{\xi}{2\sqrt{\zeta}} + \frac{\sqrt{\zeta}}{2}\right) \right) + Q_d e^{\zeta(\zeta-2\xi)/4} \end{aligned} \tag{A8}$$

where erfc is complementary error function, which is defined as $\operatorname{erfc}(x) = 1 - \operatorname{erf}(x)$. Eventually, the temperature distribution is in the form of:

$$\begin{aligned} T(x, t) &= T_0 + \frac{T_i - T_0}{2} \left(\operatorname{erfc}\left(\sqrt{\frac{\bar{\sigma}}{k_m}} \frac{x}{2\sqrt{t}} - \frac{\sqrt{\bar{\sigma} k_m}}{u} \frac{\sqrt{t}}{2}\right) \right. \\ &\quad \left. + e^{\bar{u}x/k_m} \operatorname{erfc}\left(\sqrt{\frac{\bar{\sigma}}{k_m}} \frac{x}{2\sqrt{t}} + \frac{\sqrt{\bar{\sigma} k_m}}{u} \frac{\sqrt{t}}{2}\right) \right) \\ &\quad - \frac{Q_d (T_i - T_0)}{2} \left(\frac{\bar{u}^2 t}{\bar{\sigma} k_m} - \frac{\bar{u}x}{k_m} \right) \operatorname{erfc}\left(\sqrt{\frac{\bar{\sigma}}{k_m}} \frac{x}{2\sqrt{t}} - \frac{\sqrt{\bar{\sigma} k_m}}{u} \frac{\sqrt{t}}{2}\right) \\ &\quad + \left(\frac{\bar{u}^2 t}{\bar{\sigma} k_m} + \frac{\bar{u}x}{k_m} \right) e^{\bar{u}x/k_m} \operatorname{erfc}\left(\sqrt{\frac{\bar{\sigma}}{k_m}} \frac{x}{2\sqrt{t}} + \frac{\sqrt{\bar{\sigma} k_m}}{u} \frac{\sqrt{t}}{2}\right) \\ &\quad + Q_d \frac{\bar{u}^2 (T_i - T_0)}{\bar{\sigma} k_m} t \end{aligned} \tag{A9}$$

References

- [1] M. Liu, Y. Shi, J. Yan, Y. Yan, Lattice Boltzmann simulation of flow and heat transfer in random porous media constructed by simulated annealing algorithm, *Appl. Therm. Eng.* 115 (2017) 1348–1356, <https://doi.org/10.1016/j.applthermaleng.2016.12.107>.
- [2] Z. Guo, T.S. Zhao, Lattice Boltzmann model for incompressible flows through porous media, *Phys. Rev. E* 66 (2002) 1–9, <https://doi.org/10.1103/PhysRevE.66.036304>.
- [3] S. Ergun, Fluid flow through packed columns, *Chem. Eng. Prog.* 48 (1952) 89–94.
- [4] D. Nihad, B. Özer, M. Özdemir, Experimental flow in various porous media and reconciliation of Forchheimer and Ergun relations, *Exp. Thermal Fluid Sci.* 57 (2014) 425–433, <https://doi.org/10.1016/j.expthermflusc.2014.06.011>.
- [5] Z. Guo, C. Zheng, B. Shi, Discrete lattice effects on the forcing term in the lattice Boltzmann method Zhaoli, *Phys. Rev. E* 65 (2002) 1–6, <https://doi.org/10.1103/PhysRevE.65.046308>.
- [6] S. Farnoush, M.T. Manzari, An investigation on the body force modeling in a lattice Boltzmann BGK simulation of generalized Newtonian fluids, *Phys. A* 415 (2014) 315–332, <https://doi.org/10.1016/j.physa.2014.08.014>.
- [7] J.M. Buick, C.A. Greated, Gravity in a lattice Boltzmann model, *Phys. Rev. E* 61 (5) (2000) 5307.
- [8] X. He, L.-S. Luo, Lattice Boltzmann model for the incompressible Navier–Stokes equation, *J. Stat. Phys.* 88 (3) (1997) 927–944, <https://doi.org/10.1023/B:JOS5.0000015179.12689.e4>.
- [9] J.R. Third, Y. Chen, C.R. Müller, Comparison between finite volume and lattice-Boltzmann method simulations of gas-fluidised beds: bed expansion and

- particle-fluid interaction force, *Comput. Particle Mech.* 3 (3) (2016) 373–381, <https://doi.org/10.1007/s40571-015-0086-z>.
- [10] Z. Guo, T.S. Zhao, A lattice Boltzmann model for convection heat transfer in porous media, *Numer. Heat Transf.* 47 (2005) 157–177, <https://doi.org/10.1080/10407790590883405>.
- [11] P. Yang, Z. Wen, R. Dou, X. Liu, Heat transfer characteristics in random porous media based on the 3D lattice Boltzmann method, *Int. J. Heat Mass Transf.* 109 (2017) 647–656, <https://doi.org/10.1016/j.ijheatmasstransfer.2017.01.126>.
- [12] L. Wang, Z. Zeng, L. Zhang, H. Xie, G. Liang, Y. Lu, A lattice Boltzmann model for thermal flows through porous media, *Appl. Therm. Eng.* 108 (2016) 66–75, <https://doi.org/10.1016/j.applthermaleng.2016.07.092>.
- [13] D. Gao, Z. Chen, L. Chen, A thermal lattice Boltzmann model for natural convection in porous media under local thermal non-equilibrium conditions, *Int. J. Heat Mass Transf.* 70 (2014) 979–989, <https://doi.org/10.1016/j.ijheatmasstransfer.2013.11.050>.
- [14] A. Amiri, K. Vafai, Transient analysis of incompressible flow through a packed bed, *Int. J. Heat Mass Transf.* 41 (24) (1998) 4259–4279.
- [15] A.V. Kuznetsov, K. Vafai, Analytical comparison and criteria for heat and mass transfer models in metal hydride packed beds, *Int. J. Heat Mass Transf.* 38 (15) (1995) 2873–2884.
- [16] M. Sözen, K. Vafai, Analysis of oscillating compressible flow through a packed bed, *Int. J. Heat Fluid Flow* 12 (2) (1991) 130–136.
- [17] Q. Liu, Y.-I. He, Double multiple-relaxation-time lattice Boltzmann model for solid-liquid phase change with natural convection in porous media, *Phys. A* 438 (2015) 94–106, <https://doi.org/10.1016/j.physa.2015.06.018>.
- [18] L. Wang, J. Mi, Z. Guo, A modified lattice Bhatnagar–Gross–Krook model for convection heat transfer in porous media, *Int. J. Heat Mass Transf.* 94 (2016) 269–291, <https://doi.org/10.1016/j.ijheatmasstransfer.2015.11.040>.
- [19] H.W. Zheng, C. Shu, Y.-T. Chew, A lattice Boltzmann model for multiphase flows with large density ratio, *J. Comput. Phys.* 218 (1) (2006) 353–371.
- [20] Z. Chai, T.S. Zhao, Lattice Boltzmann model for the convection-diffusion equation, *Phys. Rev. E* 87 (6) (2013) 63309, <https://doi.org/10.1103/PhysRevE.87.063309>.
- [21] S. Chen, B. Yang, C. Zheng, A lattice Boltzmann model for heat transfer in porous media, *Int. J. Heat Mass Transf.* 111 (2017) 1019–1022, <https://doi.org/10.1016/j.ijheatmasstransfer.2017.04.054>.
- [22] P. Nithiarasu, K.N. Seetharamu, T. Sundararajan, Natural convective heat transfer in a fluid saturated variable porosity medium, *Int. J. Heat Mass Transf.* 40 (16) (1997) 3955–3967, [https://doi.org/10.1016/S0017-9310\(97\)00008-2](https://doi.org/10.1016/S0017-9310(97)00008-2).
- [23] P. Nithiarasu, K.N. Seetharamu, T. Sundararajan, Effect of porosity on natural convective heat transfer in a fluid saturated porous medium, *Int. J. Heat Fluid Flow* 19 (1998) 56–58, [https://doi.org/10.1016/S0142-727X\(97\)10008-X](https://doi.org/10.1016/S0142-727X(97)10008-X).
- [24] W. Zhong, M. Zhang, B. Jin, Z. Yuan, Flow behaviors of a large spout-fluid bed at high pressure and temperature by 3D simulation with kinetic theory of granular flow, *Powder Technol.* 175 (2) (2007) 90–103.
- [25] K. Yu, Analytical modeling of transient heat transfer coupled with fluid flow in heavy oil reservoirs during thermal recovery Processes (2014).
- [26] D. Vieru, C. Fetecau, C. Fetecau, N. Nigar, Magneto-hydrodynamic natural convection flow with Newtonian Heating and Mass Diffusion over an Infinite Plate that applies shear stress to a viscous fluid, *Z. Naturforsch. A* 69 (12) (2014) 714–724, <https://doi.org/10.5560/ZNA.2014-0068>.

Publication IV

M. Kiani-Oshtorjani, and P. Jalali,

Thermal discrete element method for transient heat conduction in granular packing under compressive forces

Reprinted with permission from

International Journal of Heat and Mass Transfer

Vol. 145, 2019

© 2019, Elsevier



Contents lists available at ScienceDirect

International Journal of Heat and Mass Transfer

journal homepage: www.elsevier.com/locate/ijhmt

Thermal discrete element method for transient heat conduction in granular packing under compressive forces

Mehran Kiani-Oshtorjani^{a,b,*}, Payman Jalali^{a,b}^aLaboratory of Thermodynamics, School of Energy Systems, Lappeenranta University of Technology, Lappeenranta, Finland^bSIM-Platform, Lappeenranta University of Technology, Lappeenranta, Finland

ARTICLE INFO

Article history:

Received 17 June 2019
 Received in revised form 6 September 2019
 Accepted 17 September 2019
 Available online 26 September 2019

Keywords:

Energy equation
 Discrete element method
 Granular packed bed
 Temperature distribution
 Heat conduction

ABSTRACT

A thermal discrete element method is introduced in granular packs. This method is applicable to 3D packing in either static or dynamic states coupled with the ordinary discrete element method code. This method resolves the local heat fluxes and temperature of particles relying on particles conductivity and the deformation of particles at various contact points. Using this method, the time evolution of temperature is studied within packed beds under various compressive forces. Our results match very well with the analytical solution as if the value of the effective conductivity is properly adjusted, which is found to be related to the pressure exponentially. We have also shown that the compression of the granular packing exponentially increases the thermal characteristic time of the bed.

© 2019 Elsevier Ltd. All rights reserved.

1. Introduction

Granular materials are found extensively in nature as well as industrial processes from energy, food processing, manufacturing and chemical technologies. In the technologies related to the energy production in packed beds or fluidized beds, the thermal performance of plants is directly linked to the behaviour of the particulate medium as the main carrier of thermal energy controlled by the known mechanisms of conduction, convection and radiation.

Granular materials have been theoretically studied using both the Eulerian and Lagrangian approaches. The Eulerian approach treats the granular medium as a continuum. The interactions of existing phases (gas-solid or solid-solid) within a control volume are represented by proper correlations that specify an average volumetric estimation of forces. There have been a number of studies adopting Eulerian methods, e.g. Jalali et al. [1] for modelling the hydrodynamics of circulating fluidized beds using multiphase Eulerian method, as well as Kiani-Oshtorjani and Jalali [2] for modelling the hydrodynamic and thermal characteristics of packed beds using a novel lattice Boltzmann method. Other alternatives to the Eulerian approach to simulate heat transfer between

granular particles are finite element method (FEM) [3,4] and lattice element method (LEM) [5,6].

Unlike the continuum description of particulate systems in Eulerian approach, the Lagrangian approach sees individual particles and tracks them every time step. The well-known Lagrangian approach applied extensively in simulations of granular materials is the discrete element method (DEM) that is used to build static packs, Suikkanen et al. [7], or to analyze the dynamics of particle mixtures, Jalali and Hyppänen [8].

The thermal analysis of packed beds is performed by solving the energy equation for particles configuration subject to proper boundary conditions. Siu and Lee [9] assigned each particle a uniform temperature given at its center. In this approach known as the thermal network, a number of heat pipes are assumed between particles through which heat fluxes transport to other particles. There is a thermal resistance for each connection (contact). As Feng et al. [10] mentioned, this model mostly relies on an ad-hoc manner, not on a theoretical base.

Feng et al. [10,11] suggested a 2D model based on the boundary element method (BEM), which first resolved the steady state and then the transient condition inspired by the thermal network method. They presented an analytical solution to the energy equation at steady state for an individual particle subject to the Neumann boundary condition. Then they assigned an accurate temperature to the particle using a boundary integral method. The heat fluxes were obtained from the contacts of particle with neighbouring particles. Their work was limited to 2D space as they

* Corresponding author at: Laboratory of Thermodynamics, School of Energy Systems, Lappeenranta University of Technology, Lappeenranta, Finland.

E-mail addresses: mehran.kiani@lut.fi (M. Kiani-Oshtorjani), payman.jalali@lut.fi (P. Jalali).

Nomenclature

α_T	thermal diffusivity [$\frac{m^2}{s}$]	σ	Poisson's ratio
\bar{m}	reduced mass [kg]	θ	angle [rad]
\bar{Q}_{jP}	flux on contact j of particle P [W]	c_p	specific heat capacity [$\frac{J}{kg \cdot K}$]
α_i	angular acceleration [$\frac{1}{s^2}$]	d	particle diameter [m]
\mathbf{a}_i	linear acceleration [$\frac{m}{s^2}$]	E	Young's modulus [Pa]
\mathbf{e}_n	unit vector in n direction	G	shear modulus [Pa]
\mathbf{e}_t	unit vector in t direction	I_i	moment of inertia $kg \cdot m^2$
\mathbf{g}	gravity acceleration [$\frac{m}{s^2}$]	K_n	spring stiffness in n direction [$\frac{N}{m}$]
\mathbf{v}_r	relative velocity [$\frac{m}{s}$]	K_t	spring stiffness in t direction [$\frac{N}{m}$]
\mathbf{v}_s	relative slip velocity [$\frac{m}{s}$]	L	length of bed [m]
δ_m	mean overlap [m]	m_i	particle mass [kg]
δ_n	normal overlap [m]	P_f	Legendre polynomials
δ_t	tangential displacement [m]	P_{fg}	associated Legendre polynomials
η_n	damping coefficient in n direction [$\frac{Ns}{m}$]	q	heat flux [$\frac{W}{m^2}$]
η_t	damping coefficient in t direction [$\frac{Ns}{m}$]	R_c	packed bed radius [m]
κ_p	heat conductivity of particle P [$\frac{W}{m \cdot K}$]	R_p	particle radius [m]
κ_{eff}	effective thermal conductivity of bed [$\frac{W}{m \cdot K}$]	S_i	surface area of contact i [m^2]
μ	friction coefficient	T	temperature [K]
ϕ	angle [rad]	T_p^0	temperature at the center of particle P [K]
ρ	particle density [kg/m^3]	T_p	temperature at contact i of particle P [K]

admitted they could not find any integral solution for 3D geometries.

He et al. [12] proposed a numerical manifold method (NMM) to model transient heat conduction in granular materials. In this model, some elementary geometries like circles, squares, or their combinations are defined to inscribe the particles known as mathematical covers. Then using the intersections between particles and mathematical covers, some manifold elements are extracted. The manifold elements are defined without any overlap between the elements. It is argued in that paper that unlike FEM as a continuum approach, and thermal discrete element method (TDEM) as a discrete approach, the NMM can describe both continuum and discrete views to the problem. In other words, this model resembles the FEM, where, the temperature step changes at contact interfaces are included in the model, too.

In the studies of heat conduction in granular materials, the effective thermal conductivity (ETC) of the packed bed is a characteristic quantity. There are a number of studies to obtain this parameter theoretically [13–15], computationally [3], or experimentally [16–18].

Liang [19,14] utilized the thermal resistance presented by Feng et al. [10] to derive a theoretical formula for the ETC. They applied the formula to a 2D packed bed under a uniform strain. This formula was obtained based on a parallel-column model in which the granular bed was constructed by particle columns. Then the ETC of each column was obtained from the corresponding thermal resistance. The ETC of entire bed was calculated from the ETC of each column.

Kovalev and Gusarov [20] presented theoretical relation for ETC based on statistical mechanics. They also simulated the thermal behaviour of different packed beds consisted of different particle shapes. They employed the thermal resistance proposed by Feng et al. [10] for 2D problems to calculate the heat flux between particles.

The aim of the present paper is to introduce a thermal DEM approach for resolving transient heat conduction in 3D granular packing. The results of this study present the propagation of heat in different packed beds under various compressive pressures.

2. Thermal discrete element method

This section contains the derivation of TDEM. It starts with finding a steady-state solution to the heat conduction equation. By adding the transient term to the balance equation, the transient heat transfer equation will be obtained.

2.1. Solution of heat conduction equation

Our starting point for TDEM is to find an analytical solution to the Laplace equation (heat conduction) in spherical coordinate system. This equation is written with the Neumann boundary condition on the boundary $\partial\Omega$ in the spherical domain Ω as:

$$\begin{aligned} \kappa_p \nabla^2 T &= 0 \quad \text{in } \Omega \\ \kappa_p \frac{\partial T}{\partial n} &= q(\theta, \phi) \quad \text{on } \partial\Omega \end{aligned} \quad (1)$$

where θ and ϕ are the spherical angular coordinates as depicted in Fig. 1a, q is heat flux, and κ stands for the thermal conductivity of particles. The solution of the Laplace equation in spherical coordinate system can be obtained based on separation of variables as:

$$T(r, \theta, \phi) = \sum_{f=0}^{\infty} \sum_{g=0}^f \left(A_f r^f + \frac{B_f}{r^{f+1}} \right) P_{fg}(\cos\phi) (C_g \sin(g\theta) + D_g \cos(g\theta)) + T_p^0 \quad (2)$$

where f and g are the summation indices, T_p^0 is the temperature at the center of particle P , and the functions P_{fg} are Legendre polynomials.

Considering the azimuthally symmetric case where T does not depend on θ , i.e. $g = 0$, and the boundary condition at the center of sphere leading to $B_f = 0$, Eq. (2) is simplified as:

$$T(r, \phi) = \sum_{f=0}^{\infty} A_f r^f P_f(\cos(\phi)) + T_p^0 \quad (3)$$

where, the coefficients A_f should be determined based on the boundary condition on $\partial\Omega$ which finally yields:

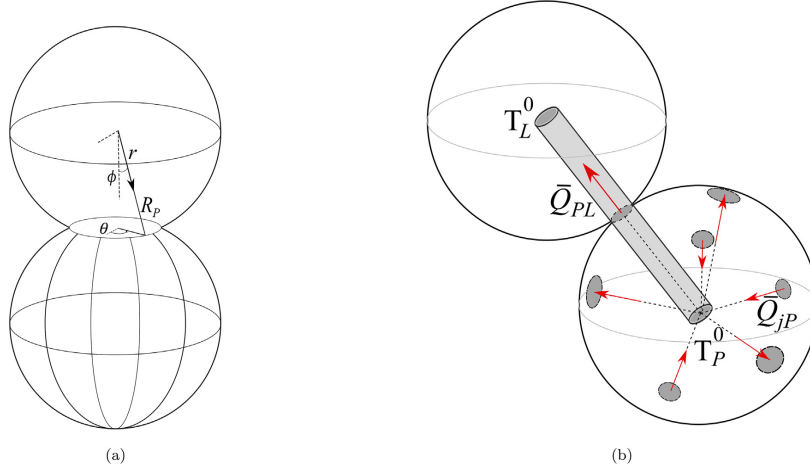


Fig. 1. Schematic of (a) contacting particles in spherical coordinate system (b) the pipe model connecting contact areas to the center of particles.

$$A_f = \frac{2f+1}{2fR_p^{f-1}\kappa} \int_0^\pi q(\psi)P_f(\cos(\psi))\sin(\psi)d\psi \quad (4)$$

By substituting Eq. (4) into (3), we obtain:

$$T(r, \phi) = \frac{R_p}{\kappa_p} \int_0^\pi q(\psi)\sin(\psi) \sum_{m=1}^\infty \frac{2m+1}{2m} \left(\frac{r}{R_p}\right)^m P_m(\cos\psi)P_m(\cos\phi) d\psi + T_p^0 \quad (5)$$

The mean temperature \$T_p^i\$ on the \$i\$-th contact, and the flux \$\bar{Q}_{jP}\$ on any contact \$j\$ can be calculated as:

$$T_p^i = \frac{1}{S_i} \int_{S_i} T_p(\theta, \phi)dS = \frac{2\pi R_p^2}{S_i} \int_0^{\phi_i} T_p^i(\phi)\sin(\phi)d\phi \quad (6)$$

$$\bar{Q}_{jP} = 2\pi R_p^2 \int_{\phi_{j1}}^{\phi_{j2}} q_{jP}(\phi)\sin\phi d\phi \quad (7)$$

where \$S_i\$ is the surface area of contact \$i\$, and \$\phi_{j1}\$ and \$\phi_{j2}\$ are the angles characterizing the influential region of contact \$j\$ in the direction \$\phi\$. In Eq. (6), \$T_p^i(\phi)\$ is the temperature distribution over the contact surface \$i\$ of particle \$P\$ obtained from Eq. (5) after substituting \$r = R_p\$ and breaking the integral to the summation over influential regions of all the contacts (covering the entire surface of particle), which yields:

$$T_p^i(\phi) = \frac{R_p}{\kappa_p} \sum_{j=1}^k \int_{\phi_{j1}}^{\phi_{j2}} q_{jP}(\psi)\sin(\psi) \sum_{m=1}^\infty \frac{2m+1}{2m} P_m(\cos\psi)P_m(\cos\phi) d\psi d\phi + T_p^0 \quad (8)$$

As a result, the mean temperature on contact \$i\$ can be estimated by combining Eqs. (8) and (6):

$$T_p^i = \frac{2\pi R_p^2}{S_i} \frac{R_p}{\kappa_p} \sum_{j=1}^k \int_0^{\phi_{j1}} \int_{\phi_{j1}}^{\phi_{j2}} q_{jP}(\psi)\sin(\psi)\sin(\phi) \times \sum_{m=1}^\infty \frac{2m+1}{2m} P_m(\cos\psi)P_m(\cos\phi) d\psi d\phi + T_p^0 \quad (9)$$

By assuming a constant flux for each contact \$q_{jP}(\psi) = \bar{q}_{jP}\$, Eq. (7) will be:

$$\bar{Q}_{jP} = S_j \bar{q}_{jP} = 2\pi R_p^2 \bar{q}_{jP} (\cos(\phi_{j1}) - \cos(\phi_{j2})) \quad (10)$$

and using the identity of \$\cos(2x) = 1 - 2\sin^2(x)\$ we have:

$$\begin{aligned} \bar{Q}_{jP} &= 4\pi R_p^2 \bar{q}_{jP} \left(\sin^2\left(\frac{\phi_{j2}}{2}\right) - \sin^2\left(\frac{\phi_{j1}}{2}\right) \right) \\ &= 4\pi R_p^2 \bar{q}_{jP} \left(\sin\left(\frac{\phi_{j2}}{2}\right) - \sin\left(\frac{\phi_{j1}}{2}\right) \right) \left(\sin\left(\frac{\phi_{j2}}{2}\right) + \sin\left(\frac{\phi_{j1}}{2}\right) \right) \end{aligned} \quad (11)$$

then, by considering \$\phi_{j2} = \phi_{j1} + \Delta\phi_j\$ and using the identity of \$\sin\left(\frac{\phi_{j2}}{2}\right) = \sin\left(\frac{\phi_{j1}}{2} + \frac{\Delta\phi_j}{2}\right) = \sin\left(\frac{\phi_{j1}}{2}\right)\cos\left(\frac{\Delta\phi_j}{2}\right) + \sin\left(\frac{\Delta\phi_j}{2}\right)\cos\left(\frac{\phi_{j1}}{2}\right) \approx \sin\left(\frac{\phi_{j1}}{2}\right) + \frac{\Delta\phi_j}{2}\cos\left(\frac{\phi_{j1}}{2}\right)\$, Eq. (11) simplifies to:

$$\bar{Q}_{jP} = 2\pi R_p^2 \bar{q}_{jP} \Delta\phi_j \cos\left(\frac{\phi_{j1}}{2}\right) \left(\sin\left(\frac{\phi_{j2}}{2}\right) + \sin\left(\frac{\phi_{j1}}{2}\right) \right) \quad (12)$$

Substituting \$q_{jP}\$ from Eq. (12) into Eq. (9) yields:

$$T_p^i = \sum_{j=1}^k \left[\frac{R_p \bar{Q}_{jP}}{\kappa_p S_i \Delta\phi_j \cos\left(\frac{\phi_{j1}}{2}\right) \left(\sin\left(\frac{\phi_{j1}}{2}\right) + \sin\left(\frac{\phi_{j2}}{2}\right) \right)} \times \int_0^{\phi_i} \int_{\phi_{j1}}^{\phi_{j2}} \sin(\psi)\sin(\phi) \sum_{m=1}^\infty \frac{2m+1}{2m} P_m(\cos\psi)P_m(\cos\phi) d\psi d\phi \right] + T_p^0 \quad (13)$$

Christoffel-Darboux identity [21] guarantees that \$\sum_{m=1}^\infty (2m+1)P_m(\cos\psi)P_m(\cos\phi)\$ converges to \$-1\$, hence, \$\sum_{m=1}^\infty \frac{2m+1}{2m} P_m(\cos\psi)P_m(\cos\phi)\$ will converge to a negative constant \$\lambda\$, which is computationally obtained as \$-0.6846\$. Consequently, Eq. (13) can be simplified as:

$$T_p^i = \sum_{j=1}^k \frac{R_p \bar{Q}_{jP} \lambda}{\kappa_p S_i \Delta\phi_j \cos\left(\frac{\phi_{j1}}{2}\right) \left(\sin\left(\frac{\phi_{j1}}{2}\right) + \sin\left(\frac{\phi_{j2}}{2}\right) \right)} \times \int_{\phi_{j1}}^{\phi_{j2}} \sin(\psi) \int_0^{\phi_i} \sin(\phi) d\phi d\psi + T_p^0 \quad (14)$$

Eventually, by using $S_i = \pi R_p^2 \sin^2(\phi_i) \approx \pi R_p^2 \phi_i^2$ and $\int_0^{\phi_i} \sin(\phi) d\phi = 1 - \cos(\phi_i) = 2\sin^2(\frac{\phi_i}{2}) \approx \frac{\phi_i^2}{2}$, we can reduce Eq. (14) to:

$$T_p^i = \sum_{j=1}^k \frac{\bar{Q}_{LP} \lambda}{2\kappa_p \pi R_p \Delta\phi_j \cos(\frac{\phi_{j1}}{2}) \left(\sin(\frac{\phi_{j1}}{2}) + \sin(\frac{\phi_{j2}}{2}) \right)} \int_{\phi_{j1}}^{\phi_{j2}} \sin(\psi) d\psi + T_p^0 \quad (15)$$

2.2. Two particle pipe model

For a central particle making several contacts with its neighbouring particles, we note that Eq. (15) determines the temperature of any contact area i based on all the contacts of the central particle. The main idea behind the two-particle pipe thermal model is to take into account the accumulative effects from the contacting particles on the temperature of contact i . In other words, the heat is exchanged between contact areas and the center of particle P , where all the fluxes contribute in building up any of heat fluxes exchanged between the contact area i and the central particle P as shown in Fig. 1b. In the pipe model, a pipe is attached to each contact through which a heat flux is transferred between the neighbouring particle and the central particle. In addition, the share of any contact j on T_p^i depends on the contact position represented by $\frac{\int_{\phi_{j1}}^{\phi_{j2}} \sin(\psi) d\psi}{\cos(\frac{\phi_{j1}}{2}) \left(\sin(\frac{\phi_{j1}}{2}) + \sin(\frac{\phi_{j2}}{2}) \right)}$ in Eq. (15) assuming that \bar{Q}_{LP} and $\Delta\phi_j$ are in the same order for all contacts. Thus, effective values of these two quantities can be introduced for the contact i and taken out of the summation. This simplifies Eq. (15) to the following equation:

$$T_p^i = \frac{\bar{Q}_{LP} \lambda}{2\kappa_p \pi R_p \Delta\phi_i} \sum_{j=1}^k \frac{\int_{\phi_{j1}}^{\phi_{j2}} \sin(\psi) d\psi}{\cos(\frac{\phi_{j1}}{2}) \left(\sin(\frac{\phi_{j1}}{2}) + \sin(\frac{\phi_{j2}}{2}) \right)} + T_p^0 \quad (16)$$

in which the value of $\sum_{j=1}^k \frac{\int_{\phi_{j1}}^{\phi_{j2}} \sin(\psi) d\psi}{\cos(\frac{\phi_{j1}}{2}) \left(\sin(\frac{\phi_{j1}}{2}) + \sin(\frac{\phi_{j2}}{2}) \right)}$ is computationally calculated to be π . Note that ϕ_{j1} and ϕ_{j2} correspond to the contact j .

Eventually, Eq. (16) reaches to a final form after substituting the summation by π , which results in:

$$T_p^i = \frac{\bar{Q}_{LP} \lambda}{2\kappa_p R_p \Delta\phi_i} + T_p^0 \quad (17)$$

As a result, one can consider a pipe with the heat flow \bar{Q}_{LP} and thermal resistance of $Re_p = \frac{\lambda}{2\kappa_p R_p \Delta\phi_i}$ in the particle P side connecting the centers of two particles. According to this definition of the thermal resistance Re_p , it is inversely proportional to the deformation angle characterized by $\Delta\phi_i$. Equivalently, the effective conductivity between particles increases proportional to the deformation angle.

Consider two particles P and L assuming $T_p^0 > T_L^0$ and write the conservation equation for thermal energy. The direction of energy flux is from particle P toward particle L across the contact areas i and m of particles P and L , respectively. Thus the temperature at the i -th contact of particle P , T_p^i , due to the heat flux from particle L can be determined from Eq. (17) as,

$$T_p^i = -Re_p \bar{Q}_{PL} + T_p^0 \quad (18)$$

On the other hand, the temperature at the m -th contact of particle L , T_L^m , due to the flux from particle P is calculated as,

$$T_L^m = Re_L \bar{Q}_{PL} + T_L^0 \quad (19)$$

where $Re_p = \frac{\lambda}{2\kappa_p R_p \Delta\phi_i}$ and $Re_L = \frac{\lambda}{2\kappa_L R_L \Delta\phi_m}$. Obviously, we have $T_p^i = T_L^m$ and $\Delta\phi_i = \Delta\phi_m$. By subtracting Eq. (19) from Eq. (18), we reach to the following equation for heat flux:

$$k_{PL} \begin{bmatrix} 1 & -1 \\ -1 & 1 \end{bmatrix} \begin{bmatrix} T_p^0 \\ T_L^0 \end{bmatrix} = \begin{bmatrix} Q^{PL} \\ -Q^{PL} \end{bmatrix} \quad (20)$$

where $k_{PL} = 1/(Re_p + Re_L)$.

Balancing the steady and transient terms in the heat conservation equation will yield the transient energy equation. Therefore, the energy equation governing the transient heat conduction in any individual particle p can be presented by,

$$C_p \dot{T}_p(t) + \sum_{j=1}^N Q_{pj} = 0 \quad (21)$$

where J stands for the neighbour particles having contact with particle P . In addition, using Eq. (20) we have $Q_{pj} = k_{pj} (T_j^0 - T_p^0)$, and $C_p = \frac{4}{3} \pi \rho R^3 c_p$. This equation can be solved by marching in time.

3. Discrete element method

In the discrete element method (DEM), the trajectory of any individual particle is calculated through successive time steps. Starting from an initial non-overlapping configuration of particles with certain initial velocity distribution, particle-particle and wall-particle overlaps are created in time. The overlaps create normal forces as well as history-dependent frictional forces and torques in all contact areas. As a result of having forces and torques at each time step, the translational and angular accelerations are known, which in turn, the velocity and position of particles are determined by proper integrations in time. It is worth mentioning that the contact forces are represented by a spring-dashpot model [22]. The Hertzian theory [13] relating the force and deformation of particles is employed to calculate the normal and tangential force components for a linear spring-dashpot model at contact points as [23,8]:

$$\mathbf{F}_n = \left(-K_n \delta_n^{\frac{3}{2}} - \eta_n \mathbf{v}_n \cdot \mathbf{e}_n \right) \mathbf{e}_n \quad (22)$$

$$\mathbf{F}_t = (-K_t \delta_t - \eta_t \mathbf{v}_s) \quad (23)$$

Here, K_n and K_t stand for spring normal and tangential stiffnesses, η_n and η_t are for damping coefficients of dashpots in the normal \mathbf{e}_n and tangential \mathbf{e}_t directions, respectively. In addition, the direction of \mathbf{F}_n always relies on the unit vector \mathbf{e}_n which is along the centerline of two particles i and j . The normal overlapping δ_n vector is simply calculated from the position of the centers of contacting particles and tangential displacement δ_t is obtained from $\delta_t = F_t/K_t$. Moreover, the direction of frictional (tangential) force \mathbf{F}_t is determined from the direction of relative slip velocity \mathbf{v}_s . The relative velocities of \mathbf{v}_s and \mathbf{v}_t are as follows:

$$\mathbf{v}_t = \mathbf{v}_i - \mathbf{v}_j \quad (24)$$

$$\mathbf{v}_s = \mathbf{v}_t - (\mathbf{v}_t \cdot \mathbf{n}) \mathbf{e}_n + 0.5(d_i \boldsymbol{\omega}_i + d_j \boldsymbol{\omega}_j) \times \mathbf{e}_n \quad (25)$$

where d and $\boldsymbol{\omega}$ are the diameter and angular velocity of a particle, respectively. It should be emphasized that Eq. (23) is only valid for sliding condition. In static condition, the tangential component of force should be calculated by $\mathbf{F}_t = -\mu |F_{cnij}| \mathbf{e}_t$ in which μ is the friction coefficient.

It should be mentioned that the normal and tangential spring stiffnesses K_n, K_t are obtained using the Hertzian contact theory for contacting spheres as follows:

$$K_n = \frac{4\sqrt{R_i R_j}}{3\left(\frac{1-\sigma_i^2}{E_i} + \frac{1-\sigma_j^2}{E_j}\right)\sqrt{R_i + R_j}} \quad (26)$$

$$K_t = \frac{8\sqrt{R_i R_j}}{3\left(\frac{1-\sigma_i^2}{G_i} + \frac{1-\sigma_j^2}{G_j}\right)\sqrt{R_i + R_j}} \delta_n^{\frac{3}{2}} \quad (27)$$

Here, σ , E , and $G = E(1 + \sigma)/2$ are Poisson's ratio, Young's modulus, and shear modulus, respectively. It is worth mentioning that the contact of particles and wall can be resolved using the same normal stiffness expression in which the radius of wall tends to infinity. On the other hand, the normal and tangential dashpot coefficients may be taken equal as:

$$\eta_n = \eta_t = \alpha(\bar{m}K_n)^{\frac{1}{2}}\delta_n^{\frac{3}{2}} \quad (28)$$

where $\bar{m} = \left(\frac{1}{m_i} + \frac{1}{m_j}\right)^{-1}$ is the reduced mass. α is a function of restitution coefficient e as:

$$\alpha = \frac{-\sqrt{5}\ln(e)}{\sqrt{\pi^2 + \ln^2(e)}} \quad (29)$$

The net force and torque on a particle is the summation on all contacts as follows:

$$\mathbf{F}_i = \sum_j (\mathbf{F}_{nij} + \mathbf{F}_{tij}) \quad (30)$$

$$\mathbf{T}_i = \frac{1}{2} \sum_j (d_i \mathbf{e}_n \times \mathbf{F}_{tij}) \quad (31)$$

Consequently, the linear and angular accelerations can be calculated as:

$$\mathbf{a}_i = \frac{\mathbf{F}_i}{m_i} + \mathbf{g} \quad (32)$$

$$\boldsymbol{\alpha}_i = \frac{\mathbf{T}_i}{I_i} \quad (33)$$

where \mathbf{g} is gravitational acceleration and I_i is the moment of inertia of particle i .

4. Results and discussion

In this section, a comparison is performed between the current model and other models in literature including the FEM. Then the packed beds under investigation are described and in continuation, the code is validated by comparing the results of simulations with analytical solution. Finally, the impact of compressive pressure on thermal conductivity is presented in different packed beds under various compressive pressures.

4.1. Present model versus existing ones

Considering two colliding particles, Batchelor and O'Brien [24], Carslow [25] and Yovanovich [26] have independently presented the following analytical formula for thermal conductivity assuming the same physical properties for both particles as:

$$k_{BOB} = 2\kappa_p \left(\frac{3F_n(1-\sigma^2)R_p}{4E} \right)^{\frac{1}{2}} \quad (34)$$

where F_n is the magnitude of normal contact force. In addition, Argento and Bouvard [27] have argued that Batchelor and O'Brien (BOB) formula is confined to small deformations. They tried to modify the BOB relation by introducing a fitting parameter calculated based on FEM simulations. Their proposed formula is:

$$k_{AB} = \frac{\pi}{2\beta} \kappa_p \left(\frac{3F_n(1-\sigma^2)R_p}{4E} \right)^{\frac{1}{2}} \quad (35)$$

in which the fitting parameter β is reported as 0.899. Later, Ott [28,29] used the same analogy by performing other FEM simulations and reported 0.952 as the value of parameter β . It is worth mentioning that according to Refs. [30–32], the basis of these models relies on uniform temperature distribution assumption inside particles which needs some modifications. They considered the conductivity of surrounding fluid as a reason to make the temperature distribution inside particles as non-uniform. Then they modified the thermal resistance by adding an additional term for a non-uniform temperature distribution. This additional term is only characterized by the surrounding fluid properties. Moreover, another source for non-uniform temperature distribution inside an individual particle is different contacts through which various heat fluxes coming in or going out of particle.

On the other hand, by using the definition of thermal resistance, we can derive a new thermal conductance formula as:

$$k_{New} = \frac{-2\kappa_p}{\lambda} \frac{1}{\frac{1}{R_p \Delta\phi_i} + \frac{1}{R_i \Delta\phi_m}} \quad (36)$$

By considering the same radius for particles, $R_p \Delta\phi_i = R_i \Delta\phi_m$. Then Eq. (36) will be reduced to:

$$k_{New} = \frac{-\kappa_p}{\lambda} R_p \Delta\phi_i \quad (37)$$

The value of $R_p \Delta\phi_i$ can be calculated using Euclid's formula which is: $[R_p \Delta\phi_i]^2 = \left(R_p^2 - \left(R_p - \frac{F_n}{K_n}\right)^2\right) = R_p \delta_n$. The normal deformation δ_n will be obtained by assuming two particles at rest and using Eq. (22) as $\delta_n = \left(\frac{F_n}{K_n}\right)^{\frac{2}{3}}$. As a result, we can conclude that:

$$R_p \Delta\phi_i = \sqrt{R_p} \left(\frac{F_n}{K_n}\right)^{\frac{1}{3}} \quad (38)$$

On the other hand, Eq. (26) will be simplified to the following equation by considering the same physical properties for both contacting particles:

$$K_n = \frac{4E}{6(1-\sigma^2)} \sqrt{\frac{R_p}{2}} \quad (39)$$

By substituting Eq. (39) into (38) and Eq. (38) into (37), the thermal conductivity will be obtained as:

$$k_{New} = 2.066\kappa_p \left(\frac{3F_n(1-\sigma^2)R_p}{4E} \right)^{\frac{1}{2}} \quad (40)$$

The thermal conductivity obtained in Eq. (40) is similar to the BOB equation presented in Eq. (34). The thermal conductivity of a contacting pair of particles, with the physical properties tabulated in Table 1, are plotted versus the imposed load in Fig. 2b. As this figure illustrates, the new equation is pretty close to the BOB model (~3 percent difference). However, the difference with

Table 1
Simulation parameters.

Particle density	ρ	2500 $\frac{\text{kg}}{\text{m}^3}$
Particle radius	R_p	0.002 m
Radius of packed bed	R_c	0.0305 m
Poissons ratio of particle	σ	0.2
Restitution coefficient	e	0.865
Modulus of longitudinal elasticity	E	5×10^{10} Pa
Friction coefficient	μ	0.3
Gravity acceleration	g	9.81 $\frac{\text{m}}{\text{s}^2}$
Thermal conductivity	κ	205 $\frac{\text{W}}{\text{m}\cdot\text{K}}$
Specific heat	c_p	900 $\frac{\text{J}}{\text{kg}\cdot\text{K}}$

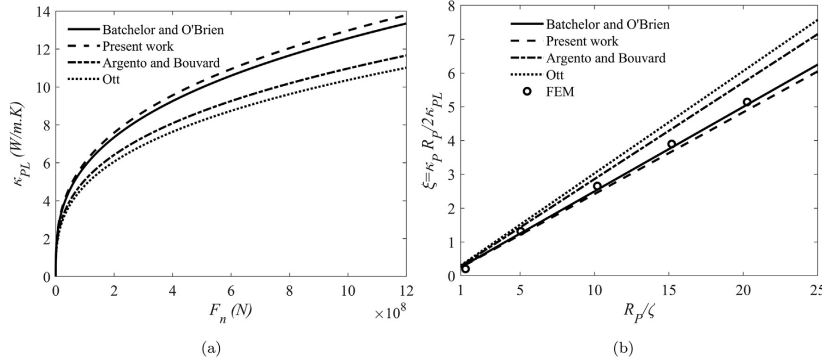


Fig. 2. Comparison of various models for (a) thermal conductivity versus normal compressive force (b) dimensionless parameter ξ versus dimensionless parameter $\frac{R_p}{\chi}$.

other equations could be due to the fact that the effects of all contacts are accumulated in the new model. As a result, a higher heat flux makes a higher thermal conductance.

By introducing $\zeta = \left(\frac{3f_n(1-\sigma^2)R_p}{4E} \right)^{\frac{1}{2}}$ and two dimensionless parameters of $\frac{R_p}{\zeta}$ and $\xi = \frac{\kappa_P R_p}{2\kappa_{PL}}$, the new model is compared with other models, including FEM simulations of [29], in Fig. 2b. This figure depicts the new model is fairly close to the BOB model as well as FEM simulations.

4.2. Case study

The studied case is a cylindrical packed bed built using the DEM code in which a non-overlapping dilute particle configuration settles down under gravitational force to create a dense packed bed. The radius of packed bed is $R_c = 30.5$ mm which contains 7500 particles with the physical properties of aluminium listed in Table 1. It is worth mentioning that the performance of the model should not be dependent of physical properties including the range of thermal conductivity.

To construct the packed bed, the position of non-overlapping particles are generated randomly inside the cylindrical chamber. Then they fall down under gravity and eventually stack a dense pack. After completion of particles settlement, the system is compressed by moving the upper plate downward with the rate of $4 \frac{\text{mm}}{\text{s}}$ for a certain time to deliver a desired compressive force. The granular packed bed is illustrated in Fig. 3. This figure demonstrates two packed beds under the compressive forces of 4770 N (left) and 1.184×10^5 N (right). The corresponding pressures are 16 bar and 405 bar, respectively. The particles configuration under the achieved compressive force is taken to perform the calculations of the conduction problem, which will be presented in Section 4.4. The height of the bed is decreased by 12.1 mm (3.025 d) and 2.9 mm (0.725 d) due to the compressive forces of 1.184×10^5 N and 4770 N, respectively. It can be directly observed from the two stacks that compression leads to highly ordered packing. The detailed analysis of packing structures with their connection to the compression and heat conduction will be studied in future works.

The force exerted on the upper plate during the compression is plotted versus time in Fig. 4. In fact, this force is obtained while the upper plate moves downward with a uniform rate of $4 \frac{\text{mm}}{\text{s}}$. Before looking into the dependence of the ETC on the compressive

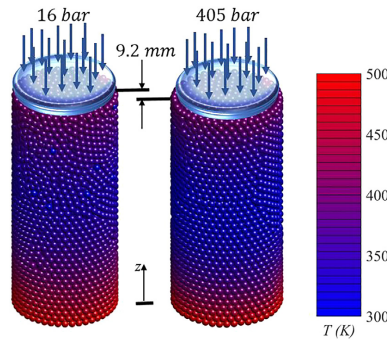


Fig. 3. Packed beds used in simulations; (left) the compressive force of 4770 N (pressure of 16 bar) exerted on the bed and (right) the compressive force of 1.184×10^5 N (pressure of 405 bar). Colors of particles represent their temperatures at $t = 0.5$ s.

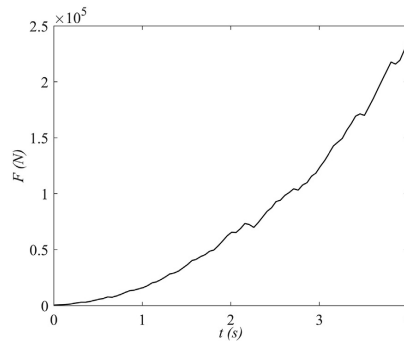


Fig. 4. Variation of the force exerted on the upper plate versus time during compression.

pressure, one may have an insight into the possible role of structural characteristics. For this purpose, we find the azimuthal angle of contacts, shown by ϕ_c , which is measured for each contact of the central particle in the coordinate system attached to the particle as shown in Fig. 1a. Fig. 5 demonstrates the probability distribution function (PDF) of ϕ_c in the two packs compressed with 16 and 405 bars. Interestingly, the fingerprint of high compression can be observed as a peak appearing at $\phi_c \approx \pi/3$ for the high pressure of 405 bar. Moreover, the PDF at high pressure relatively drops in $\pi/6 < \phi_c < \pi/3$. The decrease of contacts in this range of ϕ_c can reduce the vertical heat flux (the direction of imposed temperature gradient). This leads to the reduction of the effective conductivity in vertical direction. Note that the decay of PDF within $\pi/2 > \phi_c > 2\pi/5$ for high pressure is not as important as that within $\pi/6 < \phi_c < \pi/3$. This is because the role of horizontally oriented contacts is of less importance as they are perpendicular to the temperature gradient carrying insignificant heat fluxes.

4.3. Comparison to analytical solution

The results of the TDEM code is performed are compared to the analytical predictions presented in Appendix A. Two distinguished

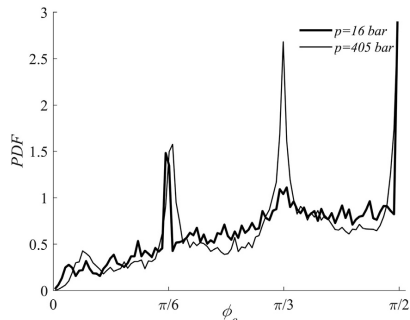


Fig. 5. Probability distribution function (PDF) of azimuthal angular position of contacts measured in coordinates attached to central particles.

thermal cases are considered, in both of which the temperature at the bottom of bed is kept at 500 K. In the first case, the top wall and initial temperatures of entire particles are set to 300 K and 400 K, respectively. In the second case, the top wall and initial temperatures of entire particles are set to 400 K and 300 K, respectively. The temperatures of the top and bottom walls are kept fixed in time for both cases.

Fig. 6a depicts the temperature profile along the bed for the first case obtained from the analytical solution and the TDEM. For TDEM, the mean temperature is calculated for any bin centered at a cross section of given heights. Mean temperature of a bin is calculated as the weighted average of particles temperatures within the bin weighted by the partial volume of particles lying in the bin. The results shown in Fig. 6a indicate that the TDEM results matches closely to the analytical solution. Additionally, the results corresponding to the second case are demonstrated in Fig. 6b. These results also confirm that the TDEM data closely match to those of the analytical solution in various times.

It should be noted that in the analytical solution presented in Appendix A, the ETC of the bed is present in the formulas. The ETC can be assumed proportional to the particle conductivity as $\kappa_{eff} = \gamma \kappa_p$, in which κ_p is the particle thermal conductivity and γ is the coefficient of proportionality [33–35]. This coefficient γ can be obtained by matching the TDEM and analytical results in any packing under a certain compressive pressure, which is shown in Fig. 7. This figure indicates that γ depends on the compressive pressure exponentially, which means it drops sharply with pressure by an order of magnitude with little changes within a wide range of pressure increase.

4.4. Effect of compressive pressure on thermal conduction

In this section, the compressive pressure on the packed bed is varied and it is demonstrated how it affects on the thermal conduction features. First, the profiles of temperature are shown in Fig. 8a–d at different times for 4 different pressures ranging from 0.28 bar to 405 bar. The boundary values of temperature are 500 K and 400 K for the bottom and top walls, respectively. The initial temperature of bed particles is 300 K. As Fig. 8 illustrates, the compressive pressure delays the evolution of temperature profile to the steady one. The temperature profile already develops to

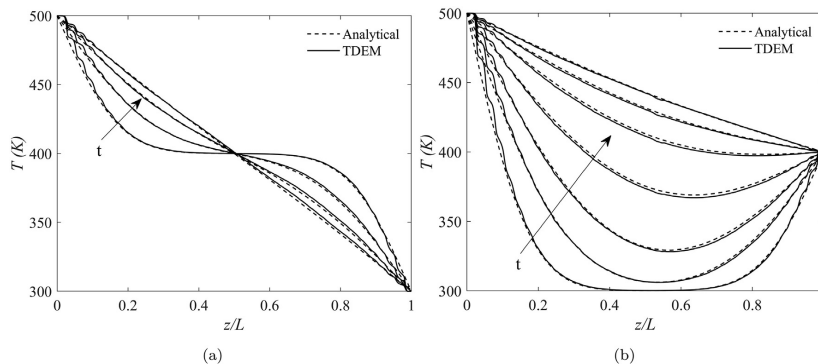


Fig. 6. Temperature profile at different times for analytical (dash line) and TDEM (solid line) results for (a) first case and (b) second case. (a) Temperature of the bottom and top walls are 500 K and 300 K, respectively. Initial temperature of particles is 400 K. Different lines represent the times of $t = 0.2, 0.5, 1.0, 2.0$ s. (b) Temperature of the bottom and top walls are 500 K and 400 K, respectively. Initial temperature of particles is 300 K. Different lines for the times of $t = 0.2, 0.5, 1.0, 2.0, 3.5, 5.0, 7.0$ s. The arrows show the direction of time increase in both parts.

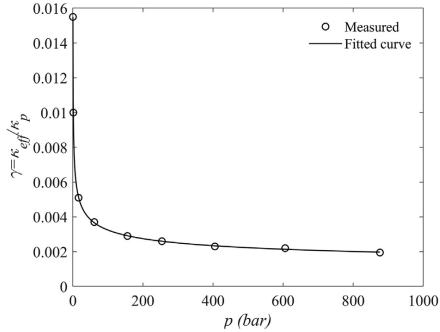


Fig. 7. Variation of γ vs. compression pressure. The fitted function for γ is obtained as $\gamma = 0.01039p^{-0.2919} + 5.353 \times 10^{-4}$.

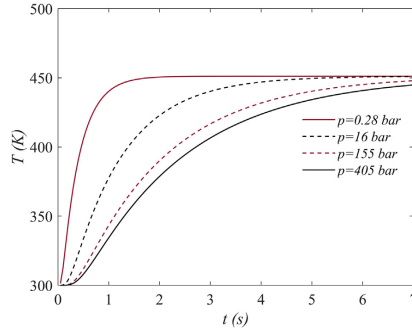


Fig. 9. Time evolution of temperature at the middle of packed bed under different compressive pressures.

the steady one at $t = 2$ s for the pressure of 0.28 bar, while it is still under development for the greater pressures. It is evident that as pressure rises, the delay in developing the temperature profile increases. The thermal response of the system becomes fairly similar for the compressive pressures of 155 bar and 405 bar.

In order to clarify the time evolution of temperature under various compressive pressures, the variation of temperature at the middle of the bed is demonstrated with time in Fig. 9 for the compressive pressures mentioned above. An immediate observation from this figure is that the local temperature reaches to the steady

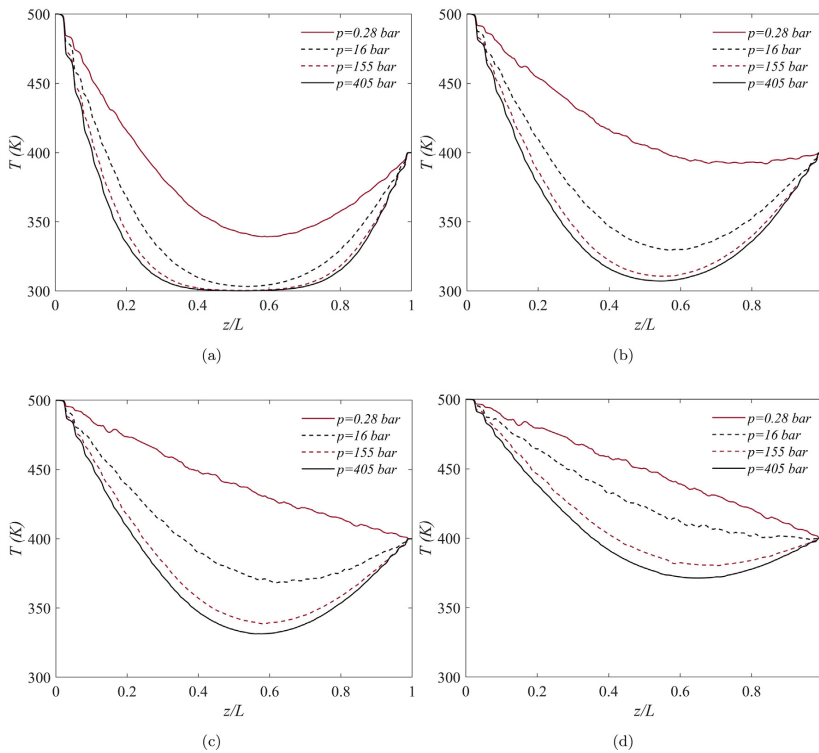


Fig. 8. Temperature profiles in the packed beds under different compressive pressures at (a) 0.2 s (b) 0.5 s (c) 1 s (d) 2 s.

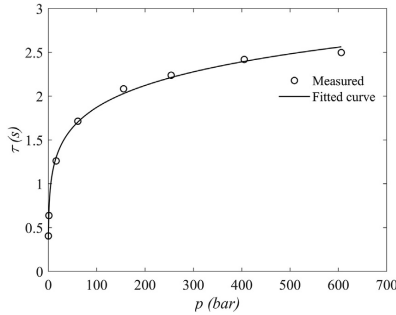


Fig. 10. Variation of conduction characteristic time versus compressive pressure. The fitted line is $\tau = 1.945p^{0.1084} - 1.332$.

state value much earlier in the lowest pressure than those in the higher pressures. Therefore, one may define a conduction characteristic time as,

$$\tau = \frac{\int_0^{\infty} (T_{\text{steady}} - T) dt}{T_{\text{steady}} - T_{\text{init}}} \quad (41)$$

Here, T_{steady} is the steady state temperature, T_{init} is the initial temperature and $T(t)$ is the temperature of the section as a function of time. The variation of the characteristic time in the packs under different compressive pressures are shown versus the compressive pressure in Fig. 10. This figure reveals that the characteristic time increases with compressive pressure in a power of pressure as about 0.1, that is, it increases rapidly in lower pressures below 80 bar and it grows in a slower rate beyond this pressure.

5. Conclusion

In this paper, a novel thermal discrete element method (TDEM) is introduced to resolve heat conduction in the packs of spherical particles, though it can be also extended to any arbitrary shape of particles. This model can be implemented in both static and dynamic packs with transient heat conduction. Simulations were performed on various dense packs generated using an in-house code of DEM. The dense packs were obtained by releasing non-overlapping particles to settle at the bottom of a cylindrical container due to the gravity. After the gravity driven settlement, the upper plate was pushed down with a small constant velocity to exert a desired compressive pressure on the bed. The compressed bed was then fed to the TDEM code to perform conduction simulations. First, the code was validated by the analytical solution in which the ratio of medium conductivity to the particle conductivity was obtained by matching up the TDEM solution with the analytical solution. Then the simulation code was utilized to determine how the compressive pressure affects the conduction by showing the evolution of temperature profiles in time under various pressures. Also, the conduction characteristic time was calculated based on the local variation of temperature under different compressive pressures. These results revealed that the effective conductivity of the packed bed is proportional to the particle thermal conductivity and the coefficient of proportionality depends on the compressive pressure exponentially. Moreover, it was shown that increasing the compressive pressure slows down the heat conduction, which can be connected to the role of pressure in decreasing the effective conductivity. In this regard, it was demonstrated that the conduction characteristic time is described by a power

function of the pressure. The decay of effective conductivity with pressure may be associated with the changes in contacts and the mean direction of the centerlines at contact points. This will be investigated in future studies in details.

Declaration of Competing Interest

The authors declared that there is no conflict of interest.

Acknowledgment

Authors would like to acknowledge the financial support for this work by the SIM-Platform at LUT, and also the Academy of Finland under Grant No. 311138.

Appendix A. Analytical solution of energy equation

Here, the energy equation of (A1) is analytically solved for granular packed beds. By averaging the solid volume fraction (SVF) over each cross section, the 3D problem is simplified to 1D problem with the equation as:

$$\frac{\partial T}{\partial t} = \alpha_T \frac{\partial^2 T}{\partial x^2} \quad \text{in } \Omega \quad (A1)$$

which is subject to the initial and boundary conditions of:

$$\begin{aligned} T(0, t) &= T_0 \\ T(L, t) &= T_L \\ T(x, 0) &= T_{\text{init}} \end{aligned} \quad (A2)$$

Here, $\alpha_T = \frac{\kappa_{\text{eff}}}{\rho c_p}$ is the thermal diffusivity and κ_{eff} is the effective thermal conductivity of bed. Introducing $T(x, t) = v(x) + w(x, t)$, the problem can be simplified as:

$$\frac{\partial w}{\partial t} = \alpha_T \frac{\partial^2 w}{\partial x^2} \quad \text{in } \Omega \quad (A3)$$

with the initial and boundary conditions of:

$$\begin{aligned} w(0, t) &= T_0 - v(0) \\ w(L, t) &= T_L - v(L) \\ w(x, 0) &= T_{\text{init}} - v(x) \end{aligned} \quad (A4)$$

As a result, $v(x)$ should be such that the boundary conditions are homogeneous, i.e., $v(x) = T_0 + \frac{x}{L}(T_L - T_0)$. Therefore, the final solution for $T(x, t)$ is obtained as:

$$T(x, t) = T_0 + \frac{x}{L}(T_L - T_0) + \sum_{m=1}^{\infty} C_m \exp\left(-\frac{m^2 \pi^2 \alpha_T t}{L^2}\right) \sin\left(\frac{m\pi x}{L}\right) \quad (A5)$$

where

$$C_m = \frac{2}{m\pi} T_{\text{in}} [1 - (-1)^m] + \frac{2}{m\pi} [(-1)^m T_L - T_0] \quad (A6)$$

References

- [1] P. Jalali, M. Nikku, J. Ritvanen, T. Hyppänen, Flow characteristics of circulating fluidized beds near terminal velocity: Eulerian model of a lab-scale apparatus, *Powder Technol.* 339 (2018) 569–584.
- [2] M. Kiani-Oshorjani, P. Jalali, Thermal and hydraulic properties of sphere packings using a novel lattice Boltzmann model, *Int. J. Heat Mass Transf.* 130 (2019) 98–108.
- [3] H. Zhang, Y. Zhao, F. Wang, D. Li, A 3D discrete element-finite difference coupling model for predicting the effective thermal conductivity of metal powder beds, *Int. J. Heat Mass Transf.* 132 (2019) 1–10.
- [4] J. Chen, H. Wang, L. Li, Determination of effective thermal conductivity of asphalt concrete with random aggregate microstructure, *J. Mater. Civ. Eng.* 27 (12) (2015) 4015045.
- [5] A.S. Sattari, Z.H. Rizvi, H.B. Motra, F. Wuttke, Meso-scale modeling of heat transport in a heterogeneous cemented geomaterial by lattice element method, *Granular Matter* 19 (4) (2017) 66.

- [6] Z.H. Rizvi, D. Shrestha, A.S. Sattari, F. Wuttke, Numerical modelling of effective thermal conductivity for modified geomaterial using lattice element method, *Heat Mass Transf.* 54 (2) (2018) 483–499.
- [7] H. Suikkanen, J. Ritvanen, P. Jalali, R. Kyrki-Rajamäki, Discrete element modelling of pebble packing in pebble bed reactors, *Nucl. Eng. Des.* 273 (2014) 24–32.
- [8] P. Jalali, T. Hyppänen, Momentum transport between two granular phases of spherical particles with large size ratio: two-fluid model versus discrete element method, *Powder Technol.* 273 (2015) 13–18.
- [9] W.W.M. Siu, S.-K. Lee, Transient temperature computation of spheres in three-dimensional random packings, *Int. J. Heat Mass Transfer* 47 (5) (2004) 887–898.
- [10] Y.T. Feng, K. Han, C.F. Li, D.R.J. Owen, Discrete thermal element modelling of heat conduction in particle systems: basic formulations, *J. Comput. Phys.* 227 (10) (2008) 5072–5089.
- [11] Y.T. Feng, K. Han, D.R.J. Owen, Discrete thermal element modelling of heat conduction in particle systems: pipe-network model and transient analysis, *Powder Technol.* 193 (3) (2009) 248–256.
- [12] J. He, Q. Liu, Z. Wu, X. Xu, Modelling transient heat conduction of granular materials by numerical manifold method, *Eng. Anal. Boundary Elem.* 86 (2018) 45–55.
- [13] E. Tsotsas, Particle-particle heat transfer in thermal DEM: three competing models and a new equation, *Int. J. Heat Mass Transf.* 132 (2019) 939–943.
- [14] Y. Liang, H. Niu, Y. Lou, Expression for ETC of the solid phase of randomly packed granular materials, *Appl. Therm. Eng.* 109 (2016) 44–52.
- [15] W. Van Antwerpen, C.G. Du Toit, P.G. Rousseau, A review of correlations to model the packing structure and effective thermal conductivity in packed beds of mono-sized spherical particles, *Nucl. Eng. Des.* 240 (7) (2010) 1803–1818.
- [16] C.-W. Nan, R. Birringer, D.R. Clarke, H. Gleiter, Effective thermal conductivity of particulate composites with interfacial thermal resistance, *J. Appl. Phys.* 81 (10) (1997) 6692–6699.
- [17] M.H. Esfe, S. Saedodin, S. Wongwises, D. Toghraie, An experimental study on the effect of diameter on thermal conductivity and dynamic viscosity of Fe/water nanofluids, *J. Therm. Anal. Calorim.* 119 (3) (2015) 1817–1824.
- [18] C.H. Li, G.P. Peterson, Experimental investigation of temperature and volume fraction variations on the effective thermal conductivity of nanoparticle suspensions (nanofluids), *J. Appl. Phys.* 99 (8) (2006) 84314.
- [19] Y. Liang, Expression for effective thermal conductivity of randomly packed granular material, *Int. J. Heat Mass Transf.* 90 (2015) 1105–1108.
- [20] O.B. Kovalev, A.V. Gusarov, Modeling of granular packed beds, their statistical analyses and evaluation of effective thermal conductivity, *Int. J. Therm. Sci.* 114 (2017) 327–341.
- [21] A. Arzhang, A survey on Christoffel–Darboux type identities of Legendre, Laguerre and Hermite polynomials, *Math. Sci.* 9 (4) (2015) 193–197.
- [22] Y. Tsuji, T. Tanaka, T. Ishida, Lagrangian numerical simulation of plug flow of cohesionless particles in a horizontal pipe, *Powder Technol.* 71 (3) (1992) 239–250.
- [23] P. Jalali, M. Nikku, T. Hyppänen, Particle-cloud drag force in dilute particle systems: discrete element method versus Eulerian simulations, *Ind. Eng. Chem. Res.* 52 (11) (2013) 4342–4350.
- [24] G.K. Batchelor, R.W. O'Brien, Thermal or electrical conduction through a granular material, *Proc. Roy. Soc. London. A. Math. Phys. Sci.* 355 (1682) (1977) 313–333.
- [25] H.S. Carslaw, J.C. Jaeger, *Conduction of Heat in Solids*, second ed., Clarendon Press, Oxford, 1959.
- [26] M.M. Yovanovich, Thermal contact resistance across elastically deformed spheres, *J. Spacecraft Rockets* 4 (1) (1967) 119–122.
- [27] C. Argento, D. Bouvard, Modeling the effective thermal conductivity of random packing of spheres through densification, *Int. J. Heat Mass Transf.* 39 (7) (1996) 1343–1350.
- [28] J.K. Ott, *Modeling the microstructural and micromechanical influence on effective properties of granular electrode structures: with regard to solid oxide fuel cells and lithium ion batteries*, 2015.
- [29] O. Birkholz, Y. Gan, M. Kamlah, Modeling the effective conductivity of the solid and the pore phase in granular materials using resistor networks, *Powder Technol.* 351 (2019) 54–65.
- [30] W. Dai, D. Hanaor, Y. Gan, The effects of packing structure on the effective thermal conductivity of granular media: a grain scale investigation, *Int. J. Therm. Sci.* 142 (2019) 266–279.
- [31] M. Moscardini, Y. Gan, S. Papeschi, M. Kamlah, Discrete element method for effective thermal conductivity of packed pebbles accounting for the Smoluchowski effect, *Fusion Eng. Des.* 127 (2018) 192–201.
- [32] A.R. Peeketi, M. Moscardini, A. Vijayan, Y. Gan, M. Kamlah, R.K. Annabattula, Effective thermal conductivity of a compacted pebble bed in a stagnant gaseous environment: an analytical approach together with dem, *Fusion Eng. Des.* 130 (2018) 80–88.
- [33] M. Kwapinska, G. Saage, E. Tsotsas, Continuous versus discrete modelling of heat transfer to agitated beds, *Powder Technol.* 181 (3) (2008) 331–342.
- [34] I. Terreros, I. Iordanoff, J.-L. Charles, Simulation of continuum heat conduction using DEM domains, *Comput. Mater. Sci.* 69 (2013) 46–52.
- [35] H. Zhong, J.R. Lukes, Interfacial thermal resistance between carbon nanotubes: molecular dynamics simulations and analytical thermal modeling, *Phys. Rev. B* 74 (12) (2006) 125403.

ACTA UNIVERSITATIS LAPPEENRANTAENSIS

906. JOHN, MIIA. Separation efficiencies of freeze crystallization in wastewater purification. 2020. Diss.
907. VUOJOLAINEN, JOUNI. Identification of magnetically levitated machines. 2020. Diss.
908. KC, RAGHU. The role of efficient forest biomass logistics on optimisation of environmental sustainability of bioenergy. 2020. Diss.
909. NEISI, NEDA. Dynamic and thermal modeling of touch-down bearings considering bearing non-idealities. 2020. Diss.
910. YAN, FANGPING. The deposition and light absorption property of carbonaceous matter in the Himalayas and Tibetan Plateau. 2020. Diss.
911. NJOCK BAYOCK, FRANCOIS MITERAND. Thermal analysis of dissimilar weld joints of high-strength and ultra-high-strength steels. 2020. Diss.
912. KINNUNEN, SINI-KAISU. Modelling the value of fleet data in the ecosystems of asset management. 2020. Diss.
913. MUSIKKA, TATU. Usability and limitations of behavioural component models in IGBT short-circuit modelling. 2020. Diss.
914. SHNAI, IULIA. The technology of flipped classroom: assessments, resources and systematic design. 2020. Diss.
915. SAFAEI, ZAHRA. Application of differential ion mobility spectrometry for detection of water pollutants. 2020. Diss.
916. FILIMONOV, ROMAN. Computational fluid dynamics as a tool for process engineering. 2020. Diss.
917. VIRTANEN, TIINA. Real-time monitoring of membrane fouling caused by phenolic compounds. 2020. Diss.
918. AZZUNI, ABDELRAHMAN. Energy security evaluation for the present and the future on a global level. 2020. Diss.
919. NOKELAINEN, JOHANNES. Interplay of local moments and itinerant electrons. 2020. Diss.
920. HONKANEN, JARI. Control design issues in grid-connected single-phase converters, with the focus on power factor correction. 2020. Diss.
921. KEMPPINEN, JUHA. The development and implementation of the clinical decision support system for integrated mental and addiction care. 2020. Diss.
922. KORHONEN, SATU. The journeys of becoming and being an international entrepreneur: A narrative inquiry of the "I" in international entrepreneurship. 2020. Diss.
923. SIRKIÄ, JUKKA. Leveraging digitalization opportunities to improve the business model. 2020. Diss.
924. SHEMYAKIN, VLADIMIR. Parameter estimation of large-scale chaotic systems. 2020. Diss.

925. AALTONEN, PAIVI. Exploring novelty in the internationalization process - understanding disruptive events. 2020. Diss.
926. VADANA, IUSTIN. Internationalization of born-digital companies. 2020. Diss.
927. FARFAN OROZCO, FRANCISCO JAVIER. In-depth analysis of the global power infrastructure - Opportunities for sustainable evolution of the power sector. 2020. Diss.
928. KRAINOV, IGOR. Properties of exchange interactions in magnetic semiconductors. 2020. Diss.
929. KARPPANEN, JANNE. Assessing the applicability of low voltage direct current in electricity distribution - Key factors and design aspects. 2020. Diss.
930. NIEMINEN, HARRI. Power-to-methanol via membrane contactor-based CO₂ capture and low-temperature chemical synthesis. 2020. Diss.
931. CALDERA, UPEKSHA. The role of renewable energy based seawater reverse osmosis (SWRO) in meeting the global water challenges in the decades to come. 2020. Diss.
932. KIVISTÖ, TIMO. Processes and tools to promote community benefits in public procurement. 2020. Diss.
933. NAQVI, BILAL. Towards aligning security and usability during the system development lifecycle. 2020. Diss.
934. XIN, YAN. Knowledge sharing and reuse in product-service systems with a product lifecycle perspective. 2020. Diss.
935. PALACIN SILVA, VICTORIA. Participation in digital citizen science. 2020. Diss.
936. PUOLAKKA, TIINA. Managing operations in professional organisations – interplay between professionals and managers in court workflow control. 2020. Diss.
937. AHOLA, ANTTI. Stress components and local effects in the fatigue strength assessment of fillet weld joints made of ultra-high-strength steels. 2020. Diss.
938. METSOLA, JAAKKO. Good for wealth or bad for health? Socioemotional wealth in the internationalisation process of family SMEs from a network perspective. 2020. Diss.
939. VELT, HANNES. Entrepreneurial ecosystems and born global start-ups. 2020. Diss.
940. JI, HAIBIAO. Study of key techniques in the vacuum vessel assembly for the future fusion reactor. 2020. Diss.
941. KAZARNIKOV, ALEXEY. Statistical parameter identification of reaction-diffusion systems by Turing patterns. 2020. Diss.
942. SORMUNEN, PETRI. Ecodesign of construction and demolition waste-derived thermoplastic composites. 2020. Diss.
943. MANKONEN, ALEKSI. Fluidized bed combustion and humidified gas turbines as thermal energy conversion processes of the future. 2020. Diss.



ISBN 978-952-335-608-5
ISBN 978-952-335-609-2 (PDF)
ISSN-L 1456-4491
ISSN 1456-4491
Lappeenranta 2020